UNIVERSITÀ DEGLI STUDI DI MILANO
FACOLTÀ DI SCIENZE MM.FF.NN.

SCUOLA DI DOTTORATO DI RICERCA IN FISICA, ASTROFISICA E FISICA APPLICATA

ELECTRON AND PHOTON ENERGY RECONSTRUCTION IN THE ELECTROMAGNETIC CALORIMETER OF ATLAS

Tutore: Prof. L. MANDELLI

Coordinatore: Prof. G. BELLINI

Candidato: Dott. Danilo BANFI

Settore scientifico : FIS/04

ANNO ACCADEMICO 2005-2006
CICLO XIX

Contents

List of Figures

List of Tables

Chapter 1

LHC and Atlas

In this chapter the main features of the Large Hadron Collider (LHC) [1] and some details of the Atlas (A Toroidal Lhc ApparatuS) [2] experiment will be briefly introduced. The relevant accelerator parameters and the physics program allowed by the machine potential will be reviewed, trying to give an overview of the main aspects of the experimental working conditions at the LHC.

1.1 Introduction to LHC

1.1.1 Machine parameters and physics program

The Large Hadron Collider (LHC) [1] is a proton-proton and heavy-ion collider with a center-of-mass energy, when operating in the pp mode, of 14 TeV .

The first beam-beam collision are planned in November 2007 at low energy in a test run. First collisions at high energy are expected mid-2008.

The Large Hadron Collider is being built in the circular tunnel previously devoted to LEP, 27 km long. The tunnel is buried around 50 to 175 m. underground. It straddles the Swiss and French borders on the outskirts of Geneva.

The magnetic field needed to keep the beam circulating in the machine is provided by 1232 superconducting dipoles providing a 8.4 Tesla magnetic field. Bunches of protons, separated by 25 ns and with an RMS length of 75 mm, intersect at four points, as shown in figure (1.1), where experiments are placed: Atlas and CMS are general-purpose experiments designed for both searches for new physics signatures and precision measurements. LHCb is a B physics and CP violation dedicated detector while ALICE is an heavy ion experiment which will study the behavior of nuclear matter at very high energies and densities.

The LHC project will allow an ambitious physics program [3]. The main topics are briefly summarized in the following list:

- Search for a Standard Model Higgs . If an Higgs boson will be discovered, its mass, width and couplings could be measured.

- Search for Supersymmetry , Extra Dimensions and other signals of physics beyond the Standard Model up to masses $\backsim$ of 5 TeV
- Precision measurements of the SM observables such as the W and top quark masses and couplings.
- B physics and CP violation in the B hadron systems.
- Study of phase transitions from hadronic matter to a plasma of deconfined quarks and gluons.

1.1.2 Experimental environment

The high center-of-mass energy and luminosity impose to the LHC experiments to deal with complex working conditions: the review presented in the following sections will be focused on general purpose detectors.

Two operational phases are foreseen for the LHC: a first “low luminosity” phase, in the first year, with a luminosity $\mathcal{L} \simeq 10^{33} cm^{-2} s^{-1}$; the “high luminosity phase”,$\mathcal{L} \simeq 10^{34} cm^{-2} s^{-1}$, will be reached later. The machine will also be able to accelerate heavy ions allowing for example Pb-Pb collisions at 1150 TeV in the center of mass and luminosity up to $10^{27}\mathrm{cm}^{-2}\ \mathrm{s}^{-1}$. The nominal pp luminosity and center of mass energy

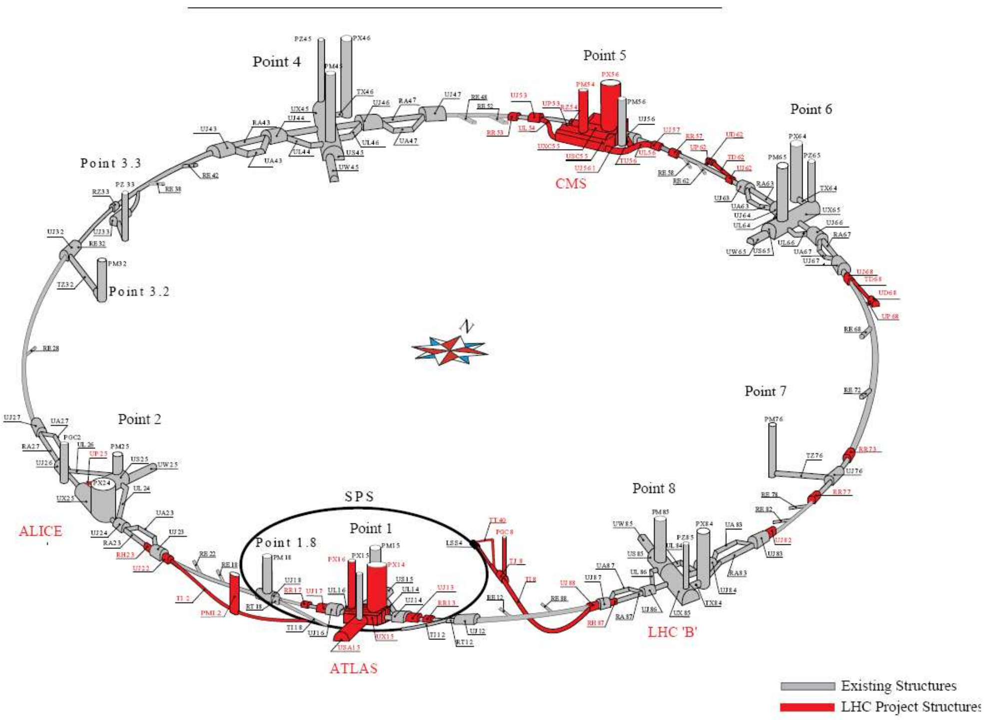

Figure 1.1: Visual of the LHC sites for the experiments

will allow to search for new particle with masses up to ∼5 TeV. In one year of running at high luminosity LHC will provide an integrated luminosity of:

$$L = \int_{10^7 s} \mathcal{L} dt \simeq 100 fb^{-1} \tag{1.1}$$

The total inelastic pp cross-section at a center of mass energy of 14 TeV is $\sigma_{pp}^{tot} \simeq 80mb$. So the event rate R expected at high luminosity is

$$R = \sigma_{pp}^{tot} \times \mathcal{L} = 80mb \times 10^{34} cm^{-2} s^{-1} \simeq 10^9 s^{-1} \tag{1.2}$$

The physics events that will occur at LHC could be classified as follow:

- **hard collisions** : they are due to short range interactions in which head-on collisions take place between two partons of the incoming protons. In these interactions the momentum transfer can be large, allowing the production of final states with high p_T particles and the creation of new massive particles. At the LHC the high p_T events are dominated by QCD jet production from quarks and gluons fragmentation in the final state which has a large cross section. Rare events with new particle production have a cross section which is usually some orders of magnitude smaller than the jet production and therefore hadronic final state can not be used to detect rare events such as SM higgs boson decay: in these conditions only decays into leptons and photons can be used even if their branching ratio are much smaller than decays into quarks

- **soft collisions** : they are due to long-distance collisions between the two incoming protons. The final state particles from soft collisions have large longitudinal momentum and a small transverse momentum with $< p_T > \simeq$ 500 MeV. These events are also called *minimum bias events* and represent by far the majority of the pp collision.

1.1.3 LHC experimental challenges

The LHC detectors have to face severe constrains , most of them related to the machine bunch crossing frequency , luminosity , and to the physics of the pp collisions.

The LHC protons are grouped in bunches of $\sim 10^{11}$, colliding every 25 ns at each interacting point. At the interaction rate for the high luminosity phase, on average 25 *minimum bias* events (soft interaction) will occur every bunch crossing. These interactions will produce around 700 charged particles in the detector pseudorapidity region $|\ \eta\ | \leq 2.5$. For each high p_T event , ∼25 additional soft events will be produced and overlap to the interesting one (*pile-up*).

To face with the severe condition imposed by the LHC machine the detectors have stringent requirement, like the one listed below :

- **Response time** : a fast detector response is required to minimize the pile-up. The response time is different for the various subdetectors and represents the best compromise between technological limits and detector features.

- **Granularity** : To reduce the impact of the pile-up, detectors with high granularity are required: this imply a large number of read-out channels with a challenging acquisition, calibration and monitoring system.

- **Radiation tolerance** : the radiation flux coming from the pp collision, depends on the subdetector position with respect to the intaction point. In the forward region, for example, the integrated flux of particle over ten years of operation in the high luminosity conditions will amounts up to $\backsim 10^{17}$ neutrons/cm^{-2} and $\sim 10^{7}$ Gy. Due to this huge particle flux all subdetector components should pass severe radiation hardness criteria.

- **Hermeticity** : at hadron colliders the energy of interacting quarks and gluons is not known and therefore the missing energy in the final state cannot be determined. On the other hand the initial total transverse momentum is negligible and the missing transverse momentum can be measured with an acceptable accuracy provided that the calorimeter system has full coverage in the azimuthal angle and in the $|\eta| \leq 5$ region.

- **Mass and momentum resolution** : excellent mass and momentum resolution is needed for particles decaying into photons, electrons and muons. Leptons should be identified and measured over a p_T range from a few GeV up to a few TeV.

- **Particle identification capabilities** : particle identification is a crucial point at the LHC. Several stringent requirements on the identification of electrons, photons, b-jets , taus, etc. must be satisfied.

- **Trigger** : the trigger is another critical issue in the LHC experiments. The interaction rate of 10^{9} ev/s must be reduced to $\backsim 100$ recorded ev/s due to the storage system limits. Therefore an efficient and selective trigger is needed to provide the required 10^{7} rejection factor.

1.2 The Atlas Detector

The Large Hadron Collider opens a new frontier in particle physics due to its higher collision energy and luminosity compared to the existing accelerators. The guiding principle in optimizing the Atlas experiment has been maximizing the discovery potential for new physics such as Higgs bosons and supersymmetric particles, while keeping the capability of high-accuracy measurements of known objects such as heavy quarks and gauge bosons.

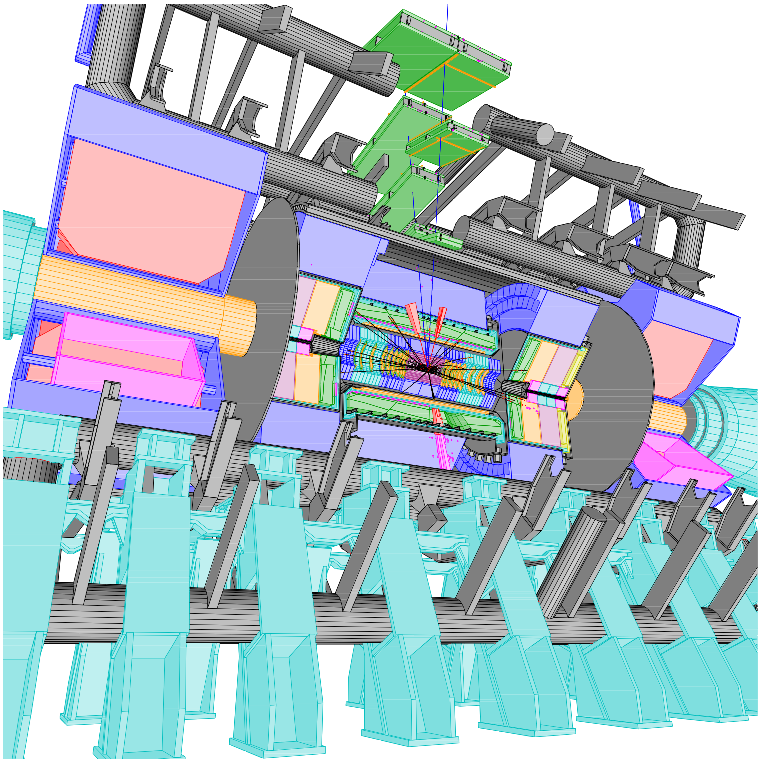

Figure 1.2: Global view of Atlas detector, with a simulated events

The Atlas [2], shown in figure (1.2) design is typical of a large scale multi-purpose detector. An inner detector in a 2 T solenoidal magnetic field is used to select and measure charged particles momentum as well as to detect secondary vertexes. The calorimeter system consists of an electromagnetic calorimeter for energy and position reconstruction of electrons and photons followed, in the radial direction by an hadronic calorimeter which, joined to the electromagnetic calorimeter, gives a measure of hadrons and jets energy and position. The calorimeters provide also a missing transverse momentum measure and contribute to the particle identification. The calorimetric system is surrounded by a muon spectrometer which identifies muons and measures their momentum (together with the inner detector): an air-core toroid system provides the required bending magnetic field. In the following sections a brief review of the Atlas subdetectors and systems is reported.

1.2.1 Nomenclature

The beam direction defines the z-axis, and the x-y plane is the plane transverse to the beam direction. The positive x-axis is defined as pointing from the interaction point to the center of the LHC ring, and the positive y-axis is pointing upwards. The azimuthal angle ϕ is measured around the beam axis, and the polar angle θ is the angle from the beam axis. The pseudorapidity is defined as:

$$\eta = -\log(\tan\frac{\theta}{2}) \tag{1.3}$$

The transverse momentum p_T and the transverse energy E_T, as well as the missing transverse energy E_T^{miss} and other transverse variables, are defined in the xy plane unless stated otherwise. .

1.2.2 Magnet System

The Atlas superconducting magnet system [**?**] can be seen in Figure 1.3

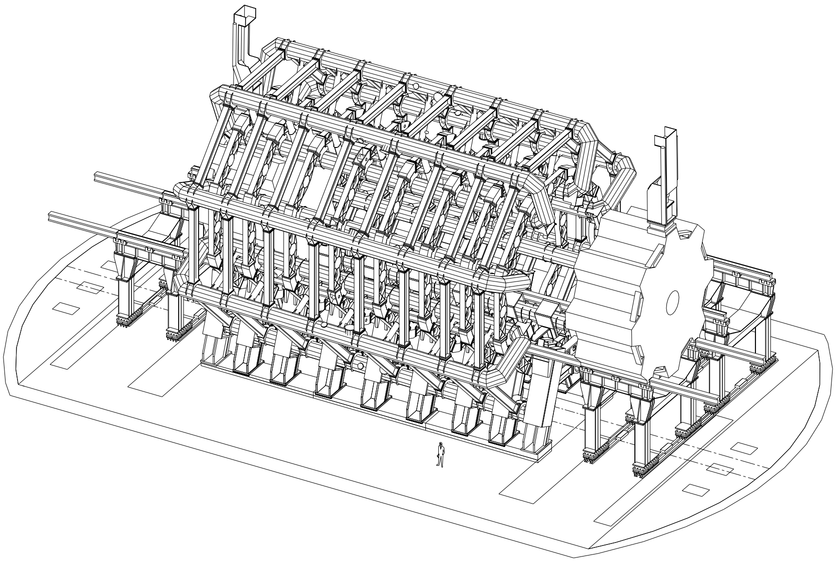

Figure 1.3: Overview of the magnetic system

It is an arrangement of a central solenoid (CS) providing the magnetic field for the Inner Detector, not visible in figure (1.3), surrounded by a system of three large air-core toroids generating the magnetic field for the muon spectrometer. The overall dimensions of the central toroid are 26 m in length and 20 m in diameter. The two end-cap toroids (ECT) are inserted in the barrel toroid (BT) at each end and line up with the CS. They have a length of 5 m, an outer diameter of 10.7 m and an inner bore of 1.65 m. The CS extends over a length of 5.3 m and has a bore of 2.4 m.

The CS provides a central field of 2 T with a peak magnetic field of 2.6 T at the superconductor itself. The position of the CS in front of the EM calorimeter demands a careful minimization of the material in order to achieve the desired calorimeter performance. As a consequence, the CS and the LAr calorimeter share one common vacuum vessel, and also the CS coil is designed to be as thin as possible without sacrificing the operational safety and reliability.

Each of the three toroids consists of eight coils assembled radially and symmetrically around the beam axis. The coils of the central toroid are housed in individual cryostats taking up the forces between the coils.

The magnets are indirectly cooled by forced flow of helium at 4.5 K through tubes welded on the casing of the windings.

1.2.3 Inner Detector

The layout of the Inner Detector (ID) [4] is shown in Figure (1.4)

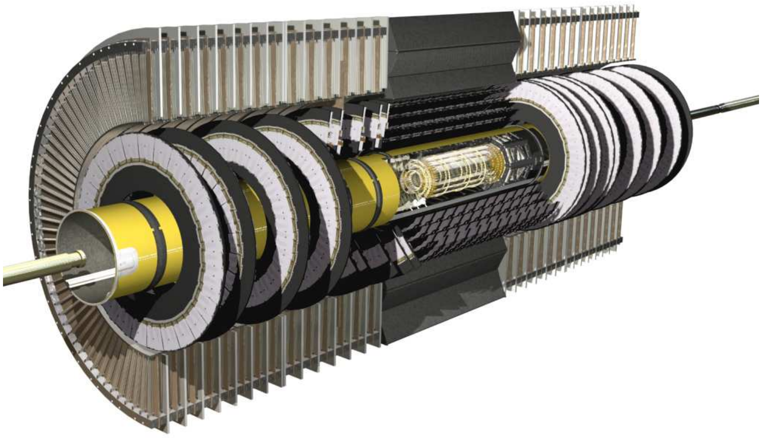

Figure 1.4: Overview of the Inner Detector

It combines high-resolution detectors at the inner radii with continuous tracking elements at the outer radii, all contained in the central solenoid which provides a nominal magnetic field of 2 T. The momentum and vertex resolution requirements from physics call for high-precision measurements to be made with fine-granularity detectors, given the very large track density expected at the LHC.

Semiconductor tracking detectors, using silicon microstrip (SCT) and pixel technologies offer these features. The highest granularity is achieved around the vertex region using semi-conductor pixel detectors. The total number of precision layers must be limited because of the material they introduce, and because of their high cost. Typically, three pixel layers and eight strip layers (four space points) are crossed by each track. A large number of tracking points (typically 36 per track) is provided by the straw tube tracker (TRT) , which provides continuous track-following with much less material per point and a lower cost. The straw hits at the outer radius contribute significantly to the momentum measurement, since the lower precision per point compared to the silicon is compensated by the large number of measurements and the higher average radius.

The outer radius of the ID cavity is 115 cm, fixed by the inner dimension of the cryostat containing the LAr EM calorimeter, and the total length is 7 m, limited by the

System	Position	Area (m^2)	Resolution $\sigma(\mu m)$	Channels (10^6)	$\mid \eta \mid$ coverage
Pixels	1 removable barrel layer (B-layer)	0.2	$R\phi = 12$, $z = 66$	16	≤ 2.5
	2 barrel layers	1.4	$R\phi = 12$, $z = 66$	81	≤ 1.7
	5 end-cap disks on each side	0.7	$R\phi = 12$, $R = 77$	43	1.7-2.5
Silicon strips	4 barrel layers	34.4	$R\phi = 16$, $z = 580$	3.2	≤ 1.4
	9 end-cap wheels on each side	26.7	$R\phi = 16$, $R = 580$	3.0	1.4-2.5
TRT	Axial barrel straws		170 (per straw)	0.1	≤ 0.7
	Radial end-cap straws		170 (per straw)	0.32	0.7-2.5
	36 straws per track				

Table 1.1: Parameters of the Inner Detector. The resolutions quoted are typical values (the actual resolution in each detector depends on the impact angle).

position of the end-cap calorimeters. Mechanically, the ID consists of three units: a barrel part extending over 80 cm, and two identical end-caps covering the rest of the cylindrical cavity. The precision tracking elements are contained within a radius of 56 cm, followed by the continuous tracking, and finally the general support and service region at the outermost radius.

In the barrel region, the high-precision detector layers are arranged on concentric cylinders around the beam axis, while the end-cap detectors are mounted on disks perpendicular to the beam axis. The barrel TRT straws are parallel to the beam direction. All the end-cap tracking elements are located in planes perpendicular to the beam axis.

The basic layout parameters and the expected measurement resolutions are summarized in table (1.1). The layout provides full tracking coverage over $\mid \eta \mid < 2.5$, including impact parameter measurements and vertexing for heavy-flavors and τ tagging. The secondary vertex measurement performance is enhanced by the innermost layer of pixels, at a radius of about 4 cm, as close as is practical to the beam pipe. The lifetime of such a detector will be limited by radiation damage, and may need replacement after a few years. In the next sections more details on each subdetector will be given.

Pixel detector

The pixel detector [5] is designed to provide a very high-granularity, high-precision set of measurements as close to the interaction point as possible. The system provides three precision measurements over the full acceptance, and mostly determines the impact parameter resolution and the ability of the Inner Detector to find short-lived particles such as B hadrons and τ leptons.

The system contains a total of 140 million detector elements, each 50 μm in the Rϕ direction and 300 μm in z. The system consists of three barrels at average radii of $\sim$4 cm, 10 cm, and 13 cm, and five disks on each side, between radii of 11 and 20 cm, which complete the angular coverage. The system is designed to be highly modular, containing approximately 1500 barrel modules and 700 disk modules, and uses only one type of support structure in the barrel and two types in the disks. The pixel modules are designed to be identical in the barrel and the disks. Each module is 62.4 mm long and 21.4 mm wide, with 61440 pixel elements read out by 16 chips, each serving an array of 24 by 160 pixels. The modules are overlapped on the support structure in order to give hermetic coverage. The thickness of each layer is expected to be about 1.7% of a radiation length at normal incidence.

Semiconductor tracker

The SCT system is designed to provide eight precision measurements per track in the intermediate radial range, contributing to the measurement of momentum, impact parameter and vertex position, as well as providing good pattern recognition by the use of high granularity.

The barrel SCT uses eight layers of silicon microstrip detectors to provide precision points in the Rϕ and z coordinates. Each silicon detector is 6.36$\times$6.40 cm^2 with 768 readout strips of 80 μm pitch. Each module consists of four singlesided p-on-n silicon detectors. On each side of the module, two detectors are wire-bonded together to form 12.8 cm long strips. Two such detector pairs are then glued together back-to-back at a 40 μrad angle, separated by a heat transport plate, and the electronics is mounted above the detectors on a hybrid. The readout chain consists of a front-end amplifier and discriminator, followed by a binary pipeline which stores the hits above threshold until the level-1 trigger decision.

The end-cap modules are very similar in construction but use tapered strips, with one set aligned radially. To obtain optimal η-coverage across all end-cap wheels, end-cap modules consist of strips of either $\sim$12 cm length (at the outer radii) or 6-7 cm length (at the innermost radius). The detector contains 61 m^2 of silicon detectors, with 6.2 million readout channels. The spatial resolution is 16 μm in Rϕ and 580 μm in z, per module containing one Rϕ and one stereo measurement. Tracks can be distinguished if separated by more than $\sim$200 μm.

The barrel modules are mounted on carbon-fiber cylinders which carry the cooling system; the four complete barrels at radii of 30.0, 37.3, 44.7 and 52.0 cm are then linked together. The endcap modules are mounted in up to three rings onto nine wheels, which are interconnected by a space-frame. The radial range of each disk is adapted to limit the coverage to $\mid \eta \mid \leq 2.5$ by equipping each one with the minimum number of rings and by using the appropriate set of modules.

Transition radiation tracker

The TRT is based on the use of straw detectors, which can operate at the very high rates expected at the LHC by virtue of their small diameter and the isolation of the sense wires within individual gas volumes. Electron identification capability is added by employing xenon gas to detect transition-radiation photons created in a radiator between the straws. This technique is intrinsically radiation hard, and allows a large number of measurements, typically 36, to be made on every track at modest cost.

Each straw is 4 mm in diameter and equipped with a 30 μm diameter gold-plated W-Re wire, giving a fast response and good mechanical and electrical properties for a maximum straw length of 144 cm in the barrel. The barrel contains about 50 000 straws, each divided in two at the center, in order to reduce the occupancy, and read out at each end. The end-caps contain 320000 radial straws, with the readout at the outer radius. The total number of electronic channels is 420000.

Each channel provides a drift-time measurement, giving a spatial resolution of 170 μm per straw.

1.2.4 Calorimeters

A schematic view of the Atlas calorimeters is presented in Figure (1.5)

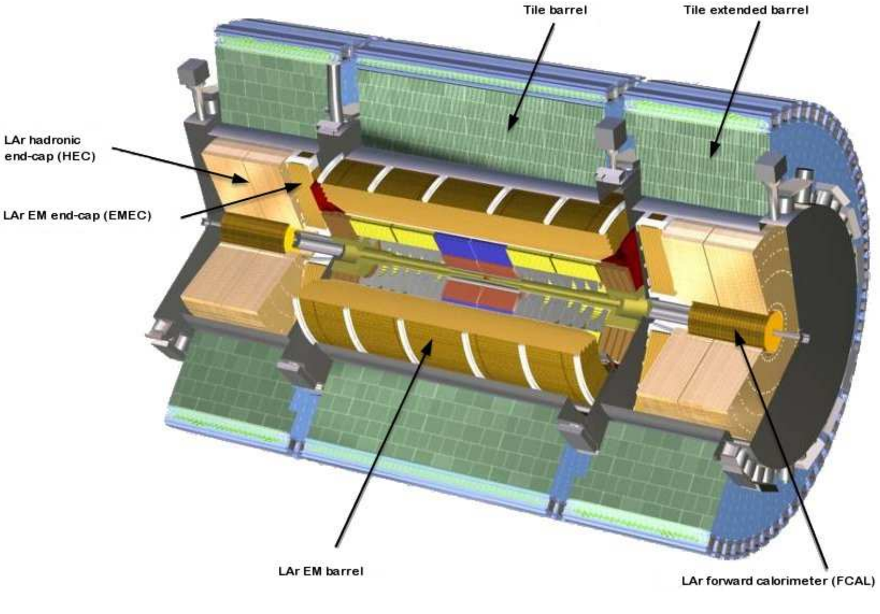

Figure 1.5: Overview of the calorimetric system

The calorimetry consists of an electromagnetic (EM) calorimeter covering the pseudorapidity region $|\eta| \leq 3.2$, a hadronic barrel calorimeter covering $|\eta| \leq 1.7$, hadronic end-cap calorimeters covering $1.5 \leq |\eta| \leq 3.2$, and forward calorimeters covering $3.1 \leq |\eta| \leq 4.9$.

The EM calorimeter is a lead/liquid-argon (LAr) detector with accordion geometry . Over the pseudorapidity range $| \eta | \leq 1.8$, it is preceded by a presampler detector, installed immediately behind the cryostat cold wall, and used to correct for the energy lost in the material (ID, cryostats, coil) upstream of the calorimeter.

The hadronic barrel calorimeter is a cylinder divided into three sections: the central barrel and two identical extended barrels. It is based on a sampling technique with plastic scintillator plates (tiles) embedded in an iron absorber .

At larger pseudorapidities, where higher radiation resistance is needed, the intrinsically radiation-hard LAr technology is used for all the calorimeters : the hadronic end-cap calorimeter, a copper LAr detector with parallel-plate geometry, and the forward calorimeter, a dense LAr calorimeter with rod-shaped electrodes in a tungsten matrix.

The barrel EM calorimeter is contained in a barrel cryostat, which surrounds the Inner Detector cavity. The solenoid which supplies the 2 T magnetic field to the Inner Detector is integrated into the vacuum of the barrel cryostat and is placed in front of the EM calorimeter. Two end-cap cryostats house the end-cap EM and hadronic calorimeters, as well as the integrated forward calorimeter. The barrel and extended barrel tile calorimeters support the LAr cryostats and also act as the main solenoid flux return.

The pseudorapidity coverage, granularity and longitudinal segmentation of the Atlas calorimeters are summarized in Table (1.2).

Electromagnetic calorimeter

The electromagnetic calorimeters [6] are the main topics of this thesis and will be discussed in details in the next chapter.

Hadronic calorimeters

The Atlas hadronic calorimeters cover the range $| \eta | \leq 4.9$ using different techniques best suited for the widely varying requirements and radiation environment over the large η-range. Over the range $| \eta | \leq 1.7$, the iron scintillating-tile technique is used for the barrel and extended barrel tile calorimeters and for partially instrumenting the gap between them with the intermediate tile calorimeter (ITC). This gap provides space for cables and services from the innermost detectors.

Over the range $1.5 \leq | \eta | \leq 4.9$, LAr calorimeters were chosen: the hadronic end-cap calorimeter (HEC) extends to $| \eta | \leq 3.2$, while the range $3.1 \leq | \eta | \leq 4.9$ is covered by the highdensity forward calorimeter (FCAL). Both the HEC and the FCAL are integrated in the same cryostat as that housing the EM end-caps.

An important parameter in the design of the hadronic calorimeter is its thickness: it has to provide good containment for hadronic showers and reduce punch-through into the muon system to a minimum. The total thickness is 11 interaction lengths (λ) at $\eta = 0$, including about 1.5 λ from the outer support, which has been shown both by

EM CALORIMETER	Barrel	End-cap	
Coverage	$\mid \eta \mid < 1.475$	$1.375 < \mid \eta \mid < 3.2$	
Longitudinal segmentation	3 samplings	3 samplings	$1.5 < \mid \eta \mid < 2.5$
		2 samplings	$1.375 < \mid \eta \mid < 1.5$
			$2.5 < \mid \eta \mid < 3.2$
Granularity ($\Delta\eta \times \Delta\phi$)			
Sampling 1	0.003×0.1	0.025×0.025	$1.375 < \mid \eta \mid < 1.5$
		0.05×0.025	$1.5 < \mid \eta \mid < 1.8$
		0.025×0.1	$1.8 < \mid \eta \mid < 2.0$
		0.003×0.1	$2.0 < \mid \eta \mid < 2.5$
		0.004×0.1	$2.5 < \mid \eta \mid < 3.2$
Sampling 2	0.006×0.1	0.1×0.1	$1.375 < \mid \eta \mid < 2.5$
		0.025×0.025	$2.5 < \mid \eta \mid < 3.2$
Sampling 3	0.1×0.1	0.05×0.025	$1.5 < \mid \eta \mid < 2.5$
PRESAMPLER	Barrel	End-cap	
Coverage	$\mid \eta \mid < 1.52$	$1.5 < \mid \eta \mid < 1.8$	
Longitudinal segmentation	1 sampling	1 sampling	
Granularity ($\Delta\eta \times \Delta\phi$)	0.025×0.1	0.025×0.1	
HADRONIC TILE	Barrel	Extended barrel	
Coverage	$\mid \eta \mid < 1.0$	$0.8 < \mid \eta \mid < 1.7$	
Longitudinal segmentation	3 samplings	3 samplings	
Granularity ($\Delta\eta \times \Delta\phi$)	Samplings 1 and 2	0.1×0.1	0.2×0.1
	Sampling 3	0.1×0.1	0.2×0.1
HADRONIC LAr		End-cap	
Coverage		$1.5 < \mid \eta \mid < 3.2$	
Longitudinal segmentation		4 samplings	
Granularity ($\Delta\eta \times \Delta\phi$)		0.1×0.1	$1.5 < \mid \eta \mid < 2.5$
		0.2×0.2	$2.5 < \mid \eta \mid < 3.2$
FORWARD CALORIMETER		Forward	
Coverage		$3.1 < \mid \eta \mid < 4.9$	
Longitudinal segmentation		3 samplings	
Granularity ($\Delta\eta \times \Delta\phi$)		$\sim 0.2 \times 0.2$	

Table 1.2: Pseudorapidity coverage, granularity and longitudinal segmentation of the Atlas calorimeters.

measurements and simulation to be sufficient to reduce the punch-through well below the irreducible level of prompt or decay muons. Close to 10 λ of active calorimeter are adequate to provide good resolution for high energy jets. Together with the large η-coverage, this will also guarantee a good E_T^{miss} measurement, which is important for many physics signatures and in particular for SUSY particle searches.

Tile calorimeter

The large hadronic barrel calorimeter is a sampling calorimeter using iron as the absorber and scintillating tiles as the active material [7]. The tiles are placed radially and staggered in depth. The structure is periodic along z. The tiles are 3 mm thick and the total thickness of the iron plates in one period is 14 mm. Two sides of the scintillating tiles are read out by wavelength shifting (WLS) fibres into two separate photomultipliers (PMTs).

The tile calorimeter is composed of one barrel and two extended barrels. Radially the tile calorimeter extends from an inner radius of 2.28 m to an outer radius of 4.25 m. It is longitudinally segmented in three layers, approximately 1.4, 4.0 and 1.8 interaction lengths thick at $\eta = 0$. The resulting granularity is $\Delta\eta \times \Delta\phi = 0.1\times0.1$ (0.2×0.1 in the last layer), as shown in Table (1.2). The total number of channels is about 10000. The calorimeter is placed behind the EM calorimeter ($\gg 1.2\ \lambda$) and the solenoid coil. The total thickness at the outer edge of the tile-instrumented region is 9.2 λ at η=0. The thickness of the calorimeter in the gap is improved by the ITC, which has the same segmentation as the rest of the tile calorimeter. It is composed of two radial sections attached on the face of the extended barrel. The outer section, 31 cm thick, starts at the outer radius and covers 45 cm in radius. It is followed by the inner section which is 9 cm thick and extends over 45 cm to lower radii. The ITC is extended further inwards by a scintillator sheet, covering the inner part of the extended barrel and extending to the region between the LAr barrel and end-cap cryostats over $1.0 \leq |\eta| \leq 1.6$. This scintillator samples the energy lost in the cryostat walls and dead material. It is segmented in three sections of $\Delta\eta \sim 0.2$. The signals produced by the scintillating tiles and collected by the WLS fibres are fast. The PMTs have low dark current and are also fast. The shaper transforms the current pulse from the PMT into a unipolar pulse of FWHM of 50 ns.

Liquid-argon hadronic end-cap calorimeters

Each HEC consists of two independent wheels, of outer radius 2.03 m. The upstream wheel is built out of 25 mm copper plates, while the cheaper other one, farther from the interaction point, uses 50 mm plates. In both wheels, the 8.5 mm gap between consecutive copper plates is equipped with three parallel electrodes, splitting the gap into four drift spaces of about 1.8 mm. The readout electrode is the central one, which is a three layer printed circuit, as in the EM calorimeter. The two layer printed circuits on either side serve only as high-voltage carriers.

Primarily in order to limit the capacitance seen by a single preamplifier, and thus to allow for a fast response, only two gaps are ganged together at the pad level. Miniature coaxial cables running between the sectors carry signals to the preamplifier boards located at the wheel periphery. Output signals from (typically) four preamplifiers are summed together on the same board. A buffer stage drives the output signal up to the cold-to-warm feedthroughs.

Liquid-argon forward calorimeter

The FCAL is a particularly challenging detector owing to the high level of radiation it has to cope with. In Atlas, the forward calorimeter is integrated into the end-cap cryostat, with a front face at about 4.7 m from the interaction point. The integrated FCAL provides clear benefits in terms of uniformity of the calorimetric coverage as well as reduced radiation background levels in the muon spectrometer.

The FCAL consists of three sections: the first one is made of copper, while the other two are made out of tungsten. In each section the calorimeter consists of a metal matrix with regularly spaced longitudinal channels filled with concentric rods and tubes. The rods are at positive high voltage while the tubes and matrix are grounded. The LAr in the gap between is the sensitive medium. This geometry allows for an excellent control of the gaps which are as small as 250 mm in the first section.

1.2.5 Muon Spectrometer

The layout of the muon spectrometer [8] is visible in Figure (1.6).

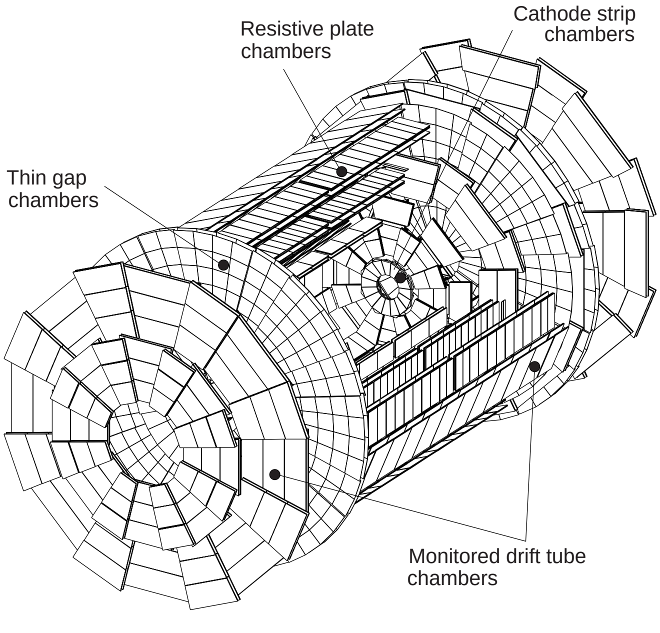

Figure 1.6: Overview of the muon spectrometer

It is based on the magnetic deflection of muon tracks in the large superconducting air-core toroid magnets, instrumented with separate trigger and high-precision tracking chambers. Over the range $|\eta| < 1.0$, magnetic bending is provided by the large barrel toroid. For $1.4 <\mid \eta \mid< 2.7$, muon tracks are bent by two smaller end-cap magnets inserted into both ends of the barrel toroid. Over $1.0 <\mid \eta \mid< 1.4$, usually referred to as the transition region, magnetic deflection is provided by a combination of barrel and end-cap fields. This magnet configuration provides a field that is mostly orthogonal to the muon trajectories, while minimizing the degradation of resolution due to multiple scattering.

Over most of the η-range, a precision measurement of the track coordinates in the principal bending direction of the magnetic field is provided by Monitored Drift Tubes (MDTs). At large pseudorapidities and close to the interaction point, Cathode Strip Chambers (CSCs) with higher granularity are used in the innermost plane over $2 <\mid \eta \mid< 2.7$, to withstand the demanding rate and background conditions. Optical alignment systems have been designed to meet the stringent requirements on the mechanical accuracy and the survey of the precision chambers.

The precision measurement of the muon tracks is made in the Rz projection, in a direction parallel to the bending direction of the magnetic field.

Muon chamber layout

The overall layout of the muon chambers in the Atlas detector is shown in Figure (1.6), which indicates the different regions in which the four chamber technologies described above are employed.

The chambers are arranged such that particles from the interaction point traverse three stations of chambers. The positions of these stations are optimized for essentially full coverage and momentum resolution. In the barrel, particles are measured near the inner and outer field boundaries, and inside the field volume, in order to determine the momentum from the sagitta of the trajectory. In the end-cap regions, for $\mid \eta \mid> 1.4$, the magnet cryostats do not allow the positioning of chambers inside the field volume. Instead, the chambers are arranged to determine the momentum with the best possible resolution from a point-angle measurement (this is also the case in the barrel region in the vicinity of the coils).

The barrel chambers form three cylinders concentric with the beam axis, at radii of about 5, 7.5, and 10 m. They cover the pseudorapidity range $\mid \eta \mid< 1$. The end-cap chambers cover the range $1 <\mid \eta \mid< 2.7$ and are arranged in four disks at distances of 7, 10, 14, and 21-23 m from the interaction point, concentric with the beam axis. The trigger function in the barrel is provided by three stations of RPCs. They are located on both sides of the middle MDT station, and directly inside the outer MDT station. In the end-caps, the trigger is provided by three stations of TGCs located near the middle MDT station.

Monitored drift-tube chambers (MDT)

The basic detection elements of the MDT chambers are aluminium tubes of 30 mm diameter and 400 μm wall thickness, with a 50 μm diameter central WRe wire. The tubes are operated with a non-flammable mixture of 93% Ar and 7% CO2 at 3 bar absolute pressure and have a total volume of 800 m^3. The single-wire resolution is 80 μm. The tubes are produced by extrusion from a hard aluminium alloy, and are available commercially. The tube lengths vary from 70 cm to 630 cm. To improve the resolution of a chamber beyond the single-wire limit and to achieve adequate redundancy for pattern recognition, the MDT chambers are constructed from 24 monolayers of drift tubes for the inner station and 23 monolayers for the middle and outer stations. The tubes are arranged in multilayer pairs of three or four monolayers, respectively, on opposite sides of a rigid support structure. The support structures (spacer frames) provide for accurate positioning of the drift tubes with respect to each other, and for mechanical integrity under effects of temperature and gravity. The frames need to be constructed to a moderate mechanical accuracy of 0.5 mm only; accurate positioning of the drift tubes is provided by the assembly procedure. Once a chamber is installed in its final location in the spectrometer, mechanical deformations are monitored by an in-plane optical system; hence the name monitored drift-tube chambers. Each drift tube is read out at one end by a low-impedance current sensitive preamplifier, with a threshold five times above the noise level. The preamplifier is followed by a differential amplifier, a shaping amplifier and a discriminator. The output of the shaping amplifier is also connected to a simple ADC, to correct the drift-time measurement for time-slewing using the charge integrated signal.

Cathode strip chambers (CSC)

The CSCs are multiwire proportional chambers with cathode strip readout and with a symmetric cell in which the anode-cathode spacing is equal to the anode wire pitch. The precision coordinate is obtained by measuring the charge induced on the segmented cathode by the avalanche formed on the anode wire. Good spatial resolution is achieved by segmentation of the readout cathode and by charge interpolation between neighboring strips. Position resolutions of better than 60 μm have been measured in several prototypes. A measurement of the transverse coordinate is obtained from orthogonal strips, i.e. oriented parallel to the anode wires, which form the second cathode of the chamber. The CSCs are arranged in 2×4 layers. The baseline CSC gas is a non-flammable mixture of 30% Ar, 50% CO2 and 20% CF4, with a total volume of 1.1 m^3. The front-end section of the strip readout electronics consists of a charge-sensitive preamplifier that drives a pulse-shaping amplifier. This is followed by analogue storage of the peak cathode pulse height during the level-1 trigger latency. After a level-1 trigger, the analogue data are multiplexed into a 10-bit ADC.

Resistive plate chambers (RPC)

The RPC is a gaseous detector providing a typical spacetime resolution of 1 cm $\times$ 1 ns with digital readout. The basic RPC unit is a narrow gas gap formed by two parallel resistive bakelite plates, separated by insulating spacers. The primary ionization electrons are multiplied into avalanches by a high, uniform electric field of typically 4.5 kV/mm. The gas mixture is based on tetrafluoroethane (C2H2F4) with some small admixture of SF6, a non-flammable and environmentally safe gas that allows for a relatively low operating voltage. The signal is read out via capacitive coupling by metal strips on both sides of the detector. A trigger chamber is made from two rectangular detector layers, each one read out by two orthogonal series of pick-up strips: the η strips are parallel to the MDT wires and provide the bending view of the trigger detector; the ϕ strips, orthogonal to the MDT wires, provide the second-coordinate measurement which is also required for the offline pattern recognition. The readout strips are arranged with a pitch varying from 30.0 to 39.5 mm. Each chamber is made from two detector layers and four readout strip panels. These elements are rigidly held together by two support panels which provide the required mechanical stiffness of the chambers. To preserve the excellent intrinsic time resolution of the RPCs, the readout strips are optimized for good transmission properties and are terminated at both ends to avoid signal reflections. The front-end electronics are based on a three-stage voltage amplifier followed by a variable threshold comparator. They are mounted on printed circuit boards attached to the edges of the readout panels.

Thin gap chambers (TGC)

The TGCs are similar in design to multiwire proportional chambers, with the difference that the anode wire pitch is larger than the cathode-anode distance. Signals from the anode wires, arranged parallel to the MDT wires, provide the trigger information together with readout strips arranged orthogonal to the wires. These readout strips are also used to measure the second coordinate. The gas mixture is highly flammable and requires adequate safety precautions. The main dimensional characteristics of the chambers are a cathode-cathode distance (gas gap) of 2.8 mm, a wire pitch of 1.8 mm, and a wire diameter of 50 μm. The operating high voltage foreseen is 3.1 kV. The electric field configuration and the small wire distance provide for a short drift time and thus a good time resolution. The TGCs are constructed in doublets and in triplets of chambers. The inner station consists of one doublet and is only used to measure the second coordinate. The seven chamber layers in the middle station are arranged in one triplet and two doublets which provide the trigger and the second coordinate measurements. On the backside of the cathode plates facing the center plane of the chamber, etched copper strips provide the readout of the azimuthal coordinate; no readout strips are foreseen for the central layer of a triplet.

Alignment

The requirements on the momentum resolution of the spectrometer call for an accuracy of the relative positioning of chambers traversed by a muon track that matches the intrinsic resolution and the mechanical tolerances of the precision chambers. Over the large global dimensions of the spectrometer, however, it is not possible to stabilize the dimensions and positions of the chambers at the 30 μm level. Therefore, chamber deformations and positions are constantly monitored by means of optical alignment systems and displacements up to $\sim$ 1 cm can readily be corrected for in the offline analysis. All alignment systems are based on optically monitoring deviations from straight lines. For reasons of cost, optical monitoring in the barrel is foreseen only for the large sectors of chambers. Chambers in the small sectors are aligned with particle tracks, exploiting the overlap with chambers in the large sectors. Alignment with tracks will also serve to cross-calibrate the optical survey of the large sectors. The very high accuracy of 30 μm is required only for the positioning of chambers within a projective tower. The accuracy required for the relative positioning of different towers to obtain adequate mass resolutions for multimuon final states is in the millimeter range. This accuracy is easily achieved by the initial positioning and survey of chambers at installation time. The relative alignment of muon spectrometer, calorimeters and Inner Detector will rely on high-momentum muon trajectories.

1.2.6 Trigger and Data acquisition

The Atlas trigger and data-acquisition (DAQ) system is based on three levels of online event selection [9]. Each trigger level refines the decisions made at the previous level and, where necessary, applies additional selection criteria. Starting from an initial bunch-crossing rate of 40 MHz (interaction rate of $\sim 10^9$ Hz at a luminosity of 10^{34} cm^{-2}s^{-1}), the rate of selected events must be reduced to $\sim$100 Hz for permanent storage. While this requires an overall rejection factor of 10^7 against *minimum-bias* events, excellent efficiency must be retained for the rare new physics processes, such as Higgs boson decays, which will be searched for in Atlas. Figure (1.7) shows a simplified functional view of the Trigger/DAQ system.

The level-1 (LVL1) trigger makes an initial selection based on reduced-granularity information from a subset of detectors [10]. Trigger information is provided for a number of sets of p_T thresholds (generally 68 sets of thresholds per object type). Most of the physics requirements of Atlas can be met by using, at the LVL1 trigger level, fairly simple selection criteria of a rather inclusive nature. However, the trigger implementation is flexible and it can be programmed to select events using more complicated signatures. The maximum rate at which the Atlas front-end systems can accept LVL1 triggers is limited to 75 kHz (upgradable to 100 kHz). It is important to keep the LVL1 latency (time taken to form and distribute the LVL1 trigger decision) to a minimum. During this time, information for all detector channels has to be conserved in “pipeline” memories. The LVL1 latency, measured from the time of the proton-proton collision until the trigger decision is available to the front-end electronics, is required to be less than 2.5 ms. Events selected by LVL1 are read out from the front-end electronics systems of the detectors into readout drivers (RODs) and then into readout buffers (ROBs).

All the detector data for the bunch crossing selected by the LVL1 trigger are held in the ROBs, either until the event is rejected by the level-2 (LVL2) trigger (in which

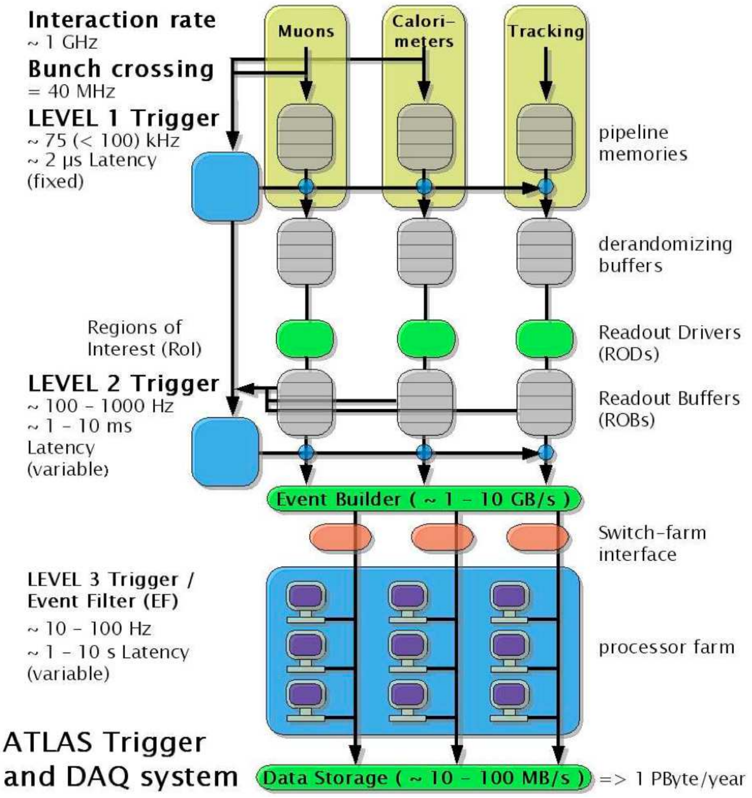

Figure 1.7: Functional view of the Trigger/DAQ system

case the data are discarded), or, in case the event is accepted by LVL2, until the data have been successfully transferred by the DAQ system to storage associated with the Event Filter (which makes the third level of event selection). The process of moving data from the ROBs to the Event Filter (EF) is called event building.

The LVL2 trigger makes use of “region-of-interest” (RoI) information provided by the LVL1 trigger. This includes information on the position (η and ϕ) and p_T of candidate objects (high-p_T muons, electrons/g, hadrons/τ, jets), and energy sums (missing-E_T vector and scalar E_T value). The RoI data are sent by LVL1 to LVL2, for all events selected by the LVL1 trigger, using a dedicated data path. The LVL2 trigger has access to all of the event data, if necessary with the full precision and granularity.

It is expected that LVL2 will reduce the rate to $\sim$1 kHz. In contrast to the 75 kHz (upgradable to 100 kHz) limit for LVL1 that comes from the design of the detector front-end electronics, this is not a hard number. The latency of the LVL2 trigger is variable from event to event and is expected to be in the range 110 ms.

The last stage of the online selection (LVL3) is performed by the EF. It will employ offline algorithms and methods, adapted to the online environment, and use the most up to date calibration and alignment information and the magnetic field map. The EF will make the final selection of physics events which will be written to mass storage for subsequent full offline analysis. The output rate from LVL2 should then be reduced by an order of magnitude, giving ∼100 Hz, corresponding to an output data rate of ∼100 MB/s if the full event data are to be recorded. It is envisaged that the first task of the EF will be to confirm the results of the LVL2 decision and subsequently use the results of the LVL2 to seed its own analysis. The rejection power of the EF comes from:

- using refined algorithms and, where necessary, tighter p_T thresholds compared to those used in the LVL2;
- the availability of all data relevant to the specific event in calculations and selection criteria;
- the use of complex algorithms and criteria which, due to processing time limits, cannot be performed at LVL2, an example being vertex and track fitting using bremsstrahlung recovery for electrons.

1.3 Simulation

The challenging experimental conditions at the LHC and the variety and complexity of the different Atlas subdetectors made it absolutely necessary to provide accurate detectors simulation and reconstruction programs in order to evaluate in detail the detector behavior and physics performance. Many tools have been developed in the past both on the simulation and reconstruction side : a GEANT 3 based detector simulation interface and a fortran reconstruction program, called ATRECON were fully working. Few years ago a completely new object oriented/C++ framework called *Athena* , has been created aiming to integrate all the required tools, interfaces and databases [11].

Input for simulation comes from event generators after a particle filtering stage. Data objects representing Monte Carlo truth information from the generators are read by simulation and processed. Hits produced by the simulation can be directly processed by the digitization algorithm and transformed into Raw Data Objects (RDOs). Alternatively they can be sent first to the pile-up algorithm and then passed to the digitization stage.

RDOs produced by the simulation data-flow pipeline are used directly by the reconstruction processing pipeline. Thus the simulation and reconstruction pipelines are coupled together by the RDOs which act as the output from the simulation pipeline and the input to the reconstruction pipeline.

1.3.1 Generators

Event generators are indispensable as tools for the modelling of the complex physics processes that lead to the production of hundreds of particles per event at LHC energies. Generators are used to set detector requirements, to formulate analysis strategies, or to calculate acceptance corrections. They also illustrate uncertainties in the physics modelling. Generators model the physics of hard processes, initial and final state radiation, multiple interactions and beam remnants, hadronization and decays, and how these pieces come together. The individual generators are run from inside Athena. A container of these is placed into the transient event store under StoreGate and can be made persistent. The event is presented for downstream use by simulation, for example by G4Atlas simulation (using Geant4) .

The current list of supported Generators includes Herwig, Pythia, Isajet, Hijing, AcerMC, CompHep, AlpGen, Tauola, Photos, Phojet and ParticleGenerator. Some utility classes to enable filtering of events and facilitate handling of Monte Carlo Truth are also provided.

1.3.2 Atlas Geant4 Simulation (G4Atlas)

The Geant4 [12, 13] toolkit provides both a framework and the necessary functionality for running detector simulation in particle physics and other applications. Provided functionalities include optimized solutions for geometry description and navigation through the geometry, the propagation of particles through detectors, the description of materials, the modelling of physics processes (e.g. a huge effort has been invested in recent years into the development and improvement of hadronic-physics models), visualization, and many more. A basic concept is that of Sensitive Detectors, which allow for the definition of active detector elements, perform corresponding actions within them, and write out hits (which may carry information like position, energy deposit, identifier of the active element, etc.).

Development activities to make use of Geant4 functionality within the Atlas-specific setup and software environment started in 2000, taking into account Atlas-specific requirements. These provide tailored packages for handling geometry, kinematics, materials, physics, fields, sensitive detectors, run-specific issues and visualization, etc. These activities culminated in 2003 with the Geant4 simulation being embedded in Athena. This migration to Athena was also done for the detector simulation packages which had been developed in detail in the standalone environment.

1.3.3 Pile-up

G4Atlas produces hits as output, which are a record of the real interactions of particles in the detector. At higher machine luminosities, however, multiple interactions can occur at each beam crossing (typically one signal event with multiple minimum-bias background events), and in addition other backgrounds (e.g. cavern background) need to be taken into account.

The Athena-based pile-up application manages multiple input streams. Random permutations of events are selected from a circular buffer of minimum-bias events. Since the various sub-detectors have different data integration times, they require individual cache retention policies. By using a two-dimensional detector and time-dependent event caching policy, memory utilization has been significantly reduced.

Pile-up is an excellent mechanism to stress test the architecture. Small problems which would normally pass unnoticed, may get enormously magnified and become visible far sooner. It is also an excellent tool to expose memory leaks, as they might become magnified by several orders of magnitude (depending on the luminosity).

1.3.4 Digitization

The hits produced either directly by G4Atlas, or from the merging of pile-up events, need to be translated into the output actually produced by the Atlas detectors. The propagation of charges (as in the tracking detectors and the LAr calorimeter) or light (as in the case of TileCal) into the active media has to be considered as well as the response of the readout electronics. Unlike the previous steps in the simulation chain, this is a very detector-specific task, and the expertise of people building and testing each of the sub-detectors is essential. The final output of the digitization step are Raw Data Objects (RDOs) that should resemble the real detector data.

Digitization operates locally at the level of each sub-detector (e.g. a pixel module or a calorimeter cell) and the same code can be used in the context of the full Atlas simulation, or a test beam or any other test. It is of key importance that digitization is tuned by comparing the RDO output to real data in system tests to produce a realistic tuning of the detector response.

Chapter 2

Electromagnetic liquid Argon calorimeter

2.1 Introduction and physics requirements

Calorimeters [6] [14] will play a crucial role at the LHC: in contrast to other detectors, such as magnetic spectrometers, their intrinsic resolution improves with energy, which makes them very suitable detectors at high-energy machines. In particular, at the LHC, calorimeters will be the leading detectors in many measurements for the reconstruction of physics channels of prime interest.

The main tasks of the calorimeters [15, 16, 17] at hadron colliders are: accurate measurement of the energy and position of electrons and photons; measurement of the energy and direction of jets, and of the missing transverse momentum of the event; particle identification, for instance separation of electrons and photons from hadrons and jets, and of τ hadronic decays from jets; event selection at the trigger level.

Although EM calorimeters will be involved in a variety of measurements at the LHC, the performance specifications come from a few “benchmark” channels: the search for a Higgs boson through the decays $\mathrm{H} \rightarrow \gamma\gamma$ and $\mathrm{H} \rightarrow 4\mathrm{e}$, and the search for heavy vector bosons (W', Z') with masses up to 5-6 TeV through the decays $W' \rightarrow e\nu$ and $Z' \rightarrow e^+e^-$.

The physics program and the difficult experimental environment set stringent requirements on detector specifications, as reported in the following list:

- **Hermeticity**: in principle the largest possible acceptance is needed to observe rare physics processes such as the already mentioned $H \rightarrow \gamma\gamma$ and the $H \rightarrow 4l$ decays. In the pseudorapidity coordinate, a $|\eta| < 2.5$ limit is set by the survivability of the inner detector to radiation. Full $0 < \phi < 2\pi$ coverage up to $\eta = 2.5$ with the best possible granularity is required for precision electrons/photons physics.

- **Electron reconstruction capability**: electron energy and position reconstruction capability from few GeV up to few TeV is required. Such wide operation range depends on the complexity of the physics program: the lower bound is set by the electrons produced in the semileptonic decays of b-quarks while the upper TeV limit is due to the electrons from heavy bosons decays.

- **Energy resolution and linearity**: excellent energy resolution is needed in order to achieve a $\gamma\gamma$ and 4 electrons reconstructed invariant mass resolution of $\sim$ 1 % in the 114-180 GeV mass range. From detailed physics simulation it has been found that a sampling term on the energy resolution at the level of 10 % $\sqrt{E}$ or less and a constant term smaller than 1 % are required. A linearity of response better than 0.5 % up to 300 GeV is also needed to ensure optimal mass resolution.

- **Energy scale precision**: the measurement of the Higgs boson mass will be dominated by the systematic errors coming from the background subtraction and from the knowledge of the energy scale: an overall precision of $\sim$ 200 MeV on the Higgs mass measurement can be achieved provided that the electromagnetic energy scale is known to $\sim$ 0.1 %.

- **Position resolution**: in order to limit the contribution of the angular term to the width of the reconstructed $\gamma\gamma$ invariant mass, the photons direction θ should be measured with a resolution of 50 mrad/$\sqrt{E}$. A good position resolution is also required for the non-pointing photons coming from the decay of a long lived neutralino in the GMSB framework.

- **Particle identification**: an excellent electron/jet, photon/jet and tau/jet separation is mandatory for the ATLAS electromagnetic calorimeter in order to minimize the impact of the reducible background on $H \rightarrow \gamma\gamma$ channel. Isolated high p_T π^0 coming from jet fragmentation are a dangerous source of background and a very fine granularity is needed to distinguish between the two overlapping photons from the π^0 decay and a single isolated photon. Detailed simulation of the $H \rightarrow \gamma\gamma$ demonstrates that a γ/jet separation of $\sim$ 3000 with a 80 % photon efficiency and a π^0 rejection factor of $\sim$ 3 with a 90 % photon efficiency are required.

- **Speed of response and noise**: the electronic and pileup noise minimization requires an high performance and fast dedicated electronics. A careful design of the complete read out chain is mandatory and advanced signal processing techniques should be adopted.

- **Granularity and longitudinal segmentation**: the optimum granularity of the detector comes from the best possible compromise between physics requirements, electronic and pileup noise minimization, particle identification and position resolution. A granularity not coarser than $\Delta\eta$ x$\Delta\phi = 0.025$ x 0.025 has been found to be the optimum over the rapidity region used for precision physics. A longitudinal segmentation in more layers is needed for particle identification and position measurements. The γ/π^0 separation requires a dedicated section with a finer granularity.

- **Radiation and lifetime**: the calorimeter design should also take into account the radiation resistance of its components. In ten years of operation a neutron fluence up to 10^{15} n/cm^2 and radiation doses up to 200 kGy is expected to be absorbed by the em calorimeter.

In order to satisfy as much as possible all the listed requirements and taking into account mechanical, technological and financial constraints, a lead - liquid Argon sampling calorimeter [18, 19, 20] with an accordion geometry was chosen . The liquid Argon, used as a ionizing medium, is intrinsically radiation tolerant and the particular geometry allows a full coverage in the ϕ coordinate without cracks and dead zones. Fast and low noise electronic readout has been designed and sophisticated signal reconstruction techniques have been developed in order to minimize the effect of electronic noise and pileup. A cell by cell electronic calibration system has also been developed.

2.2 Calorimeter Layout

2.2.1 Structure and geometry

The electromagnetic calorimeter is divided into three parts:

- **Barrel**: cover the $|\eta| < 1.475$ region. The barrel calorimeter is housed in a 6.8 m long cryostat with an outer radius of 2.25 m and an inner cavity radius of 1.15 m. It is composed of two identical half-barrels, separated by a 6 mm gap at z=0. Each half barrel consists of 1024 lead-stainless-steel converters, alternated with copper-polyimide multilayer read out electrodes ensuring a full azimuthal coverage (fig. 2.1). The LAr gap is kept constant by varying the bending angles as a function of the radius.

- **Endcaps**: cover the $1.375 < |\eta| < 3.2$ region, are placed at the two extreme of the barrel calorimeter. In the two identical endcaps the absorber plates and the electrodes are mounted in a radial arrangement, as in figure 2.1(b)), and the accordion waves increases developing in the z coordinate. For geometrical reasons the liquid Argon gap increases with the radius and, in order to partially compensate this effect, the bending angle increases with the radius accordingly. Due to feasibility reasons it was impossible to bend the absorbers and the electrods in such a way to guarantee a constant LAr gap over the full pseudorapidity range. For this reason each endcap calorimeter is divided in two coaxial wheels and the LAr gap varies as a function of r in each wheel, as in figure 2.2(a)),: the outer wheels are made of 768 absorbers and read out electrodes each and cover the region $1.375 < |\eta| < 2.5$ while the inner wheels are made of 256 absorbers and

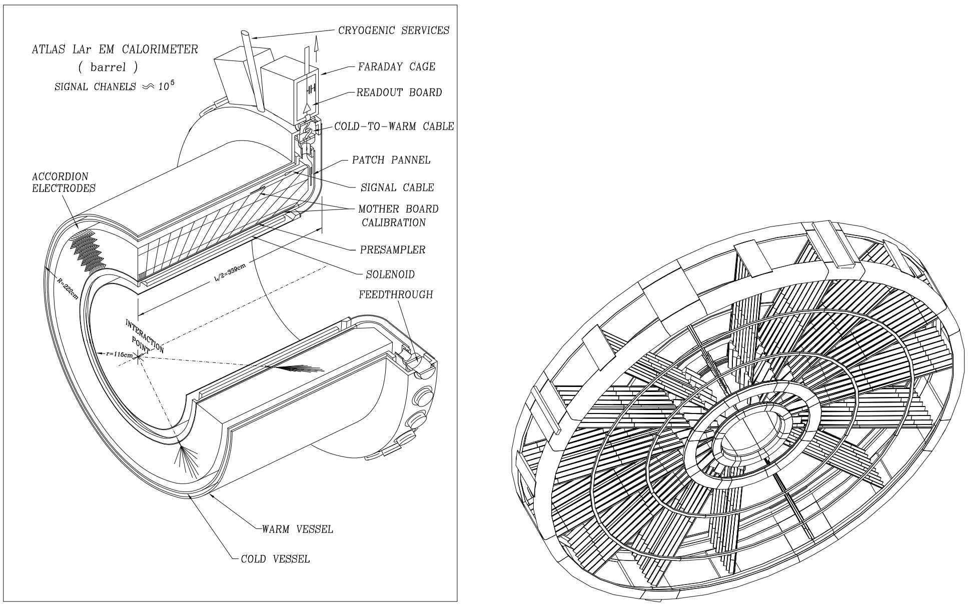

(a) (b)

Figure 2.1: Perspective view of one half barrel calorimeter (2.1(a))and one endcap wheel (2.1(b)).

electrodes covering the $2.5 < |\eta| < 3.2$ range. The μA to GeV conversion factor is kept constant by applying a radius dependent high voltage between absorbers and electrodes (fig. 2.2(b)).

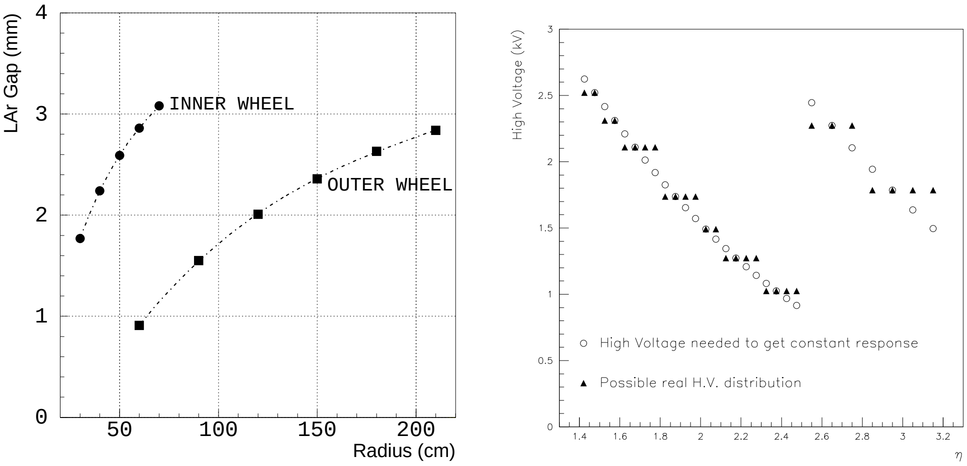

(a) (b)

Figure 2.2: Width of the LAr gap in the end-cap calorimeter as a function of the radius (2.2(a)) and compensating high voltages in the endcap calorimeter as a function of η (2.2(b)).

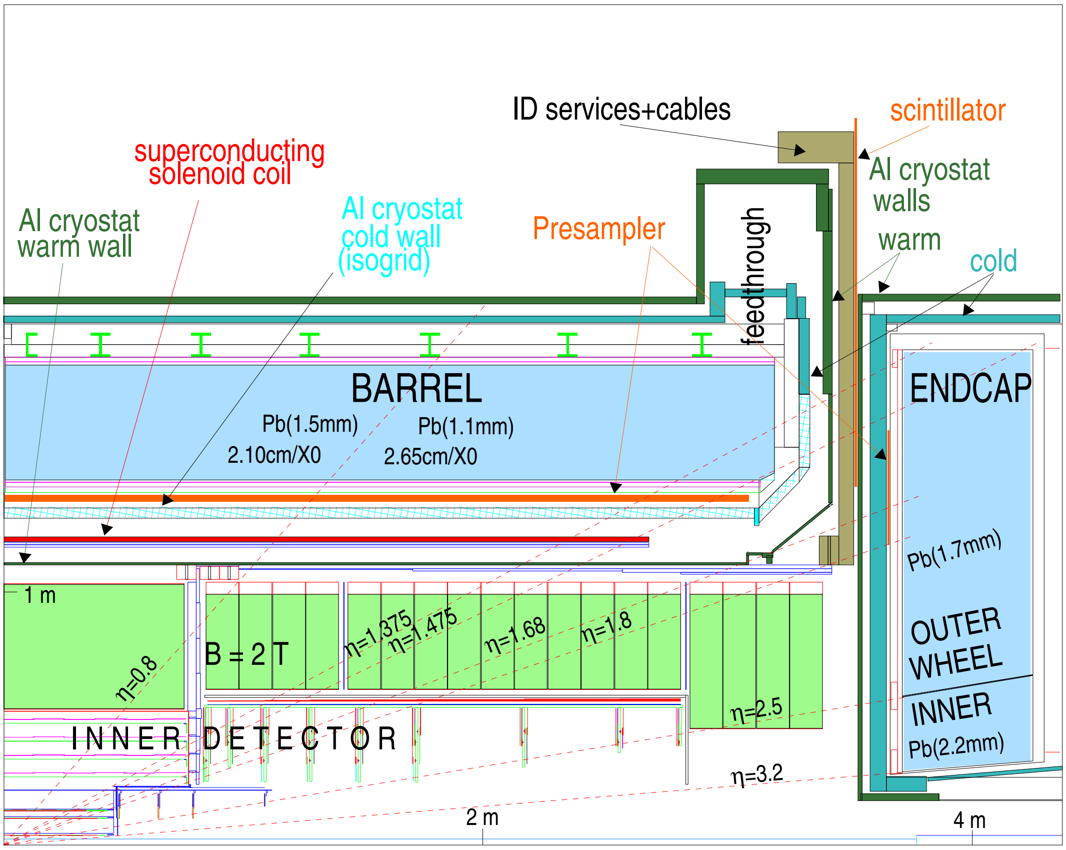

Figure 2.3: Section of the EM calorimeter

Due to the complexity of the calorimeter geometry, shown in figure (2.3) there are three regions (cracks) where the detector response is degraded with respect to the rest of the acceptance:

- $\eta = 0$: between the two half barrels a gap of 6 mm of inactive liquid Argon is present.
- $\eta \sim 1.45$: the transition region between barrel and endcap is used to route services and cables of the inner detector. In order to partially recover the energy lost in the passive materials, a scintillator slab will be placed between the barrel and endcap cryostats covering the $1.0 < |\eta| < 1.6$.
- $\eta = 2.5$: in the transition between outer and inner wheel of the endcap a small 3 mm projective gap is present. The performance in also degradate by additional dead material in front which is due to the intermediate support ring.

The read out electrodes are flexible three layers copper - kapton printed circuit boards. The two copper outer layers are connected to the high voltage while the inner layer is connected to the read-out channel and collects, by capacitive coupling, the current induced by electrons drifting in the LAr gap. In figure (2.4) the detailed view of a slice of the barrel calorimeter, where it is possible to see the accordion geometry in more detail, and a liquid Argon gap section are given. Projective read-out cells in η and longitudinal segmentation are obtained by properly etching the read out electrodes, as shown in figure (2.5). In the ϕ coordinate the desired granularity is obtained by grouping together a proper number of electrodes. Signals from different longitudinal compartments are read out at the front and back face of the electrodes.

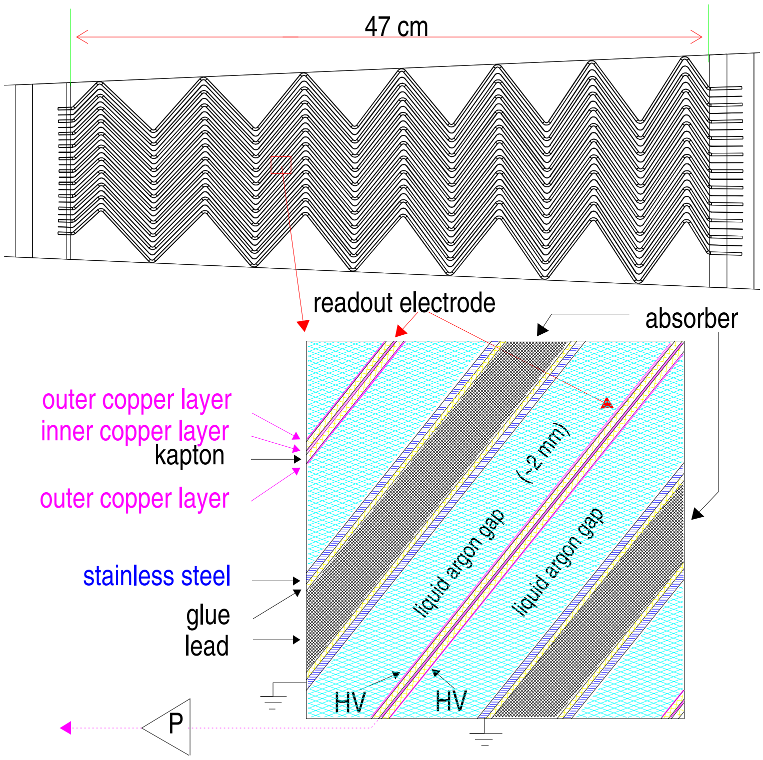

Figure 2.4: Detailed view of a barrel liquid Argon gap section

The absorber electrodes, which are at ground potential, are made of one lead sheet sandwiched between two 0.2 mm thick stainless-steel plates for high mechanical strength. In the barrel calorimeter the lead thickness is 1.5 mm in the region $\eta < 0.8$ and 1.1 mm for $\eta > 0.8$: the thinner lead for $|\eta| > 0.8$ increases the sampling fraction. This compensate for energy resolution degradation due to the decrease of sampling frequency with increasing rapidity.

2.2.2 Longitudinal segmentation and granularity

Over the region devoted to precision physics ($|\eta| < 2.5$) the calorimeter is segmented in three longitudinal samplings and a separate presampler is placed in front of the calorimeter in the $|\eta| < 1.8$ region. The number of samplings and the granularity of the

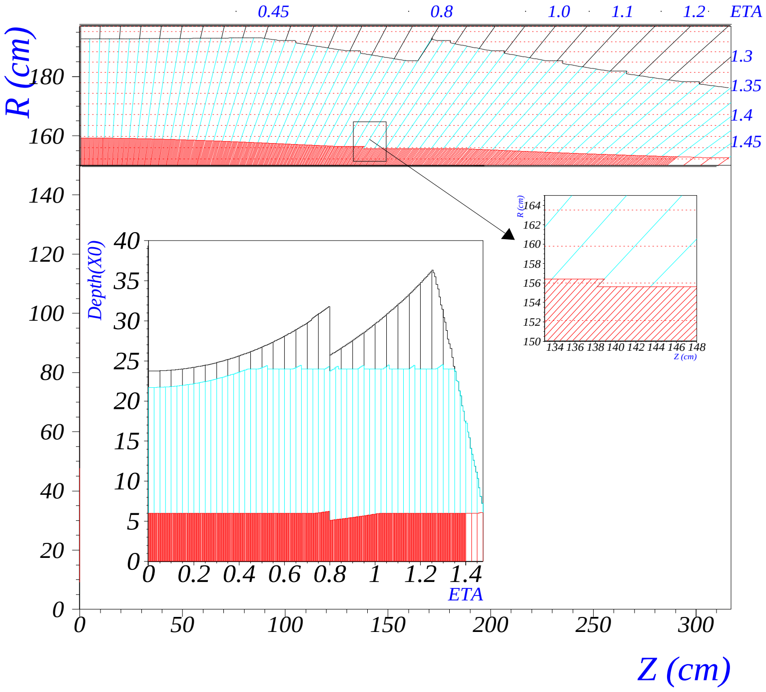

Figure 2.5: Longitudinal and η segmentation of one barrel signal electrode

samplings are summarized in table (2.1). A schematic view of the barrel calorimeter segmentation and granularity can be seen in figure (2.6). The longitudinal sampling are :

- **Presampler** : the presampler consists of an active liquid argon layer of 1.1 and 0.5 cm thickness in the barrel and in the endcap respectively with no absorbers. It can be used to correct for the energy lost by electrons and photons in the material in front of the calorimeter.

- **Sampling 1 - strips** : the first sampling is made of narrow strips with a fine granularity. It is used for the γ/π^0 separation and it provides a precise η position measurement. In order to limit the number of channels the cells are wider in azimuth with respect to the middle and back layer. In the endcaps the bins become narrower when going to larger η: the granularity of the first sampling slightly worsen while increasing eta due to the fact that for technical reason the strips width can't be made less than 5 mm.

- **Sampling 2 - middle** : the second sampling collects most of the e/γ shower energy. Including the sampling 1 the total calorimeter thickness up to the end of the middle sampling is $\sim$ 22 X_0 for $\eta = 0$ varying with the rapidity. The second calorimeter sampling is transversally segmented into squared towers of $(\Delta\eta\ \mathrm{x}\Delta\phi) \simeq (0.025 \mathrm{\ x\ } 0.025)$ which corresponds to a $\sim$ 4x4 cm^2 square for η = 0.

- **Sampling 3 - back**: The third compartment has the same ϕ granularity than the middle layer and a twice coarser granularity in the η coordinate. The total thickness varies from 2 to 12 X_0. The back sampling is used to sample high energy showers and contributes to γ / jet and electron/jet separation. For the endcap inner wheel ($|\eta| > 2.5$) the calorimeter is segmented in two longitudinal samplings only with a coarser granularity.

	Barrel	**Endcap**			
eta range	0 - 1.475	1.375 - 1.8	1.8 - 2.0	2.0 - 2.5	2.5 - 3.2
Presampler	0.025 x 0.1	0.025 x 0.1			
Sampling 1	0.003 x 0.1	0.003 x 0.1	0.004 x 0.1	0.006 x 0.1	0.1 x 0.1
Sampling 2	0.025 x 0.025	0.025 x 0.025	0.025 x 0.025	0.025 x 0.025	0.1 x 0.1
Sampling 3	0.05 x 0.025	0.05 x 0.025	0.05 x 0.025	0.05 x 0.025	

Table 2.1: Granularity in ($\Delta\eta x\Delta\phi$) of the EM calorimeter for different samplings as a function of the eta rage.

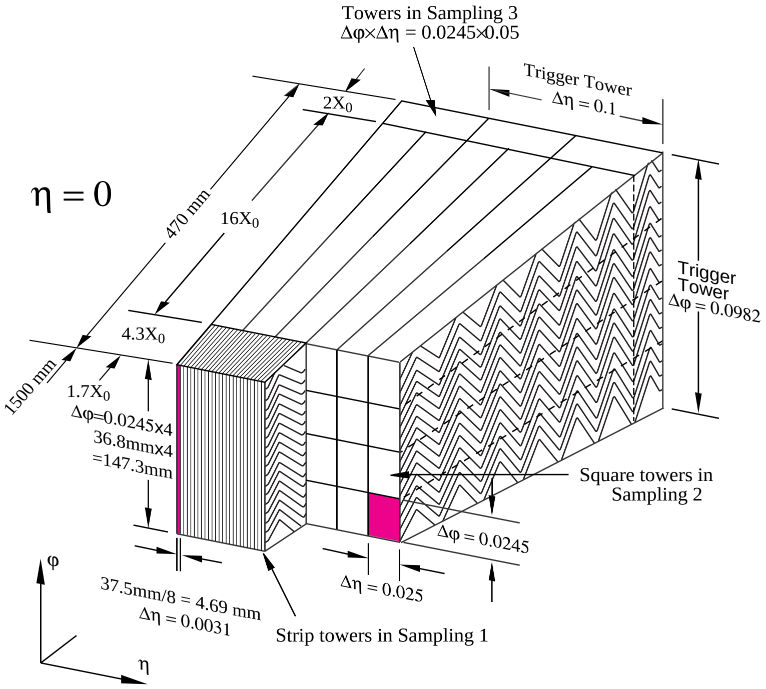

Figure 2.6: Sketch of the accordion structure and barrel granularity

A plot of the total thickness of the calorimeters is shown in figure (2.7). Of crucial importance for have the better as possible calorimeter performance is to reduce to minimum the material upstream calorimeter. In figure (2.8) the amount of material in front of calorimeter is shown.

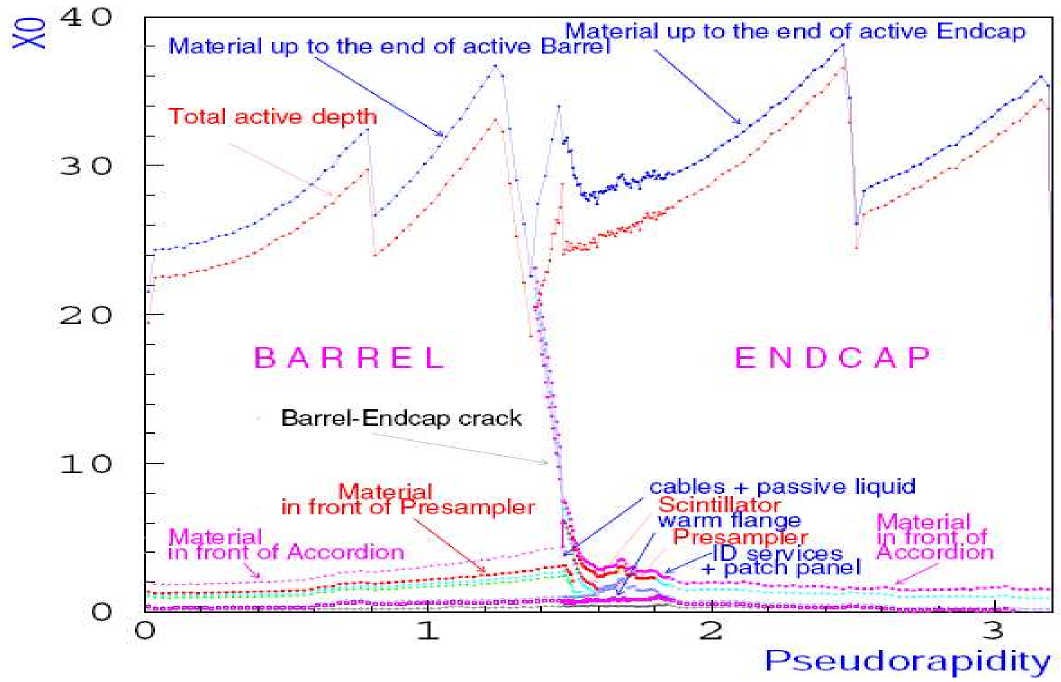

Figure 2.7: Total thickness (in X_0) as a function of η of the electromagnetic calorimeter

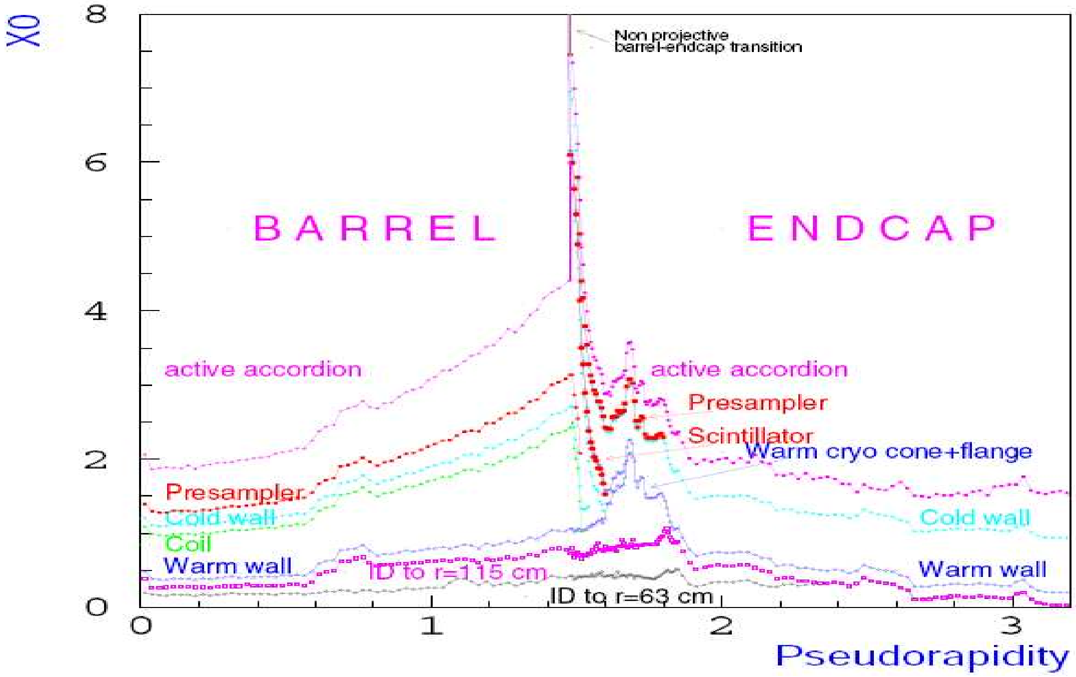

Figure 2.8: Total thickness (in X_0) of the EM material upstream calorimeter as a function of η

2.3 Signal read out

Signals from the detector are processed by various stages before being read out by the DAQ system [21]. The logical flow and the basic elements of the system are shown in figure (2.9). The first part of the electronic system is located inside the cryostat (cold electronics) and it is responsible for signal collection. The second part is placed directly on the calorimeter, outside the cryostat (front - end electronics) and provide amplification, shaping and digitization of the physics signals. The remaining part is located far from the detector, in the counting room, and performs signal processing, system control and monitoring.

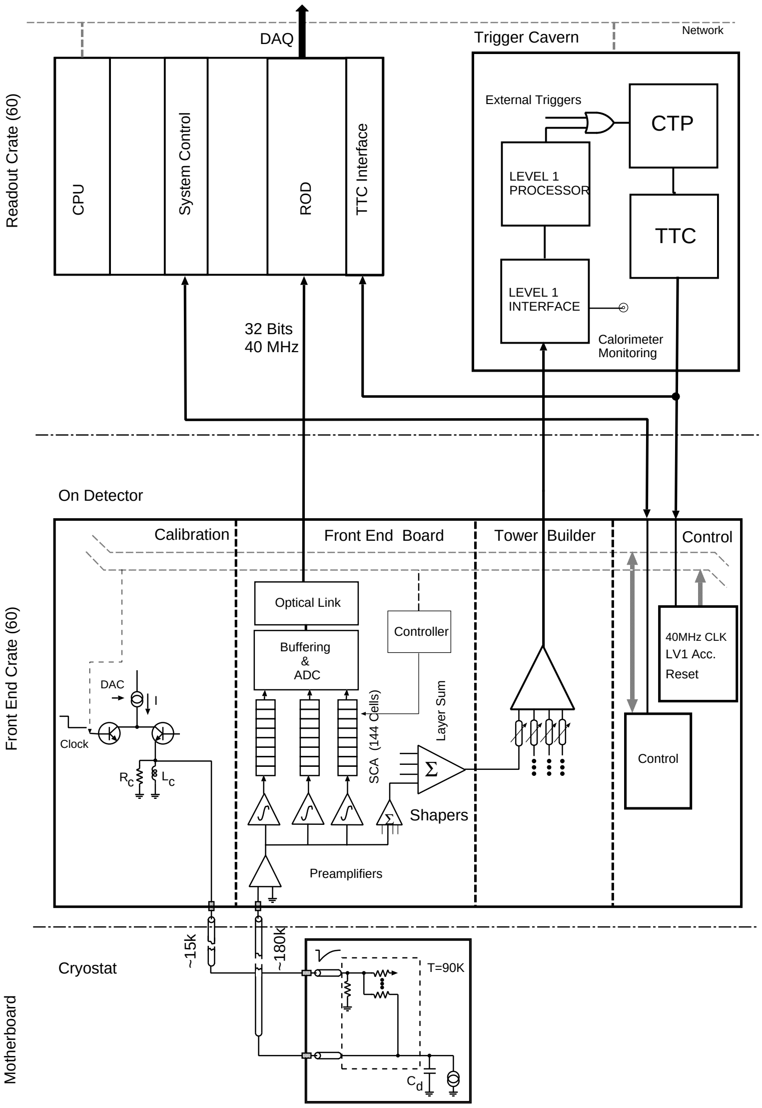

Figure 2.9: Block diagram of the electromagnetic calorimeter read out electronics.

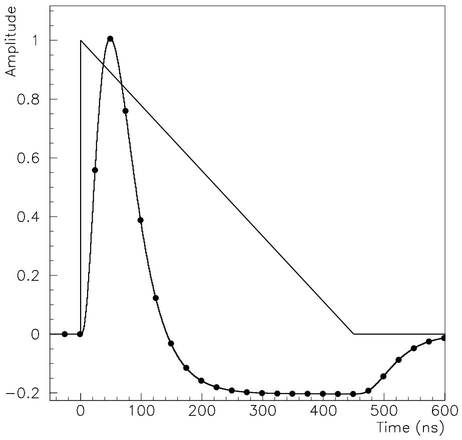

Figure 2.10: Detector signal shape (triangle) and after shaping (curve with dots). The dots on the shaped signals correspond to successive bunch-crossing.

2.3.1 Signal generation and cold electronics

Electrons and positive ions produced by an incoming particle showering in the electromagnetic calorimeter drift along the electric field and generate a triangular current signal on the electrode [22]: the signal peak is proportional to the energy deposited in the calorimeter and the signal duration depends on the electron drift time and the gap length, as shown in figure (2.10). In the barrel calorimeter an average gap thickness of 2.1 mm and the nominal 2 kV potential lead to a typical signal duration of 400 ns and a $\sim$ 2.8 μA induced currents is measured per deposited GeV. In the endcap, where the gap thickness varies with the radius, a radius-dependent high voltage is applied in order to obtain a flat $\sim$ 2.5 μA/GeV response: more details can be found in table (2.2).

	Pseudorapidity	Lead thickness	Gap thickness	$\mu A/$ GeV
Barrel	$\lvert\eta\rvert < 0.8$	1.5 mm	2.1 mm	2.74
	$0.8 < \lvert\eta\rvert < 1.475$	1.1 mm	2.1 mm	3.08
Endcap	$1.375 < \lvert\eta\rvert < 2.5$	1.7 mm	2.8-0.9 mm	2.48
	$2.5 < \lvert\eta\rvert < 3.2$	2.2 mm	3.1-1.8 mm	2.06

Table 2.2: Relevant electromagnetic calorimeter parameters as a function of the pseudorapidity range.

The signals from the calorimeter are collected at the detector front and back faces by summing boards and mother boards and routed to the front end electronics through cold-to-warm feedtroughts [23]

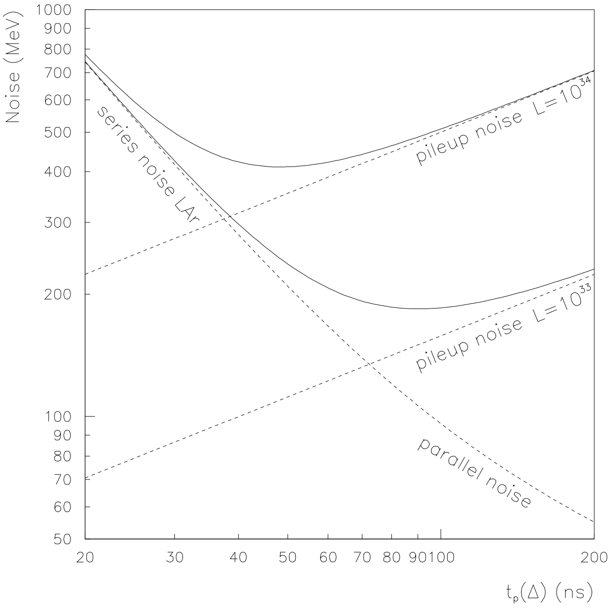

Figure 2.11: Optimization of the shaping time for high and low luminosity.

2.3.2 Front end electronics

The signals coming from the warm flange of the feedthrough are sent to the preamplifier [24].via transmission lines. The preamplifiers are placed on front end boards [25], located outside the cryostat in the front-end crates. The characteristic impedance of the readout lines is optimized on the cell capacitances in order to reduce the electronic noise contributions : 25 Ω characteristic impedance cables are used for middle and back sampling cells while 50 Ω cables for the first layer and the presampler. The warm preamplifier, called 0T , has been designed in order to match the impedance of the line over the full required frequency range. The amplified signal is shaped by a multi-gain CR-RC^2 bipolar filter [26] . The shaper internal constant has been chosen in order to minimize sum of the electronic and pileup noise at high luminosity as showed in figure (2.11): the resulting shaped signal has a typical rise time of $\sim$ 45 ns. In order to cover the full dynamic operational range the shaper provides three different outputs with relative gains of typically 1, 10, 100.

The shaped signal is sampled every 25 ns at the 40 MHz LHC bunch crossing frequency, as shown in figure (2.10). Only the first 5 samples of the signal are taken into account and they are stored in analog memories using Switching Capacitor Arrays (SCA) during the first-level trigger latency. If a physics event pass the LVL1 trigger, the corresponding signal samples are extracted from SCA, digitized and read out to the data acquisition system.

2.3.3 Electronic calibration

A cell by cell electronic calibration system [27, 28] has been developed for the electromagnetic calorimeter. The idea is to generate a calibration signal as much as possible similar to the expected physics signal in order to correct for channel to channel electronic gain variations. An exponential voltage pulse is applied across an injector resistor R_{inj} placed on the motherboard, generating on the electrodes an exponential current signal with a decay time of $\simeq$ 400 ns. The signal is acquired through the read out chain and a channel by channel ADC to μA factor is then calculated. The accuracy on electronics chain calibration contributes to the constant term of the energy resolution : the goal is to keep the this contribution to less than 0.3 %.

2.3.4 ROD system and optimal filtering

The samples of a physics signal which passed the LVL1 trigger are routed to the Read Out Board (ROD) by digital optical link, dimensioned for a LVL1 trigger rate of 75 KHz maximum. The ROD are located far from the detector, in the trigger cavern, and are responsible for the signal processing: the purpose is to extract the best possible information from the five digitized samples and a procedure based on the digital optimal filtering [29, 21] concept has been adopted. It has been demonstrated that for a given signal and noise sources with known frequency spectra it is possible to derive an analytical expression for the filter which gives the best signal to noise ratio (optimal filter). The transfer function H_A of the optimal filter at time t_0 is reported in equation (2.1) :

$$H_A = \frac{K_A G^*(\omega)}{S(\omega)} \cdot e^{-j\omega t_0} \tag{2.1}$$

where K_A is a normalization factor, G^* is the complex conjugate of the frequency spectrum of a known input signal g(t), S(ω) is the total noise power spectrum. A method based on digital filtering and multiple sampling has been proposed : it consists in a digital reshaping which allow to recover the best possible performance of the system in a wide range of operating conditions. The effect of the method is shown in figure (2.12) as a function of the machine luminosity.

Assuming that the normalized signal shape after the shaper $g(t)$ is known, a sample of the signal can be written in the following way:

$$S_i = Ag(t_i - \tau) \tag{2.2}$$

where A and τ are the unknown amplitude and the phase of the signal with respect to the clock. A and τ can be derived by properly combining the available samplings as a discrete convolution between the vector of signal samples and a set of optimal weights:

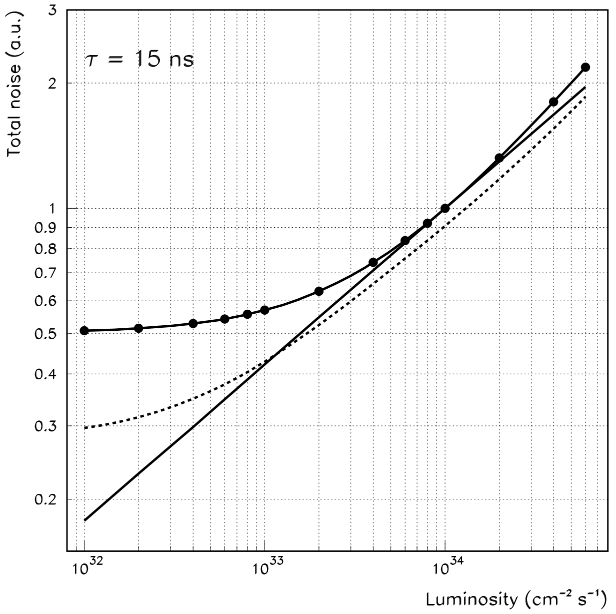

Figure 2.12: Total noise as a function of the luminosity for a shaping constant of 15 ns. The dots and dashed lines show the performance without and with the optimal filtering. The full lines shows the level of noise achievable with the optimal hardware shaper constant for each luminosity.

$$A = \sum_i w_i g(t_i - \tau) \tag{2.3}$$

$$A\tau = \sum_i v_i g(t_i - \tau) \tag{2.4}$$

The optimal filtering coefficients w_i and v_i can be calculated in the time domain by minimizing the variance on A and $A\tau$. In the frequency domain the effect of this technique is equivalent to pass the signal through a digital optimal filter since the discrete convolution in equation (2.3) becomes a simple inner product between the Fourier transform of the samples and an optimal matched transfer function.

After optimal filtering other corrections for the electronic gain variation from the calibration system are applied in the ROD leading to a signal peak value in μA units. Finally a μA to GeV conversion is performed in order to provide to the LVL2 trigger the best estimation of the deposited energy in a given calorimeter cell.

Chapter 3

Introduction to the calibration method

3.1 Calibration Hits Simulation

The simulation program for the Atlas experiment is presently operational in a full OO (Object Oriented) environment. This important physics application has been successfully integrated in the Atlas common analysis framework, Athena [11].

The GEANT4 [12, 13] Simulation for the Atlas detector is a tool implemented directly into Athena; it replaces the GEANT3 based simulation, which played the major role in Atlas during the past 10 years. The new simulation was implemented with the same accuracy and level of detail as the previous one, if not more, and follows all of the developments in the most recent construction phase of the detector.

Physics events are simulated by means of one of the event generators currently available in the Atlas software suite. The event is than modified to take the actual experimental conditions (e.g. vertex displacement) and particles are propagated through the detector. In the standard simulation the energy deposited in the detector active elements is saved into persistent objects (hits), together with all events informations which might be needed at the analysis stage (secondary vertex, secondary tracks). The *Calibration Hits* simulation technique allows to save into persistent objects also the energy deposited in the detector inactive and dead material. A code allows to know where and in which material the energy is deposited: this allows to study in great detail the shower development inside the detector and understand the physical processes that are at the base of the detector reply.

Data objects representing Monte Carlo truth information from the generators was read by simulation and processed. Hits produced by the simulation can be directly processed by the digitization algorithm and transformed into Raw Data Objects (RDO). Alternatively they can be sent to the pileup algorithm and then passed either to the digitization for RDO production or to the third level trigger chain for the final Event Filter selections, see for more details section (1.3).

3.2 Simulation Rounds

To disentangle different effects, four rounds of simulation are been used:

1. monochromatic electrons hitting the center of a middle compartment cell. No B field. These are the simplest possible conditions, see section (4.1).
2. monochromatic electrons spread uniformly over the middle compartment cell. No B field. These simulations are used to study the effects introduced by the accordion granularity, see section (4.2).
3. monochromatic electrons spread uniformly over the middle compartment cell. B field on. These simulations reproduce the real operative conditions of Atlas, see section (4.3).
4. monochromatic electrons and photons spread uniformly over the full η coverage of the calorimeter, included the endcap region. B field on. Full digitization and improved geometry, see chapter (5).

The simulation of the first three points in the previous list has been done with GEANT 4 and Athena 10.0.1. Since the standard reconstruction algorithm wasn't available at that time for the Calibration Hit simulations, a self made reconstruction code, including a clusterization algorithm, was developed. A cluster of the required dimension, typically 3×5 or 3×7, is built around the most energetic cell.

The events of the first three rounds are simulated from the Atlas center. Few samples of events simulated with a vertex spread show that the vertex spread influences only the modulation inside a cell and not the others therms of the reconstruction algorithm. All these simulations require a big computing effort, over 3.1M events simulated, and has been done on the Milan computing facility.

The fourth point in the simulation list has been studied with the CSC (Computing System Commissioning) data, available from central production and produced with Athena 11.0.5. They use the newest detector geometry, the “as built” geometry, that takes into account the known deformations of the detector. The particles are spread over the full η range of the calorimeter, including the endcap, subdivided into 100 cells; the statistic in each cell is around 500 events for each of the 7 simulated energies.

3.3 Material and energy classification

In the simulation the materials inside the Atlas detector are classified into three different classes, and hits in different materials are classified in different containers:

- active: all the active layers of each subdetector. For example, LAr between the absorbers in the Accordion

- inactive: all the inactive layers of each subdetector. For example the absorbers in the Accordion
- dead: for example the cryostat, the solenoid, the electronics, etc..

To reconstruct the electron energy from the energy deposited into the LAr an algorithm has been developed which makes use of the quantities listed below:

- E_{front} : total energy deposited in front of the PreSampler, including the cryostat and the solenoid
- E_{ps} : energy deposited into the PreSampler, divided in *active* and *inactive*
- E_{psstr} : energy deposited in the dead material between PreSampler and strips
- E_{str} : energy deposited in the first sample (strips) of the EM calorimeter, divided in *active* and *inactive*
- E_{mid} : energy deposited in the second sample (middle) of the EM calorimeter, divided in *active* and *inactive*
- E_{back} : energy deposited in the third sample (back) of the EM calorimeter, divided in *active* and *inactive*
- E_{behacc} : total energy deposited behind the EM calorimeter

3.4 Calibration method based on Longitudinal Weights

The existing calibration method [30, 31] uses four longitudinal weights to reconstruct the energy deposited by the electromagnetic shower into the detector , as in equation (3.1).

$$E_{reco} = \lambda(off + w_0 E_0 + E_1 + E_2 + w_3 E_3) \tag{3.1}$$

where : E_0,E_1,E_2 and E_3 are the energies deposited into the active layer of the PreSampler and of the 3 compartments of the calorimeter, while λ, off, w_0 and w_3 are 4 parameters to be determined.

The w_0 parameter is supposed to be correcting for the energy deposited in front of calorimeter. The off parameter is an offset motivated by Test-Beam analysis and is found to optimize simultaneously electron energy linearity and resolution. The weight w_3 for the third sampling is supposed to be correcting for the longitudinal leakage.

The 4 weights are obtained by fitting electrons of known energy through minimization of the function in equation (3.2).

$$\chi^2 = \sum_{i}^{N_{events}} \frac{(E^i_{reco} - E^i_{true})^2}{\sigma^2_{EMB}} \tag{3.2}$$

where: E_{reco} is the reconstructed energy as in equation (3.1), E_{true} is the true electron energy and σ_{EMB} is a parametrization of the calorimeter resolution.

Due to the minimization process that is at the base of the weights extraction, the parameters are not clearly correlated with the physical process of the shower. As an example, the quantity $\lambda(off + w_0 E_0)$ cannot be interpreted as the real energy deposited by the shower in front of the calorimeter, because the weights are extracted only minimizing the energy resolution and linearity, without the imposition of any "physical" constrain.

The big strength of this method is its simplicity and the independence of the weigths from the electron energy.

3.5 Calibration method based on Calibration Hits

The proposed method, based on Calibration Hits, makes use of a full parametrization of the energy deposited by the electromagnetic shower into the various detector compartment. The particle energy is computed, for $\eta \leq$1.8, with the formula:

$$\begin{aligned} E_{reco} &= \overbrace{a(E^{acc}_{reco},\eta) + b(E^{acc}_{reco},\eta)\cdot E^{cl\ LAr}_{ps}}^{E_{front}} \\ &+ \underbrace{\frac{1}{S_{Acc}(X,\eta)}\cdot\Big(\sum_{i=1,3} E_i^{cl\ LAr}\Big)}_{E_{acc}}\cdot\underbrace{(1+f_{leak}(X,\eta))}_{E_{behacc}}\cdot\ \underbrace{(F(\eta,\phi))}_{ImpactPointMod.} \end{aligned} \tag{3.3}$$

where:

- E_{reco} is the reconstructed energy of the particle
- $a(E^{acc}_{reco},\eta)$ and $b(E^{acc}_{reco},\eta)$ are parameters to be determined as a function of the energy deposited into the accordion and η
- $E^{cl\ LAr}_{ps}$ is the energy deposited in the active layer of the PreSampler, in the cluster
- $S_{Acc}(X,\eta)$ is the accordion sampling fraction in the cluster multiplied by the correction for the energy deposited out of the cluster. This factor is parametrized as a function of X, the longitudinal barycenter of the shower, and η
- $E_i^{cl\ LAr}$ is the energy deposited into the cluster in the i^{th} (i=0,3) layer of the accordion
- $f_{leak}(X,\eta)$ is the correction for the longitudinal leakage. It is parametrized as a function of η and X, the longitudinal barycenter of the shower.
- $F(\eta,\phi)$ is the energy correction depending from the impact point of the particle inside a cell (called in the next *Impact Point Modulations*)

In the equation (3.3) we make use of the variable X, called shower depth or longitudinal barycenter of the shower, and defined as:

$$X = \frac{\sum_{i=1}^{4} E_i^{LAr} X_i}{\sum_{i=1}^{4} E_i^{LAr}} \tag{3.4}$$

where E_i^{LAr} are the energies deposited in the active medium of the PreSampler and in the three calorimeter compartments (strip, middle and back), and X_i is the depth, expressed in radiation length, of the longitudinal center of each compartment, computed starting from the interaction point (center of Atlas in this simulations). It is important to note that X_i change in η due to the geometry of the calorimeter and needs to be recalculated for each η position. Figure (3.1) shows the longitudinal center X_i of each calorimeter compartment (PreSampler, strips, middle and back) as a function of η, computed in the barrel region with an approximated formula, and in the EndCap region with a dedicated simulation.

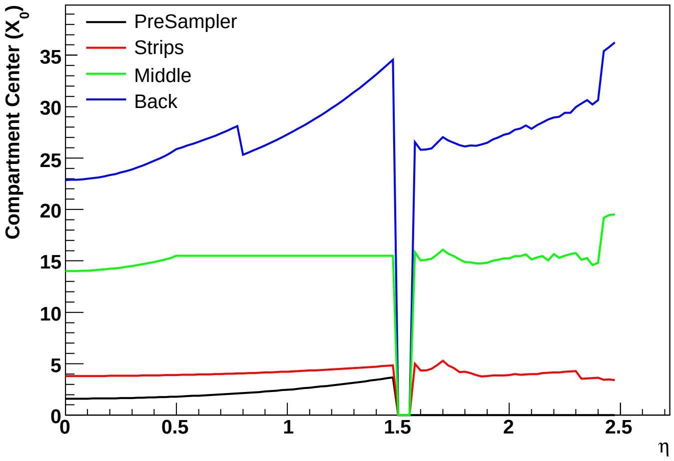

Figure 3.1: Compartments center

The reconstructed energy can be easily factorized in three part:

$$E_{reco} = E_{front} + E_{acc} + E_{behacc} \tag{3.5}$$

where:E_{front}, E_{acc}, E_{behacc} are the real energies deposited by the shower in front of the calorimeter, in the accordion and behind it, and are defined as in equation (3.3).

In the region of the calorimeter without the PreSampler ($\eta > 1.8$) the first two terms in the equation (3.3), the ones for the determination of E_{front}, are substituted by a parametrization as a function of the shower depth, as in equation (3.6):

$$E_{reco}^{front} = a(E_{reco}^{acc}, \eta) + b(E_{reco}^{acc}, \eta) \cdot X + c(E_{reco}^{acc}, \eta) \cdot X^2 \tag{3.6}$$

where $a(E^{acc}_{reco},\eta)$, $b(E^{acc}_{reco},\eta)$ and $c(E^{acc}_{reco},\eta)$ are parameters to be determined as a function of η and E^{acc}_{reco}.

This method is more complex than the calibration method based on the longitudinal weights, but have the strength of being strongly related to the physical process inside the detector. In addition it could provides the energy deposited into each detector compartment, and not only the total deposited energy by the shower, that may be usefull in several physical analysis.

Chapter 4

Milan data set analysis

4.1 Electrons hitting the cell center

To study, understand and explain the proposed calibration method we start with the simplest condition: electrons hitting the center of a cell, in the middle compartment; 11 η points (spanning from η=0.1 to η=1.2 with 0.1 steps) and 11 energies (5, 10, 15, 20, 30, 40, 50, 60, 80, 100, 200 GeV) have been simulated.

All the simulations have been done on the Milan computing facility, with Athena 10.0.1. Both reconstruction and calibration codes are selfmade including the clustering algorithm, because at the time of these simulations the official reconstruction code could not process the Calibration Hits data files. Also the digitization was not included since not yet available for Calibration Hits simulations, and the energy deposited into the active layers of the detector are taken as the detector reply.

All the analysis shown in the next paragraphs are relative to 3×5 cluster size, except where differently specified.

4.1.1 Energy distribution inside the subdetectors

To understand the proposed calibration method is important to know how the energy of the shower is shared between the different compartments of the detector.

Figures (4.1) and (4.2) show the distributions of the energy deposited by electrons of 20 GeV and 100 GeV inside the four layers of the EM calorimeter, for various η points. The distributions show the total deposited energy into active and inactive material inside each compartment of the calorimeter. It is evident that the largest part of the shower energy, up to 80%, is deposited into the middle compartment, while the others compartments receive a smaller fraction of the shower energy: 15÷25% in the strip, 1% into the PreShower and only the 0.5% into the back compartment.

In figure (4.3) the distributions of the energy deposited by the electron showers outside the calorimeter are shown: into the material upstream the PreSampler (E_{front}), into the dead material between PreSampler and strips (E_{psstr}) and behind the accordion

(E_{behacc}). It is possible to see that only a small fraction of the EM shower energy is deposited behind the calorimeter, but a relevant portion, up to 10%, is deposited in the material in front of calorimeter.

The dependence of the various distributions on η are complicated and are due to the superimposition of 2 different effects:

- the compartments length changes in η, as shown in figure (2.6)
- the material in front of calorimeter changes in η, as shown in figures (2.7) and (2.8)

The first point influences directly the energy sharing between the different compartments, while the second point influences the shower development that reflects again on the energy sharing.

4.1.2 Energy reconstruction in the Accordion

We start to reconstruct the energy deposited by the shower in the accordion. We use a single correction to go from the energy deposited in the active material in the cluster to the total energy in the accordion, including the correction for the energy deposited outside the cluster. This correction is a function of the shower depth, defined in (3.4).

In figure (4.4) the cluster sampling fraction defined in equation (4.1) is shown at 4 η values and 11 energies.

$$S_{cl} = \frac{E_{Acc}^{cl\ LAr}}{E_{Acc}^{cl\ LAr} + E_{Acc}^{cl\ Abs}} \tag{4.1}$$

where: $E_{Acc}^{cl\ LAr}$ is the energy deposited in the active medium (LAr) into the accordion cluster, $E_{Acc}^{cl\ Abs}$ is the energy deposited in the absorbers into the accordion cluster.

For comparison the figure (4.5) shows, for the same η points and energies, the total accordion sampling fraction, defined as in equation (4.2).

$$S_{tot} = \frac{E_{Acc}^{LAr}}{E_{Acc}^{LAr} + E_{Acc}^{Abs}} \tag{4.2}$$

where: E_{Acc}^{LAr} and E_{Acc}^{Abs} are the energy deposited in the active and inactive medium in the total accordion.

The total accordion sampling fraction S_{tot} shows the same behavior as the cluster sampling fraction S_{cl}, but its value is about 1% lower. This is interpreted as due to the fact that into an electron shower the fraction of very low energy photons and electrons increases with the radial distance from the shower centre. These particles, that are taken into account only in the S_{tot}, are more easily absorbed into the absorbers, lowering the sampling fraction.

The cluster sampling fraction is energy dependent, as is shown in figure (4.6), but this energy dependence becomes marginal once it is plotted as a function of the shower depth.

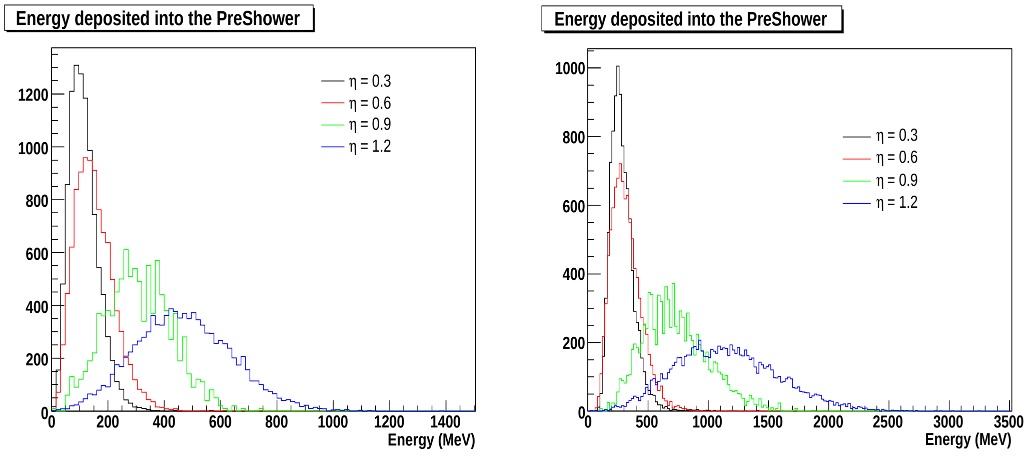

(a) E_{ps} , E=20GeV (b) E_{ps} , E=100GeV

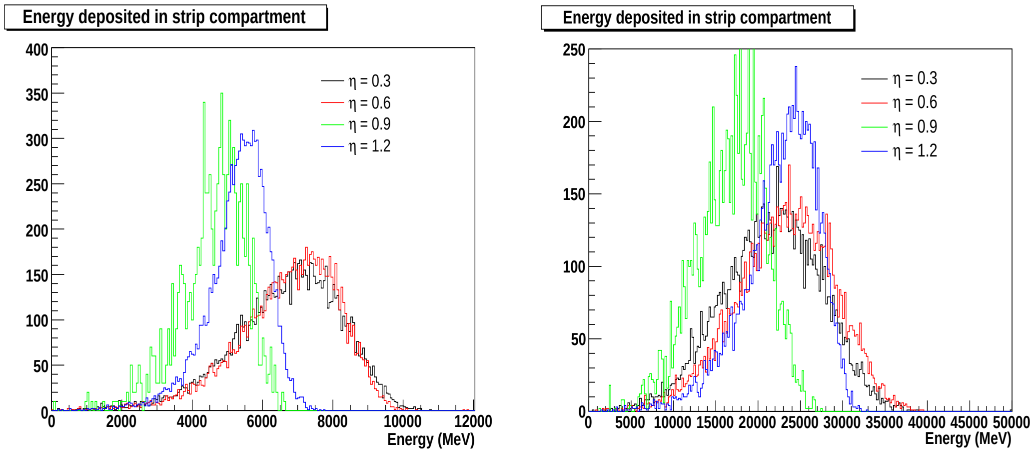

(c) E_{strip} , E=20GeV (d) E_{strip} , E=100GeV

Figure 4.1: Energy deposited in the PreSampler and Strips calorimeter compartments by 20 GeV and 100 GeV electrons, at various η points.

The fraction of energy deposited outside the cluster, as defined in equation (4.3), is shown in figure (4.7).

$$E^{outcl}(\%) = \frac{E^{outcl\ LAr}_{Acc} + E^{outcl\ Abs}_{Acc}}{E^{cl\ LAr}_{Acc} + E^{cl\ Abs}_{Acc}} \qquad (4.3)$$

where: $E^{outcl\ LAr}_{Acc}$ and $E^{outcl\ Abs}_{Acc}$ are the energies deposited outside the accordion cluster into the active and inactive material, $E^{cl\ LAr}_{Acc}$ and $E^{cl\ Abs}_{Acc}$ are the energies deposited into the accordion cluster in the active and inactive material.

Also for this quantity the energy dependence becomes negligible once expressed as a function of the shower depth. A residual energy dependence is visible at larger η and for very low electron energy (5GeV), but proved to be uninfluent on the performances

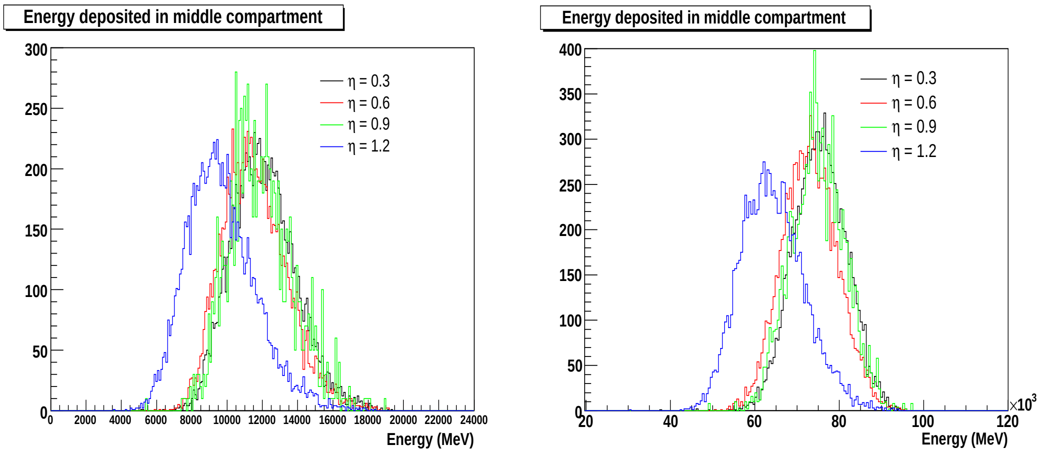

(a) E_{middle} , E=20GeV (b) E_{middle} , E=100GeV

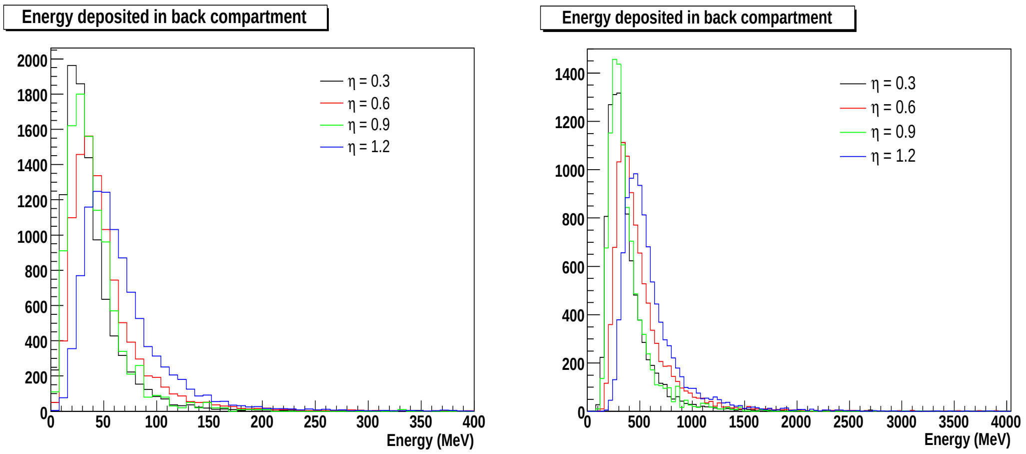

(c) E_{back} , E=20GeV (d) E_{back} , E=100GeV

Figure 4.2: Energy deposited in Middle and Back calorimeter compartments by 20 GeV and 100 GeV electrons, at various η points.

of the method: an energy dependent parametrization has been tested to give results, in term of energy resolution and linearity, comparable to the one obtained with an energy averaged parametrization.

To calibrate the accordion two different approaches are possible:

1. use a single correction to go from the energy deposited in the cluster into the LAr to the total energy deposited into the accordion. This correction is shown in figure (4.8), where different colour refer to different energy values of the incident particles, and it is defined as in equation (4.4):

$$C_{tot} = \frac{E^{LAr}_{Acc} + E^{Abs}_{Acc}}{E^{cl\ LAr}_{Acc}} \tag{4.4}$$

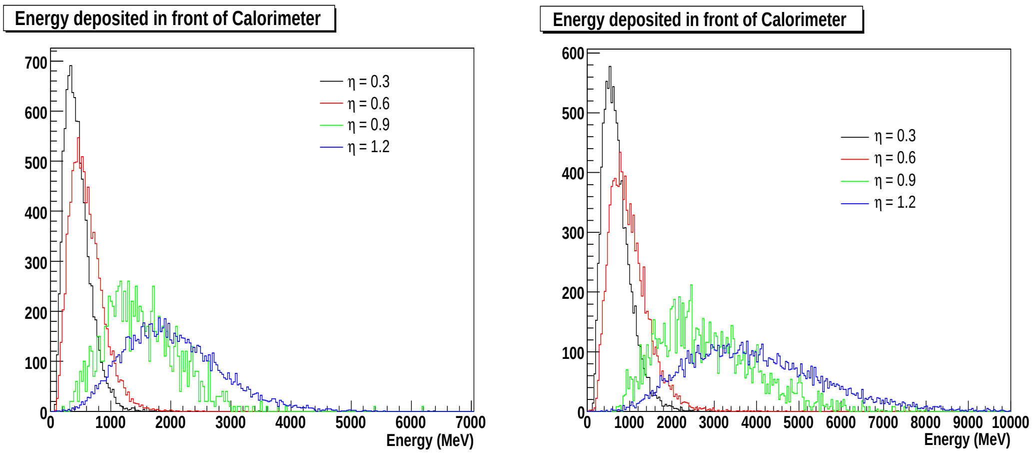

(a) E_{front} , E=20GeV (b) E_{front} , E=100GeV

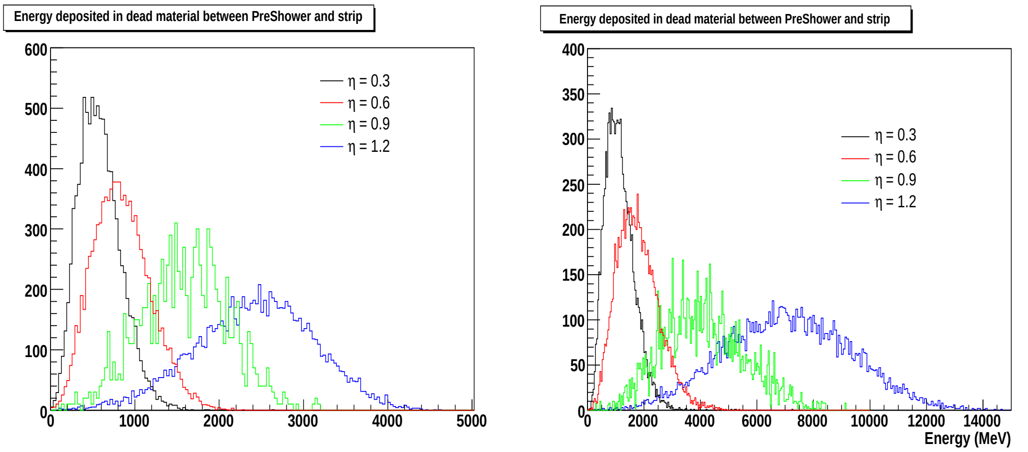

(c) E_{psstr} , E=20GeV (d) E_{psstr} , E=100GeV

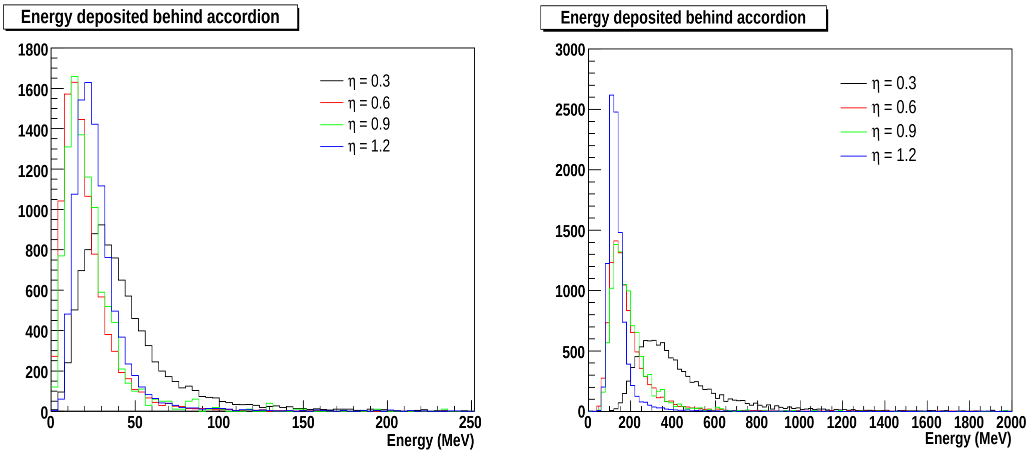

(e) E_{behacc} , E=20GeV (f) E_{behacc} , E=100GeV

Figure 4.3: Energy deposited by 20 GeV and 100 GeV electrons in front of calorimeter, in the dead material between PreSampler and Strips, and behind the accordion, at various η points.

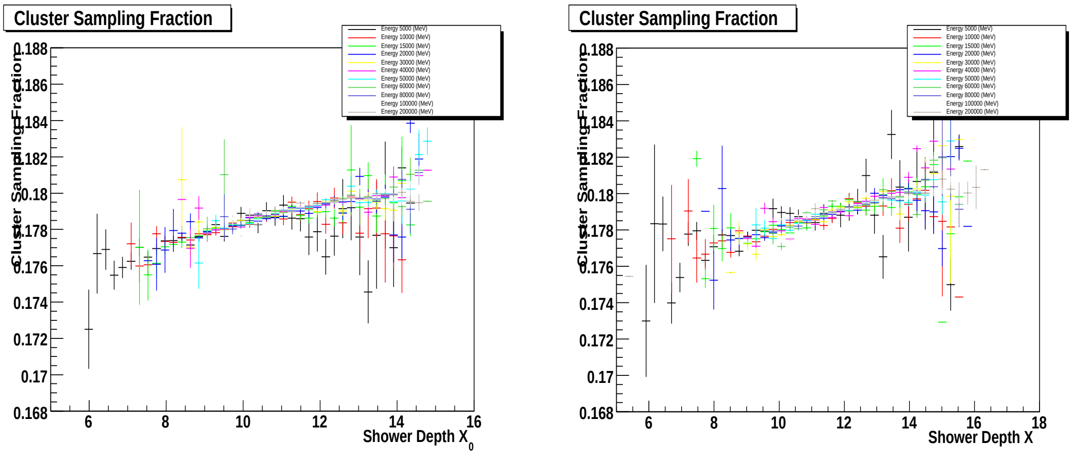

(a) η=0.3 (b) η=0.6

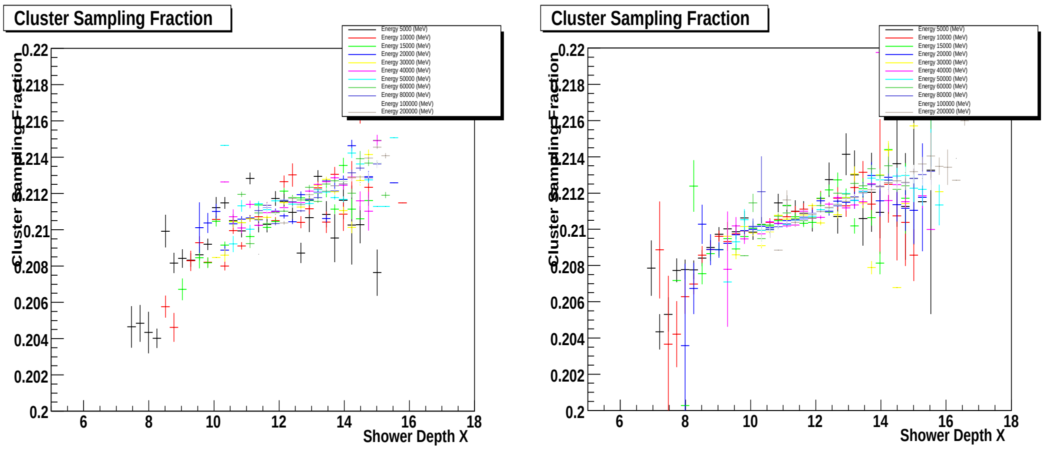

(c) η=0.9 (d) η=1.2

Figure 4.4: Cluster Sampling Fraction as a function of the shower depth X at various η points and energies.

The red dashed line is the adopted parametrization obtained from the energy averaged fit.

2. use a correction to go from the energy deposited in the cluster in the LAr to the total energy deposited into the accordion cluster. This correction is shown in figure (4.9), as a function of the shower depth, and it is the inverse of the cluster sampling fraction S_{cl}. Once reconstructed the total energy deposited into the accordion cluster it is necessary to apply a correction that take into account the energy deposited outside the cluster, as shown in figure (4.7).

Both methods have been tested and give comparable results in term of energy resolution and linearity. In the attempt of reducing the number of calibration coefficients to the minimum, the first method is used with the events simulated at cell center.

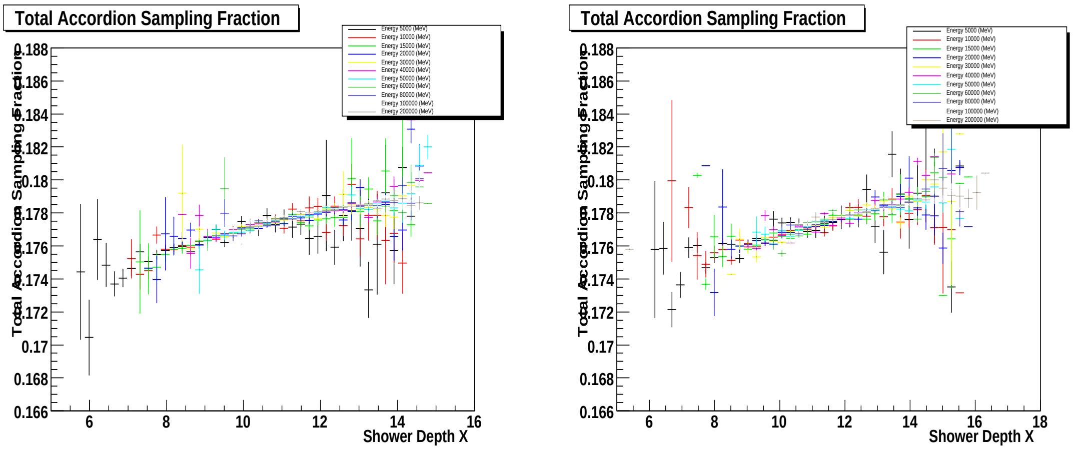

(a) η=0.3 (b) η=0.6

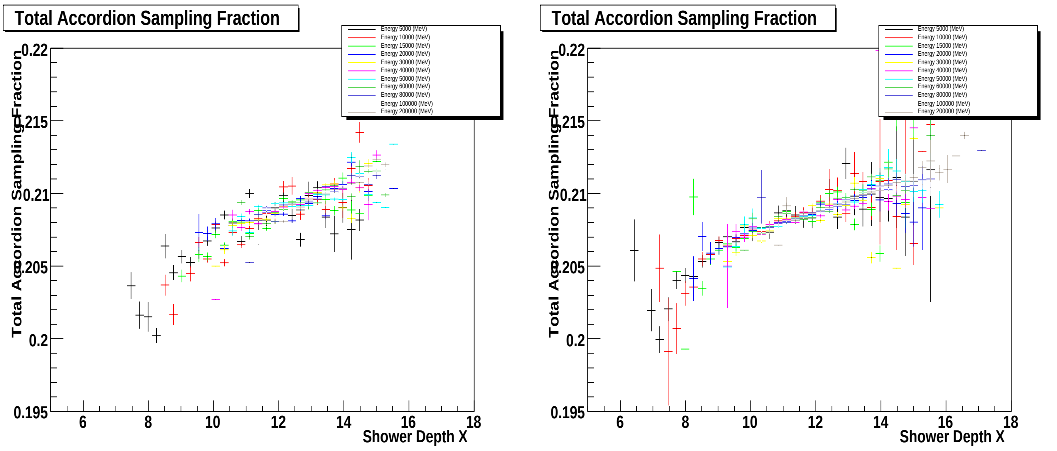

(c) η=0.9 (d) η=1.2

Figure 4.5: Total Accordion Sampling Fraction as a function of the shower depth X, at various η points and energies.

The residual energy dependence of the Total Accordion Correction factor is neglected and an averaged over electron energies correction is used, as shown in figure (4.10), where the second degree polynomial parametrization is also shown. The range of the fit is determined excluding the bins containing less than 0.5% of the total statistic. The evident variation in the values of the total accordion from the top plot to the bottom is due to the absorbers thickness variation at η=0.8, that imply a variation in the sampling fraction.

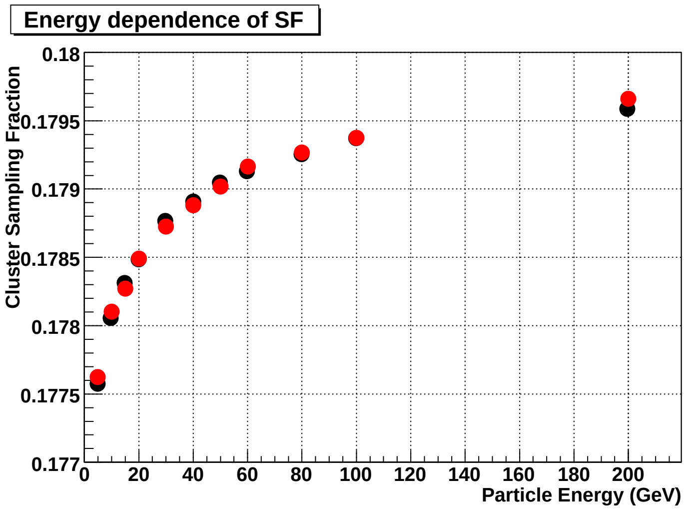

(a) η=0.3 and η=0.6

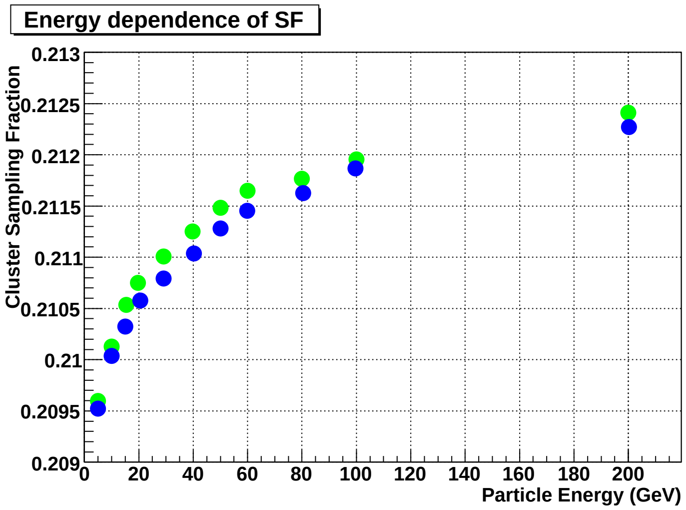

(b) η=0.9 and η=1.2

Figure 4.6: Energy dependence of the cluster sampling fraction. The black dots refer to η=0.3, the red to η=0.6, the green to η=0.9 and the blue to η=1.2 .

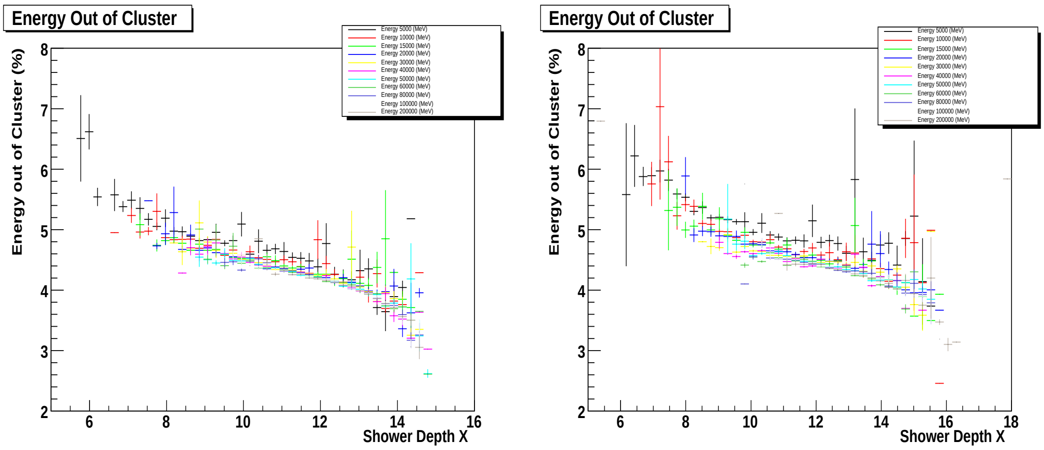

(a) η=0.3 (b) η=0.6

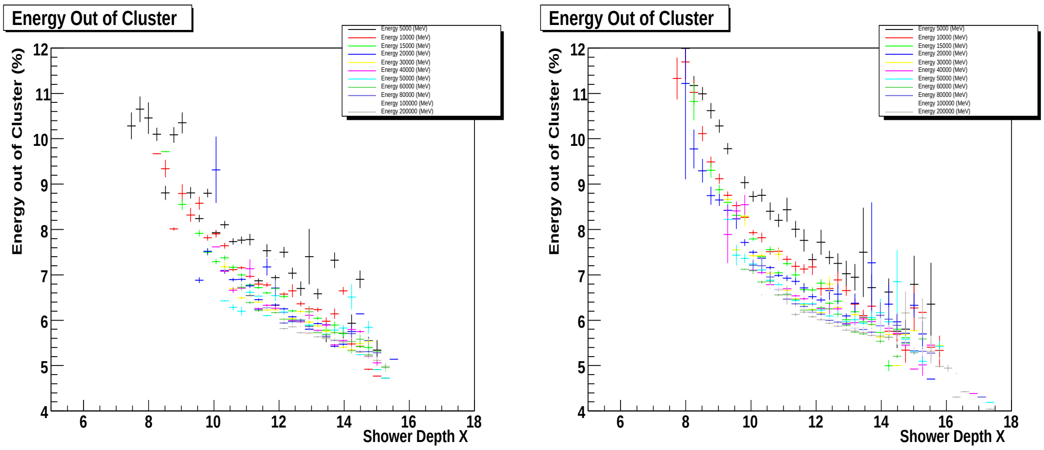

(c) η=0.9 (d) η=1.2

Figure 4.7: Energy deposited out of the cluster, expressed as a fraction (%) of the energy deposited inside the cluster, for various η points and energies.

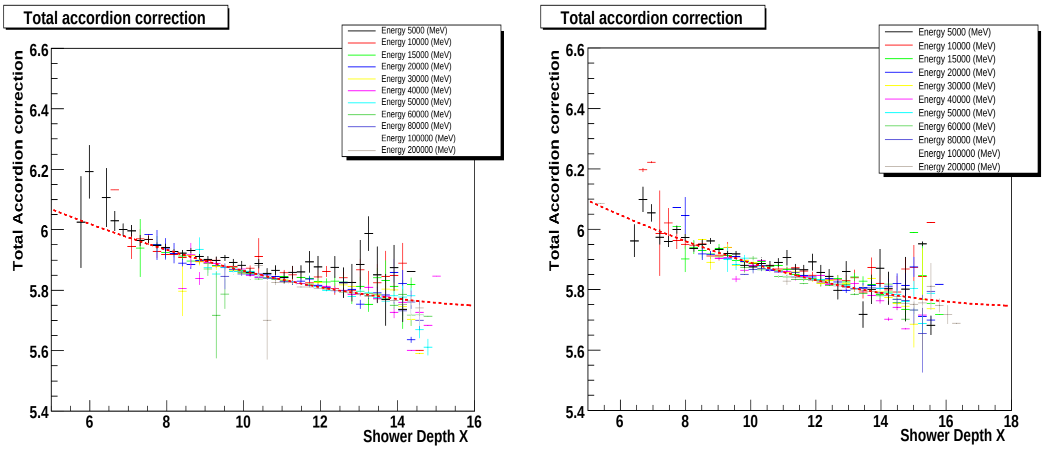

(a) η=0.3 (b) η=0.6

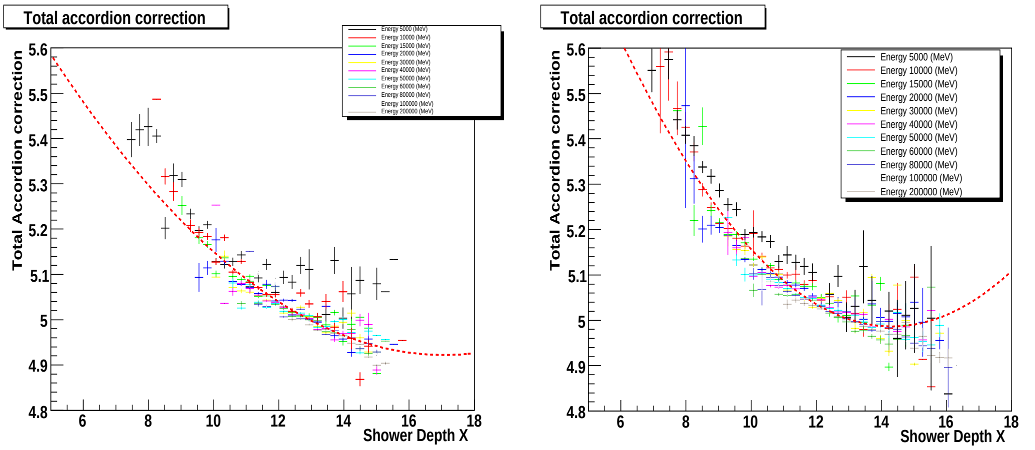

(c) η=0.9 (d) η=1.2

Figure 4.8: Total Accordion Correction factor as a function of the shower depth X, for various η points and energies. The red dashed line is the energy parametrization achieved from the fit shown in figure (4.10), and shown here only as a reference

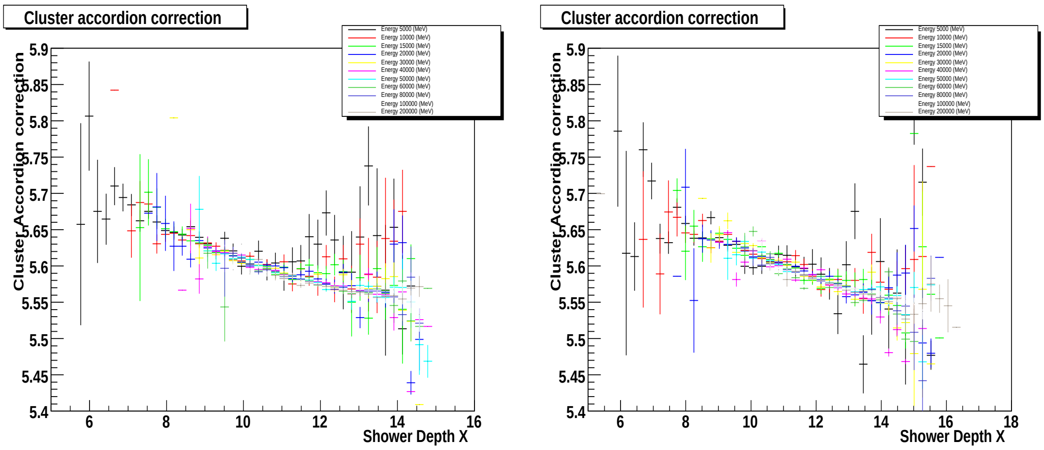

(a) η=0.3 (b) η=0.6

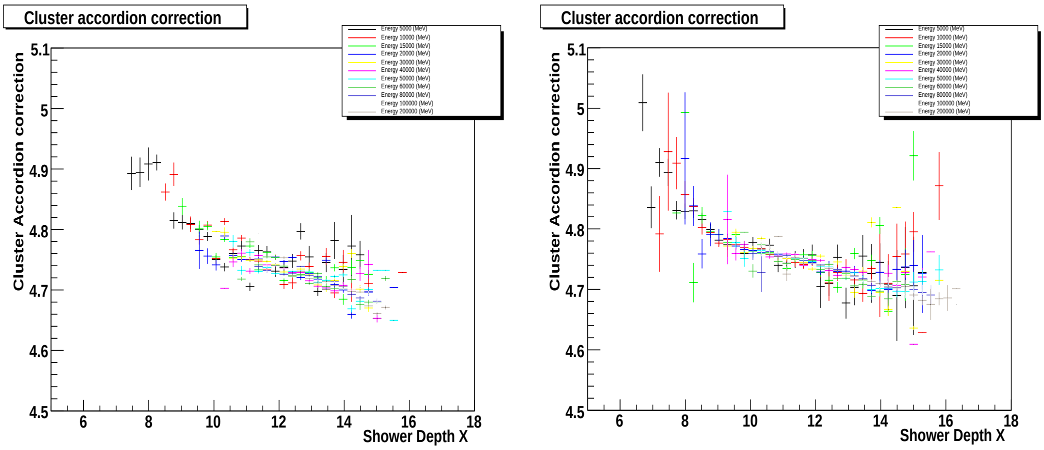

(c) η=0.9 (d) η=1.2

Figure 4.9: Cluster Accordion Correction factor as a function of Shower Depth X, for various η points and energies.

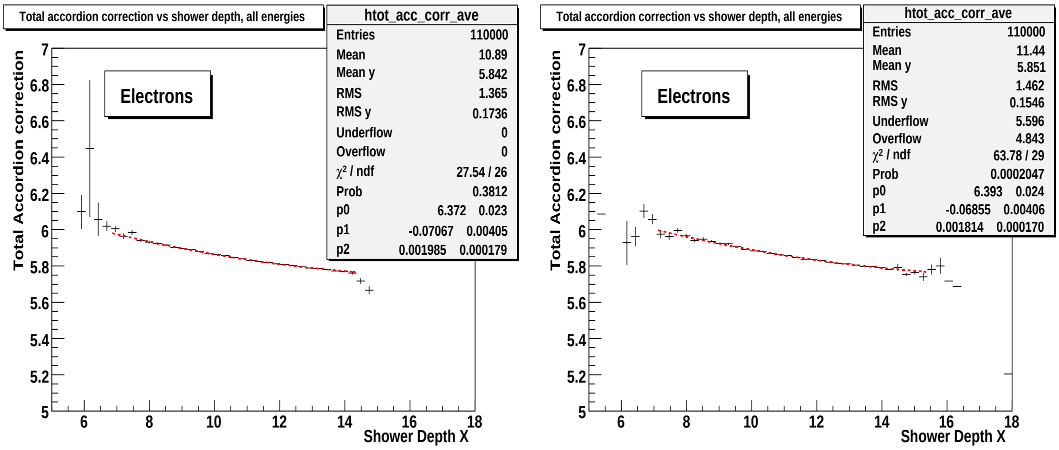

(a) η=0.3 (b) η=0.6

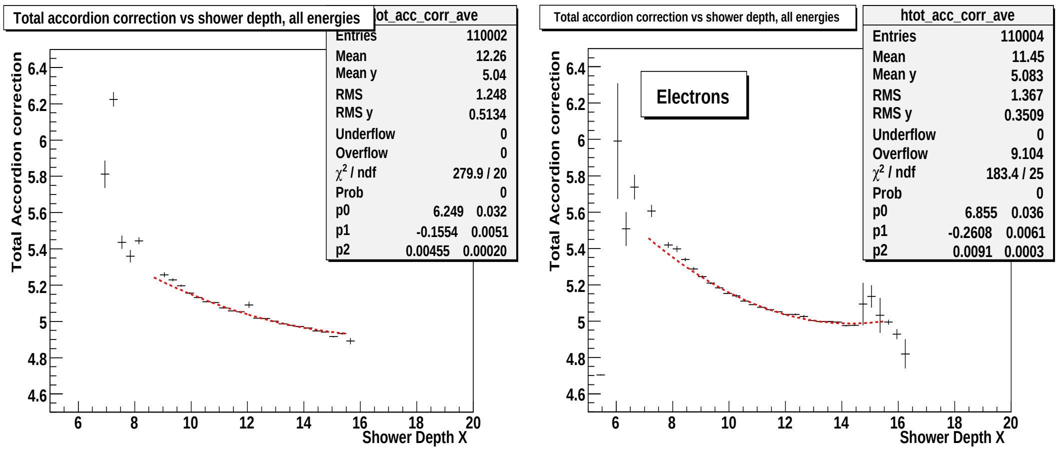

(c) η=0.9 (d) η=1.2

Figure 4.10: Total Accordion Correction factor as a function of Shower Depth X, energy averaged, for various η points, with superimposed the used parametrization.

4.1.3 Calculation of the energy deposited in front of the Accordion

The energy deposited in the materials in front of the calorimeter (Inner Detector, cryostat, coil...) is parametrized as a function of the energy deposited in the active layer of the PreShower and depends strongly on the energy of the incident electrons, as shown in figures (4.11) and (4.12), at η=0.3. The adopted parametrization with a first degree polynomial is shown by the red dashed line: higher degree polynomials have been tested without any improvement in the performances of the method. Note explicitly that here the energy deposited upstream the calorimeter includes the energy deposited into the active and inactive layers of the PreSampler, and also the energy lost in the dead material between the PreSampler and the first layer of the accordion (strips).

The parametrization with the first degree polynomial is adopted on all the η range as shown in figure (4.13), where the energy lost in front of the calorimeter by 100 GeV electrons is shown at various η points.

The parameters of the first degree polynomial (labelled *offset* and *slope*) are shown in figure (4.14) as a function of the mean energy deposited into the accordion at four η values. The dashed line represents the used parametrization, as in equations (4.5) and (4.6).

$$a(\eta) = p_0^{front} + p_1^{front} E_{tot}^{Acc} + p_2^{front} \sqrt{E_{tot}^{Acc}} \tag{4.5}$$

$$b(\eta) = p_0^{front} + p_1^{front} \log E_{tot}^{Acc} + p_2^{front} \sqrt{E_{tot}^{Acc}} \tag{4.6}$$

A not negligible amount of energy is deposited upstream calorimeter even when no energy is measured in the PreShower (offset). This amount increases with electrons energy and is much higher than the energy lost by ionization; we interpret it as due to the absorption of very low energy photons and electrons present in the early shower.

A different calibration approach for the energy lost in front of the calorimeter has been tested: it's based on the splitting of the energy lost in front of the PreSampler from the energy deposited in the dead material between PreSampler and strips. In figure (4.15(a)) the energy deposited by 100 GeV electron in the material in front of the active layer of the PreSampler as a function of the energy into active layer of PreSampler is shown, for η=0.3. Figure (4.15(b)) shows the energy deposited in the dead material between PreSampler and the strips as a function of the geometrical mean of the energy deposited into the active layer of the PreSampler and strip. Both energy distributions are parametrized with a first degree polynomial, also shown in the figures. This parametrization may results useful to better understand the energy deposition in the various layers of the detector, but gives the same performances of the method discussed before, with the addition of two more energy dependent parameters: this parametrization will not be adopted into the next studies and is here discussed only for completeness.

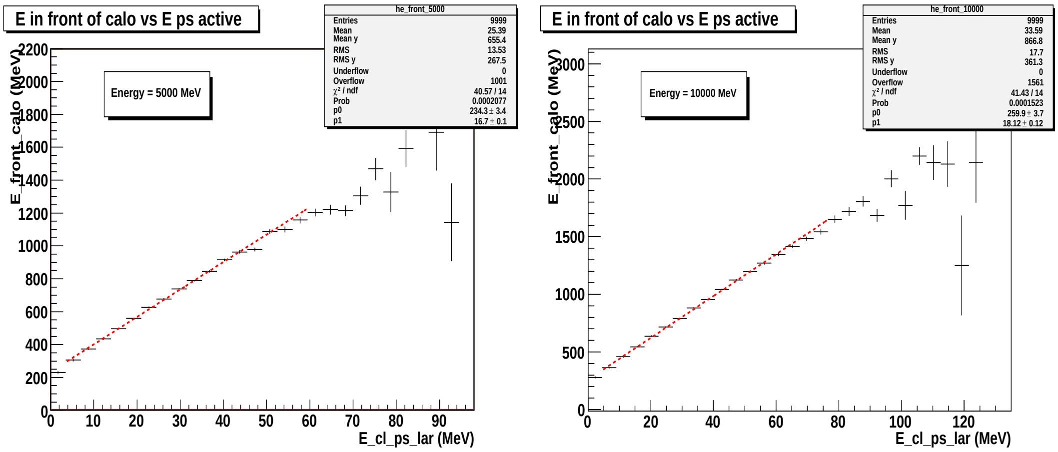

(a) E=5GeV (b) E=10GeV

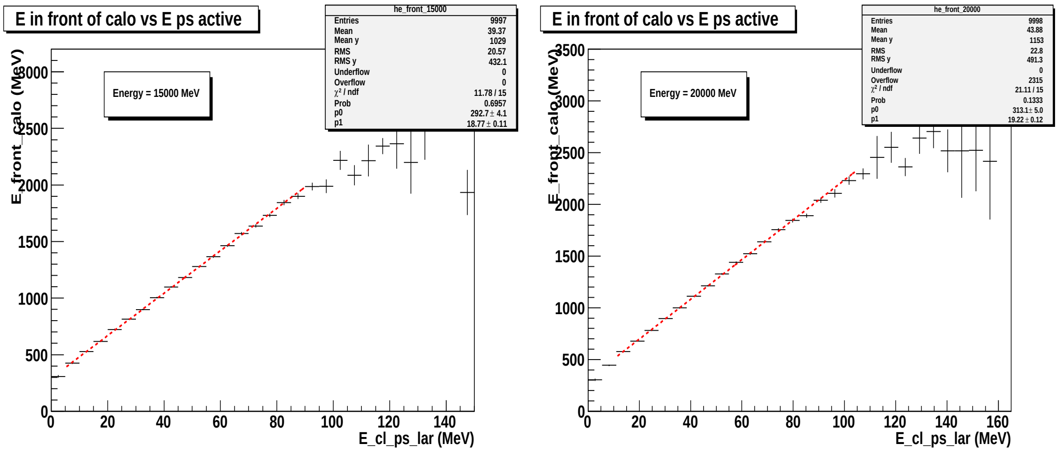

(c) E=15GeV (d) E=20GeV

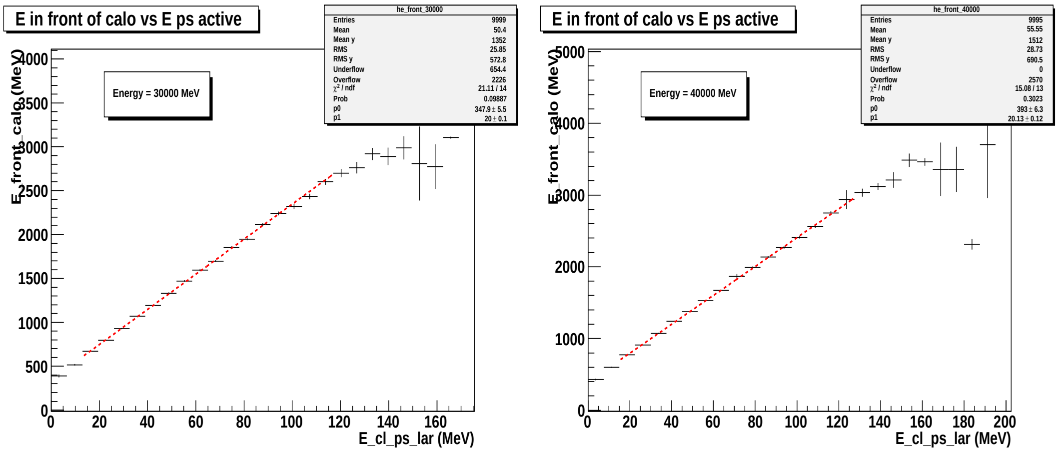

(e) E=30GeV (f) E=40GeV

Figure 4.11: Energy deposited in front of the calorimeter as a function of energy in the Pre-Sampler, η=0.3, for various electron energies.

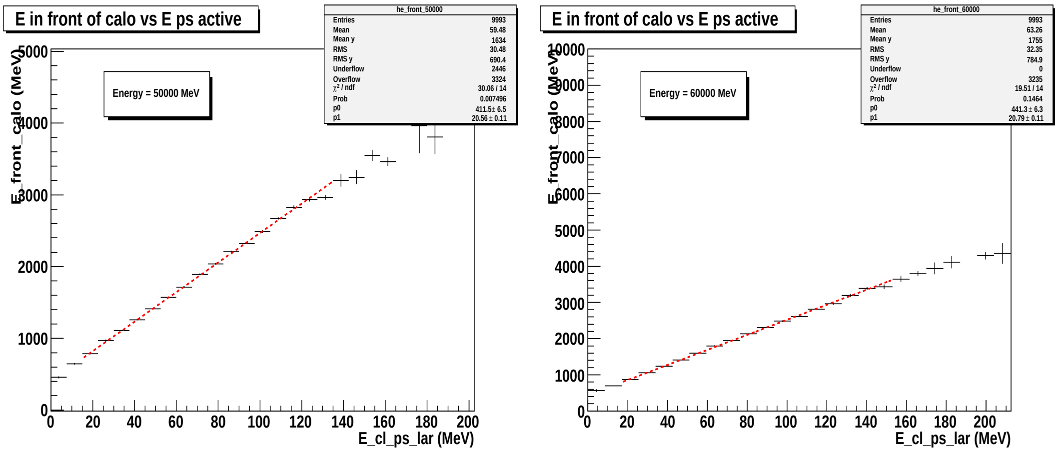

(a) E=50GeV

(b) E=60GeV

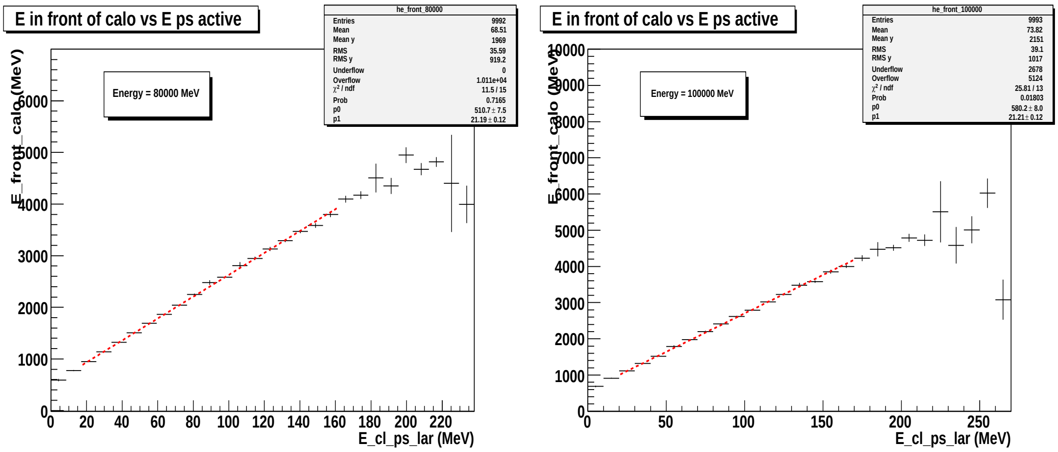

(c) E=80GeV

(d) E=100GeV

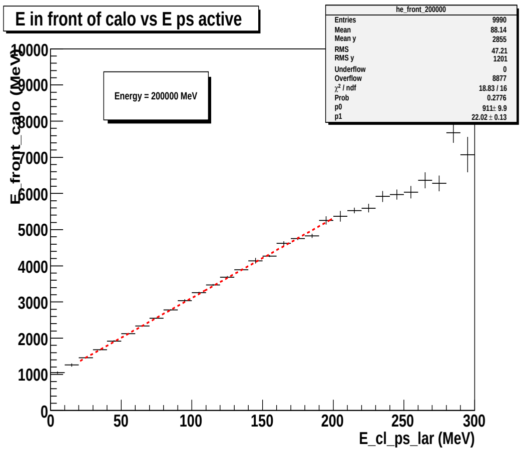

(e) E=200GeV

Figure 4.12: Energy deposited in front of the calorimeter as a function of energy in the PreShower, η=0.3, for various electron energies

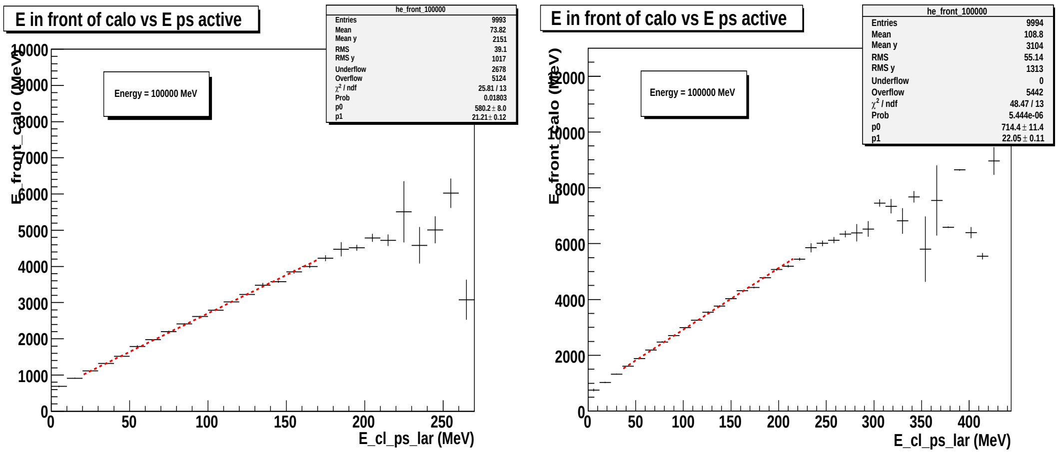

(a) η=0.3

(b) η=0.6

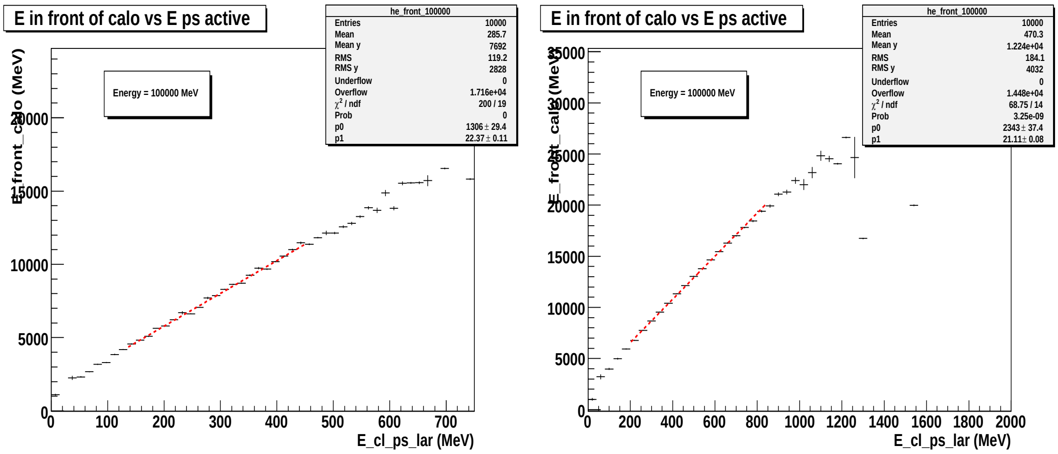

(c) η=0.9

(d) η=1.2

Figure 4.13: Energy deposited in front of the calorimeter as a function of energy in the PreShower, by 100 GeV electrons, at various η points

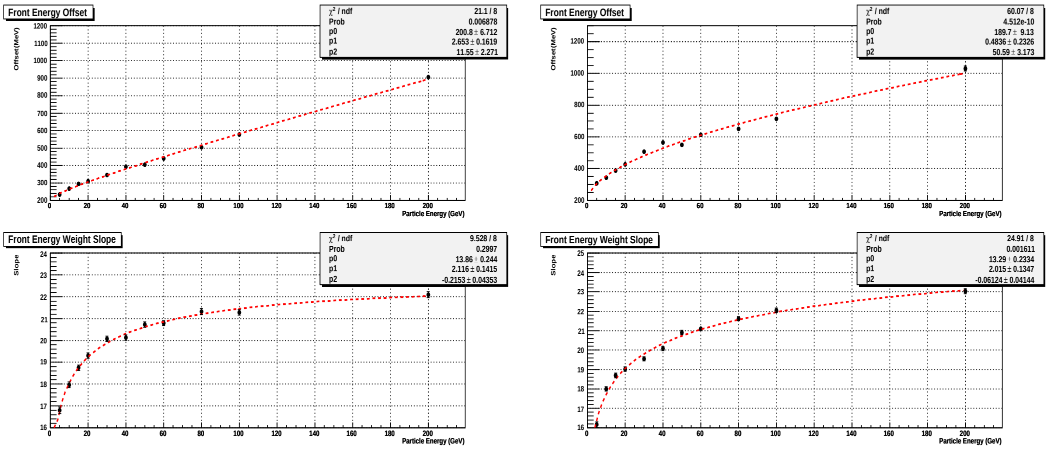

(a) η=0.3 (b) η=0.6

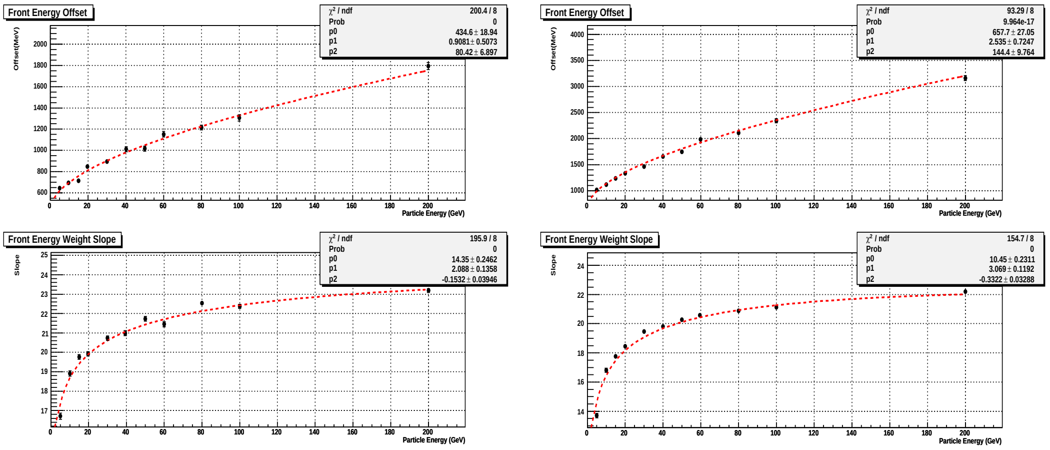

(c) η=0.9 (d) η=1.2

Figure 4.14: Parameters (offset and slope) for the reconstruction of the energy deposited in front of the calorimeter as a function of the average energy lost in the accordion, for various η points. The top plot of each η point refers to the offset, the bottom to the slope

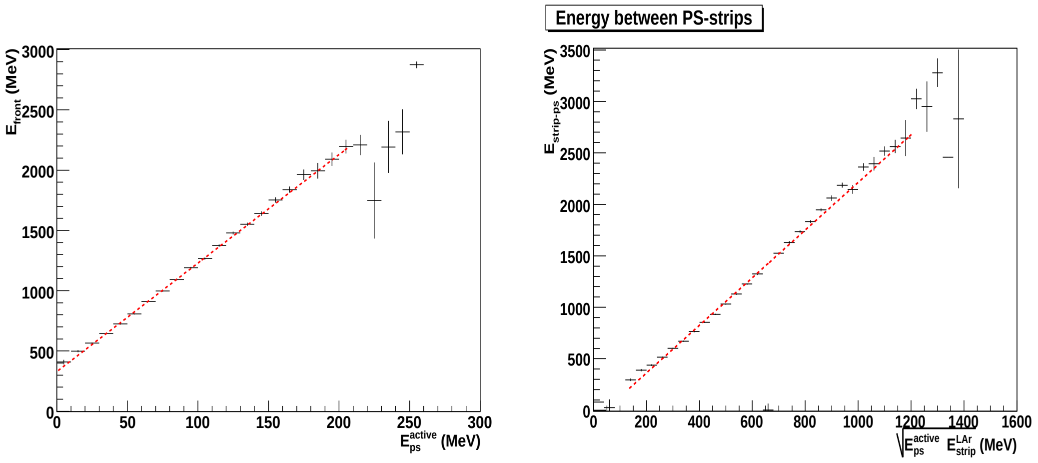

(a) E_{front} (b) E_{psstr}

Figure 4.15: Energy deposited by 100 GeV electrons in front of the PreSampler (a) and in the dead material between PreSampler and strips (b), at η=0.3.

4.1.4 Calculation of the energy deposited behind the Accordion

The energy deposited by the electron shower behind the third sampling of the accordion calorimeter is given as a fraction (%) of the energy deposited into the accordion, as defined in the equation (4.7) .

$$f_{leak}(\%) = \frac{E_{behacc}}{E_{Acc}^{Abs} + E_{Acc}^{LAr}} \tag{4.7}$$

As shown in figure (4.16) for various η values, this fraction, when parametrized as a function of the longitudinal barycenter of the shower, is fairly energy independent. The energy averaged leakage is parametrized as in the equation (4.8):

$$f_{leak}(\%) = p_0^{leak} X + p_1^{leak} e^X \tag{4.8}$$

The results of the fit on the energy averaged leakage are shown in figure (4.17), for the same η points. Note that the fraction of the energy deposited behind the accordion varies with η, consistently with the increase of the total thickness in radiation length of the calorimeter. For lower η points up to 2% of the energy of the EM shower is deposited behind accordion, while at higher η this fraction is only some per mille.

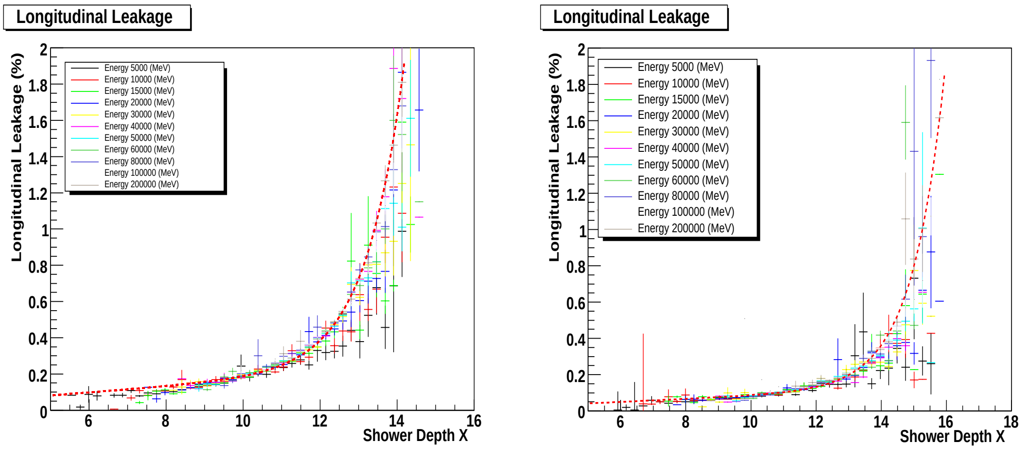

(a) η=0.3 (b) η=0.6

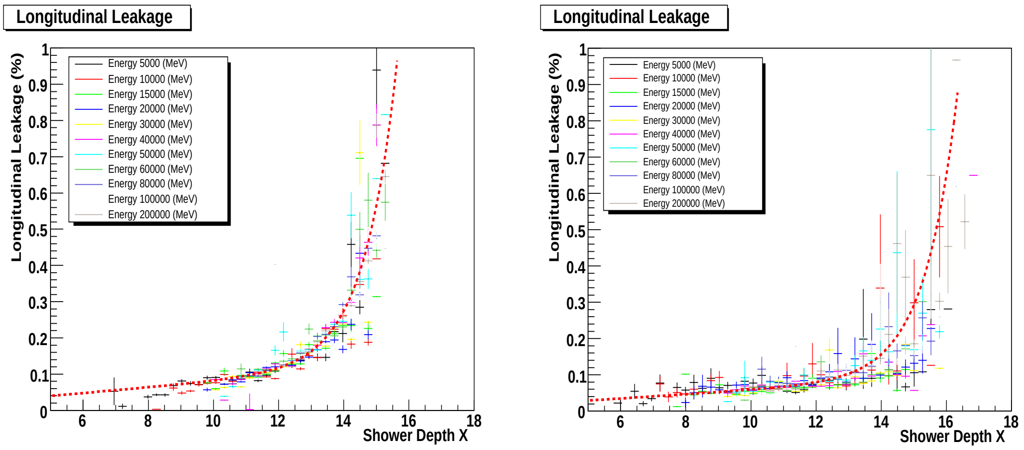

(c) η=0.9 (d) η=1.2

Figure 4.16: Longitudinal leakage, expressed as a fraction (%) of the energy deposited in the accordion, as a function of shower depth X, at various η points and energies. The red dashed line is the energy averaged parametrization, achieved from the fit in figure (4.17), and shown here only as a reference.

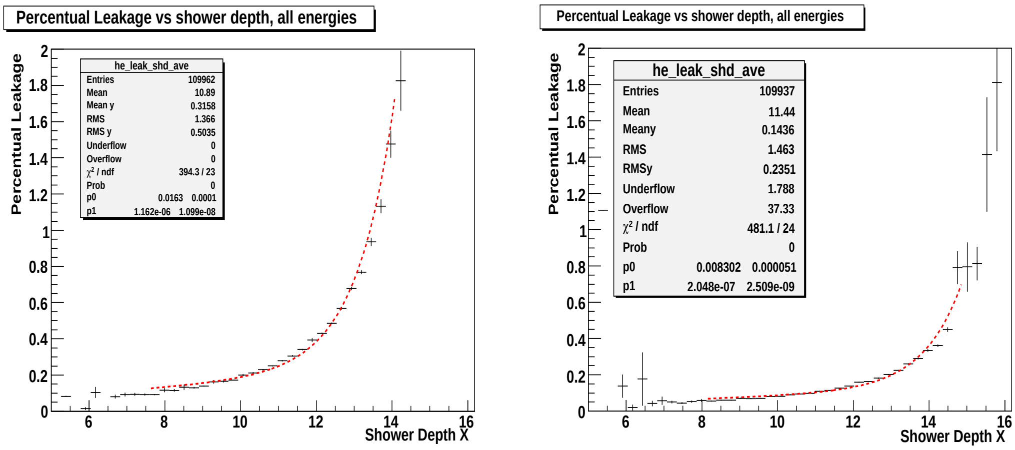

(a) η=0.3

(b) η=0.6

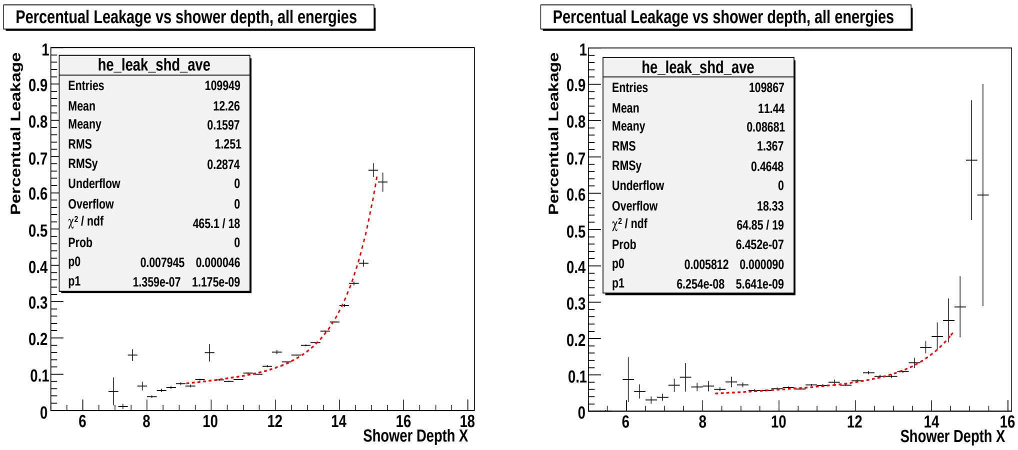

(c) η=0.9

(d) η=1.2

Figure 4.17: Longitudinal leakage as a function of Shower Depth X, energy averaged, for various η points. The red dashed line is the adopted parametrization.

4.1.5 Resolution and Linearity

In figure (4.18) are shown, as an example, the reconstructed energy profiles for the various electron energies at η=0.3 . With a gaussian fit in the interval $[-2\sigma, +2\sigma]$ the mean values and the standard deviations are obtained. As usual the energy resolution ($\frac{\sigma(E)}{E}$) is parametrized as in equation (4.9):

$$\frac{\sigma(E)}{E}(\%) = \frac{b(\%)}{\sqrt{E(MeV)}} \oplus c(\%) \tag{4.9}$$

where: b is the sampling term and c is the constant term of the calorimeter.

The resolution sampling and constant term are shown in figure (4.19), at four η points. The black points show the result when all the energies are computed with the described method. Results when only the energy in the accordion is computed while all the others energies are taken from the Monte Carlo simulations are shown with the green points. The red and the blue points refer respectively to the case in which the only computed energies are the ones deposited in front and behind the calorimeter.

Values of the sampling and constant term of the resolution as a function of η are summarized in table (4.1) together with the maximum deviation from linearity. Note that the constant term of the energy resolution is zero at all η points, as expected for the simulations at the cell center. The sampling term increases from 8.7% at low η values to 15% at higher η. This is related to the increase of the energy deposited in front of the calorimeter and to the difficulty to compute it. Note also that while for η <0.8 the dominant contribution to the energy resolution comes from the accordion, for η >0.8 the dominant contribution comes from the energy deposited in front of it, as shown in figure (4.20), where the color scheme is the same adopted in figure (4.19) and explained in the text.

The ratio of the fitted mean values and the true electron energies (labelled linearity)

η_{cell}	**b(%)**	**c(%)**	**Linearity (%)**
0.1	8.7	0	0.1
0.2	8.9	0	0.1
0.3	9.5	0	0.1
0.4	9.6	0	0.1
0.5	9.9	0	0.1
0.6	10.1	0	0.2
0.7	11.3	0	0.2
0.9	11.8	0	0.3
1.0	12.9	0	0.4
1.1	13.8	0	0.4
1.2	14.9	0	0.5

Table 4.1: Sampling and constant term of resolution and maximum deviation from linearity

is shown in figure (4.21). The meaning of the different colours are the same that for figure (4.20) and is explained in the text. The maximum absolute value of the deviation from the linearity is listed in table (4.1).

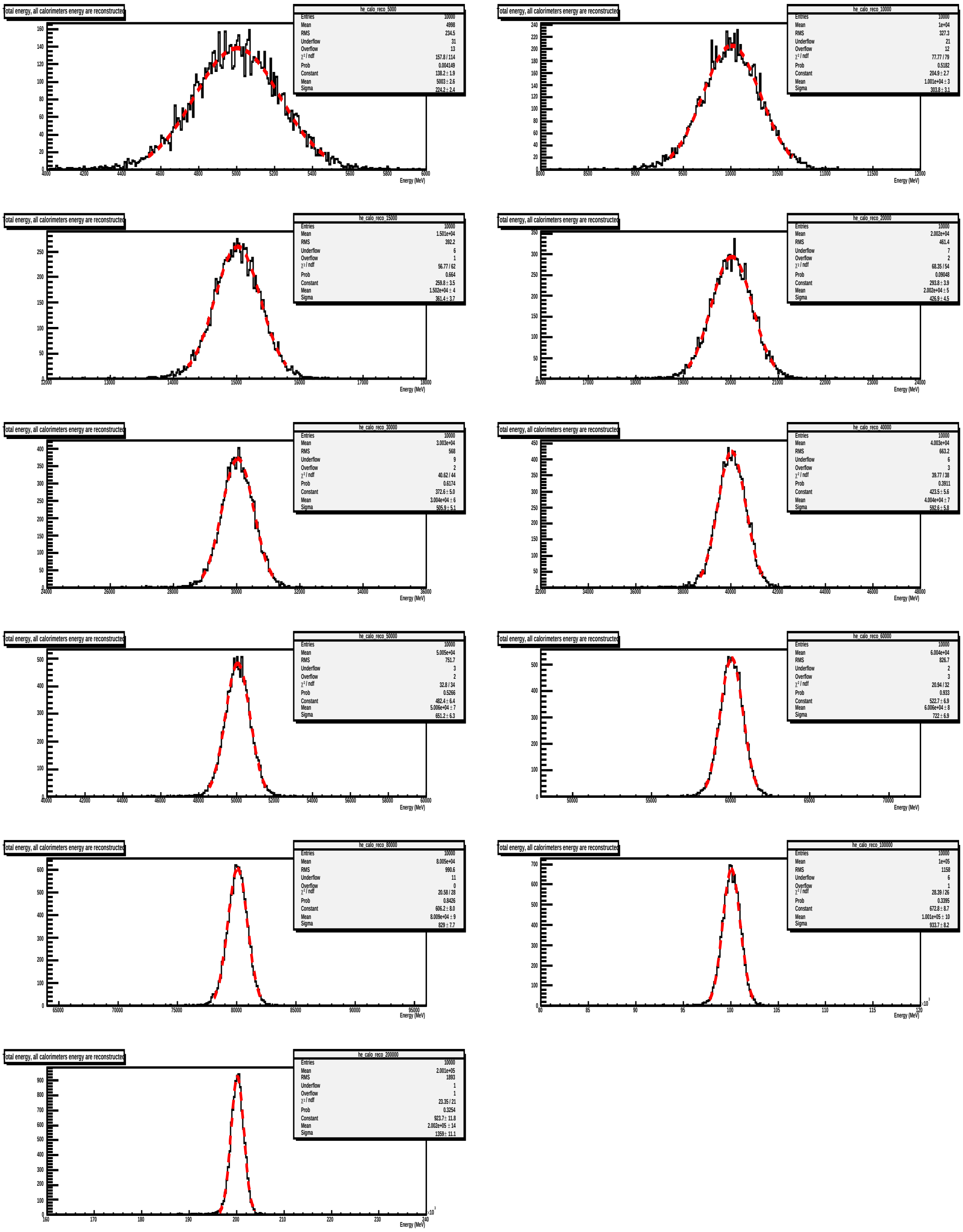

Figure 4.18: Total reconstructed energy at η=0.3, for electrons simulated at cell center. All the 11 available energies are shown, from left to right, top to bottom 5, 10, 15, 20, 30, 40, 50, 60, 80, 100, 200 GeV electrons are shown.

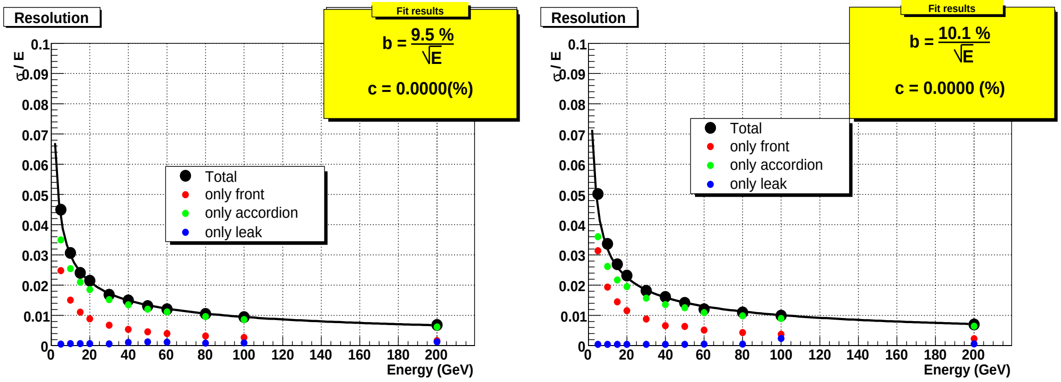

(a) η=0.3 (b) η=0.6

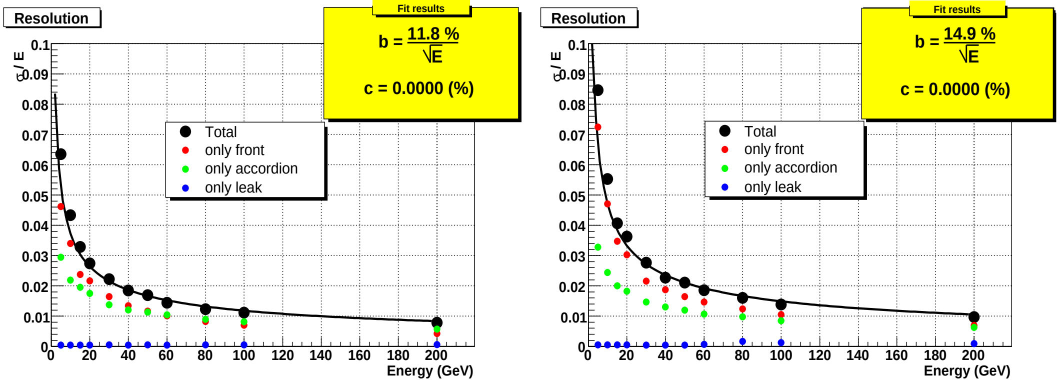

(c) η=0.9 (d) η=1.2

Figure 4.19: Energy resolution for electrons simulated at the cell center, at various η points, as a function of the electron energy.

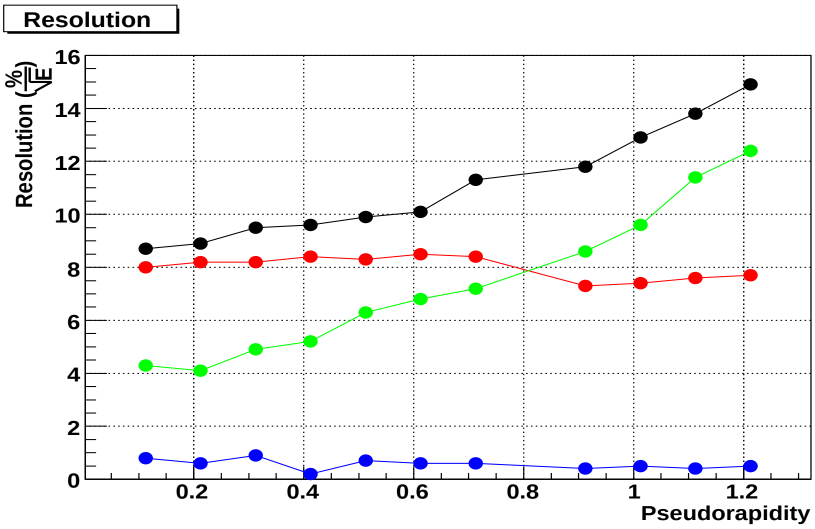

Figure 4.20: η variation of the sampling term of resolution.

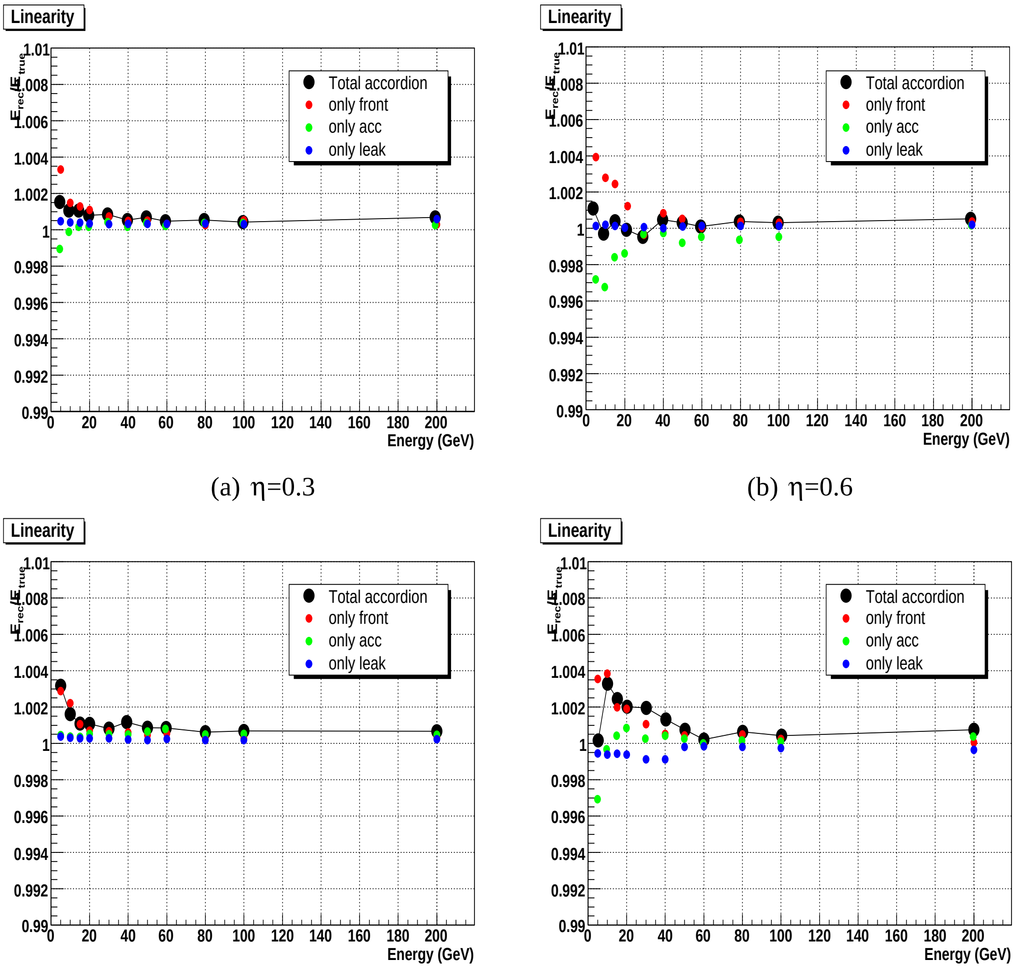

(a) η=0.3 (b) η=0.6

(c) η=0.9 (d) η=1.2

Figure 4.21: Linearity for electrons simulated at the cell center, at various η points.

4.2 Electrons spread over a middle cell

In this section we will discuss the results obtained with the proposed calibration method when applied to electrons hitting uniformly the middle compartment cell. First we look at the parametrization and at the results obtained simply applying the proposed method to the new sample, than we will introduce and discuss the corrections that depend on the impact position of the electrons inside the cell.

We simulate 30K electrons for each of the energies 5, 10, 20, 50 and 100 GeV. The cells with center of the middle compartment at 0.3125, 0.6125, 0.7125, 1.0125, 1.1125, 1.2125 have been uniformly covered by the simulated electrons.

4.2.1 Energy reconstruction in the Accordion

To compute the energy deposited into the accordion we use the same parametrization as a function of the longitudinal barycenter of the shower explained in the subsection (4.1.2). The total correction factor is shown in figure (4.22) for two η points.

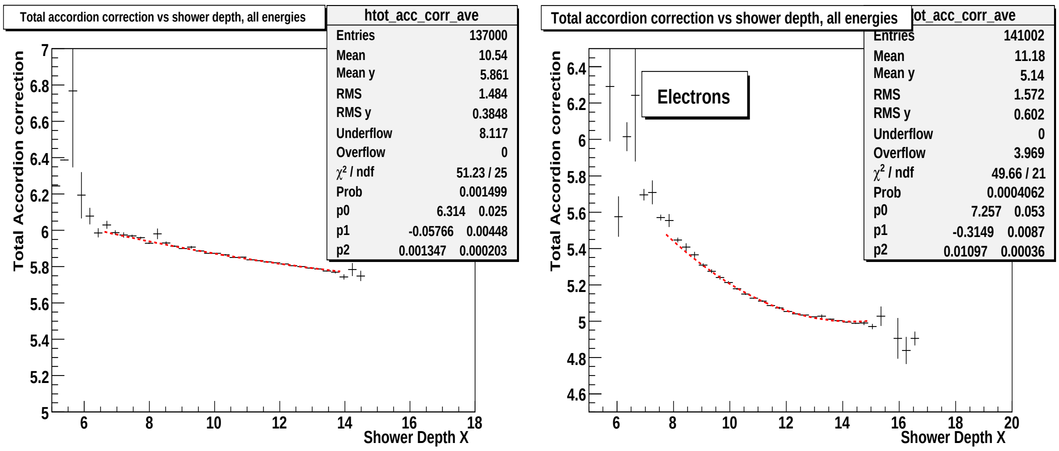

(a) η=0.3

(b) η=1.2

Figure 4.22: Total Accordion Correction factor as a function of shower depth X, averaged over the electron energies, for two η points. The red dashed line is the adopted parametrization

The achieved parameters for the total accordion calibration are summarized in table (4.2), together with the parameters achieved in the same η points with the electrons simulated at the cell center : differences on the order of 5÷10 % between the parameters in the two conditions are visible. This is interpreted as due to the different lateral containment of the shower when the electrons are not simulated all in the same position.

η	**Impact Point**	p_0	p_1	p_2
0.3	Center Cell	6.372 ± 0.023	-0.070 ± 0.004	0.0019 ± 0.0002
0.3	Full Cell	6.314 ± 0.025	-0.057 ± 0.004	0.0013 ± 0.0003
1.2	Center Cell	6.855 ± 0.036	-0.261 ± 0.006	0.0091 ± 0.0003
1.2	Full Cell	7.257 ± 0.053	-0.315 ± 0.006	0.0103 ± 0.0003

Table 4.2: Total accordion correction parameters for two η points and two impact points.

		Offset Parameters		
η	**Impact Point**	p_0	p_1	p_2
0.3	Center Cell	200.8 ± 6.7	2.653 ± 0.162	11.55 ± 2.27
0.3	Full Cell	227.1 ± 5.7	5.744 ± 0.272	-13.75± 2.75
1.2	Center Cell	657.7 ± 27.1	2.535 ± 0.724	144.4 ± 9.7
1.2	Full Cell	841 ± 18	6.542 ± 1.012	56.15 ± 10.16

		Slope Parameters		
η	**Impact Point**	p_0	p_1	p_2
0.3	Center Cell	13.86 ± 0.24	2.11 ± 0.14	-0.215 ± 0.043
0.3	Full Cell	15.86 ± 0.08	0.20 ± 0.01	-0.090 ± 0.041
1.2	Center Cell	10.45 ± 0.23	3.07 ± 0.12	-0.332 ± 0.032
1.2	Full Cell	14.01 ± 0.06	0.32 ± 0.01	-0.280 ± 0.030

Table 4.3: Front energy reconstruction parameters (offset and slope) for two η points and two impact points.

4.2.2 Calculation of the energy deposited in front of Accordion

The energy deposited by the electron shower in the material in front of the calorimeter is parametrized as explained in subsection (4.1.3).

In figures (4.23) and (4.24) the energy deposited in front of the calorimeter as a function of the energy in the PreShower is shown, at two η points and for various energies. The red dashed line is, as usual, the adopted parametrization. Deviations from linearity are visible at higher η points and for very low energies. Higher degree polynomial parametrizations have been tested, without any improvements in the performances of the method. A first degree parametrization is used for each η point and energy.

The offset and slope parameters obtained from the fits are parametrized, accordingly to equations (4.5) and (4.6), as a function of the mean energy deposited in the accordion, as shown in figure (4.25). Table (4.3) list the achieved parameters, together with the ones extracted for the electrons simulated at cell center. The parameters extracted in the two impact point conditions are very different: this is not imputable to some physical effect, but is interpreted as due to the big difference in the number of available energies and statistics in the two cases.

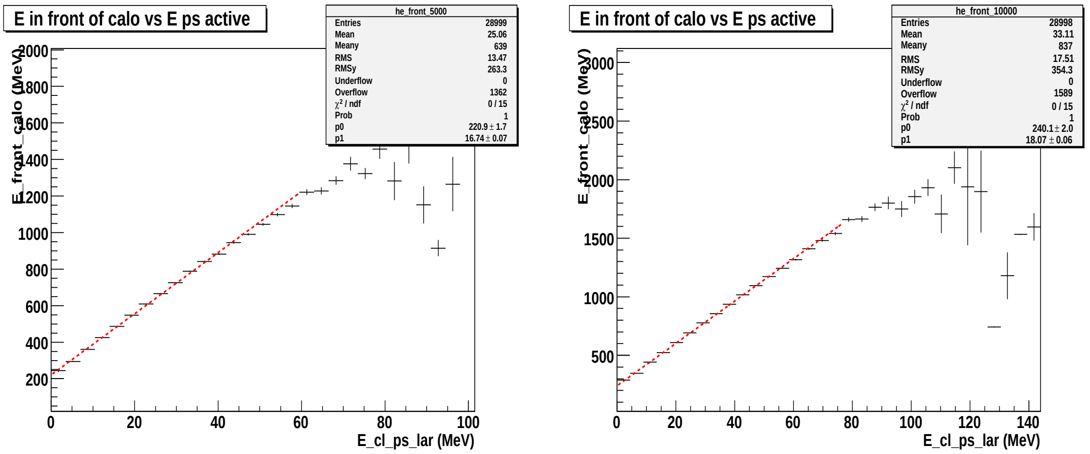

(a) E=5GeV (b) E=10GeV

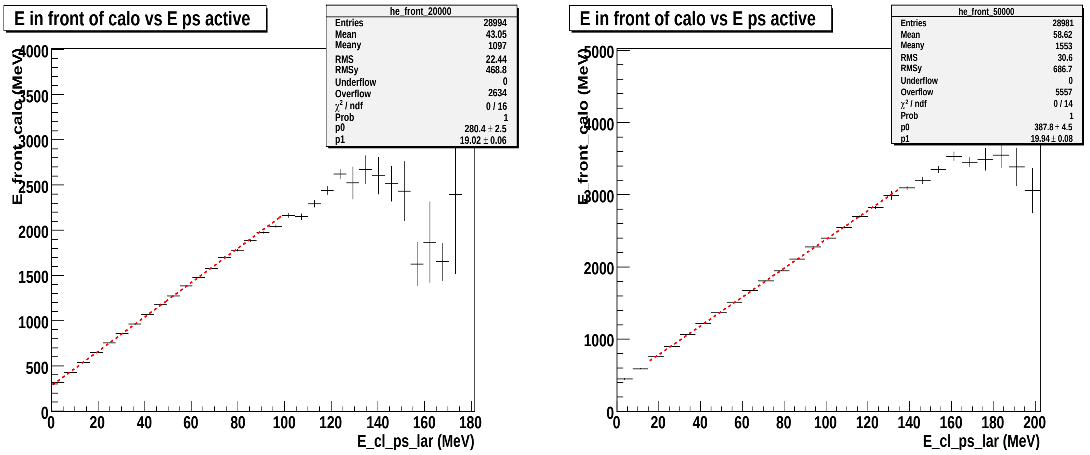

(c) E=20GeV (d) E=50GeV

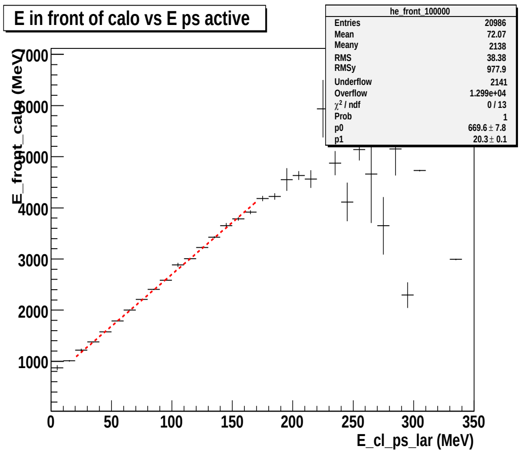

(e) E=100GeV

Figure 4.23: Energy deposited in front of the calorimeter as a function of the energy in the PreSampler at η=0.3, for various energies. The red dashed line is the adopted parametrization.

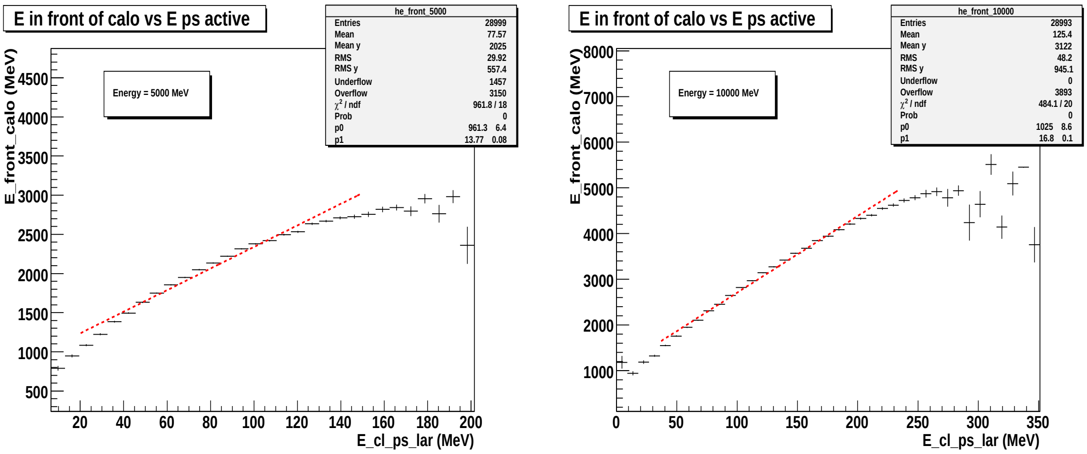

(a) E=5GeV (b) E=10GeV

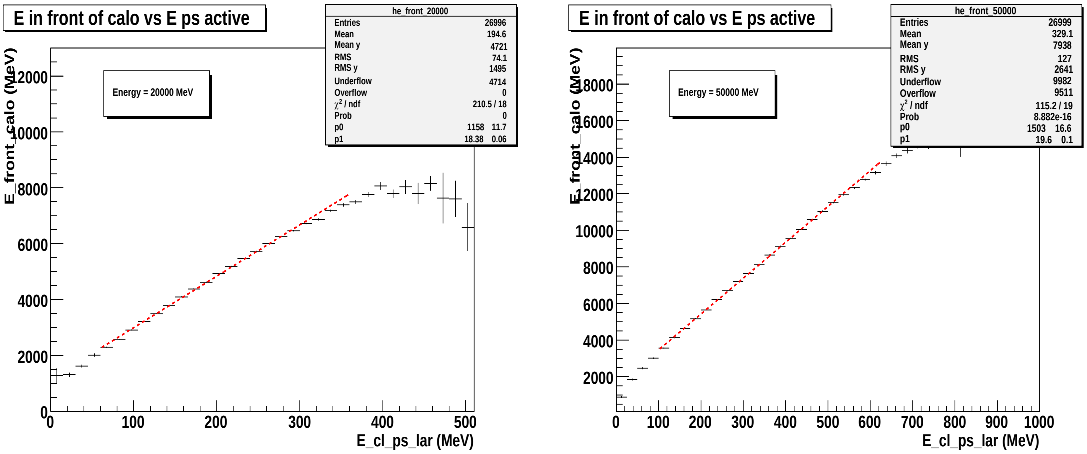

(c) E=20GeV (d) E=50GeV

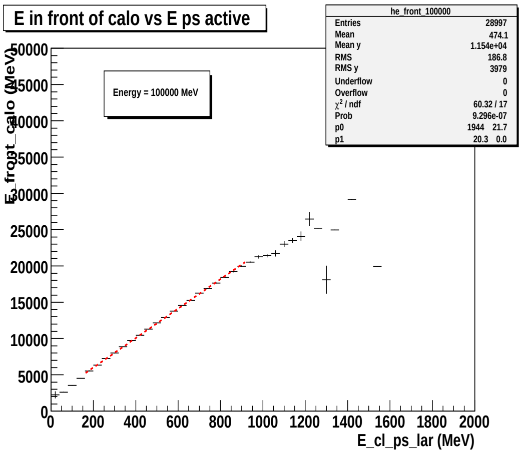

(e) E=100GeV

Figure 4.24: Energy deposited in front of the calorimeter as a function of the energy in the PreSampler at η=1.2, for various energies. The red dashed line is the adopted parametrization.

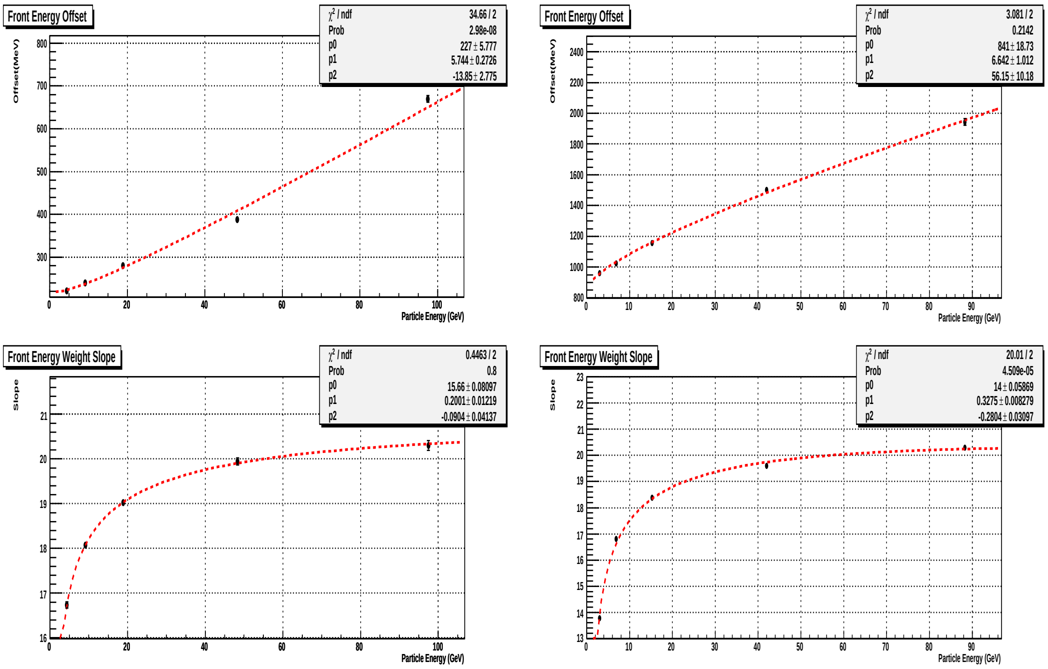

(a) η=0.3

(b) η=1.2

Figure 4.25: Parameters (offset and slope) for the reconstruction of the energy deposited in front of the calorimeter as a function of mean energy deposited in the accordion, for two η points. The top plots refer to the offset, while the bottom to the slope.

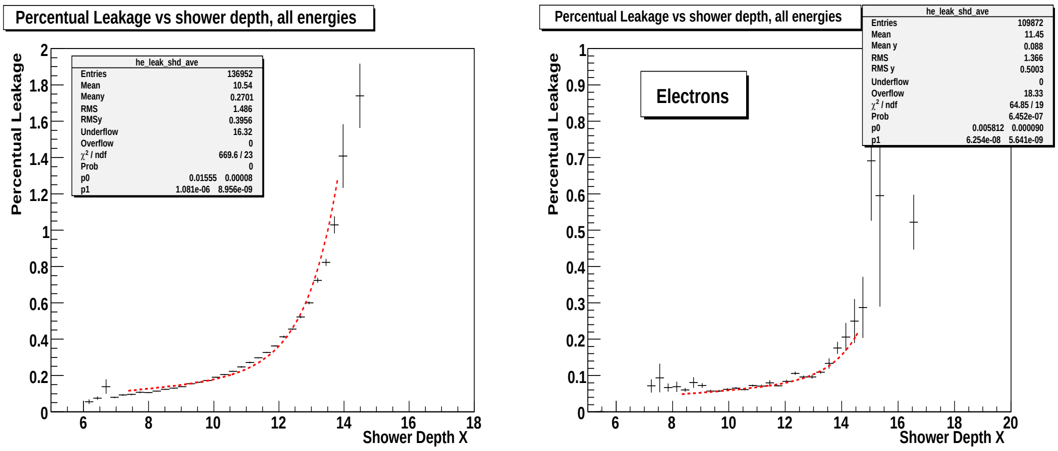

(a) η=0.3 (b) η=1.2

Figure 4.26: Energy deposited behind the accordion, expressed as a fraction (%) of the energy deposited into the accordion, as a function of the longitudinal barycenter, energy averaged. The red dashed line is the adopted parametrization

η	**Impact Point**	$\mathbf{p_0^{leak}}$	$\mathbf{p_1^{leak}}$
0.3	Center Cell	0.0163 ± 0.0001	1.16E-06 ± 1.09E-08
0.3	Full Cell	0.0165 ± 0.0001	1.08E-06 ± 8.91E-09
1.2	Center Cell	0.0058 ± 9.1E-04	6.254E-08 ± 5.642E-0.9
1.2	Full Cell	0.0059 ± 8.7E-04	6.531E-08 ± 6.513E-0.9

Table 4.4: Parameters for the reconstruction of the energy deposited behind the accordion at two η points and for two impact points.

4.2.3 Calculation of the energy deposited behind the Accordion

The energy deposited behind the accordion, expressed as a fraction (%) of the energy deposited into the accordion, is parametrized as a function of the longitudinal barycenter, as discussed in subsection (4.1.4). Figure (4.26) shows the fraction of energy deposited behind the accordion as a function of the longitudinal barycenter of the shower, energy averaged. The red dashed line is the adopted parametrization, as in equation (4.8). The parameters for the reconstruction of the energy deposited behind the accordion are summarized in table (4.4), together with the parameters extracted for the electrons simulated at the cell center. It is possible to see that the parameters extracted in the two cases are compatible, as expected for this correction that must not be influenced by the effects at the level of the calorimeter cells. The little differences (1÷2%) in the parameters are interpreted as due to the difference in the statistics of the two samples.

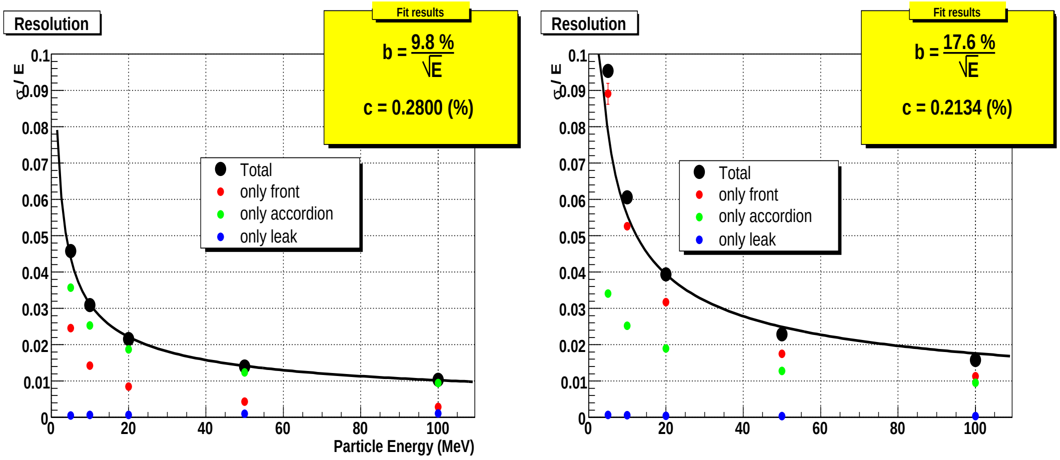

(a) η=0.3 (b) η=1.2

Figure 4.27: Resolution before impact point modulations, at two η points.

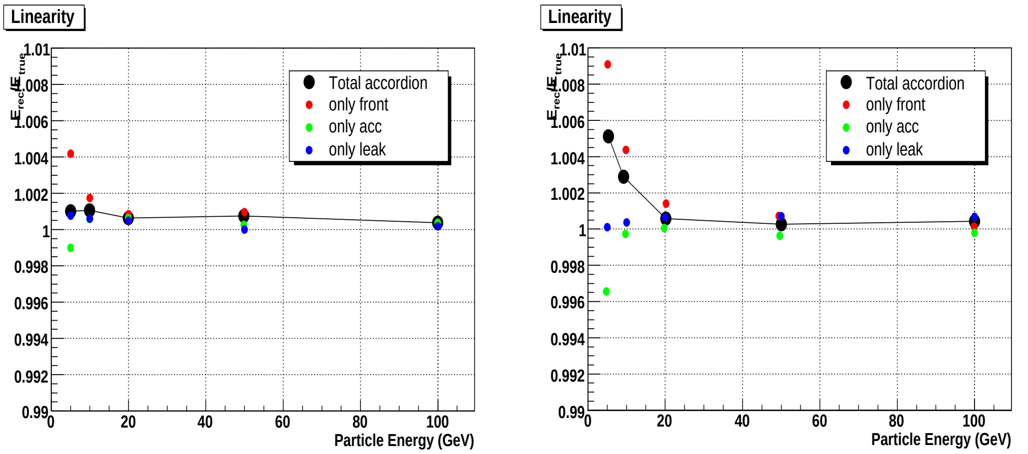

(a) η=0.3 (b) η=1.2

Figure 4.28: Linearity before impact point modulations, at two η points.

4.2.4 Resolution and Linearity

Results for the energy resolution and the linearity are shown respectively in figures (4.27) and (4.28), and are summarized in table (4.5). The sampling term *b* and the linearity are similar to those obtained with the electrons simulated at cell center, while the constant term is about 0.2÷0.3% due to the disuniformity of calorimeter response. The dependence from the impact point of the electrons inside the cell is not yet taken into account, and will be discussed in the next section.

$\eta_{\mathbf{cell}}$	b(%)	c(%)	Linearity (%)
0.3	9.8	0.280	0.1
0.6	10.6	0.242	0.2
0.7	12.1	0.220	0.3
1.0	14.1	0.275	0.3
1.1	15.5	0.247	0.4
1.2	17.6	0.213	0.5

Table 4.5: Sampling and constant term of resolution and maximum deviation from linearity, before impact point modulations

4.2.5 Computation of the impact point

First of all we would like to reconstruct the η and ϕ barycenter of the electron shower, defined as in equation (4.10).

$$B_{ary} = \frac{\sum_i^{cluster} E_i x_i}{\sum_i^{cluster} E_i} \tag{4.10}$$

where: E_i is the energy deposited into the middle layer of calorimeter in the *i*th cell of the cluster; x_i is either the η and ϕ value at the center of the middle compartment of the *i*th cell of the cluster.

Figure (4.29) shows the correlation between the simulated η position and the reconstructed η barycenter, in the middle compartment at η=0.3 and for all the energies. The effect that is clearly evident in the middle compartment is usually called *S-shape* and will be discussed later in this section.

Figure (4.30) shows the same correlation for the ϕ coordinate of the barycenter, in the middle compartment of the accordion.

In figure (4.31) the difference between the simulated ϕ positions and the reconstructed ϕ barycenter, at η=0.3, shows the presence of an offset value. No significant offset is present in the analogous η distribution, at all the tested η points. This offset is related to the relative positions of the absorber and electrode folding into the cells. The center of the cells in ϕ coordinates in the simulation is referred to the strips compartment, and is different from the center of the cells in the middle compartment, that is used for compute the reconstructed barycenter. The starting point of the middle cells on the electrodes, with respect to the first fold of the electrodes, change in η, due to the variation of strips cells length in η, and the ϕ offset change accordingly. Values of the ϕ offset are summarized in table (4.6).

$\eta_{\mathbf{cell}}$	0.3	0.6	0.7	1.0	1.1	1.2
$\phi^{\mathbf{offset}}$	0.1890	0.1869	0.1792	0.2652	0.2751	0.2897

Table 4.6: ϕ^{offset} , expressed in cell unit.

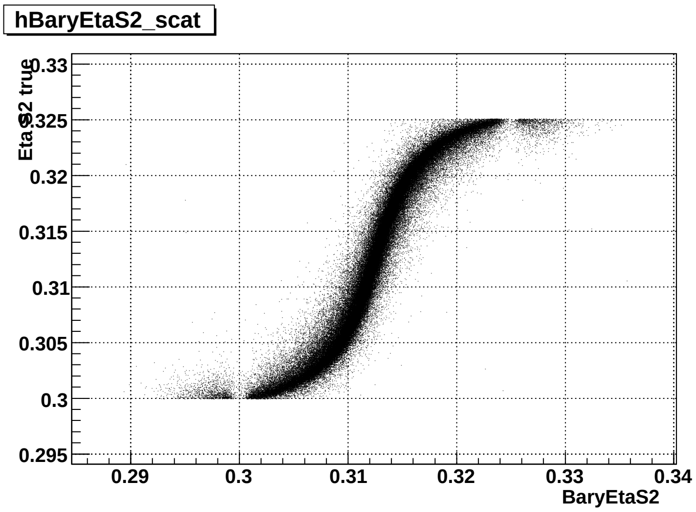

Figure 4.29: Simulated η position as a function of the reconstructed η barycenter, at η=0.3 and for electrons of all simulated energies. Cell starts at η=0.3 and ends at η=0.325. The two small spots at the extreme of the reconstructed barycenter are due to the events that are simulated very close to the cell boundary and are reconstructed with a wrong barycenter in the neighbor cells.

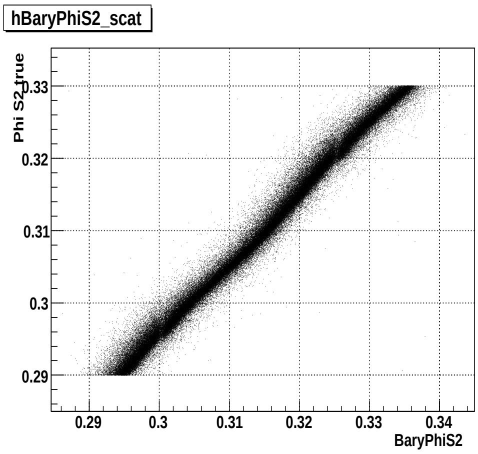

Figure 4.30: Simulated ϕ position as a function of the reconstructed ϕ barycenter, at η=0.3, for electrons of all energies.

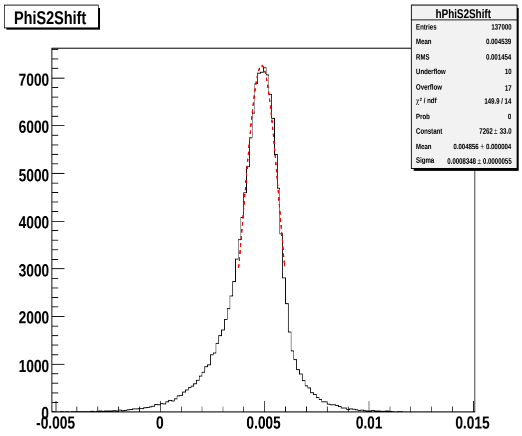

Figure 4.31: Difference between simulated ϕ position and reconstructed ϕ barycenter in the middle compartment, at η=0.3 , for electrons of all energies. The shown difference is in term of absolute pseudorapidity.

The correlation between the reconstructed barycenter and the simulated η position as a function of the position inside the cell is shown in figure (4.32). Low energy showers are larger that high energy ones, giving a more uniform energy sharing into the cells of the cluster, reducing the effect of the impact point of the particles on the

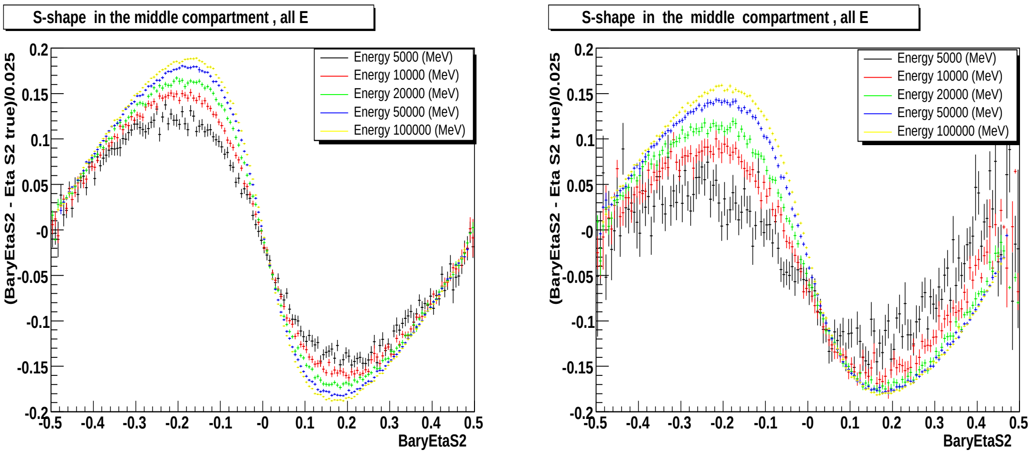

(a) η=0.3

(b) η=1.2

Figure 4.32: Difference between the simulated η position and the reconstructed η barycenter in the middle compartment, normalized to η width of the cell, as a function of the impact position inside the cell (in cell unit), for various electron energies.

barycenter reconstruction. For this reason the barycenter of the lower energy showers are better reconstructed than the higher energy ones, with differences in the order of 0.1 cell unit. This energy dependence proved to be negligible in term of the method performances, and an energy averaged S-shape modulation is used in the next studies.

The energy averaged correction for S-shape is shown in figure (4.33), for two η values, where also the adopted parametrization, defined in equation (4.11), is shown.

$$\frac{\eta_{bary} - \eta_{true}}{\Delta\eta_{cell}} = p_0 \arctan(p_1 \eta_{bary}) + p_2 \eta_{bary} + p_3 \tag{4.11}$$

$\eta_{\mathbf{cell}}$	$\mathbf{p_0}$	$\mathbf{p_1}$	$\mathbf{p_2}$	$\mathbf{p_3}$
0.3	0.310 ± 0.002	-8.49 ± 0.06	0.803 ± 0.006	-0.0044 ± 0.0001
0.6	0.306 ± 0.003	-8.60 ± 0.10	0.793 ± 0.007	-0.0107 ± 0.0002
1.0	0.294 ± 0.004	-8.19 ± 0.09	0.750 ± 0.010	-0.0204 ± 0.0002
1.1	0.277 ± 0.004	-7.93 ± 0.11	0.688 ± 0.012	-0.0257 ± 0.0002
1.2	0.297 ± 0.005	-6.91 ± 0.11	0.724 ± 0.014	-0.0306 ± 0.0002

Table 4.7: S-Shape correction parameters for various η values

The S-shape effect is interpreted as due to the shower lateral profile and to the energy sharing between different cells. When the impact point is a symmetric one (center of the cell or boundary between two cells) the energy sharing between the cells is symmetric and is possible to reconstruct the barycenter with good precision. On the other side, when the impact point is in an asymmetric position (everywhere in between the center and the boundary of the cell) the energy sharing is more asymmetric than

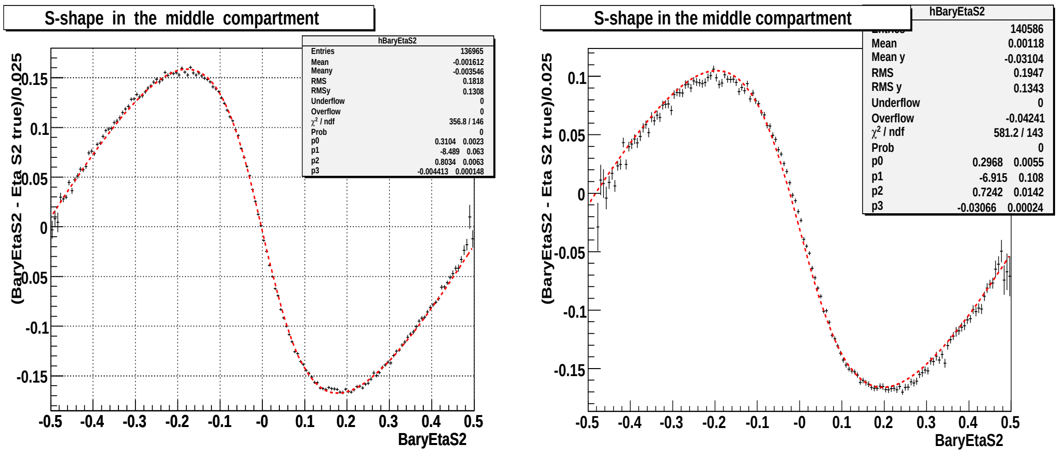

(a) η=0.3 (b) η=1.2

Figure 4.33: Difference between the simulated η position and the reconstructed η barycenter in the middle compartment, normalized to the η width of a middle cell, as a function of the impact position inside the cell (in cell unit). The figures show the energy averaged correction in two η points; the red dashed line is the adopted parametrization.

in the previous case and a bias into the reconstruction of the barycenter is introduced. Error in the barycenter reconstruction up to 20% of a cell width are visible in figure (4.32).

In this work we use only the barycenter reconstructed into the middle compartment, both in η and φ, and only the η S-Shape correction for middle compartment are used and the achieved parameters are shown, for various η points, in table (4.7), with the same meaning as in equation (4.11). φ S-shape proved to be negligible in term of the method performances.

4.2.6 Dependence of the reconstructed energy from the impact point inside a cell

The energy deposited into the accordion cluster depends from the impact point of the electrons inside the cell.

In figure (4.34) the ratio between the reconstructed electron energy and the nominal energy is shown as a function of the η impact point of the electron inside the cell, in cell unit, at η=0.3 and φ=0.3. The visible effect is due to the lateral shower profile and its incomplete containment inside the reconstructed cluster. The ratio in parametrized with a second degree polynomial, as in equation (4.12).

$$\frac{E_{reco}}{E_{true}} = p_0 + p_1 \eta_{cell} + p_2 \eta_{cell}^2 \tag{4.12}$$

As an example the computed coefficients for η=0.3 are listed in table (4.8). The energy dependence of the computed parameters is negligible in term of the performances of the method and we will use a parametrization averaged over the electrons energies. In figure (4.36) the energy averaged ratio is shown for two η points.

In figure (4.35) the ratio between the reconstructed electron energy and the nominal energy is shown as a function of the ϕ impact point of the electrons inside the cell, in cell unit, at η=0.3 and ϕ=0.3. The clearly seen four-fold symmetry reflects the absorber periodicity in ϕ inside a cell. For lower energy electrons the effect is less evident, due to the larger section of the shower that smooth the calorimeter response. Conversely, at high energy a second order modulation is visible between two consecutive maximum of the larger modulation: this is due to the presence of the read out electrodes inside each LAr gap. The ratio is parametrized as in equation (4.13), and the computed parameters are listed, for various energies, in table (4.9)

$$\frac{E_{reco}}{E_{true}} = p_0 + p_1 \cdot \sin(8\pi\phi_{cell} + p_2) \tag{4.13}$$

As in the case of the dependence from η impact point, an energy averaged correction is used. As an example, in figure (4.37) the energy averaged correction is shown for two η points.

Both the corrections for the η and ϕ impact point energy modulations are relatively raw. A detailed study of them is outside the aim of this thesis. Better ones are available

Energy(**GeV**)	**p0**	**p1**	**p2**
5GeV	1.001 ± 1E-03	-1.17E-03 ± 0.99E-03	-35.6E-03 ± 4.01E-03
10GeV	1.001 ± 1E-03	-0.79E-03 ± 0.69E-03	-29.5E-03 ± 2.72E-03
20GeV	1.001 ± 1E-03	-1.20E-03 ± 0.49E-03	-28.6E-03 ± 1.94E-03
50GeV	1.001 ± 1E-03	-0.45E-03 ± 0.34E-03	-27.8E-03 ± 1.31E-03
100GeV	1.002 ± 2E-03	-0.35E-03 ± 0.31E-03	-26.3E-03 ± 1.10E-03
Averaged	1.002 ± 2E-03	-0.62E-03 ± 0.31E-03	-30.5E-03 ± 1.21E-03

Table 4.8: η modulation parameters for various energy values. Last line list the computed coefficients after averaging on the electron energies.

Energy (GeV)	**p0**	**p1**	**p2**
5GeV	0.9976 ± 0.3E-03	-1.196E-03 ± 0.418E-03	3.324 ± 0.348
10GeV	0.9968 ± 0.2E-03	-1.218E-03 ± 0.281E-03	1.161 ± 0.233
20GeV	0.9993 ± 0.1E-03	-2.887E-03 ± 0.2E-03	0.807 ± 0.0705
50GeV	0.9976 ± 0.3E-03	-0.45E-03 ± 0.34E-03	3.324 ± 0.348
100GeV	0.999 ± 0.01E-03	0.357E-03 ± 0.132E-03	3.691 ± 0.132
Averaged	0.9992 ± 0.1E-03	-2.489E-03 ± 0.121E-03	0.589 ± 0.0496

Table 4.9: ϕ modulation parameters for various energy values. Last line list the computed coefficients after averaging on the electron energies.

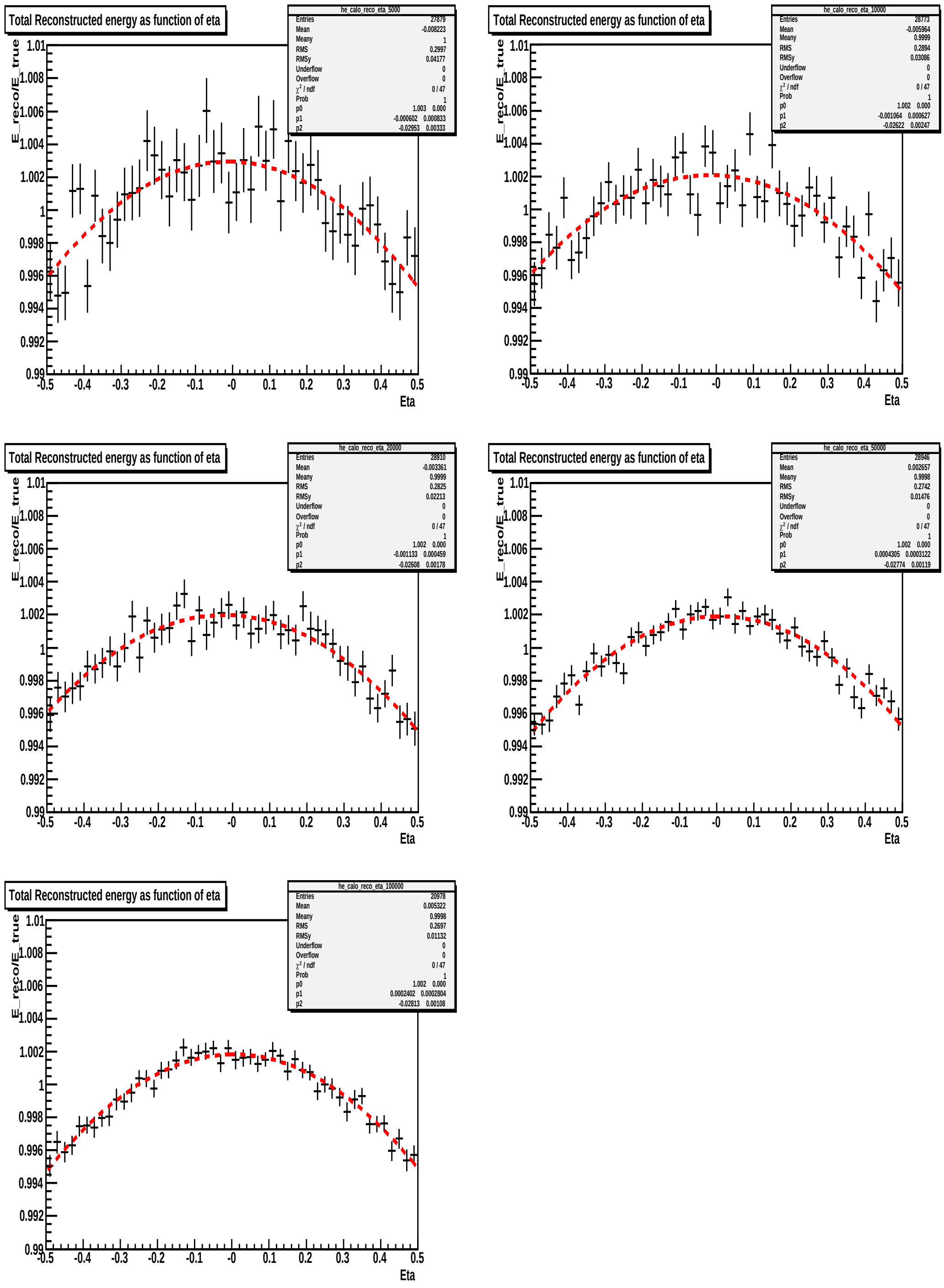

Figure 4.34: Ratio of the reconstructed and the simulated energy as a function of the η impact point inside the cell. Different energies are shown, from left to right, from top to bottom the 5, 10, 20, 50 and 100 GeV electrons are shown.

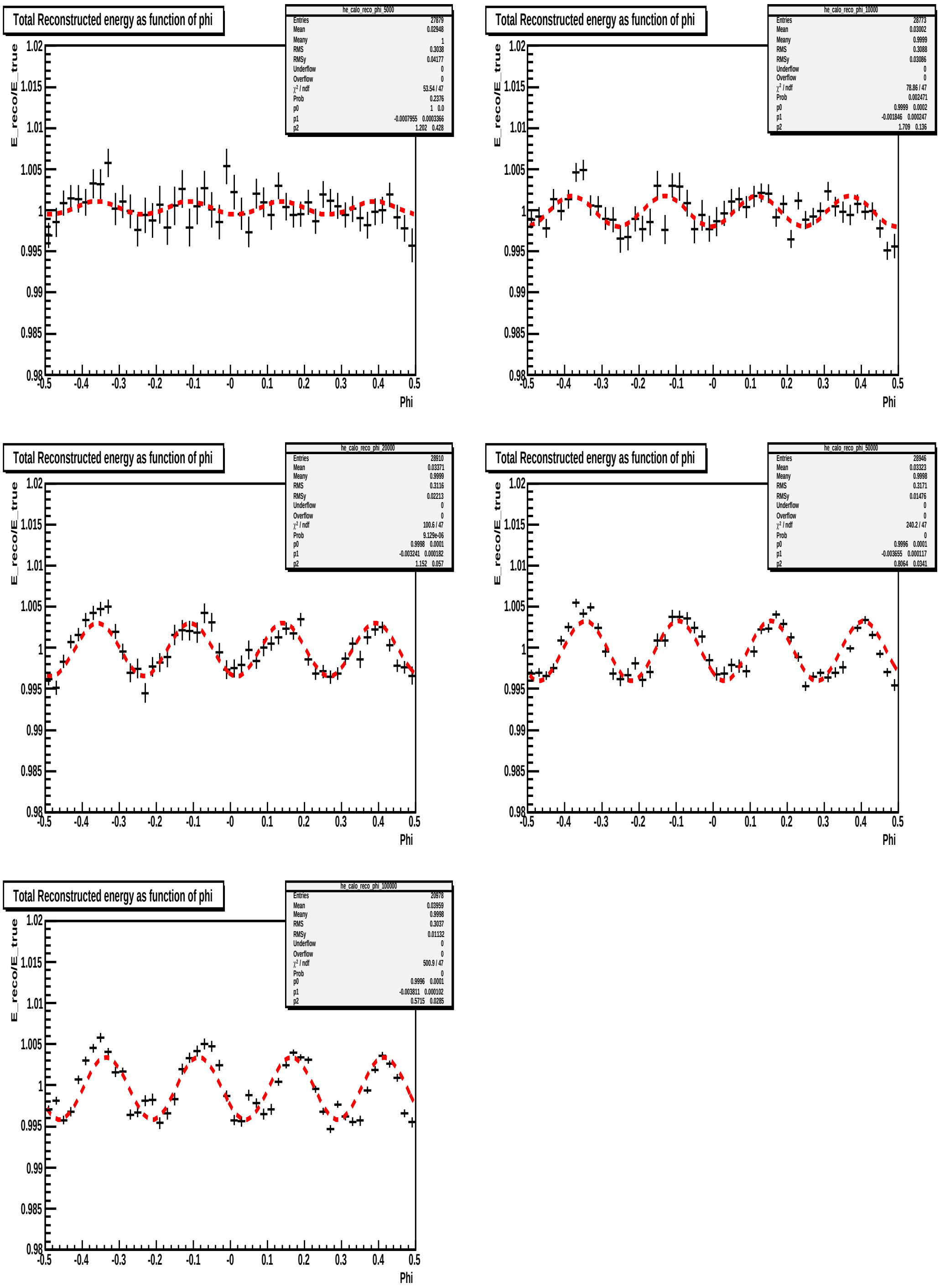

Figure 4.35: Ratio of the reconstructed and the simulated energy as a function of the ϕ impact point inside the cell. The shown energy values are, from left to right, from top to bottom : 5, 10, 20, 50 and 100 GeV.

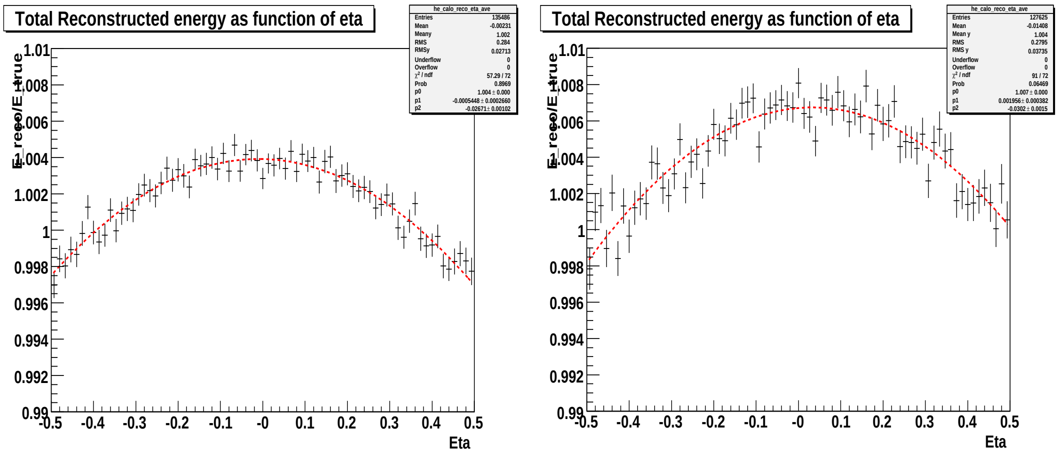

(a) η=0.3 (b) η=1.2

Figure 4.36: Ratio of the reconstructed and the simulated energy as a function of the η impact point inside the cell, averaged on all energies. The red dashed line is the adopted parametrization.

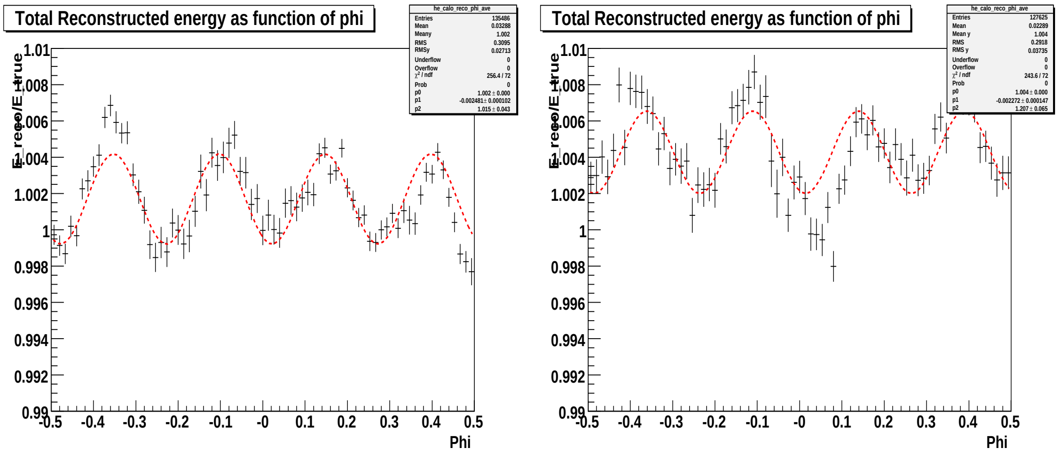

(a) η=0.3 (b) η=1.2

Figure 4.37: Ratio of the reconstructed and the simulated energy as a function of the ϕ impact point inside the cell, averaged over all energies. The red dashed lines are the adopted parametrization.

in the Athena code, but at the time of these studies it was not possible to use them with the Calibration Hits Data. It is important to note that the η and ϕ modulations mean values are normalized to unity: this is very important because the cell modulations don't have to change the mean value of the reconstructed electron energy distribution.

4.2.7 Resolution and Linearity after impact point correction

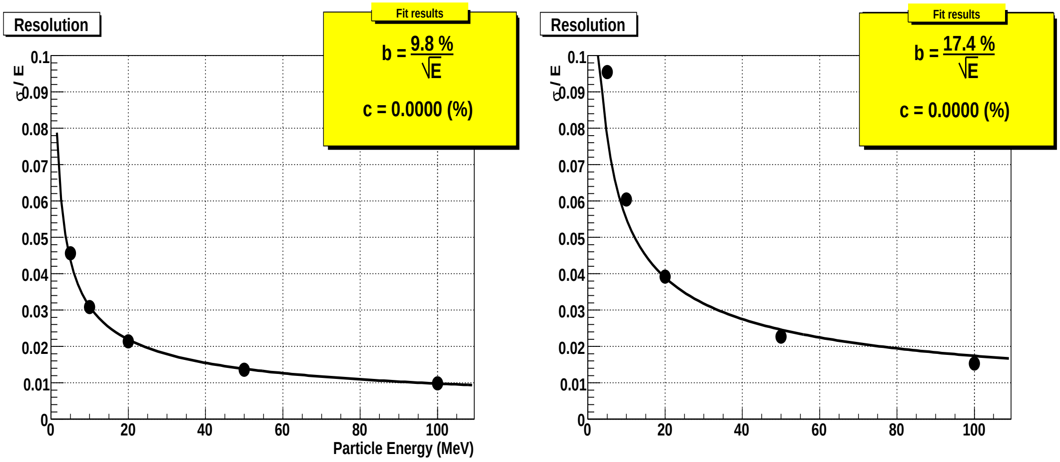

(a) η=0.3 (b) η=1.2

Figure 4.38: Energy resolution after η and ϕ modulation corrections, for two η points.

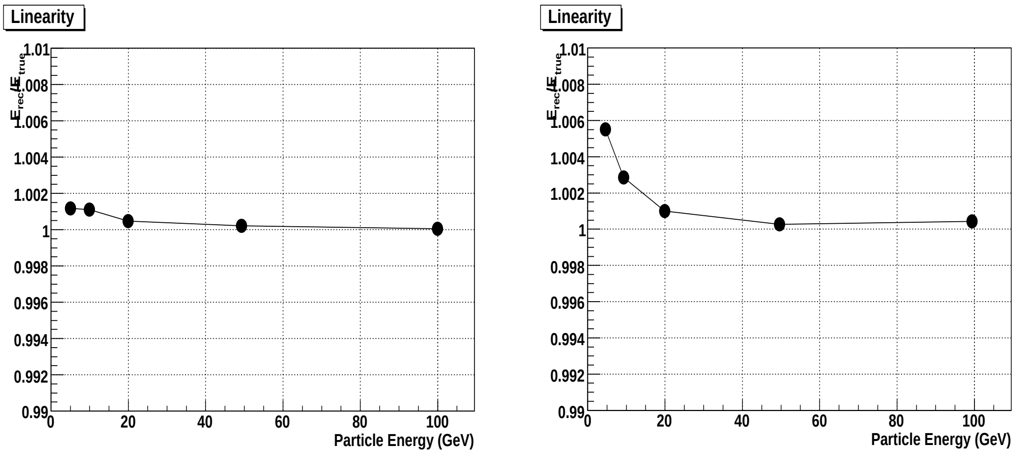

(a) η=0.3 (b) η=1.2

Figure 4.39: Linearity after η and ϕ modulation corrections, for two η points

The energy resolution and linearity after the correction for the impact point energy modulations are shown in figures (4.38) and (4.39), where two η points are shown as an example.

The sampling term, the constant term of the calorimeter and the maximum deviation from linearity are shown in table (4.10). Note that the sampling term *b* of the energy resolution and the linearity are unaffected by the modulations corrections but, as expected, the constant term *c* is now consistent with zero, because we correct for the energy disuniformity inside the cell.

η_{cell}	**b(%)**	**c(%)**	**Linearity (%)**
0.3	9.8	0	0.1
0.6	10.6	0	0.2
0.7	12.0	0	0.3
1.0	14.1	0	0.3
1.1	15.4	0	0.4
1.2	17.4	0	0.5

Table 4.10: Resolution and Linearity after the corrections for the η and ϕ energy modulations, for various η points.

4.3 Electrons spread over a middle cell with magnetic field on

Third step in our analysis is to study the effect of the magnetic field generated by the solenoid on the calorimeter calibration. We simulate 30K electrons at each of the energies 5, 10, 20, 50 and 100GeV. The cells with center of the middle compartment at η= 0.3125, 0.6125, 0.7125, 1.0125, 1.1125, 1.2125 have been uniformly covered by the simulated electrons.

It will be shown that the presence of magnetic field introduce very relevant effects, particularly for low (5-10 GeV) energy electrons, that we can summarize:

- electrons are bent in the ϕ direction
- photons emitted by bremsstrahlung may hit the calorimeter at some distance from the electrons

In figure (4.40) the energy deposited in the calorimeter by the shower generated by a 5 GeV electron generated at η=0.3 and ϕ=0.3 is shown. Two different clusters are visible: one due to the electron and one due to the 1.621 GeV photon radiated at a radius of 51.0 mm from the vertex. The use of a fixed dimension cluster algorithm built around the most energetic cell, 3×5 as the one used in this study, underestimates the electron energy by, at least, one third.

Figure (4.41(a)) shows the correlation between the simulated ϕ position and the reconstructed ϕ barycenter. The different lines are due to the 5 different electron energies taken into account, from left to right, 100, 50, 20, 10 and 5 GeV. Figure (4.41(b)) shows the difference between the simulated ϕ position and reconstructed ϕ barycenter. Note that for 5 GeV electrons the mean deflection is around 0.1 rad, i.e. about 4 middle cells. The tails of the distribution are due to the events in which the electron radiates a considerable fraction of energy.

The handling of the electron energy reconstruction when an hard bremsstrahlung occurs is outside the aim of this study: in the following we reject events in which a photon of energy greather than 40% of the initial electron energy is radiated. This cut

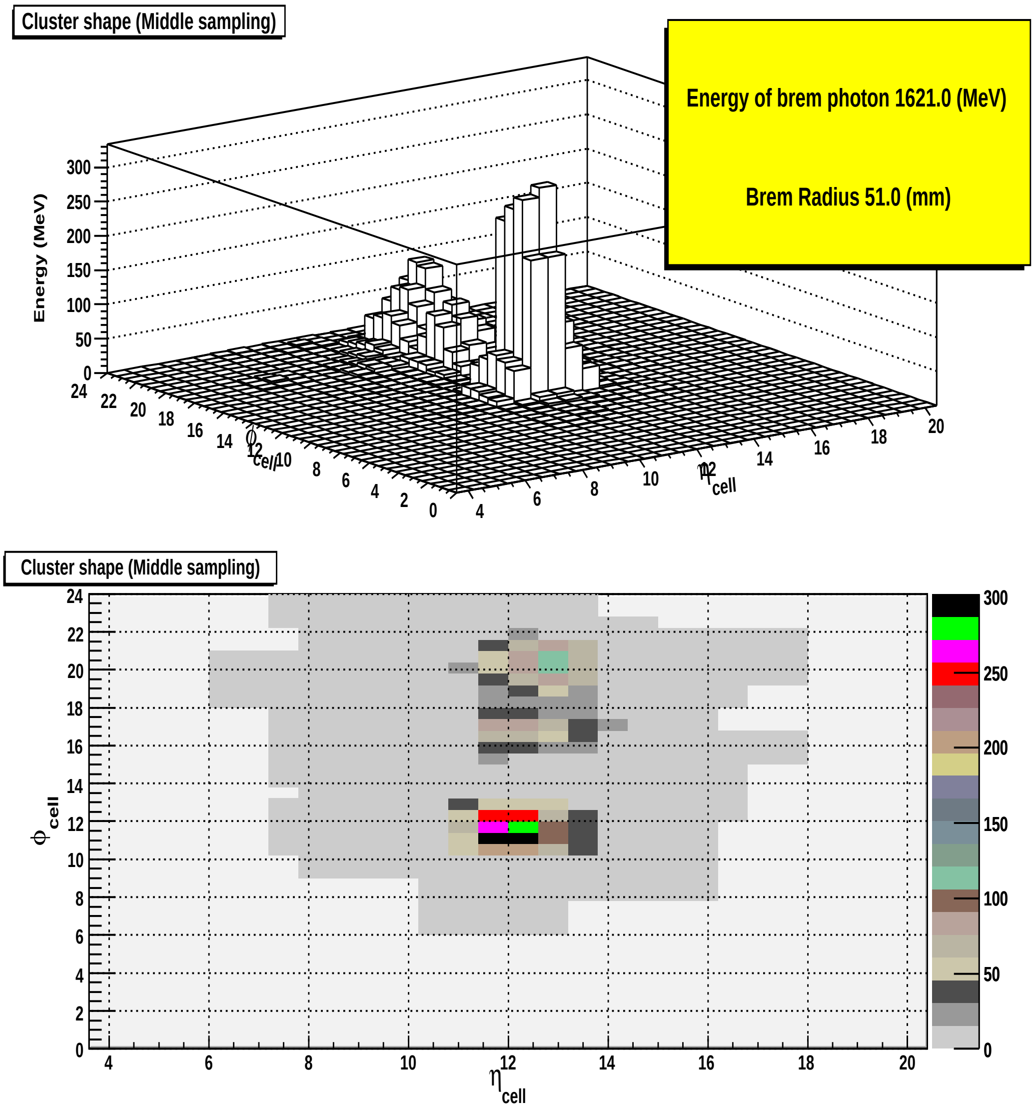

Figure 4.40: Effect of B field. In figure are shown the cells interested by an electromagnetic shower generated by one electron of 5GeV simulated at η=0.3 and ϕ=0.3. The electron emits a bremsstrahlung photon of 1.621 GeV in the inner detector giving rise to two different clusters, as clearly visible.

will be substituted with a more efficient rejection criteria in the official reconstruction code of Atlas, but it was the only appliable cut in Calibration Hits analysis at the time of these studies.

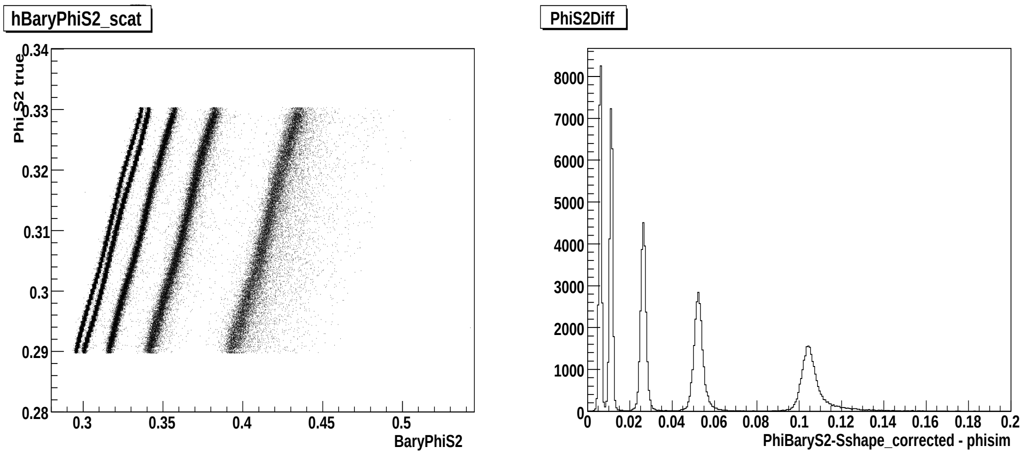

(a) (b)

Figure 4.41: The simulated ϕ position as a function of the reconstructed ϕ barycenter is shown in figure (a), while in figure (b) the difference between simulated ϕ position and reconstructed ϕ barycenter is shown for 5 energies.

4.3.1 Energy reconstruction into the Accordion

In figure (4.42) the total accordion correction factor (the factor needed to compute the total energy deposited into the accordion starting from the energy measured in the cluster) at two η points is shown. The correction factor is now strongly energy dependent, differently from what obtained without magnetic field and shown in figure (4.8). While, as shown in figure (4.43), the sampling fraction in the cluster is still energy independent, the correction for the energy deposited out of the cluster, shown in figure (4.44), is strongly energy dependent.

Low energy electrons deposit up to 50% of their energy out of the cluster. This is due to the photons radiated by the electrons and hitting the calorimeter more than three cells away from the electron impact point, strongly increasing the energy deposited outside the cluster.

Figure (4.45) shows the distribution of the energy lost out of the cluster for 5 energy values.

The energies deposited out of the reconstructed cluster for various shower depth intervals (all electrons energy are added) are shown in figure (4.46). The profiles corresponding to low values of the shower depth are more populated by low energy electrons (5 and 10 GeV), and, as expected, show longer tails.

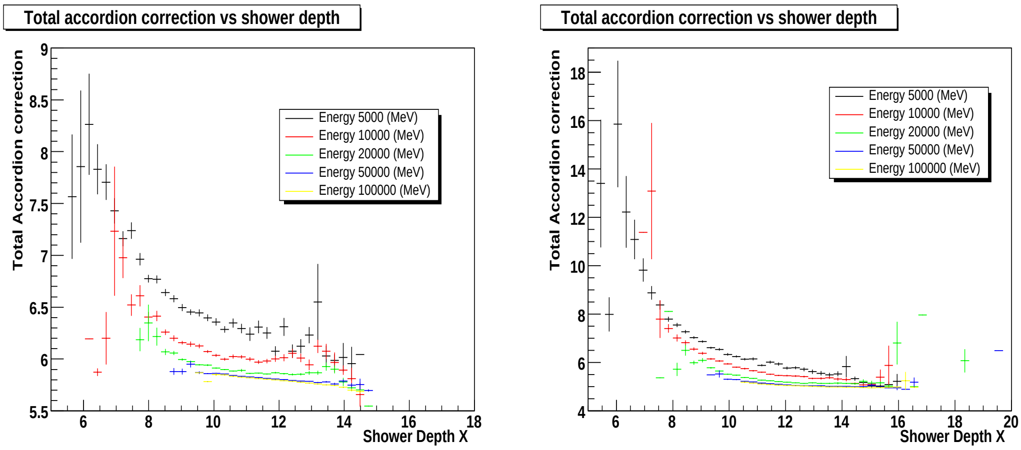

(a) η=0.3 (b) η=1.2

Figure 4.42: Total accordion correction factor with B field, for two η points.

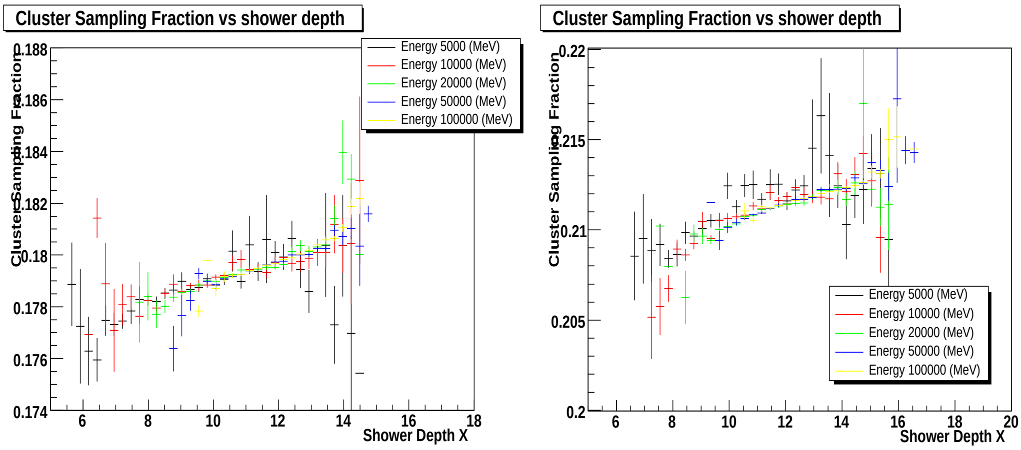

(a) η=0.3 (b) η=1.2

Figure 4.43: Cluster sampling fraction at two η points, with B field.

For each electron energy and in each shower depth interval the peak present in the out of cluster energy profile is fitted with a gaussian in the range $[-2.5\sigma, +1.5\sigma]$. Figure (4.47) shows the achieved gaussian mean value as a function of the shower depth for the various electron energies and two η points. The gaussian mean is energy independent and the dependence of the energy deposited outside the reconstructed cluster from the shower depth is similar to the one computed when the magnetic field B is off. This procedure is equivalent to consider only the electrons which radiate only little energy in the tracker system.

Finally, the fitted out of the cluster energy, averaged on all electron energies, is parametrized with a first degree polynomial as a function of the longitudinal barycenter

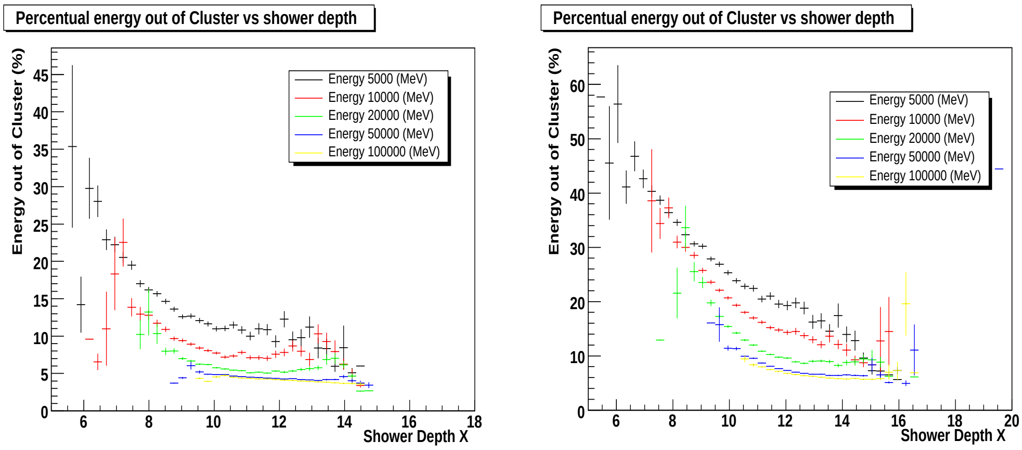

(a) η=0.3 (b) η=1.2

Figure 4.44: Energy out of cluster, expressed as a fraction (%) of the energy inside the cluster, for two η points, with B field.

and used as correction factor. The achieved correction factor is shown in figure (4.48). A non linear behavior is visible at high η values; however a higher degree polynomial parametrization does not sensibly improve the performances of the method, in term of energy resolution and linearity. A linear parametrization is used in the following.

The correction factor for reconstruct the energy deposited inside the cluster is parametrized as a function of the longitudinal barycenter with a second degree polynomial, averaged on all energies, as shown in figure (4.49).

The total energy deposited into the accordion is reconstructed starting from the energy measured in the cluster appling the accordion cluster correction, figure (4.49), and than the correction for the energy lost outside the cluster, figure (4.48).

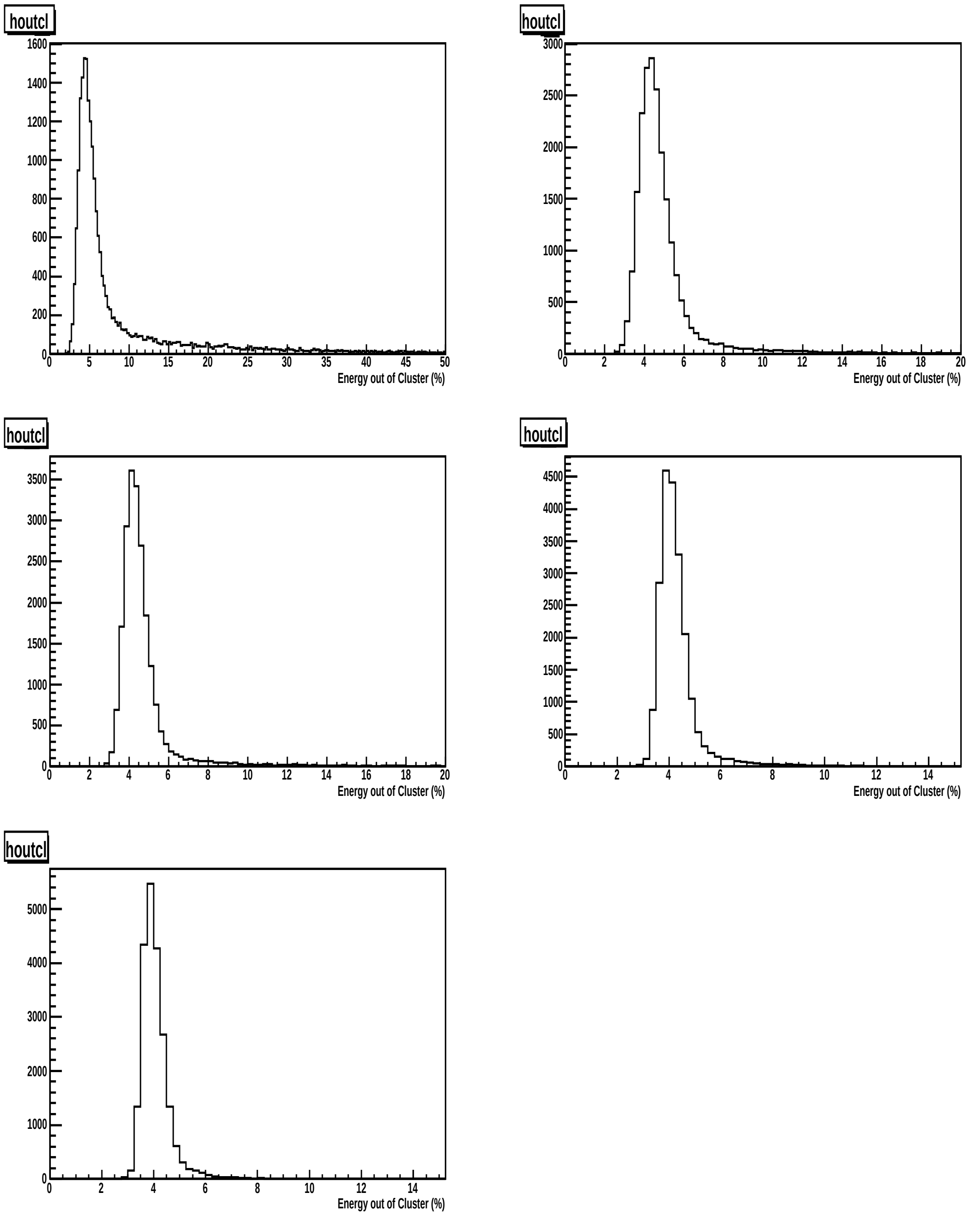

Figure 4.45: Energy deposited outside the cluster, expressed as a fraction (%) of the energy deposited inside the cluster. The energies 5, 10, 20, 50, 100 GeV are shown, from left to right, from top to bottom

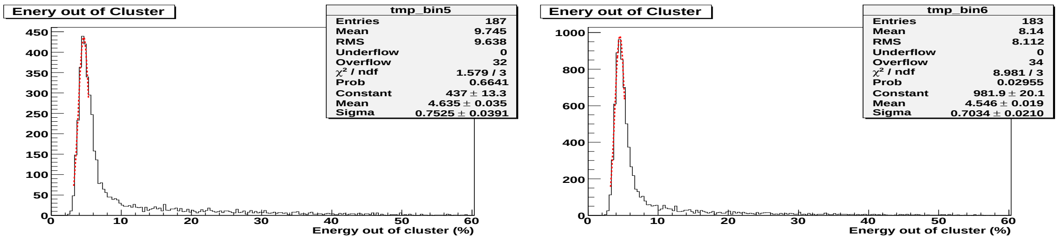

(a) bin=5 (b) bin=6

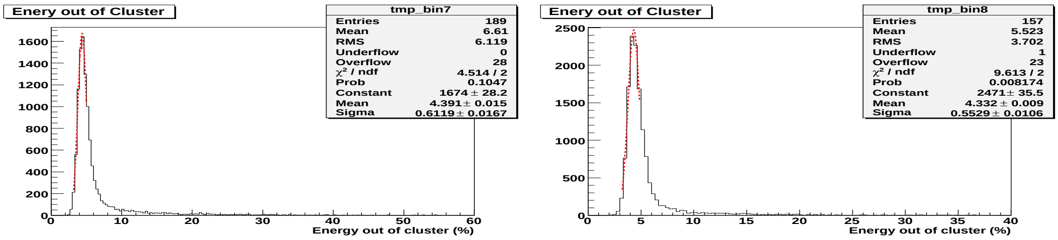

(c) bin=7 (d) bin=8

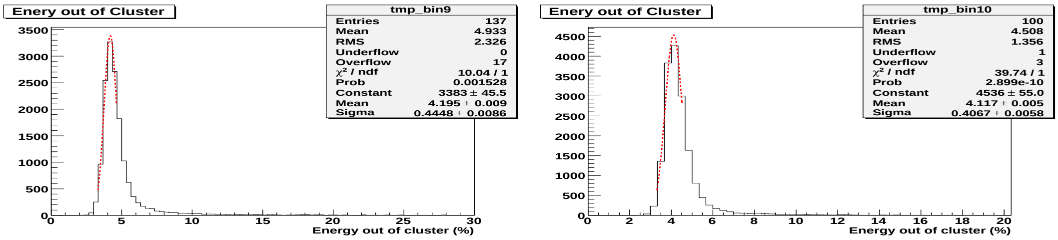

(e) bin=9 (f) bin=10

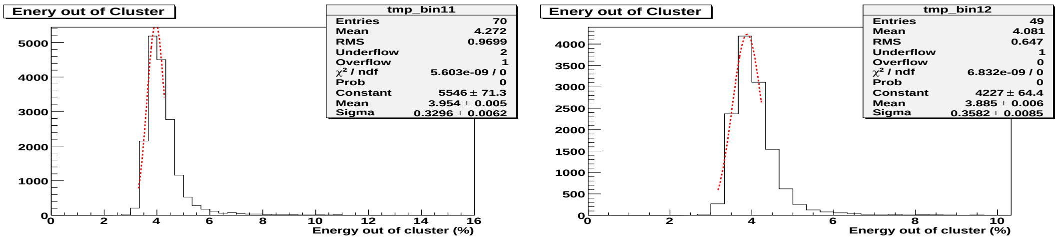

(g) bin=11 (h) bin=12

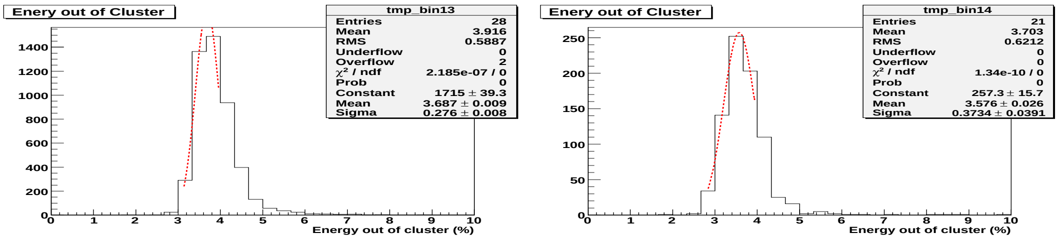

(i) bin=13 (j) bin=14

Figure 4.46: Energy deposited out of the cluster expressed as a fraction (%) of the energy inside the cluster, in various X interval and energy averaged, at η=0.3. The bin cover the shower depth range from 6 to 16 X_0

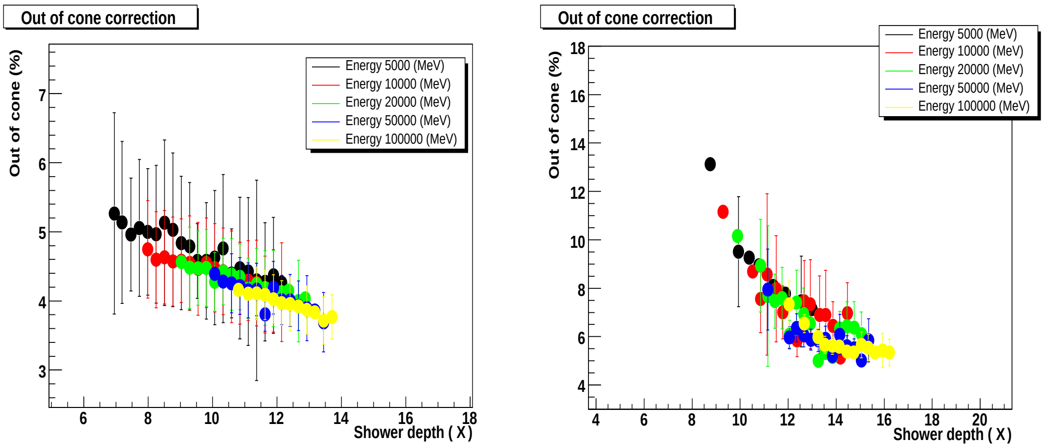

(a) η=0.3

(b) η=1.2

Figure 4.47: Energy out of cluster obtained with the gaussian fit on each X bin, as a function of the longitudinal barycenter, at two η points.

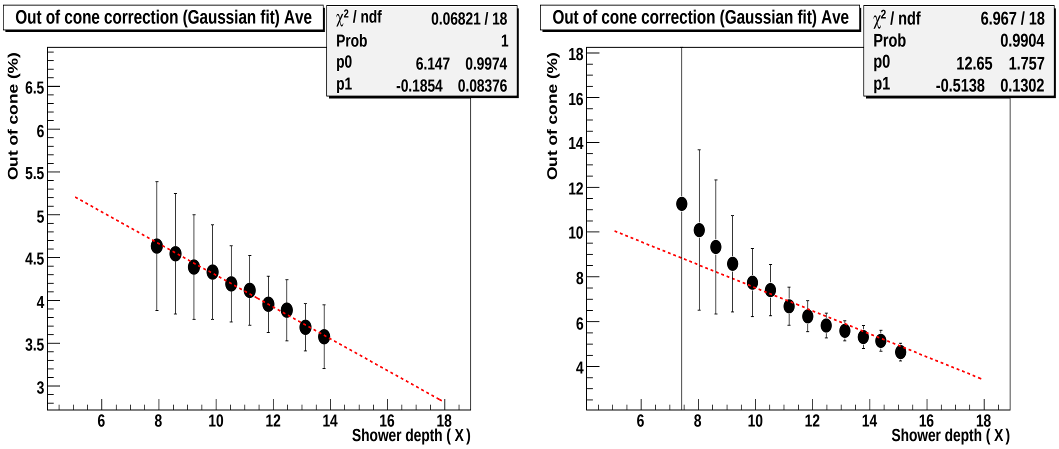

(a) η=0.3

(b) η=1.2

Figure 4.48: Energy out of cluster obtained with the gaussian fit on each X bin, as a function of the longitudinal barycenter, at two η points and energy averaged.

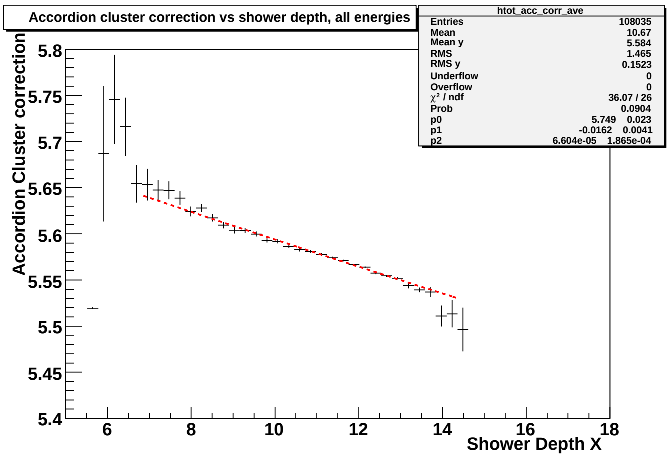

(a) η=0.3

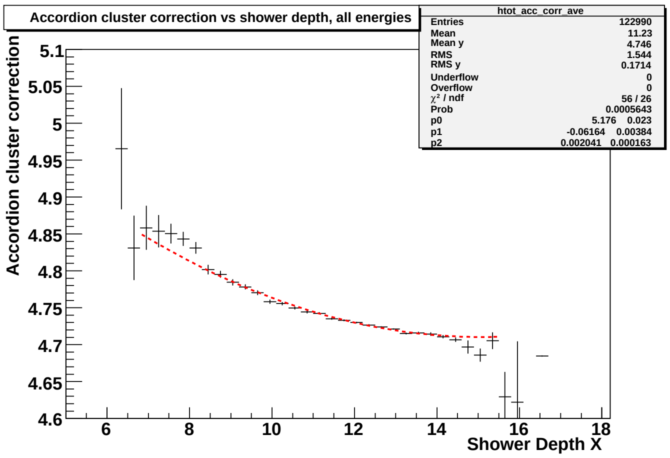

(b) η=1.2

Figure 4.49: Accordion cluster correction, averaged on all energies at two η points.

4.3.2 Calculation of the energy deposited in front of the Accordion

Also in the operative condition with the magnetic field turned on, the parametrization of the energy lost in front of the calorimeter as a function of the energy measured into the PreSampler is adopted.

Figures (4.50) and (4.51) show the energy deposited in front of the calorimeter as a function of the energy deposited into the active layer of the PreSampler, for various energies and two η points.

The coefficients extracted from the linear parametrization are parametrized as a function of the mean energy deposited into the accordion and are shown, as an example, in figure (4.52) and are summarized in table (4.11) together with the parameters achieved in the others impact point conditions. The parameters for the reconstruction of the energy deposited in front of the calorimeter are strongly influenced by the magnetic field, that introduce a different energy behavior respect to the one studied without the magnetic field.

		Offset Parameters		
η	**Impact Point**	$\mathbf{p_0}$	$\mathbf{p_1}$	$\mathbf{p_2}$
0.3	Center Cell	200.8 ± 6.7	2.653 ± 0.162	11.55 ± 2.27
0.3	Full Cell	227.1 ± 5.7	5.744 ± 0.272	-13.75± 2.75
0.3	Full Cell + B field	268.5 ± 2.7	3.881 ± 0.221	0.022 ± 0.002
1.2	Center Cell	657.7 ± 27.1	2.535 ± 0.724	144.4 ± 9.7
1.2	Full Cell	841 ± 18	6.542 ± 1.012	56.15 ± 10.16
1.2	Full Cell + B field	1682 ± 8.48	8.221 ± 0.951	-0.030± 0.011

		Slope Parameters		
η	**Impact Point**	$\mathbf{p_0}$	$\mathbf{p_1}$	$\mathbf{p_2}$
0.3	Center Cell	13.86 ± 0.24	2.11 ± 0.14	-0.215 ± 0.043
0.3	Full Cell	15.86 ± 0.08	0.20 ± 0.01	-0.090 ± 0.041
0.3	Full Cell + B field	12.81 ± 0.09	0.40 ± 0.01	-0.462 ± 0.061
1.2	Center Cell	10.45 ± 0.23	3.07 ± 0.12	-0.332 ± 0.032
1.2	Full Cell	14.01 ± 0.06	0.32 ± 0.01	-0.280 ± 0.030
1.2	Full Cell + B field	8.84 ± 0.07	0.86 ± 0.01	-1.234 ± 0.063

Table 4.11: Front energy reconstruction parameters (offset and slope) for two η points and three impact points.

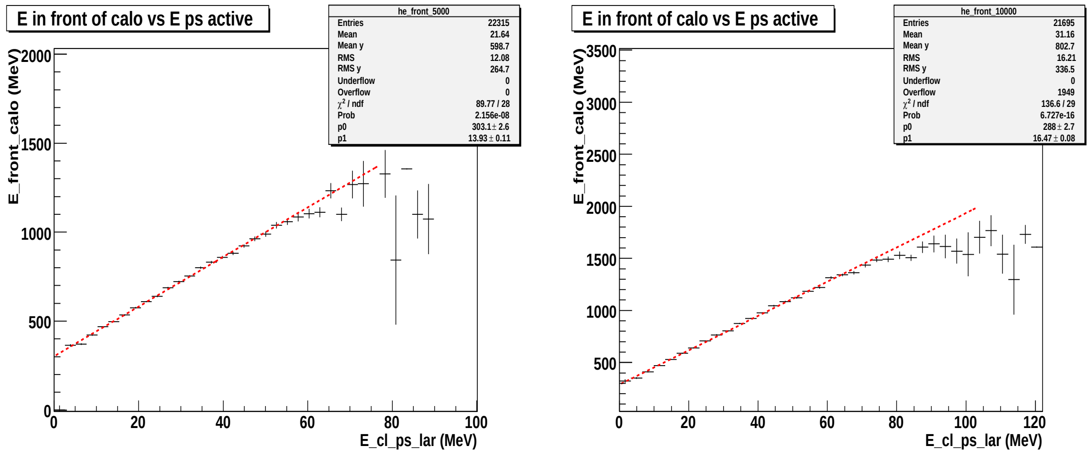

(a) E=5GeV (b) E=10GeV

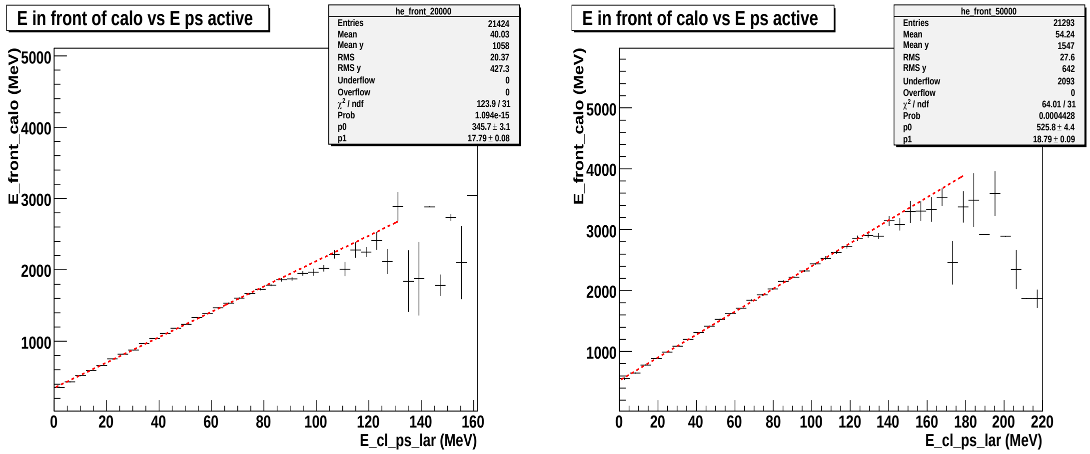

(c) E=20GeV (d) E=50GeV

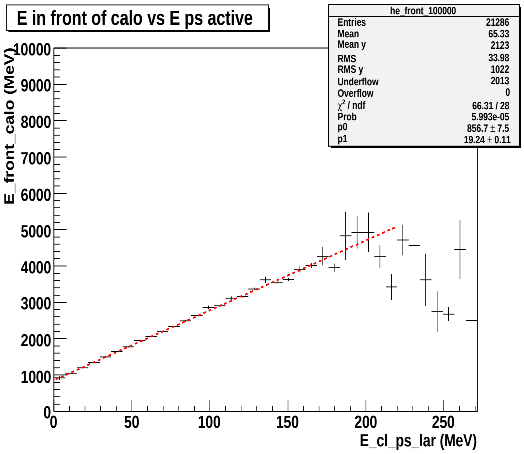

(e) E=100GeV

Figure 4.50: Energy deposited in front of the calorimeter as a function of the energy in the PreSampler, at η=0.3, for various electron energies.

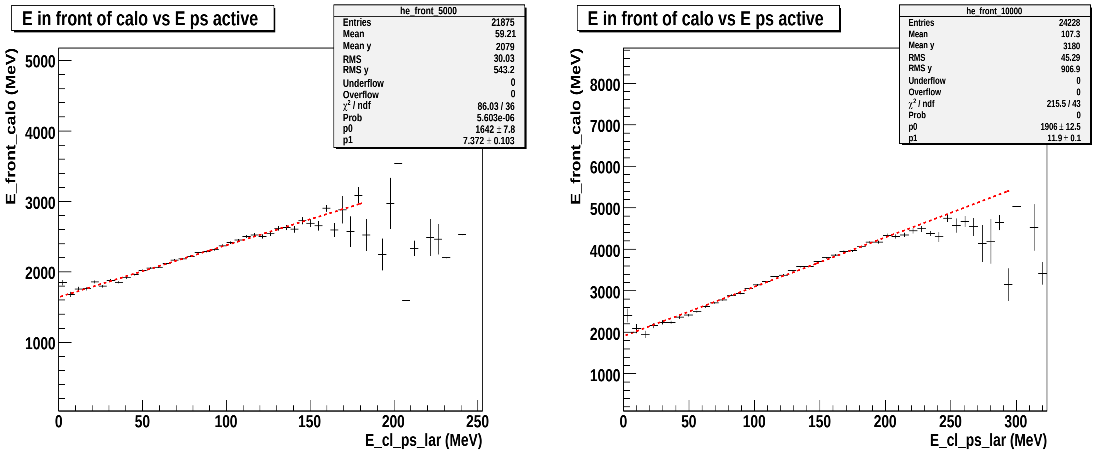

(a) E=5GeV

(b) E=10GeV

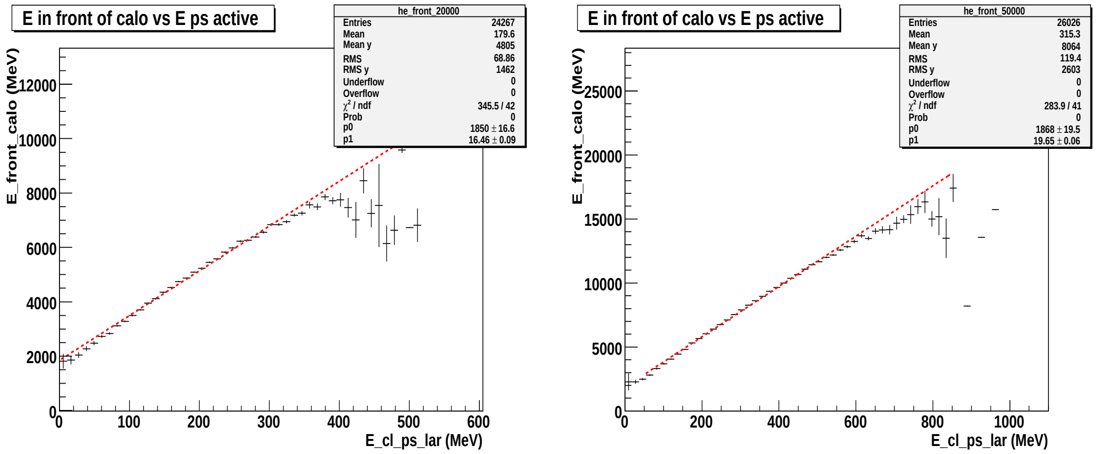

(c) E=20GeV

(d) E=50GeV

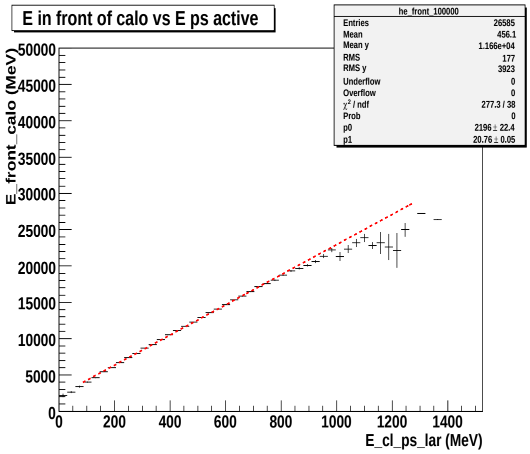

(e) E=100GeV

Figure 4.51: Energy deposited in front of the calorimeter as a function of the energy in the PreSampler, at η=1.2, for various electron energies.

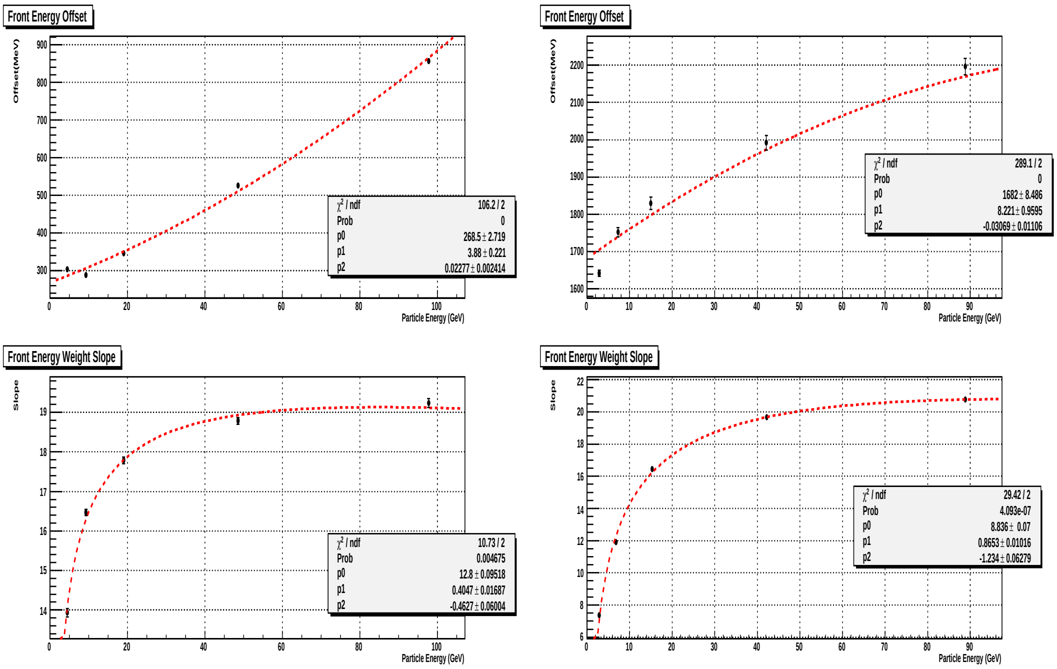

(a) η=0.3

(b) η=1.2

Figure 4.52: Parameters (offset and slope) for the reconstruction of the energy deposited in front of the calorimeter as a function of the average energy deposited in the accordion, at different value of energy of the incident particles. Two η values are shown. The top plots refer to the offset, the bottom to the slope

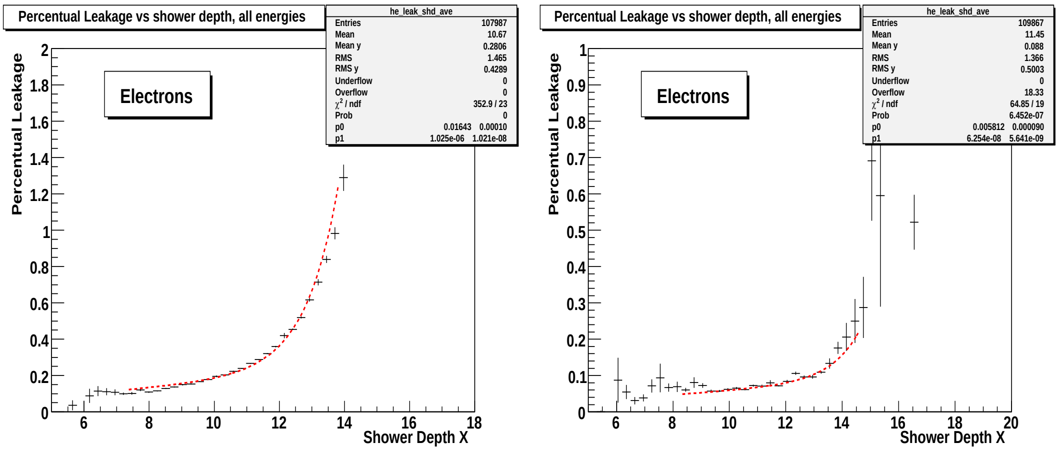

(a) η=0.3 (b) η=0.3

Figure 4.53: Energy deposited behind the accordion, expressed as a fraction (%) of the energy deposited in the accordion, as a function of the shower depth. Two η values are shown.

4.3.3 Calculation of the energy deposited behind the Accordion

The correction for the reconstruction of the energy deposited by the showers behind the accordion is parametrized as in the case without magnetic field. In figure (4.53) the ratio of the energy deposited behind and inside the accordion, averaged over all energies, is shown as a function of the longitudinal barycenter. The extracted parameters are summarized in table (4.12), together with the parameters achieved in the others impact point conditions: the effect of the magnetic field on the parameters is negligible, and they are compatible inside the errors.

η	**Impact Point**	$\mathbf{p_0^{leak}}$	$\mathbf{p_1^{leak}}$
0.3	Center Cell	0.0163 ± 0.0001	1.16E-06 ± 1.09E-08
0.3	Full Cell	0.0165 ± 0.0001	1.08E-06 ± 8.91E-09
0.3	Full Cell + B Field	0.0164 ± 0.0001	1.02E-06 ± 1.01E-08
1.2	Center Cell	0.0058 ± 9.1E-04	6.254E-08 ± 5.642E-0.9
1.2	Full Cell	0.0059 ± 8.7E-04	6.531E-08 ± 6.513E-0.9
1.2	Full Cell + B Field	0.0059 ± 7.4E-04	6.427E-08 ± 6.132E-0.9

Table 4.12: Parameters for the reconstruction of the energy deposited behind the accordion at two η points and three impact points.

4.3.4 Resolution and Linearity

The computed sampling and constant terms of the energy resolution and the maximum deviation from linearity are shown in figure (4.54) and (4.55), for two points in η. The values for all the η points are listed in table (4.13). In the last column the maximun shift from linearity is reported, when the 5 GeV electrons are not considered. The energy resolution is only marginally affected by the presence of the magnetic field B. On the contrary, the deviation from linearity are more severe, reaching up to 1.5% at large η and low energy electrons (5GeV). This is due to the combined effect of the magnetic field and the significant amount of material in front of the calorimeter.

It is possible to note that the constant term c of the resolution is different from zero. This is due to the fact that in the analysis of the data with the magnetic field is not possible to apply the corrections for the impact point: the reconstruction code used does not allow to know the impact point of the electrons on the calorimeter. In the case without magnetic field this problem can be solved simply assuming that the simulated η and ϕ position at the origin of Atlas coordinate correspond, neglecting the multiple scattering, to the impact point of the electrons on the calorimeter. In the B field case this is not possible, because, as seen before, the difference between the simulated ϕ and the one reconstructed on the calorimeter can be very large, up to 4 middle cell unit. Attempt to apply the correction for the impact point extracted for the case without B field gives poor results, due to the effect of the magnetic field on all the showering process.

η_{cell}	**b(%)**	**c(%)**	**Linearity (%)**	**Linearity E $>$ 5 GeV (%)**
0.3	9.9	0.274	0.2	0.1
0.6	10.8	0.242	0.3	0.1
0.7	12.2	0.220	0.5	0.2
1.0	13.4	0.275	0.5	0.3
1.1	15.7	0.247	0.6	0.3
1.2	16.8	0.240	1.5	0.4

Table 4.13: Resolution and Linearity, for the full cell illumination, without η and ϕ modulations, with magnetic field on. The linearity in the last column is obtained rejecting the event at E = 5GeV

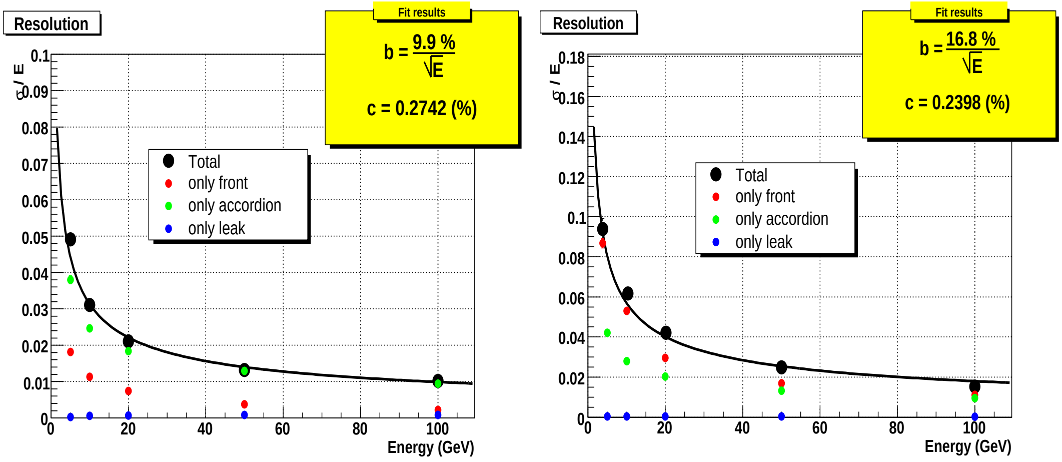

(a) η=0.3 (b) η=1.2

Figure 4.54: Energy resolution with the magnetic field turned on, for two η points, without the corrections for the impact point.

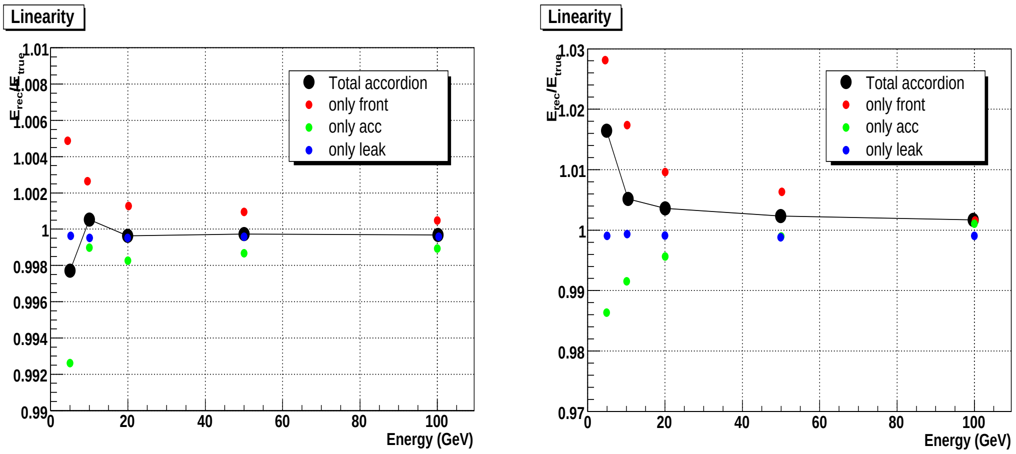

(a) η=0.3 (b) η=1.2

Figure 4.55: Linearity with the magnetic field turned on, for two η values, without the corrections for the impact point.

Chapter 5

CSC data set analysis

The CSC (Computing System Commissioning) data are available from central production, make use of the newest "as built" detector geometry which takes into account the "as installed" geometry of the various detectors.

The available energies for photons and electrons are : 10, 25, 50, 75, 100, 200 and 500 GeV. For each energy 50K events are simulated, covering uniformly both the full η ($|\eta| \leq 2.5$) and ϕ ($0 < \phi \leq 2\pi$) range.

Some differences with the Milan data set must be taken into account: in the old simulation the energies deposited into the different layers of the calorimeter come directly from the Monte Carlo simulation of the shower: no simulation of the signal and read out chain was included, and the energy deposited by the shower in the active layers of the detector was assumed as the detector reply. In the present data the full digitization is implemented: for each event the full signal generation is simulated, starting from the ionization signal into the gap of LAr to the conversion in deposited energy into the materials, reproducing the full readout chain, as explained in section (1.3.4).

Therefore, in the CSC analysis we start from the energy into the detector already approximately calibrated at the EM scale, and not from the energy deposited by the electromagnetic shower in the active layers of the calorimeter as before; as an example, the correction for the cluster energy reconstruction becomes in the CSC data analysis a "modulation" to the sampling fraction already applied into the digitization process, and has value very different from the one obtained from the previous data, which was, on contrary, the real sampling fraction of the calorimeter.

The CSC simulation does not include electronic noise and pileup.

Furthermore, in the CSC analysis the official reconstruction code is used, including the clusterization algorithm, that provides informations such as the energy measured into the active layer of the detector, the position of the shower, etc. Using the informations coming from the standard code we run the selfmade code for the Calibration Hits analysis, that provides all the informations relative to the energy deposition into the inactive and dead materials needed to compute the calibration coefficients.

All the analysis that will be shown refer to a 3×7 cluster size, chosen as a reference, except where differently indicated. Also a code for the identification of the EM particles and for the track matching is included into the reconstruction.

The identification cuts that will be used in the Atlas experiment are applied, replacing the cut on the bremsstrahlung energy applied in the previous analysis. We make use of :

- calorimeter cuts : to clean the sample from the events that have a too degraded shower profile
- track matching : to discriminate between electrons and photons

These identification cuts at higher η points (EndCap regions) and lower energies (10-25GeV) reject up to half of the events, making difficult, to extract the calibration coefficients. For this reason both electrons an photons of 10 GeV are not included in our analysis.

We will use the convention decided for the official reconstruction code to discriminate between electrons and photons: each event that have an electromagnetic cluster in the EM calorimeter with an associated track in the tracking system is an electron, otherwise if there is the EM cluster but not an associated track the event is selected as a photon.

The results shown in the next sections for the photons must be taken as preliminary, because the available statistic does not allow to treat converted and unconverted photons separately: this introduce a bias in the extaction of the calibration coefficients, particularly for the ones for the reconstruction of the energy deposited in front of the calorimeter, which is very different in the two cases.

As said before the CSC data cover uniformly all the η range of the EM calorimeter: some region of the calorimeter, not simulated in the previous analysis, need dedicated studies. These region are:

1. $\eta=0$: crack between the two half barrel. It needs dedicated calibration.
2. $|\eta|=0.8$: transition between A and B electrodes in the barrel calorimeter. The variation of the thickness of absorber lead is reflected in a variation of the sampling fraction, partially compensated with the calibration coefficients applied in the digitization process at cell level. It needs special algorithm to extract cluster corrections.
3. $1.425 \leq |\eta| \leq 1.55$: crack between barrel and endcap region of the calorimeter. It needs dedicated calibration.
4. $1.8 < |\eta| \leq 2.5$: endcap region without the PreSampler. It needs different calibration scheme for the energy deposited in front of the calorimeter.

For the moment points number 1 and 3 are not considered, because they need a dedicated calibration strategy and a larger statistic.

A set of calibration coefficients must be provided for each cell of the calorimeter: to reach the statistic needed to compute them, the events of five cells are added. In the region without any transitions or cracks the parameters are given for the central cell of the 5 cells window, and the windows is moved in one cell step. In the transition regions windows of different size are adopted.

In the CSC data the events are simulated also in the EndCap regions ($| \eta | > 1.55$), not studied in the previous analysis due to the limited computing resources available for the simulations. In these regions the calorimeter geometry is very different from the one in the barrel, as explained in section (2.2.1), and this requires some dedicated tuning of the coefficients extraction procedure.

The group of the University of Madrid, that have large background knowledge on the EndCap detector, was therefore involved in the calibration of this portion of the detector. The results shown in sections (5.1), (5.2) and (5.3) for the EndCap region must be taken as preliminary, and are obtained with coefficients extracted in Milan before the Madrid group get involved. The results shown in (5.4) are obtained with the coefficients included in the official package included in Athena, and are computed in Milan for the barrel region and in Madrid for the EndCap region.

5.1 Electron energy reconstruction

5.1.1 Energy reconstruction in the Accordion

The parametrization of the energy deposited in the accordion cluster as a function of the longitudinal barycenter, introduced in the previous chapter, is adopted over the full η range, as shown in figure (5.1), where 4 η points are shown as an example.

We use the same parametrization with a second degree polynomial over the all η range. The value of the correction is different from the one obtained with the Milan simulations because with the CSC data we start from the energies already calibrated to the EM scale, as explained before.

It is evident a different behavior between the top plots, relative to the barrel region, and the bottom plot, relative to the endcaps region. In the endcap region two different effects are added: the variation of the LAr gap, which implies an increase of the sampling fraction, and the variation of the electrical field, that imply a variation on the charge collection. The change of the sampling fraction is in part compensated by the variation of the voltage applied between electrodes and absorbers, as shown in section (2.2.1). How the superimposition of these effects act on the total accordion correction is not a priori easy to understand, taking into account that the magnitude of this effect is around 1%.

The fraction of energy deposited out of the cluster is parametrized as a function of the longitudinal barycenter of the shower. For each longitudinal barycenter interval a Gaussian fit is made on the distribution of the fraction of energy out of the cluster and the achieved mean value of the Gaussian is fitted with a first degree polynomial,

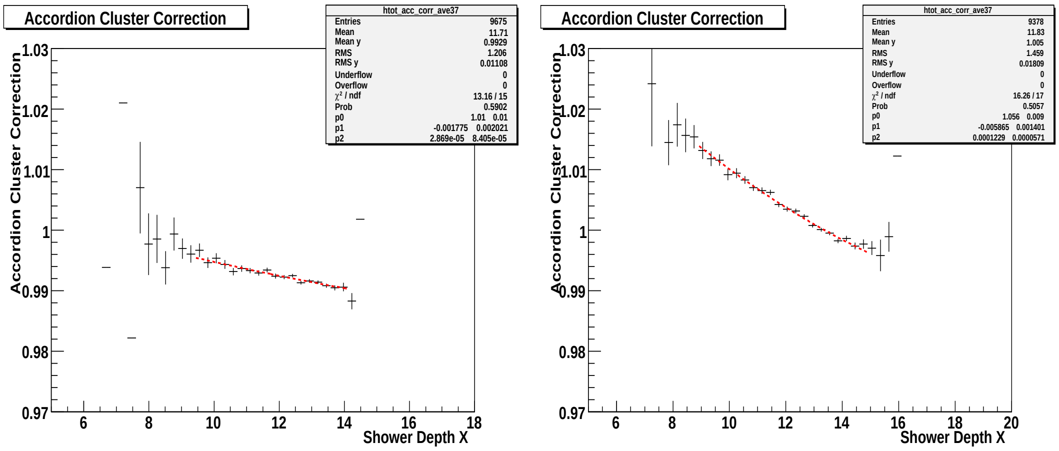

(a) η=0.3

(b) η=1.2

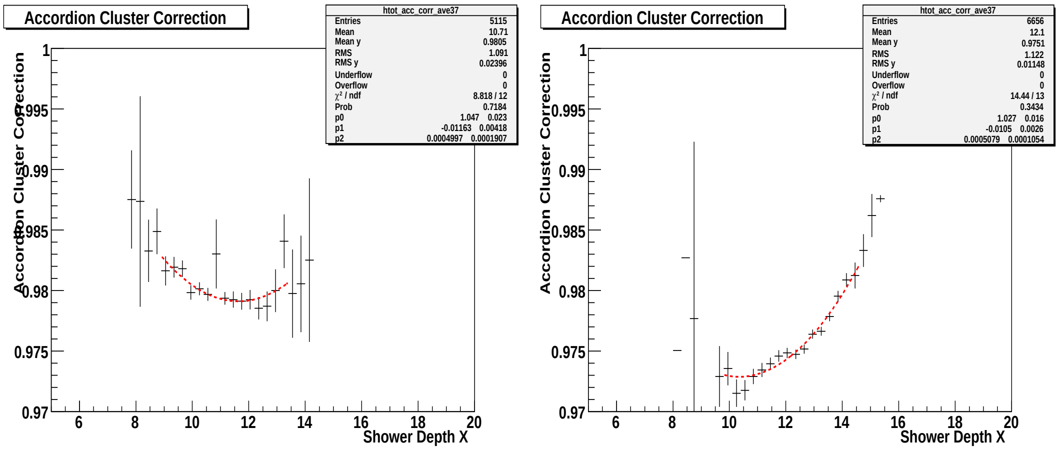

(c) η=1.65

(d) η=2.0

Figure 5.1: Accordion cluster correction, for 4 different η points with a 3×7 cluster size. The red dashed line is the adopted parametrization.

as a function of the longitudinal barycenter, as shown in figure (5.2) for 4 η points. Some deviations from linearity are visible, but proved to have negligible effect on the method performance.

It is important to note explicitly that all the cluster corrections are cluster size dependent, and need to be extracted for all the possible cluster sizes. The figures shown here are relative to a cluster size of $\Delta\eta \times \Delta\phi = 3\times7$, used as a reference, but similar parametrizations are obtained for the others cluster sizes.

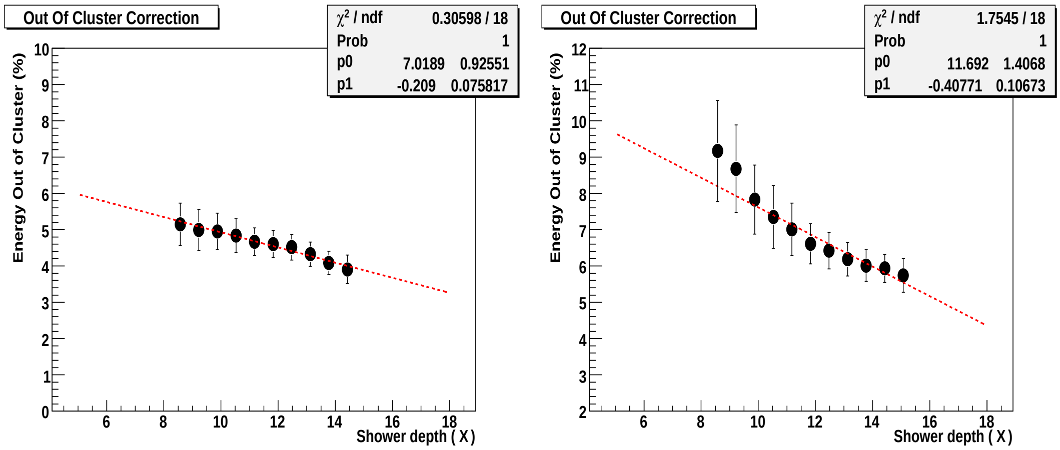

(a) η=0.3 (b) η=1.2

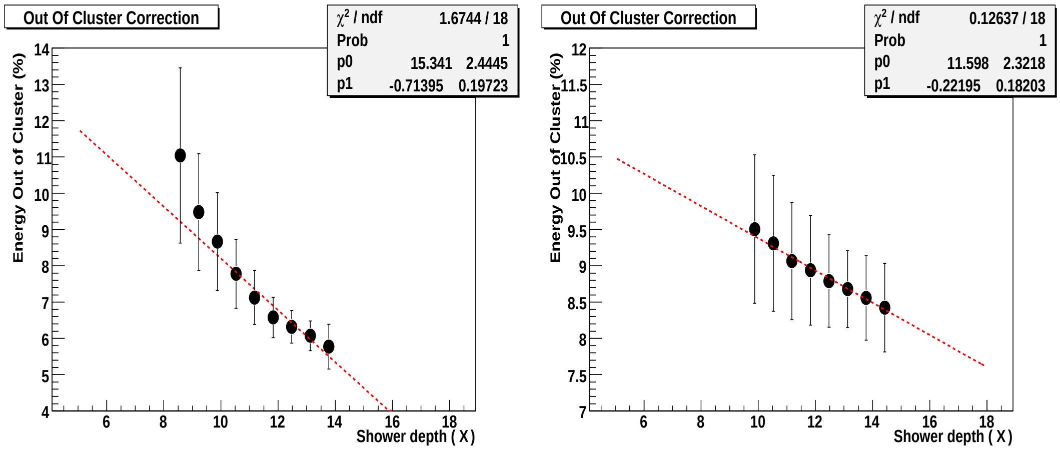

(c) η=1.65 (d) η=2.0

Figure 5.2: Accordion cluster correction factor, for a 3×7 cluster size, for 4 η points. The red dashed line is the adopted parametrization.

5.1.2 Calculation of the energy deposited in front of the Accordion

For the study of the energy deposited in front of the accordion, the calorimeter must be divided into three regions: the barrel, the endcap with the PreSampler and the endcap without the PreSampler. In the first two regions the usual parametrization of the energy deposited in front of the calorimeter, as a function of the energy deposited into the PreSampler, is adopted. In the third region the absence of the PreSampler requires a different approach, and a parametrization as a function of the longitudinal barycenter has been adopted. In the next the three different cases will be discussed in more details.

Barrel Region ($0 \leq |\eta| < 1.425$)

For the barrel region the usual parametrization of the energy deposited in the material up to the calorimeter as a function of the energy deposited into the PreSampler is adopted. As an example, in figure (5.3) the energy distribution for 100 GeV electrons at η=0.3 and η=1.2 are shown. As before, the range of the fit is determined excluding the bins that contain less than 0.5% of the total statistic.

The parameters of the first degree polynomial, labelled offset and slope, are energy dependent and are parametrized as a function of the total energy deposited into the accordion, as shown in the figure (5.4) and as explained in the previous chapter.

A parametrization with a second degree polynomial has been adopted for the offset, rather than the one with the square root term shown in equation (4.5) .

Endcap with the PreSampler ($1.55 \leq |\eta| < 1.8$)

In the region of the endcap with the PreSampler ($1.55 \leq |\eta| \leq 1.8$) the same parametrization used in the case of the barrel region is adopted. The figures (5.5) and (5.6) show the energy deposited in front of the calorimeter as a function of the energy deposited into the PreSampler and the parametrization of the achieved parameters (offset and slope) as a function of the mean energy deposited into the accordion.

It is important to note that the behavior of the extracted parameters, shown in figure (5.6) as a function of the mean energy into the accordion is different from the one shown at lower η, in the barrel region, figure (5.4). This is due to the fact that in this endcap region up to 5÷6 radiation lengths of material are present in front of the calorimeter, twice the material present in the barrel region: this makes very likely for the electrons to loose a large fraction of the original energy (up to 40% for lower energy electrons) in front of the calorimeter. There are no events with energy deposited in the PreSampler smaller than several GeV, as visible in figure (5.5). In these conditions the fitted offset is a mathematical extrapolation without physical meaning. It is also possible to see the strong correlation between offset and slope, due to the same reason.

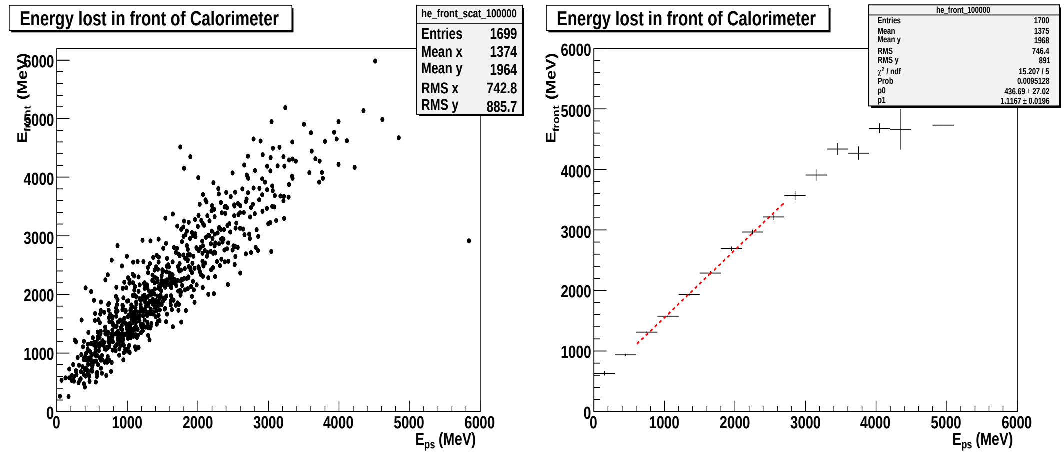

(a) η=0.3 (b) η=0.3

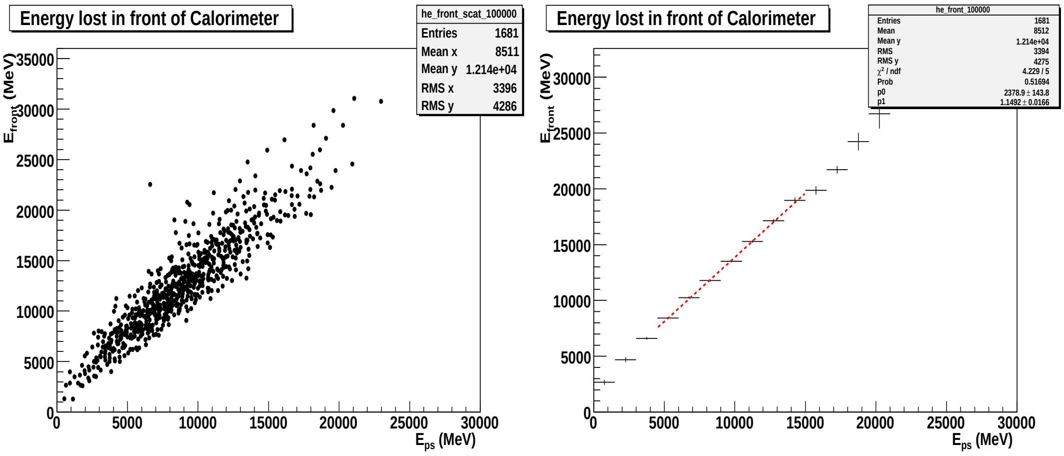

(c) η=1.2 (d) η=1.2

Figure 5.3: Energy deposited in front of the calorimeter from 100 GeV electrons, as a function of the energy deposited into the PreSampler, at two η points.

Endcap without the PreSampler (1.8$\leq|\eta|<$2.5)

The region for 1.8$\leq|\eta|<$2.5 requires a different calibration approach, due to the absence of the PreSampler. The best results are achieved parametrizing the energy deposited in the materials up to the calorimeter strips as a function of the longitudinal barycenter of the shower. In figure (5.7) the scatter plot for the energy deposited in front of the calorimeter as a function of the longitudinal barycenter (left) and the adopted parametrization with a second degree polynomial (right) are shown. The parameters are energy dependent and are parametrized as a function of the mean energy deposited in the accordion, with a second degree polynomial, as shown in figure (5.8).

A parametrization of the energy deposited in front of the calorimeter as a function of the energy deposited in the strips has also been tested, but worse results are obtained.

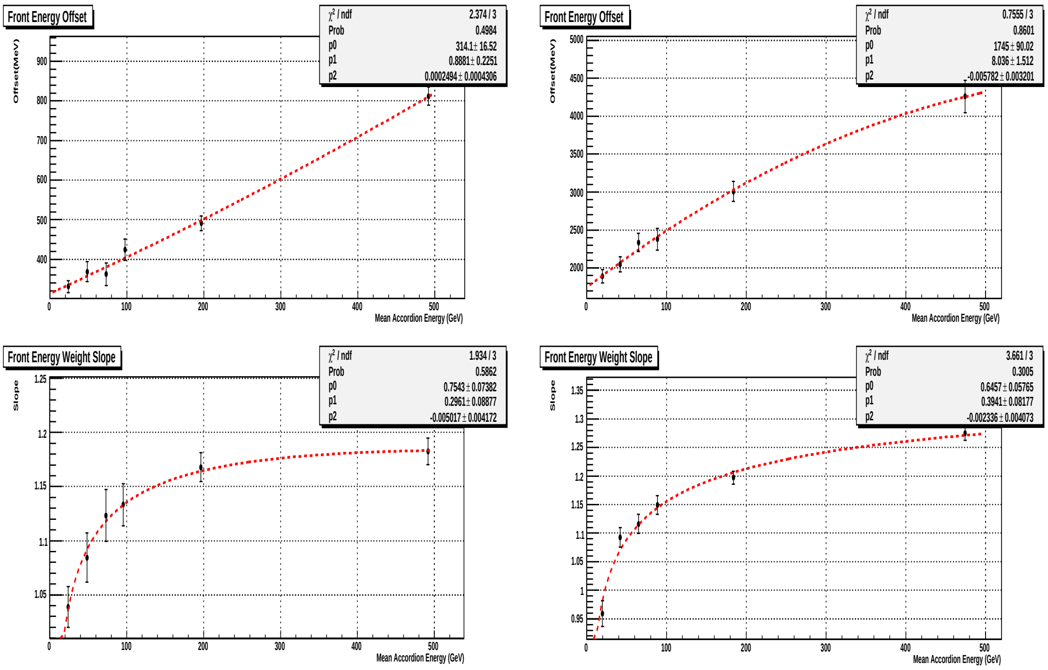

(a) η=0.3

(b) η=1.2

Figure 5.4: Energy dependence of the parameters for the front energy reconstruction, at 2 η points. Top plots refer to the offset, while bottom refer to the slope.

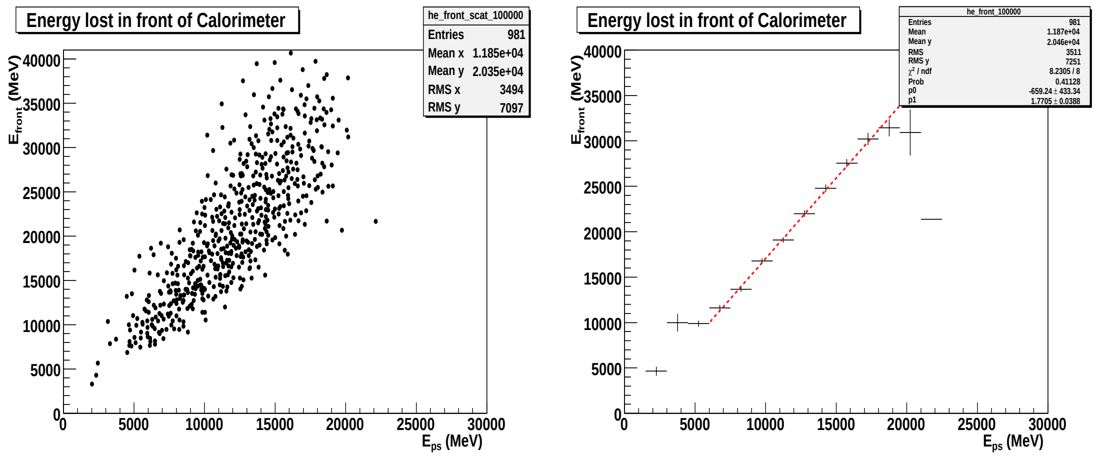

Figure 5.5: Energy deposited in front of the calorimeter from 100 GeV electrons, as a function of the energy deposited in the PreSampler at η=1.65.

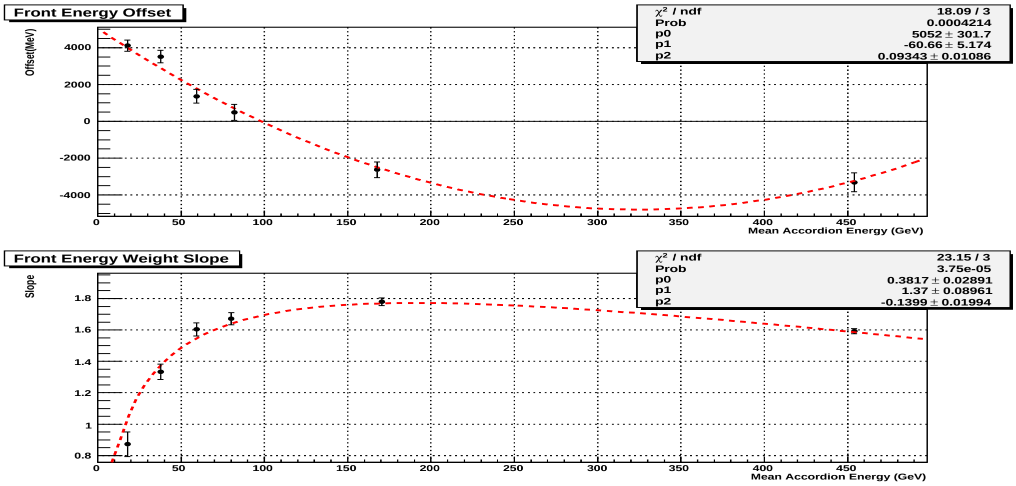

Figure 5.6: Energy dependence of the parameters for the front energy reconstruction, at η=1.65. Top plot refers to the offset, while the bottom refers to the slope.

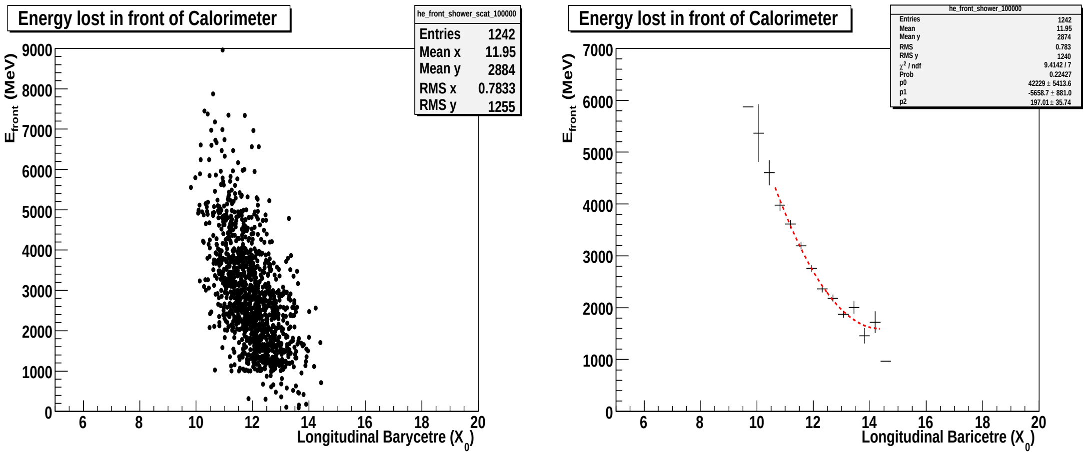

Figure 5.7: Energy deposited in front of the calorimeter strips by 100 GeV electrons, as a function of the longitudinal barycenter, at η=2.0.

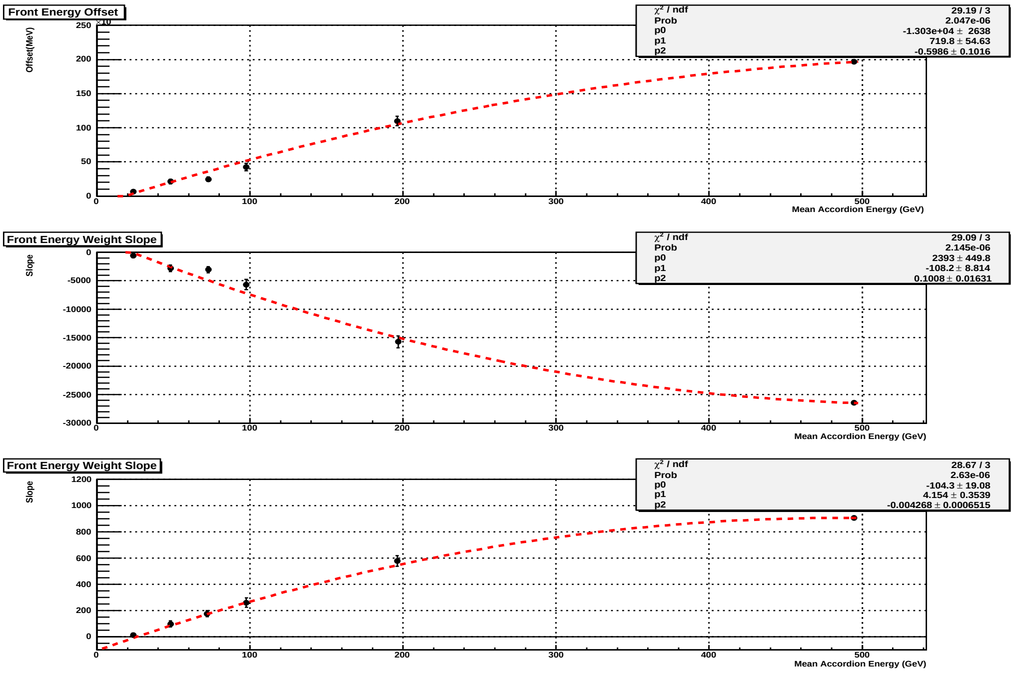

Figure 5.8: Energy dependence of the parameters for the front energy reconstruction, at η=2.0. Top plot refer to the offset, while the bottom refer to the slope.

Dependence of the energy deposited in front of calorimeter from the PreSampler cluster size

The parametrization of the energy deposited in front of the calorimeter as a function of the energy deposited in the PreSampler is in principle cluster size dependent, because in the PreShower the energy is clusterized as in the others samples of the calorimeter. Due to the granularity of the PreSampler ($\Delta\eta \times \Delta\phi = 0.025 \times 0.1$) in ϕ only 2 cells are added for clusters 3×5 and 5×5, and 2 or 3 cells are added for cluster 3×7, depending on the impact point of the particle inside the calorimeter.

In figure (5.9) the distribution of the energy deposited into the PreSampler are shown for three different cluster sizes (3x5, 3x7, 5x5) and two energies, in the η bin $0.2\leq|\eta|\leq0.5$.

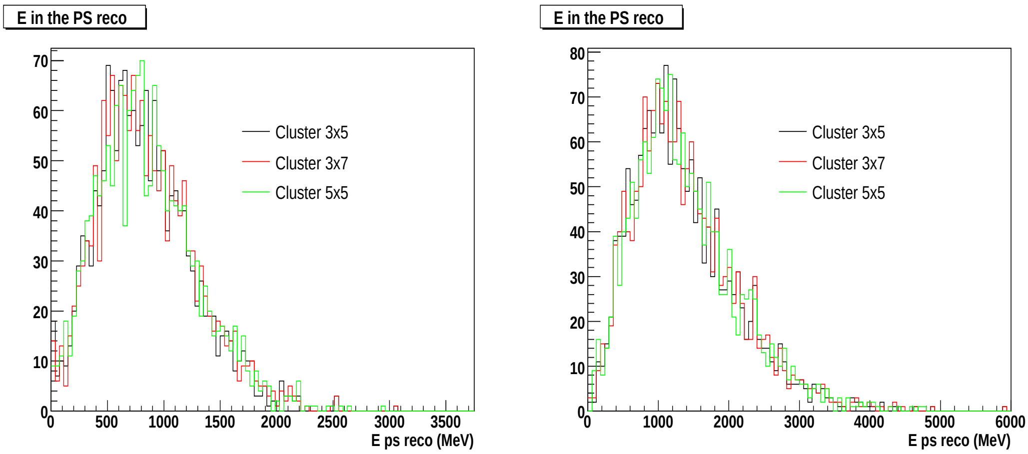

(a) E=25GeV (b) E=100GeV

Figure 5.9: Energy deposited into the PreSampler for three cluster sizes and two energy values, for $0.2\leq|\eta|\leq0.5$.

We also made some test introducing into the simulations the effect of the electronic noise, which may be important when the energy deposited is small, as in the PreSampler for 25 GeV electrons. In figure (5.10) is possible to see the effect of the electronic noise for the three cluster sizes, for electrons of 25 GeV: the effect on the RMS of the distribution is around 1%.

To understand the effect of the PreSampler cluster size on the performances of the calibration method, in term of energy resolution, some tests have been done. The calibration coefficients for the front energy reconstruction for the three cluster sizes, both with and without noise, have been computed and used for reconstructing the energy deposited by the electrons in front of the calorimeter. The energy deposited in and behind the accordion is reconstructed using a 3×7 cluster size, but similar results are achieved with others cluster sizes. In table (5.1) the achieved energy resolution ($\frac{\sigma}{E}(\%)$) is shown. The effect of the cluster size is visible at lower energies, where

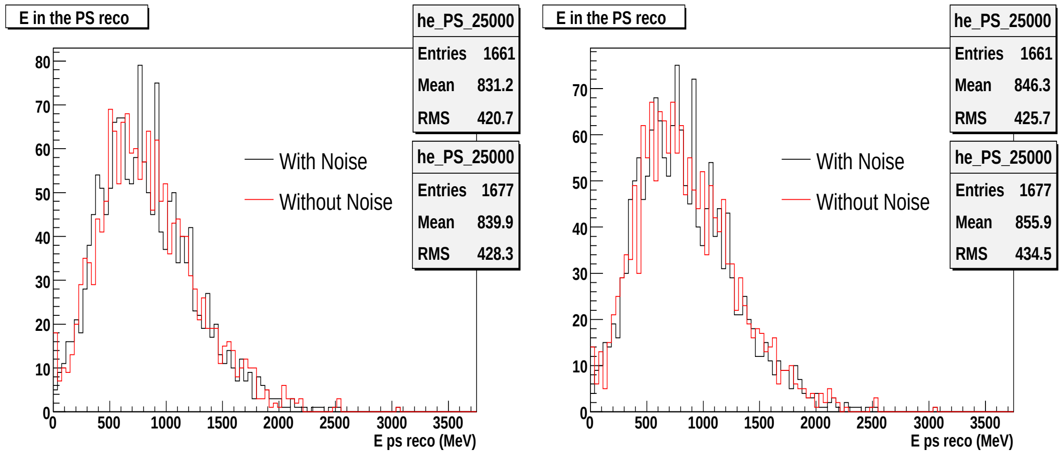

(a) Cluster size = 3×5 (b) Cluster size = 3×7

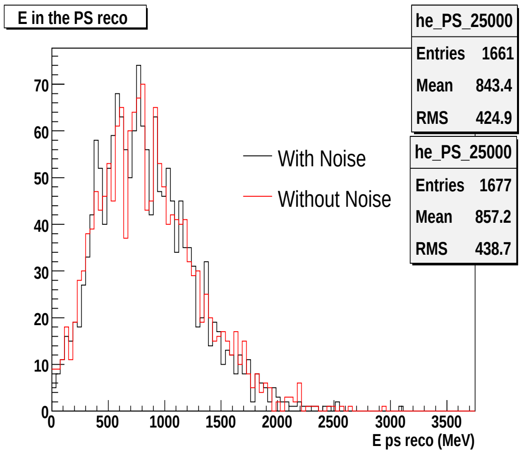

(c) Cluster size = 5×5

Figure 5.10: Effect of the electronic noise on the energy deposition into the PreSampler. All plots refer to electrons with E = 25 GeV, for various cluster size. The top statistical box is for the no noise condition, the bottom refer to the noise condition

the effect on the energy resolution is of the order of 5-10%, and can be neglected for energy greather than 100 GeV. The cluster size that give better result both with and without noise is the 3×7. It is also possible to see that the use of larger cluster size in η gives, in the case with noise, a worse performance than the smaller one: the shower is very narrow in η in the PreSampler, most of the energy is deposited in the central cells of the cluster and adding the external cells will only increase the added noise, worsening the global performance.

We propose to provide the calibration coefficients only for one fixed cluster size, that must be used for the reconstruction of the energy deposited in front of the calorimeter, independently from the cluster size adopted in the accordion. The cluster size that gives best results and is adopted is the 3×7.

$\mathbf{E_{particle}}$ (MeV)	Resolution $\frac{\sigma}{E}$(%)					
	Without Noise			*With Noise*		
	3×5	3×7	5×5	3×5	3×7	5×5
25000	0.019	0.017	0.018	0.023	0.021	0.024
50000	0.014	0.012	0.013	0.016	0.015	0.019
75000	0.011	0.010	0.011	0.012	0.011	0.012
100000	0.010	0.009	0.009	0.011	0.010	0.011
200000	0.009	0.009	0.009	0.009	0.009	0.009
500000	0.006	0.006	0.006	0.006	0.006	0.006

Table 5.1: Effect of PreSampler cluster size on energy resolution ($\frac{\sigma}{E}$).

5.1.3 Calculation of the energy deposited behind the Accordion

The energy deposited behind the accordion is parametrized over all the η range as a function of the longitudinal barycenter, as shown in previous chapter.

In figure (5.11) the fraction (%) of energy deposited behind the accordion as a function of the longitudinal barycenter, energy averaged are shown for 4 η points. The red dashed line is the adopted parametrization.

The parametrization of equation (4.8) is valid also for the higher electron energy simulated in the CSC central production (500 GeV), which were not simulated before.

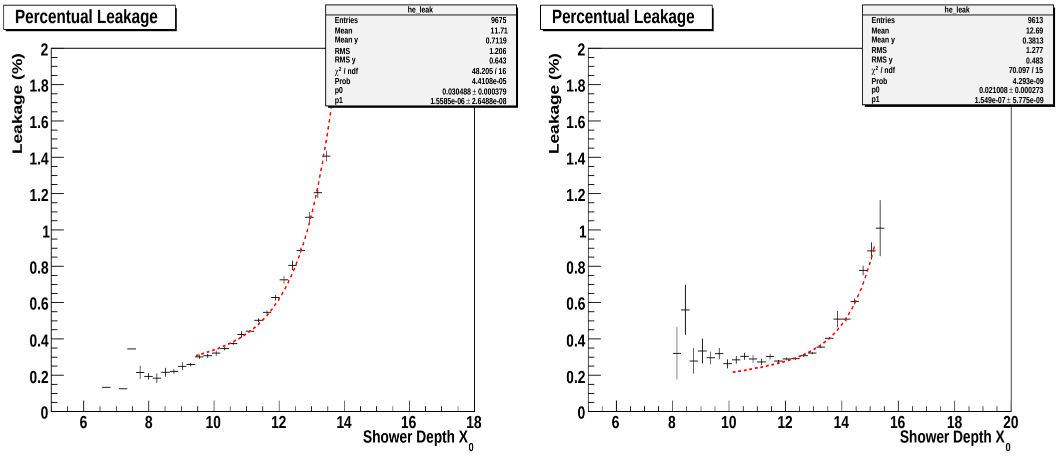

(a) η=0.3 (b) η=1.2

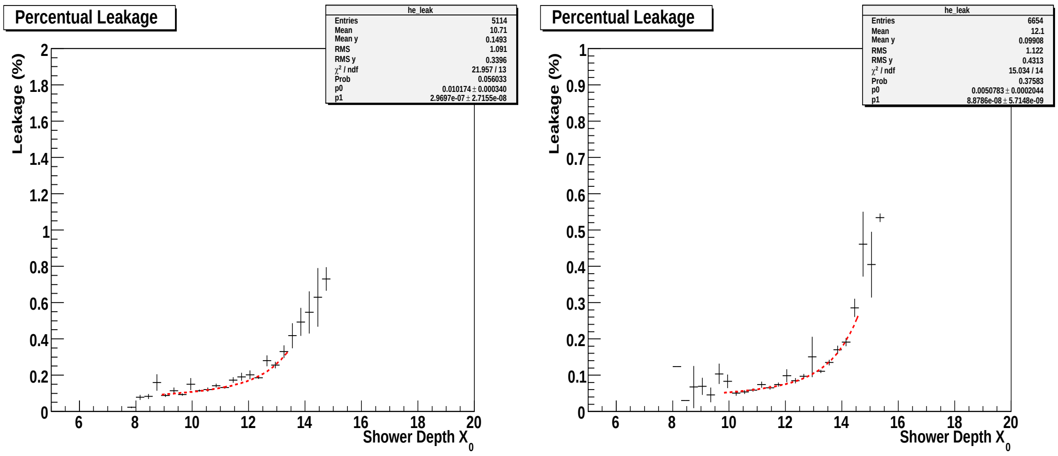

(c) η=1.65 (d) η=2.0

Figure 5.11: Energy deposited behind the calorimeter, as a function of the longitudinal barycenter, at 4 η points. The red dashed line shows the adopted parametrization

5.1.4 Resolution and linearity

In figure (5.12) the energy resolution achieved for 100 GeV electrons, over all the η range of the calorimeter, is shown. In black the resolution (σ/E) when all the energies are reconstructed with the proposed method ; in green the resolution achieved when only the energy deposited in the accordion is reconstructed, and all the others energies are taken from the Monte Carlo simulations. Finally, in red and in blue, the resolution achieved when only the energy deposited in front and behind the calorimeter are reconstructed. The region with 1.4< η <1.55 is not calibrated since it is the transition region (crack) between barrel and endcap and need a dedicated calibration strategy which is out of the aim of this thesis.

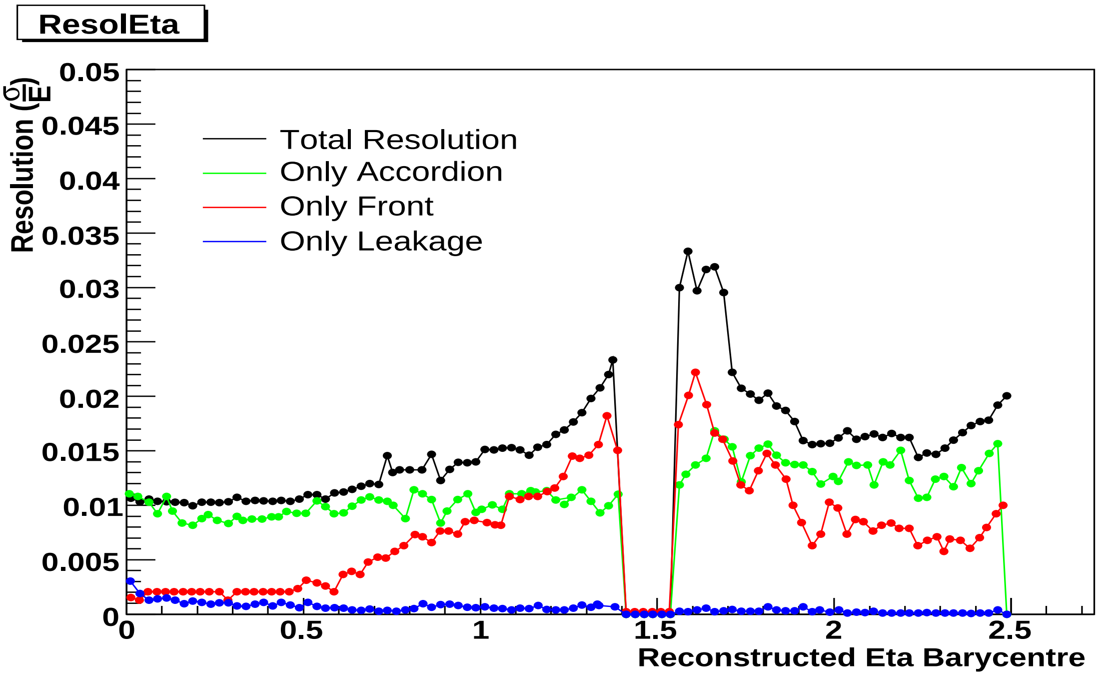

Figure 5.12: Resolution (σ/E) for 100 GeV electrons. The total resolution is shown in black, the contribution to total resolution of the front, accordion and leakage energy reconstruction are shown respectively in red, green and blue.

The contribution to the total resolution due to the reconstruction of the energy deposited into the accordion varies from the 1% in the barrel region to 1.5% in the endcap region. The contribution to the total resolution of the energy deposited in front of the calorimeter increases with η in the barrel, and reaches a maximum (3%) in the endcap region with the PreSampler. This behavior reflects the amount of material upstream the calorimeter, shown in figure (5.13) in radiation lengths. It is important to note that in the region of the endcap with the PreSampler the amount of material upstream the calorimeter reaches a maximum of about 6 radiation lengths. This value is due to the presence of the services for the Inner Detector, installed into the gap between barrel and endcap in the region at 1.55< η ≤1.7. In this region the contribution to the total resolution from the front energy reconstruction is dominant.

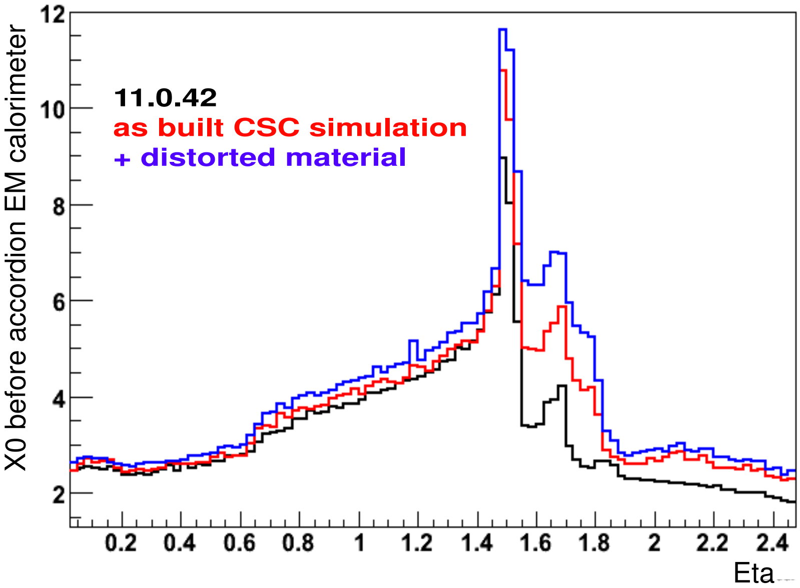

Figure 5.13: Material upstream the calorimeter in radiation lengths as a function of η. The red line refers to the geometry adopted for the CSC simulation, the black to one old version of Athena code, and the blue to the CSC with the "distorted" geometry.

In figure (5.14) the energy deposition of 100 GeV electrons in the different layers of the detector is shown, as a function of η. In green the energy deposited into the accordion, in black the energy deposited in the material up to the calorimeter strips and in red the energy deposited up to the PreSampler. Note that 100 GeV electrons can loose up to 30% of their energy in the material upstream the calorimeter, and this fraction may rise up to 50% for lower energy (25 GeV) electrons.

In figure (5.15) the resolution (σ/E) for all the available electron energies is shown. The effect of the upstream material on the resolution is visible for all the energies, even if the lower energies are the most affected.

Figure (5.16) shows the sampling term b and the constant term c of the energy resolution on all the η range. The value of the sampling term b rises smoothly on all the barrel region, going from $\sim$10% to $\sim$24% near the crack. In the region of the endcap with the PreSampler, the b term rises up to $\sim$30%. In the region without the PreSampler the b term decreases to $\sim$20%, reflecting the decreasing of the upstream material.

The costant term c is different from zero because we don't use any correction for the impact point inside the cell. These corrections are already implemented into Athena, but was not possible to use them with the calibration hits analysis code at

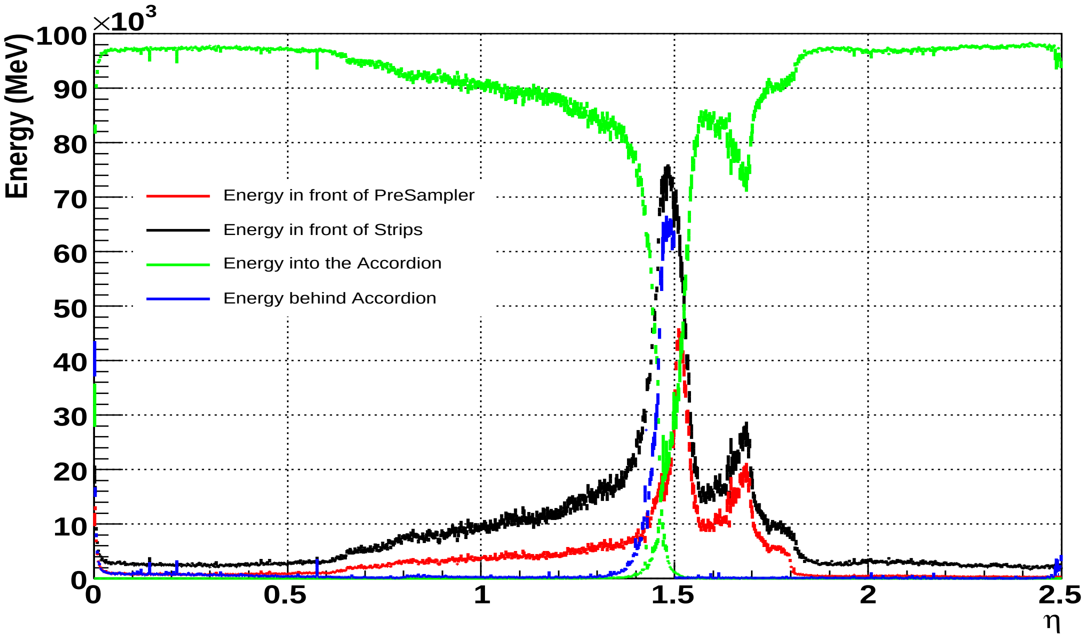

Figure 5.14: Energy deposited by 100 GeV electrons into the different detector compartments.

the time of these studies. A selfmade implementation of this corrections is out of the aim of this thesis, and a dedicated study would also be impossible due to the low statistics available. The constant term *c* is very sensitive to each disuniformity of the calorimeter, as it is possible to see in the transition region at η=0.8.

The achieved linearity is shown in figure (5.17), for different energies. The linearity is better than 0.7% at all η. Some fluctuations on the maximun deviation from the linearity are visible at lower energy values and are imputable to the low statistic, less than 500 events for each cell, due to the high rejection from the calorimeter cuts.

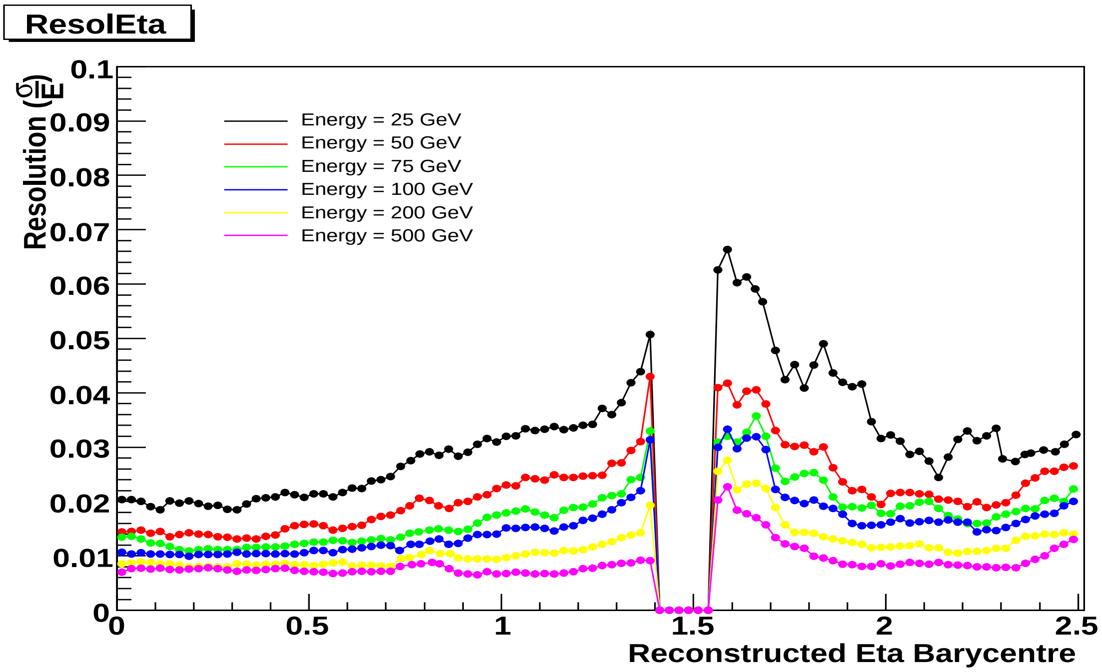

Figure 5.15: Electrons energy resolution (σ/E), for various energies .

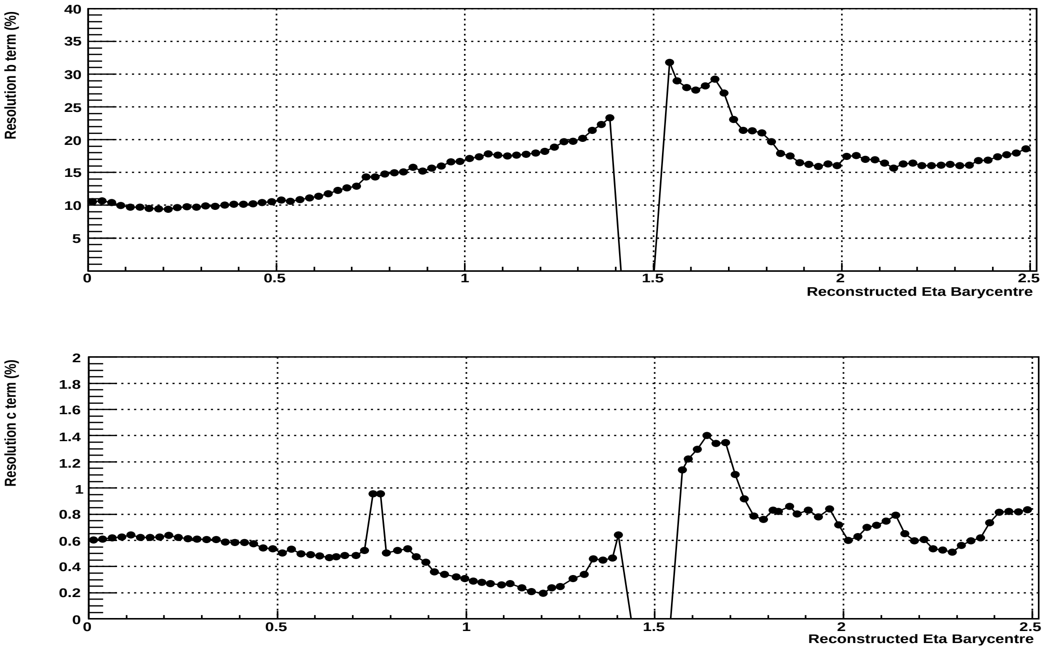

Figure 5.16: Sampling b (upper plot) and constant c (lower plot) term of the electron energy resolution.

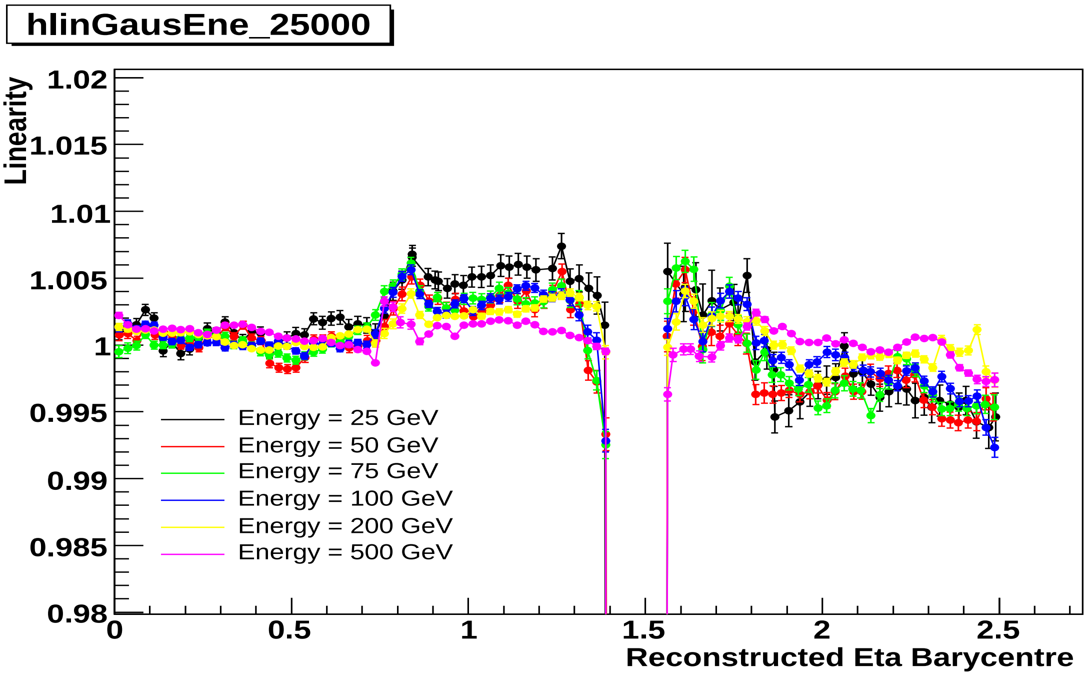

Figure 5.17: Electrons Linearity, for various energies .

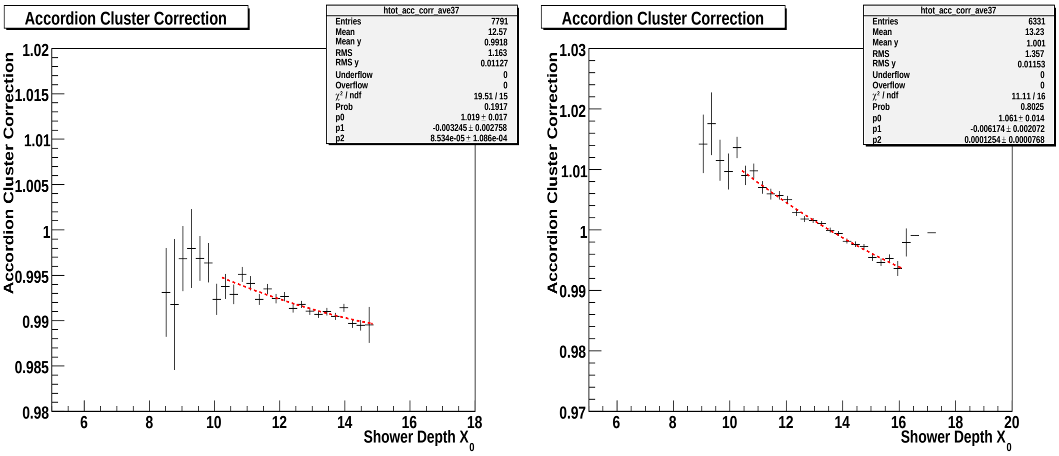

```
htot_acc_corr_ave37
Entries        7791
Mean           12.57
Mean y         0.9918
RMS            1.163
RMS y          0.01127
Underflow      0
Overflow       0
χ² / ndf       19.51 / 15
Prob           0.1917
p0             1.019 ± 0.017
p1             -0.003245 ± 0.002758
p2             8.534e-05 ± 1.086e-04
```

```
htot_acc_corr_ave37
Entries        6331
Mean           13.23
Mean y         1.001
RMS            1.357
RMS y          0.01153
Underflow      0
Overflow       0
χ² / ndf       11.11 / 16
Prob           0.8025
p0             1.061 ± 0.014
p1             -0.006174 ± 0.002072
p2             0.0001254 ± 0.0000768
```

(a) η=0.3 (b) η=1.2

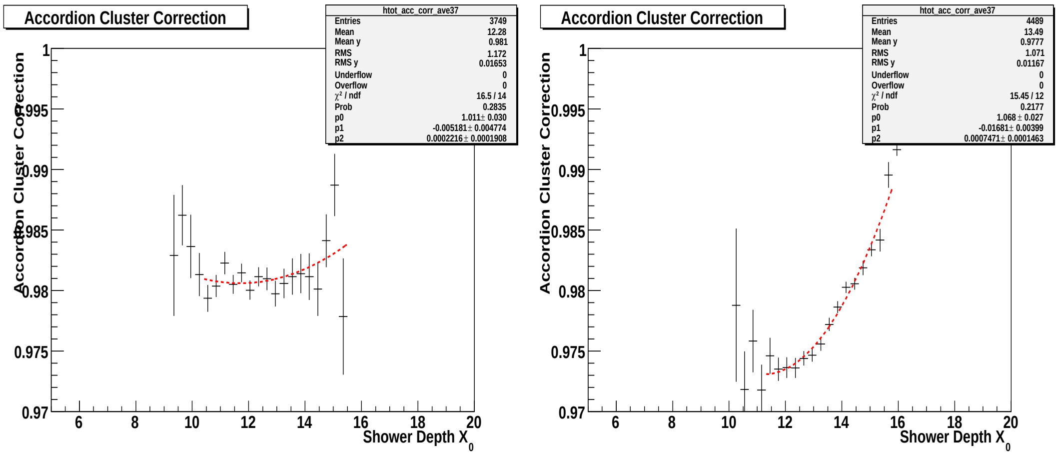

```
htot_acc_corr_ave37
Entries        3749
Mean           12.28
Mean y         0.981
RMS            1.172
RMS y          0.01653
Underflow      0
Overflow       0
χ² / ndf       16.5 / 14
Prob           0.2835
p0             1.011± 0.030
p1             -0.005181± 0.004774
p2             0.0002216 ± 0.0001908
```

```
htot_acc_corr_ave37
Entries        4489
Mean           13.49
Mean y         0.9777
RMS            1.071
RMS y          0.01167
Underflow      0
Overflow       0
χ² / ndf       15.45 / 12
Prob           0.2177
p0             1.068 ± 0.027
p1             -0.01681± 0.00399
p2             0.0007471± 0.0001463
```

(c) η=1.65 (d) η=2.0

Figure 5.18: Accordion cluster correction factor for photons, 4 η points. A cluster size of 3×7 is shown in this figures.

5.2 Photon energy reconstruction

5.2.1 Energy reconstruction in the Accordion

The correction for the energy deposited inside the accordion cluster is parametrized as a function of the longitudinal barycenter of the shower, as for the electrons, and is shown in figure (5.18) at four η points. The red dashed line is the results of the parametrization.

The energy deposited outside the cluster is parametrized as a function of the longitudinal barycenter as for electrons, as shown in figure (5.19).

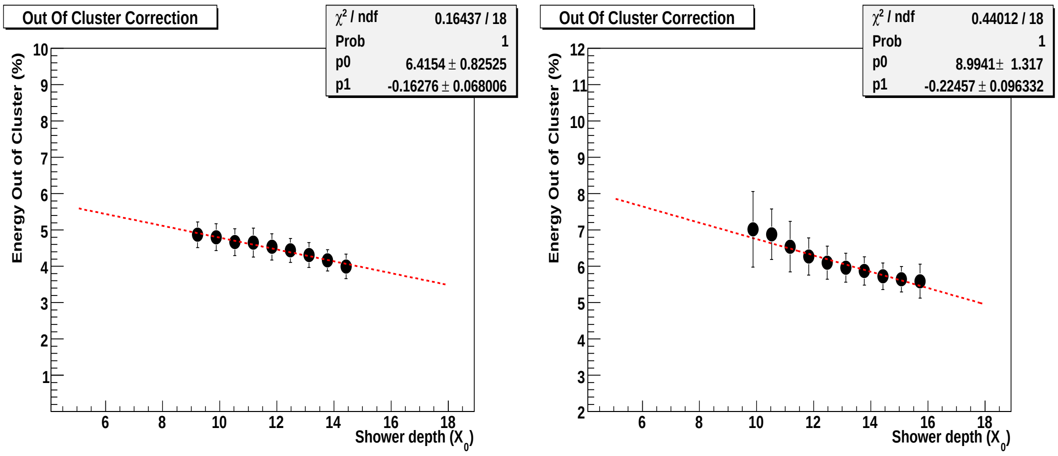

(a) η=0.3 (b) η=1.2

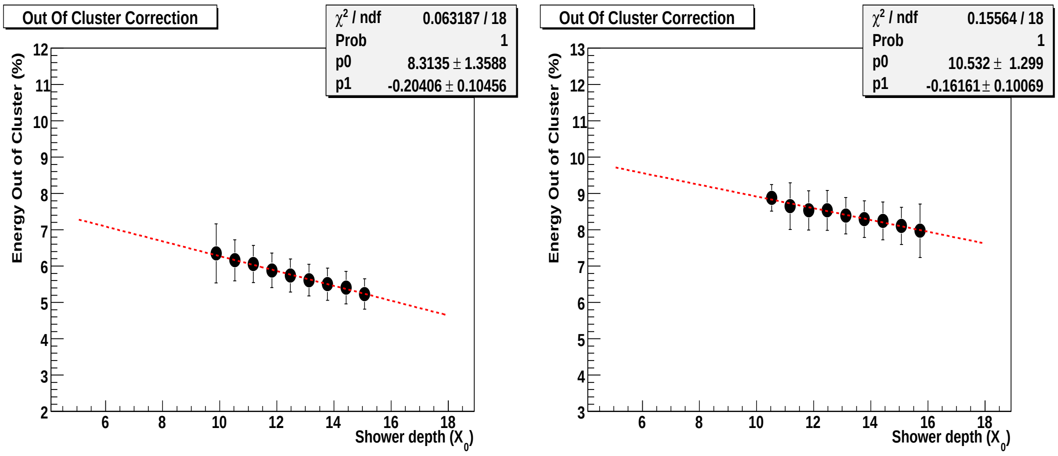

(c) η=1.65 (d) η=2.0

Figure 5.19: Fraction of energy deposited by photons out of the cluster, for a 3×7 cluster size, for 4 η points. The red dashed line is the adopted parametrization.

5.2.2 Calculation of the energy deposited in front of the Accordion

For the reconstruction of the energy deposited in front of the calorimeter by photons the same calibration scheme adopted for electrons is used. We treat as a photon a particle that gives an EM cluster in the electromagnetic calorimeter without an associated track in the tracking system. A photon that converts in the firsts layers of the tracker (early conversion) and has an associated reconstructed track is therefore classified and calibrated as an electron. All the photons that don't have an associated reconstructed track in the tracking system are analyzed together, independently from the fact that they convert or not. The performances of the calibration method could be improved in the future providing dedicated sets of calibration coefficients for the converted photons as a function of the conversion radius, but the available statistic does not allow this kind of studies.

As in the case of electrons the calorimeter is subdivided into three region, that will be discussed in the next.

Barrel Region ($0 \leq |\eta| < 1.425$)

In the barrel region the usual parametrization of the energy deposited in front of the calorimeter as a function of the energy deposited into the active layer of the PreSampler is adopted. In figure (5.20) the energy deposited by 100 GeV photons in front of the calorimeter as a function of the energy deposited in the PreSampler is shown, at two η points. A large fraction of events deposits in the PreShower a very small energy, differently from the electron case. This is due to the unconverted or lately converted photons which deposit a negligible amount of energy in the material in front of the calorimeter.

Figure (5.21) shows the energy dependence of the offset and slope, at two η points.

Endcap with the PreSampler ($1.55 \leq |\eta| < 1.8$)

In the region of the endcap with the PreSampler the parametrization as a function of the energy in the PreSampler is adopted, as in the barrel region. Two different populations are present: one population is constituted by the unconverted or lately converted photons, that loose very small energy in front of the calorimeter, and the other by the converted photons, that loose up to 25% of their energy in front of the calorimeter. The reduced available statistic forces us to treat this two different families as one, and the extracted parameters loose the physical meaning because they represent only a mean behaviours. This effect is clearly visible in this region due to the large amount of material present in front of the calorimeter, up to $\sim 6X_0$, which magnifies the different behaviour of the two families. Because of its strong correlation with the offset parameter, also the fitted slope shows “unphysical” behavior.

The usual energy parametrization of the computed parameters (offset and slope) is shown in figure (5.23), for η=1.65.

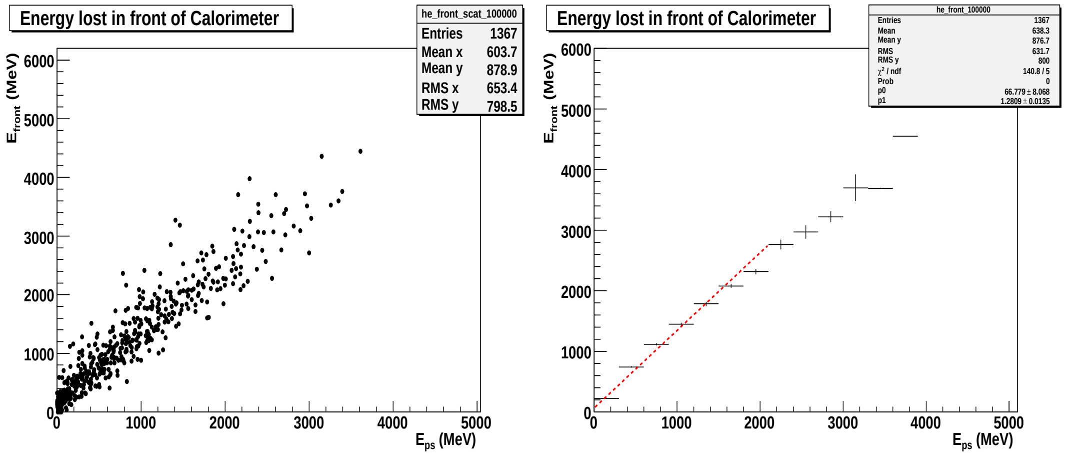

(a) η=0.3 (b) η=0.3

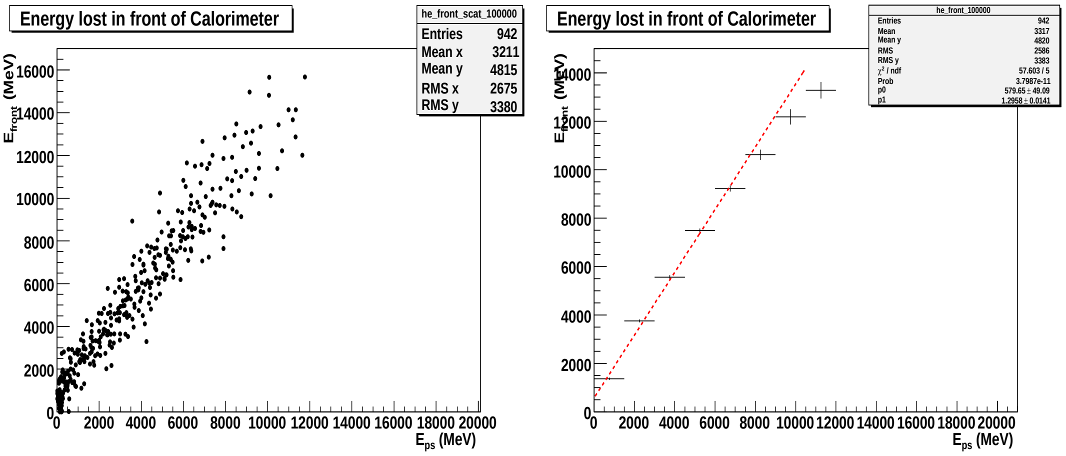

(c) η=1.2 (d) η=1.2

Figure 5.20: Energy deposited in front of the calorimeter by a 100 GeV photons, as a function of the energy deposited in the PreSampler.

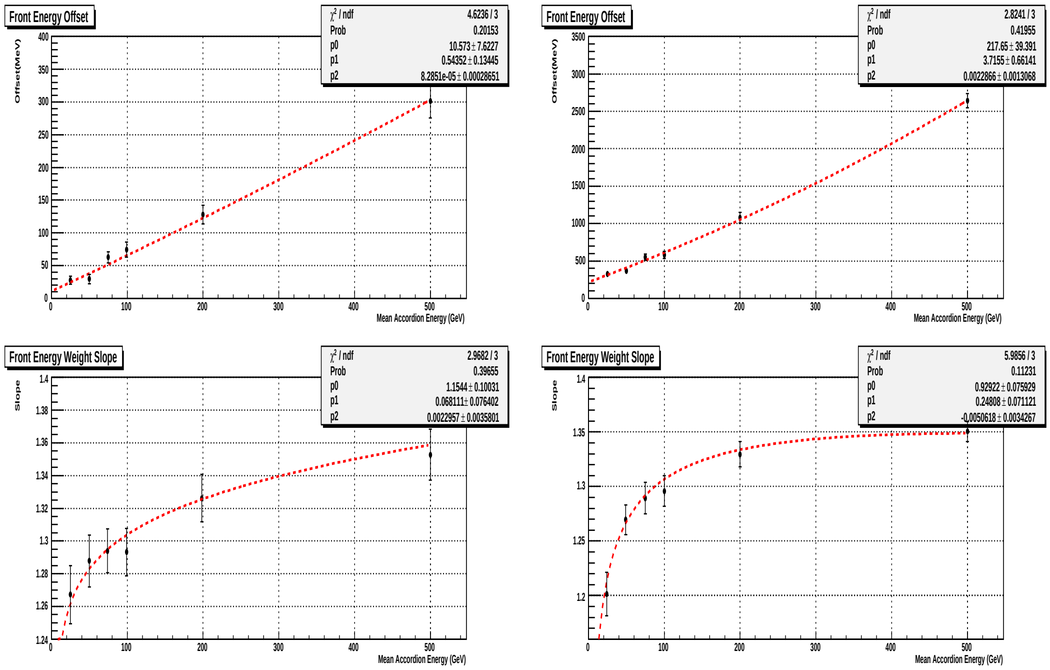

(a) η=0.3

(b) η=1.2

Figure 5.21: Energy dependence of offset and slope, at two η points.

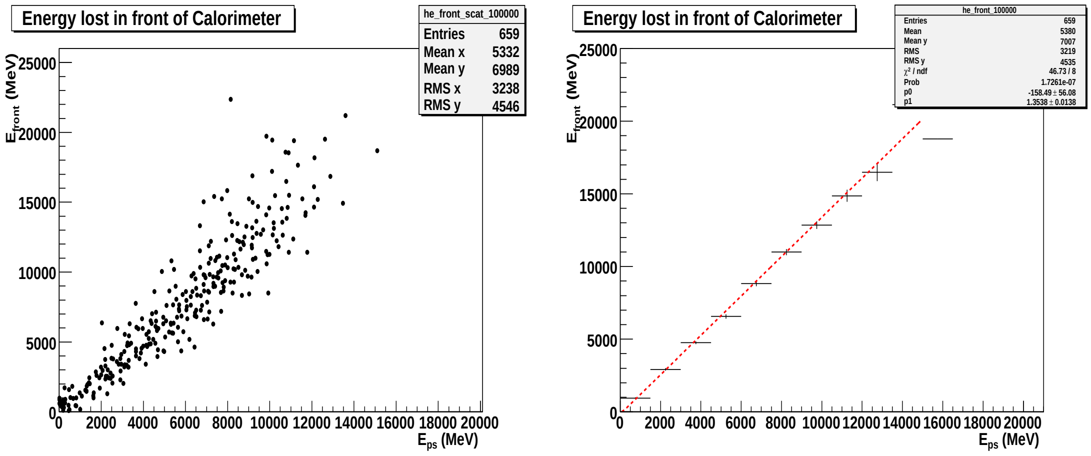

Figure 5.22: Energy deposited in front of the calorimeter by 100 GeV photons, as a function of the energy deposited into the PreSampler at η=1.65.

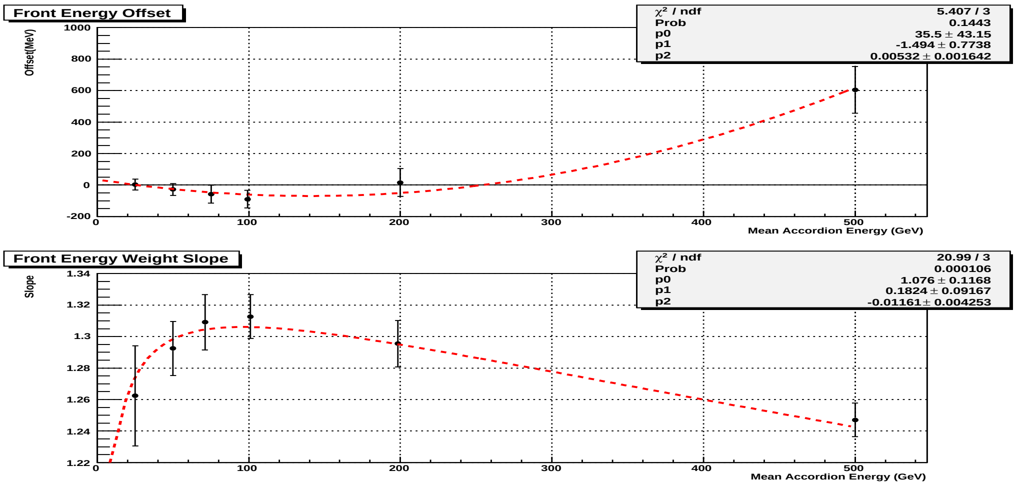

Figure 5.23: Energy dependence of the offset and slope parameters, at η=1.65.

Endcap without the PreSampler (1.8≤| η |<2.5)

In the region of the endcap without the PreSampler (η ≥1.8) the second degree polynomial parametrization of the energy deposited in front of the calorimeter as a function of the longitudinal barycenter is adopted, as shown in figure (5.24) at η=2.0 and 100 GeV photons. In figure (5.25) the energy parametrization of the three coefficients of the second degree polynomial is shown.

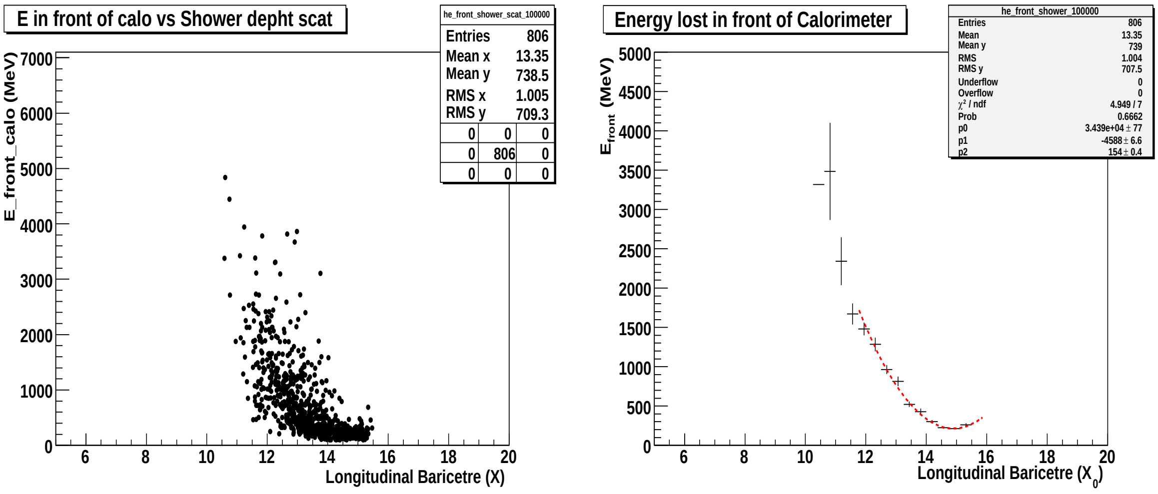

Figure 5.24: Energy deposited in front of the calorimeter by 100 GeV photons, as a function of the longitudinal barycenter at η=2.0.

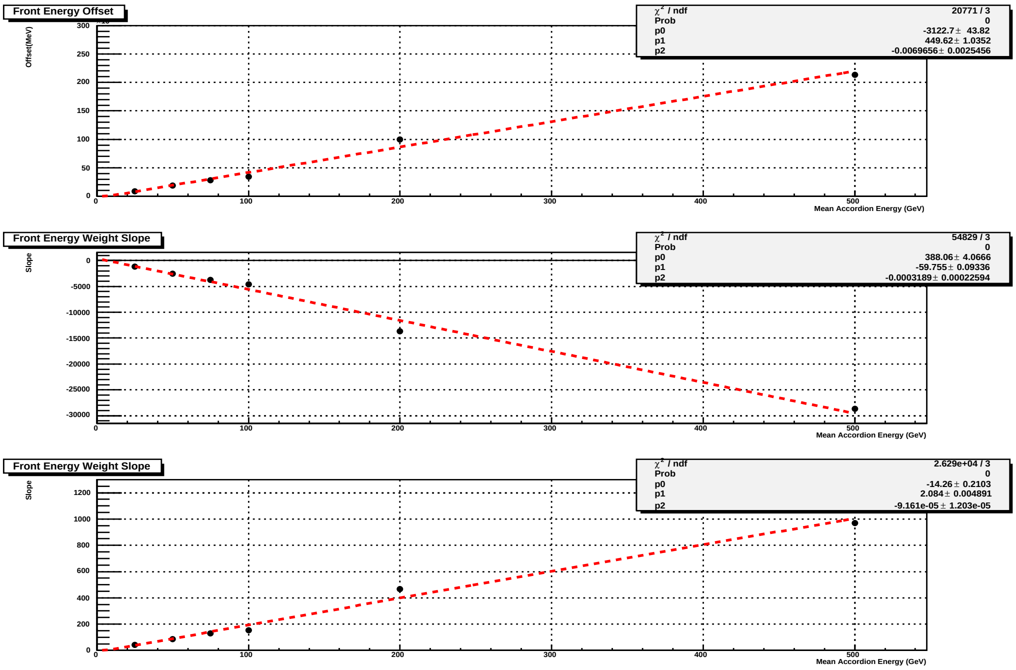

Figure 5.25: Energy dependence of the offset and slope parameters, at η=2.0.

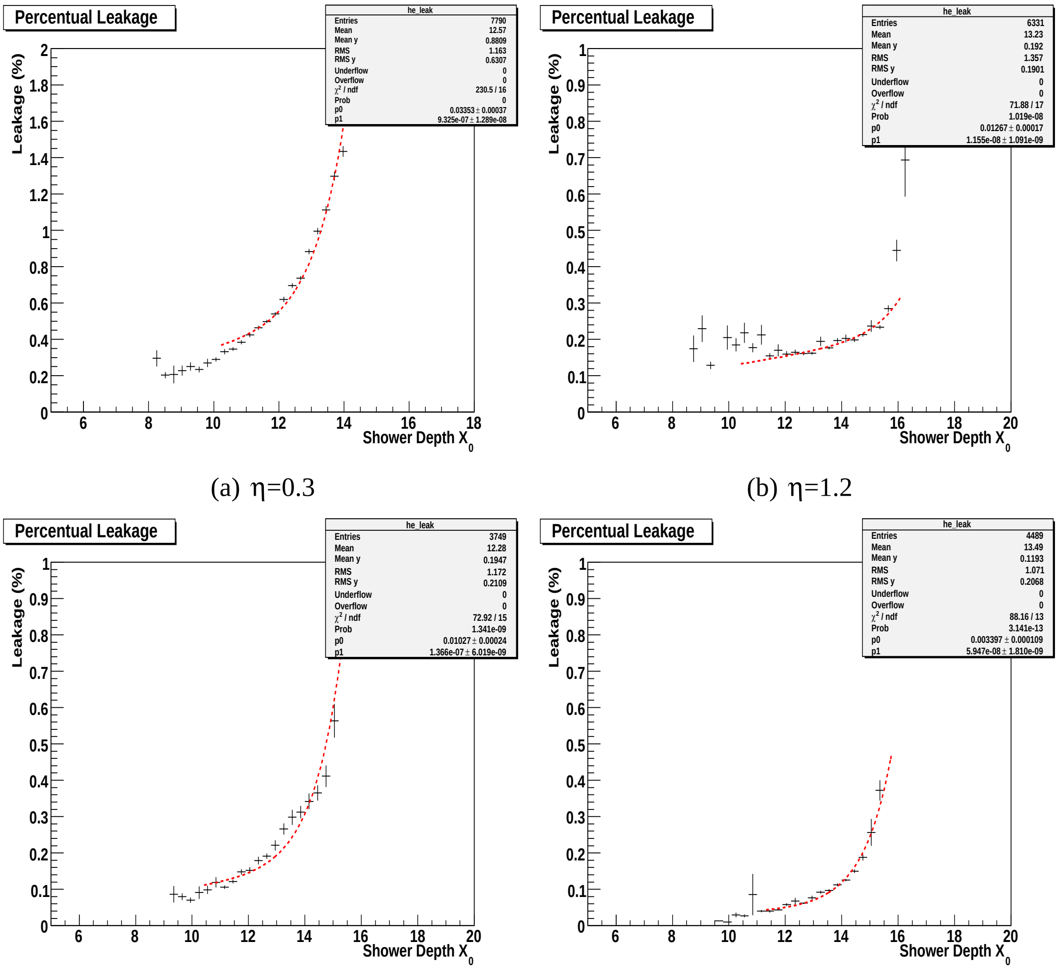

(a) η=0.3

(b) η=1.2

(c) η=1.65

(d) η=2.0

Figure 5.26: Energy deposited behind the calorimeter as a function of the longitudinal barycenter, for 4 η points and energy averaged.

5.2.3 Calculation of the energy deposited behind the Accordion

The energy deposited behind accordion is parametrized as a function of the longitudinal barycenter of the shower, and is shown in figure (5.26) for four η points.

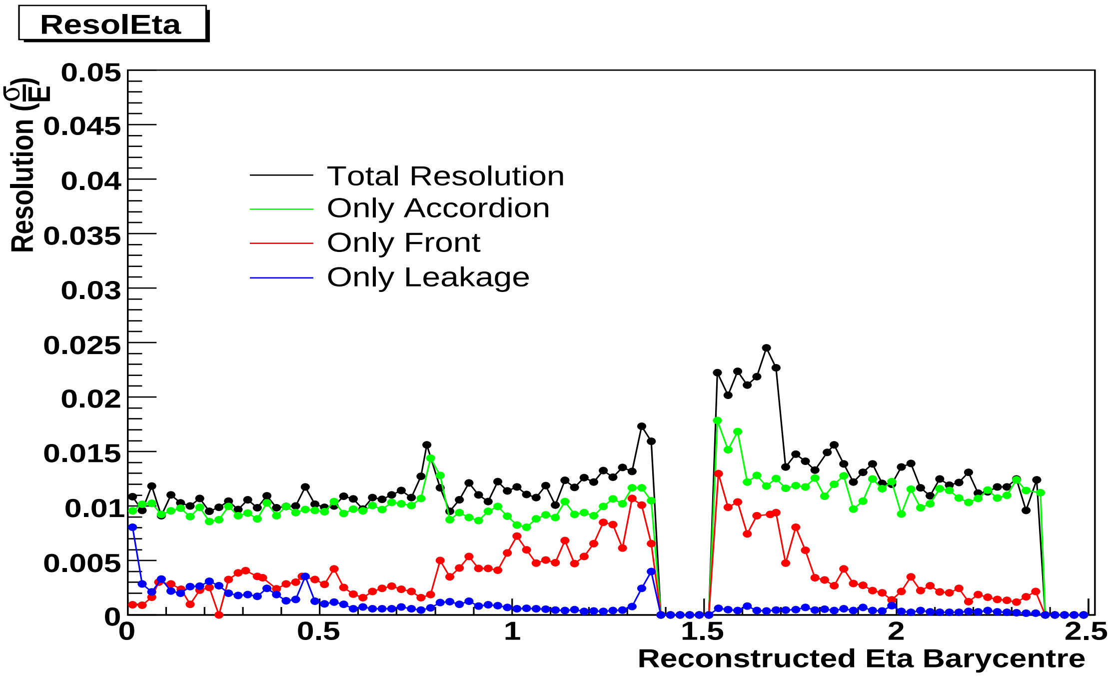

Figure 5.27: Photon resolution (σ/E) for 100 GeV photons. The total resolution is shown in black, the contribution to total resolution of the front, accordion and leakage energy reconstruction are shown respectively in red, green and blue.

5.2.4 Resolution and linearity

The achieved energy resolution for 100 GeV photons is shown in figure (5.27). In black the resolution (σ/E) when all the energy is reconstructed with the proposed method is shown; in green the resolution achieved when only the energy deposited in the accordion is reconstructed, and all the others energies are taken from the Monte Carlo simulation, is shown. Finally, in red and in blue the resolution achieved when only the energy deposited in front and behind the calorimeter is reconstructed is shown. In the case of photons the dominant contribution to the total resolution, over all the η range, comes from the accordion energy reconstruction.

In figure (5.28) the energy resolution for all the different energies is shown. Figure (5.29) shows the sampling term b and the constant term c of the energy resolution, fitted with the usual $\frac{\sigma}{E}(\%) = \frac{b(\%)}{\sqrt{E(GeV)}} \oplus c(\%)$. The sampling term b of the resolution goes from ∼9% of the central barrel region to the ∼20% near the crack region between barrel and endcap. In the endcap it is aroud ∼25% in the region with the PreSampler and ∼15% in the region without. The constant term c is different from zero since we don't apply any correction for the impact point, for the same reasons explained for electrons.

In figure (5.30) the linearity for photons of all the available energies is shown.

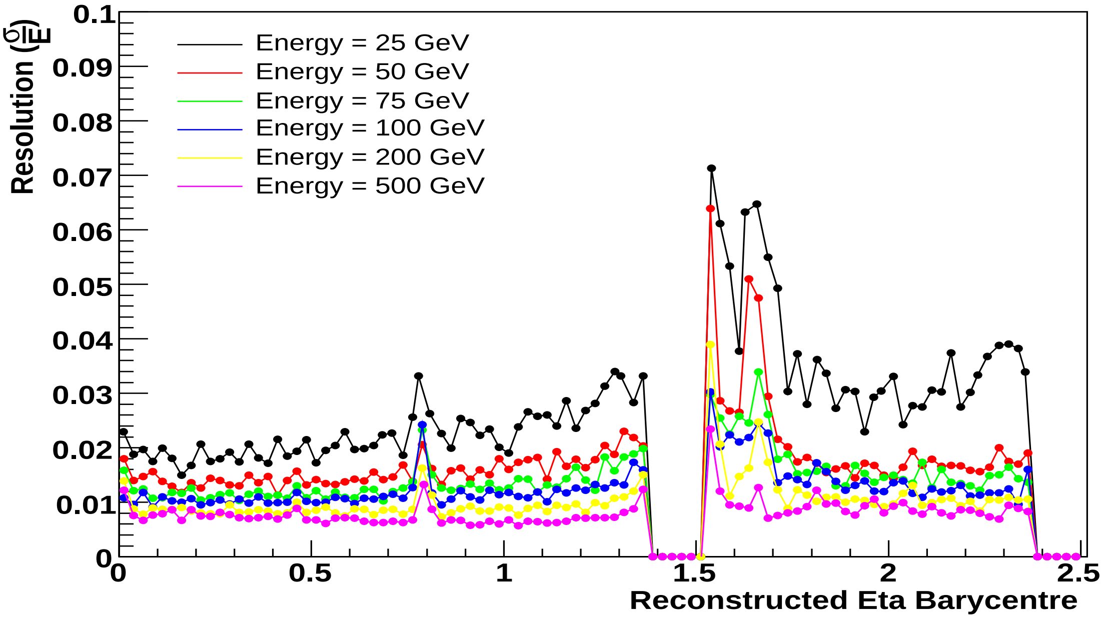

Figure 5.28: Photon energy resolution (σ/E), for various energies .

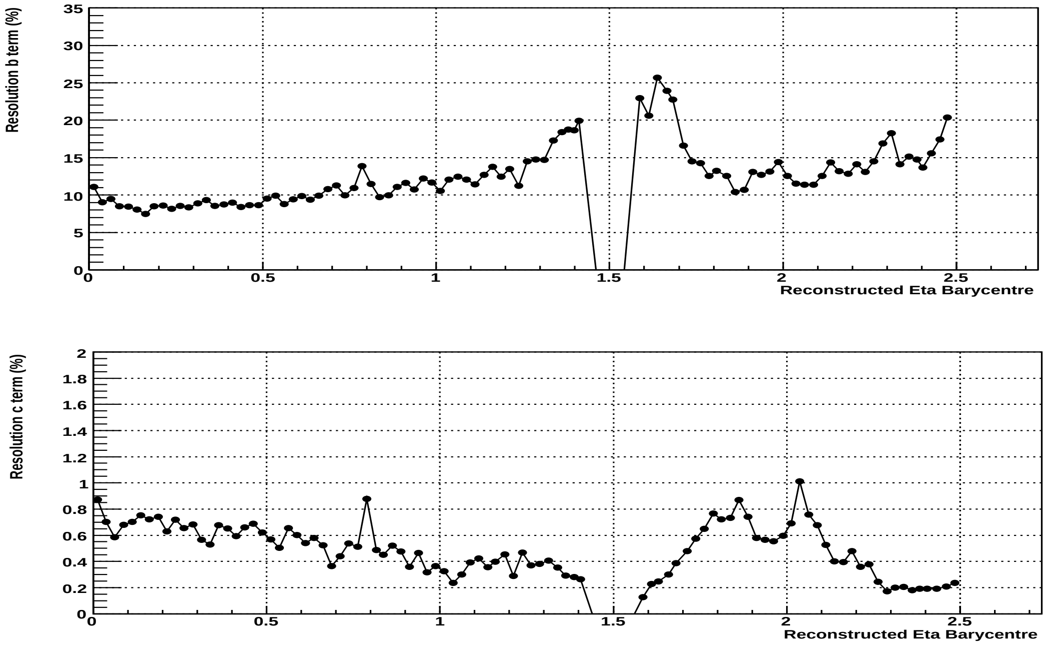

Figure 5.29: Sampling b (upper plot) and constant c (lower plot) term of photon energy resolution.

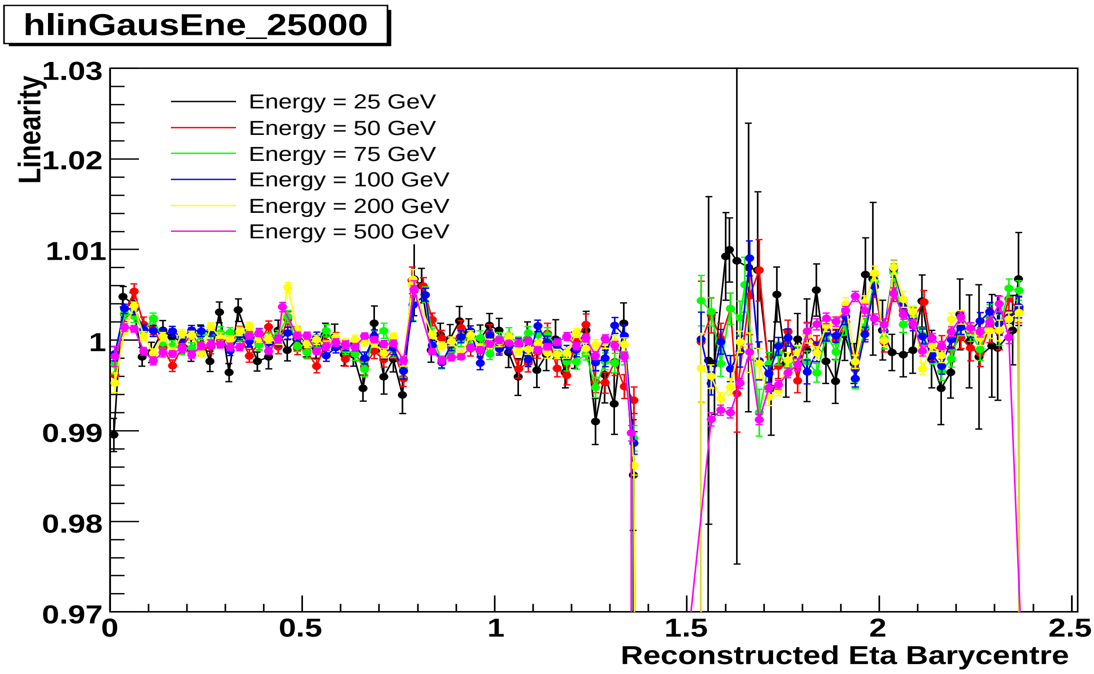

Figure 5.30: Photon Linearity for various energies .

The linearity is within 0.5% almost on all the detector, some fluctuations are visible for lower energies and at higher η points, due to the already mentioned statistical problems.

5.3 Electron-photon comparison

In these section we will investigate the differences between the behavior of photons and electrons [32], in order to understand if some calibration coefficients can be common to both particle types.

5.3.1 Calibration coefficients

In figure (5.31(a)) the accordion cluster correction factor for electrons and photons and the adopted parametrization, at η=0.3, are shown. The behavior of electrons and photons inside the accordion and in the cluster is very similar, and we propose to use a single set of calibration coefficients for both samples.

In figure (5.31(b)) the correction for the energy deposited outside the cluster is shown at η=0.3 : e^- and γ have also similar behavior. This happen only in the barrel region, as visible in figure (5.33), where the extracted coefficients for the out of cluster correction are shown for all the calorimeter cells. We use therefore two different sets of coefficients for electrons and photons.

In figures (5.31(c)) and (5.31(d)) the energy dependence of the front parameters and the longitudinal leakage parameters are shown, both for e^- and γ, which are expected to be very different.

The cluster size and particle type dependencies of the calibration coefficients are summarized in table (5.2).

Coefficient Type	**Cluster Dependent**	**Cluster Independent**	**Common e^-/γ**	**Different e^-/γ**
Front		√		√
Accordion	√		√	
Out of Cluster	√			√
Leakage		√		√

Table 5.2: Cluster size and particle type dependencies of the calibration coefficients

To reconstruct the energy deposited in front of calorimeter, 6 or 9 ($|\eta| \leq 1.8$ or $|\eta| > 1.8$) parameters are needed. To reconstruct the energy deposited in the accordion cluster 3 parameters are needed, and others 2 parameters are needed for the energy deposited out of the cluster. Only two parameters are needed to reconstruct the energy deposited behind the accordion.

For reconstruct the total energy of a particle 13 or 16 ($|\eta| \leq 1.8$ or $|\eta| > 1.8$) parameters are needed. Taking into account the cluster and particle type dependencies of the calibration coefficients 37 or 43 ($|\eta| \leq 1.8$ or $|\eta| > 1.8$) parameters are needed to calibrate electrons and photons with 3 cluster sizes, as summarized in table (5.3). For comparison, the calibration methods based on the longitudinal weigths needs 4

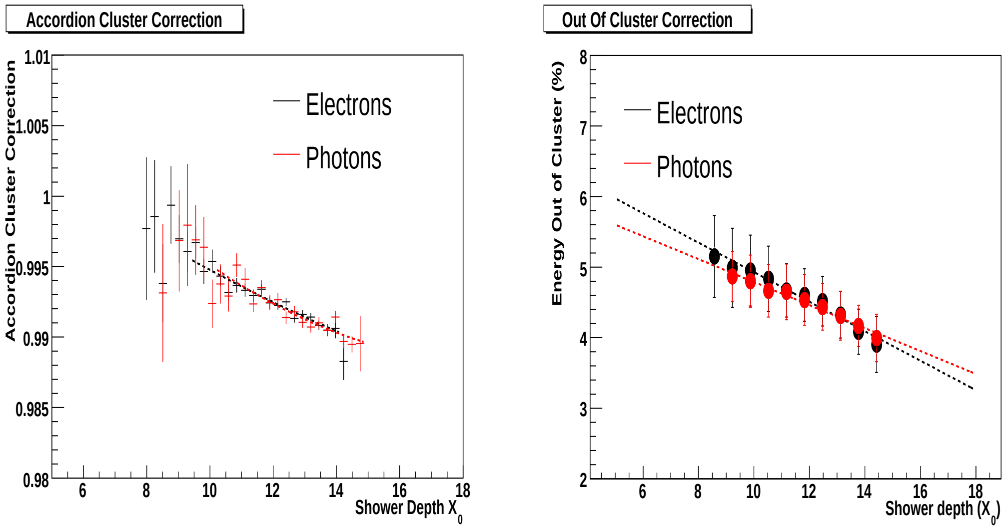

(a) Accordion Cluster Correction (b) Out of cluster correction

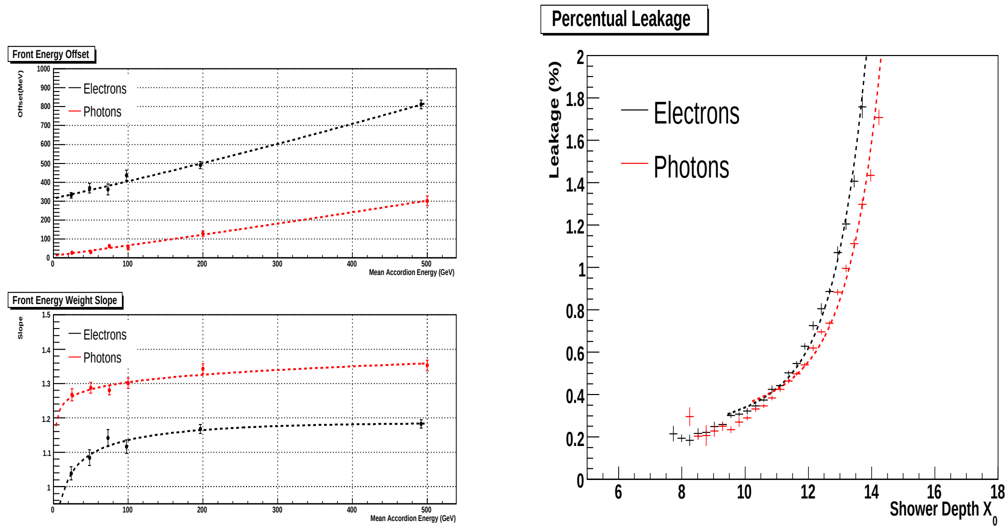

(c) Front Energy correction (d) Longitudinal leakage

Figure 5.31: Comparison between the correction for electrons (black) and photons (red), at η=0.3

parameters for each particle type and each cluster size, for a total of $4 \times 2 \times 3 = 24$ parameters, from 13 to 19 parameters less than the calibration hits methods.

5.3.2 η dependence of parameters

As said before, a set of calibration parameters must be provided for each cell of the calorimeter: the parameters achieved with the described method will be shown and discussed in this section. In black the electron parameters will be shown, while in red

Coefficient	**N**		**e^-/γ**	**CL**	**Total**	
	$\vert\eta\vert\leq 1.8$	$\vert\eta\vert > 1.8$			$\vert\eta\vert\leq 1.8$	$\vert\eta\vert > 1.8$
Front	6	9	×2	×1	12	18
Accordion	3		×1	×3	9	
Out of Cluster	2		×2	×3	12	
Leakage	2		×2	×1	4	
Total Energy	13	16			37	43

Table 5.3: Number of calibration coefficients

the photon ones.

Figure (5.32) shows the 3 parameters for reconstructing the energy deposited into the accordion cluster, starting from the energy deposited into the active layer of the accordion. They vary smoothly all over the η range, including the EndCap region, reflecting the uniformity of the response of the calorimeter. Electrons and photons show similar behavior and we will use one set of calibration parameters. The transition between the two regions of the barrel calorimeter with different thickness of the absorber gives the disuniformity at η=0.8.

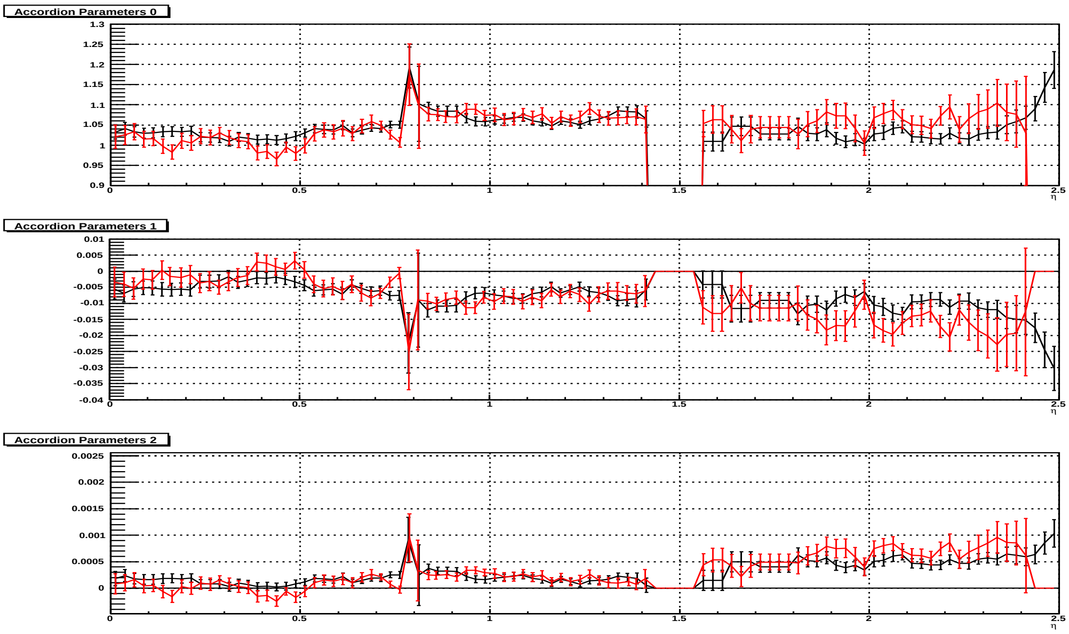

Figure 5.32: Cluster accordion correction parameters, for electrons (black) and photons (red) .

In figure (5.33) the parameters for the reconstruction of the energy deposited outside the cluster are shown. The sharp transition at η=0.8 is due to the variation of the lead absorber thickness that influences the lateral development of the shower and consequently the energy sharing between the reconstructed cluster and the cells outside the cluster.

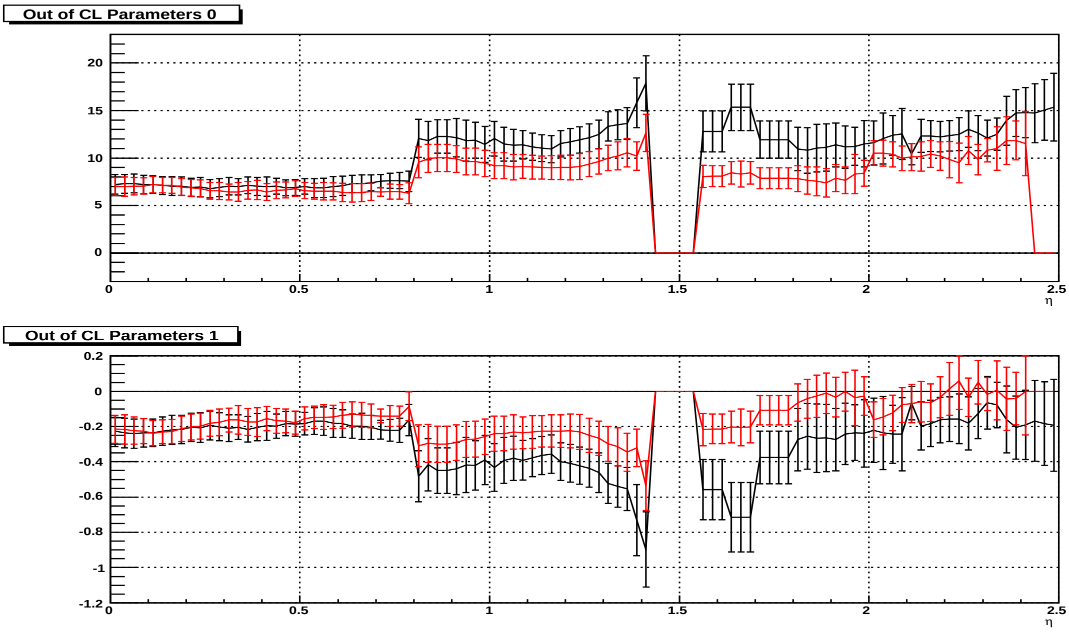

Figure 5.33: Out of Cluster Parameters, for electrons (black) and photons (red)

Figure (5.34) shows the parameters for the correction for the longitudinal leakage. They decrease in the barrel region, accordingly to the variation of the total thickness of the calorimeter, and stay small in the endcap region, where the total thickness of the calorimeter (up to $40X_0$) makes the correction for the energy deposited behind the accordion negligible.

Figures (5.35) and (5.36) show respectively the parameters for the reconstruction of the front offset and slope parameters in the region of calorimeter with the PreSampler $0 \leq |\eta| < 1.8$. It is possible to see that the parameters vary smoothly in the barrel region, but more sharply in the endcap region, reflecting the sharp variation of the material upstream calorimeter.

In figures (5.37), (5.38) and (5.39) the coefficients for reconstructing the first, second and third degree parameter for the shower depth parametrization of the energy deposited in front of the calorimeter in the region without the PreSampler, $1.8 \leq |\eta| < 2.5$, are shown. The limited statistics (up to 60% of events are rejected by the calorimeter cuts) is responsible for the seen fluctuations. More statistic is needed to achieve better parameters.

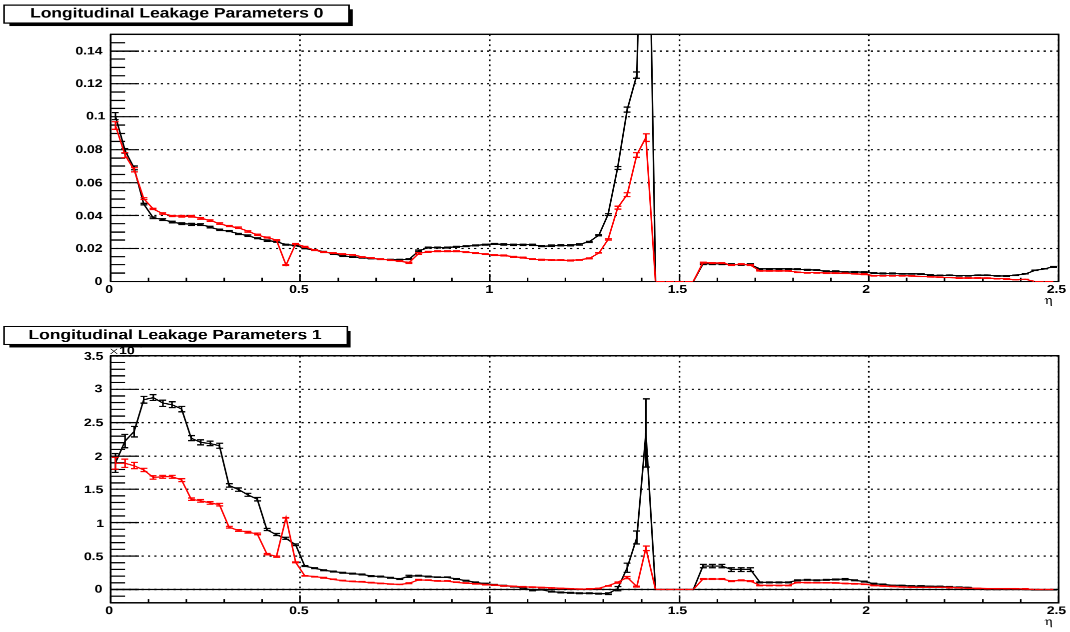

Figure 5.34: Longitudinal leakage parameters, for electrons (black) and photons (red)

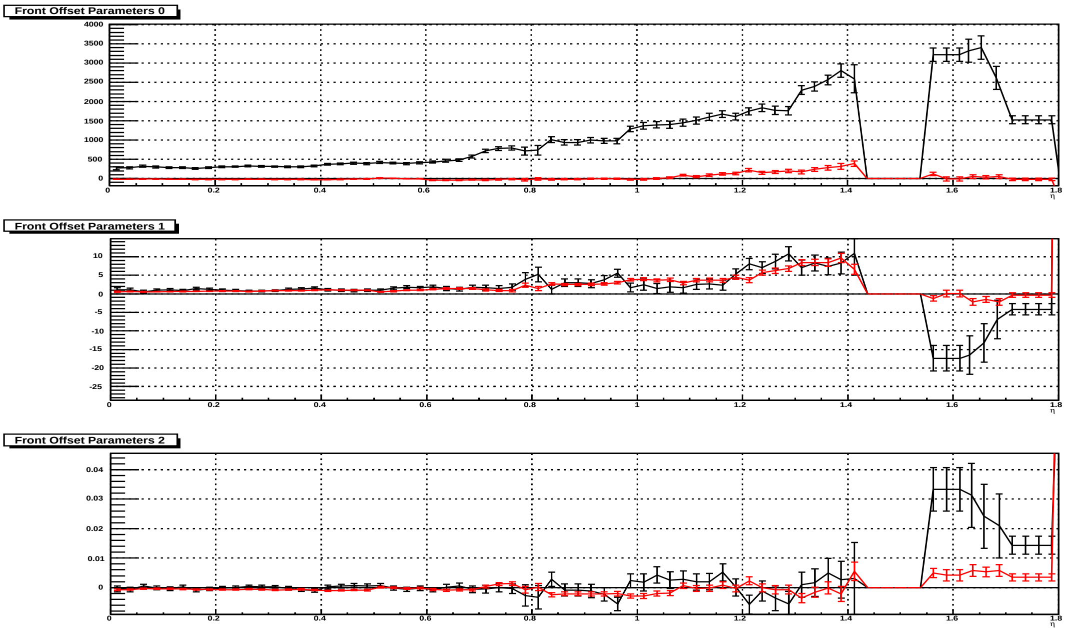

Figure 5.35: Coefficients for the front offset energy parametrization, $0<|\eta|<1.8$, for electrons (black) and photons (red)

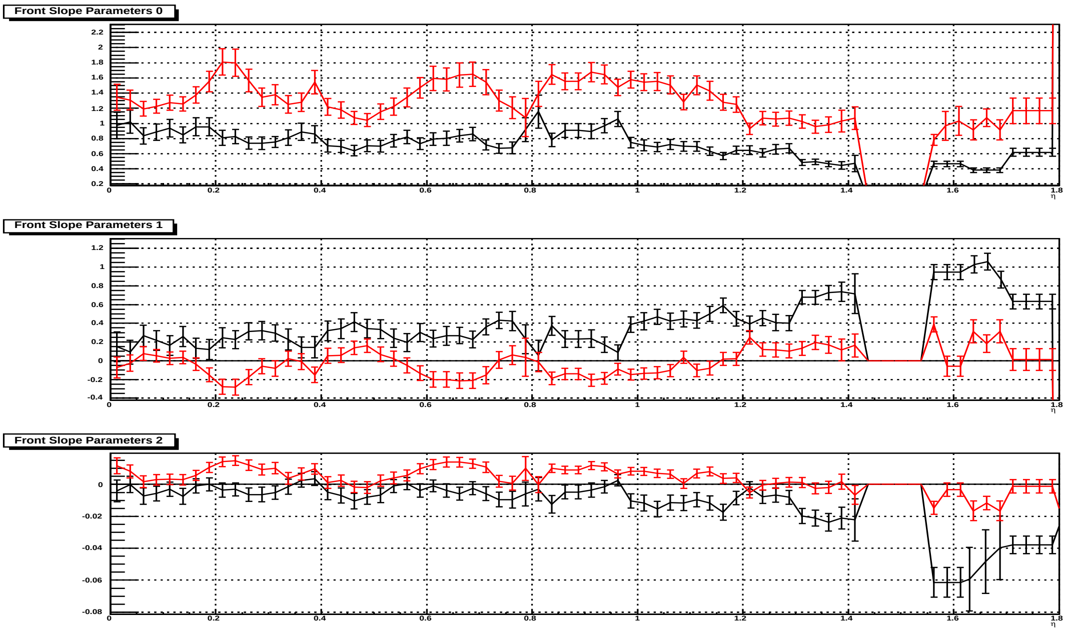

Figure 5.36: Coefficients for the front slope energy parametrization , 0<| η |<1.8, for electrons (black) and photons (red)

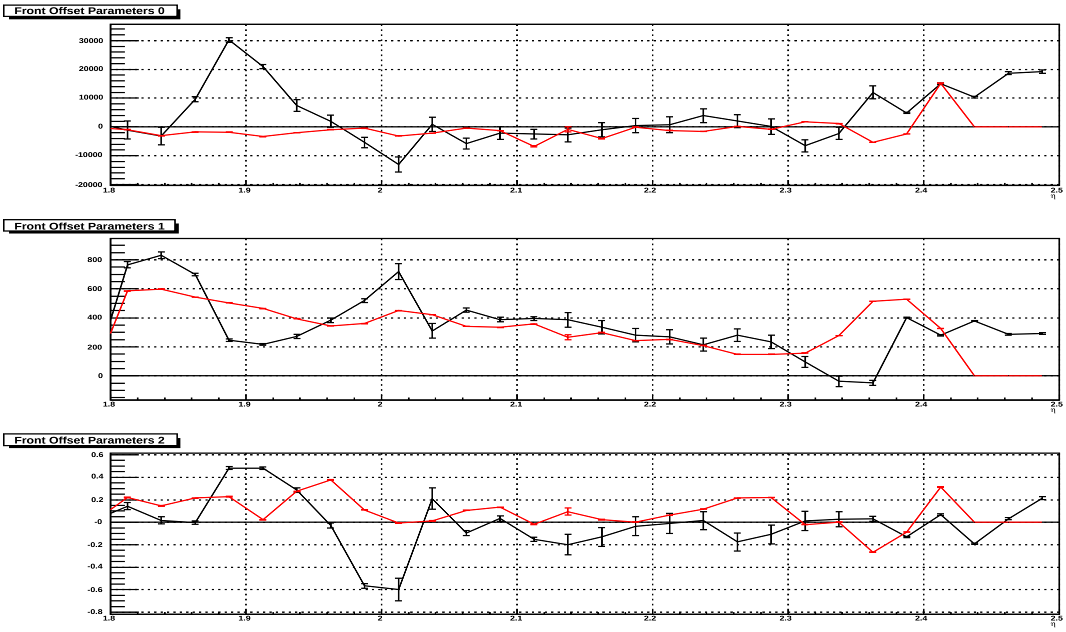

Figure 5.37: Parameters for the offset coefficient energy parametrization, 1.8<| η |<2.5, for electrons (black) and photons (red)

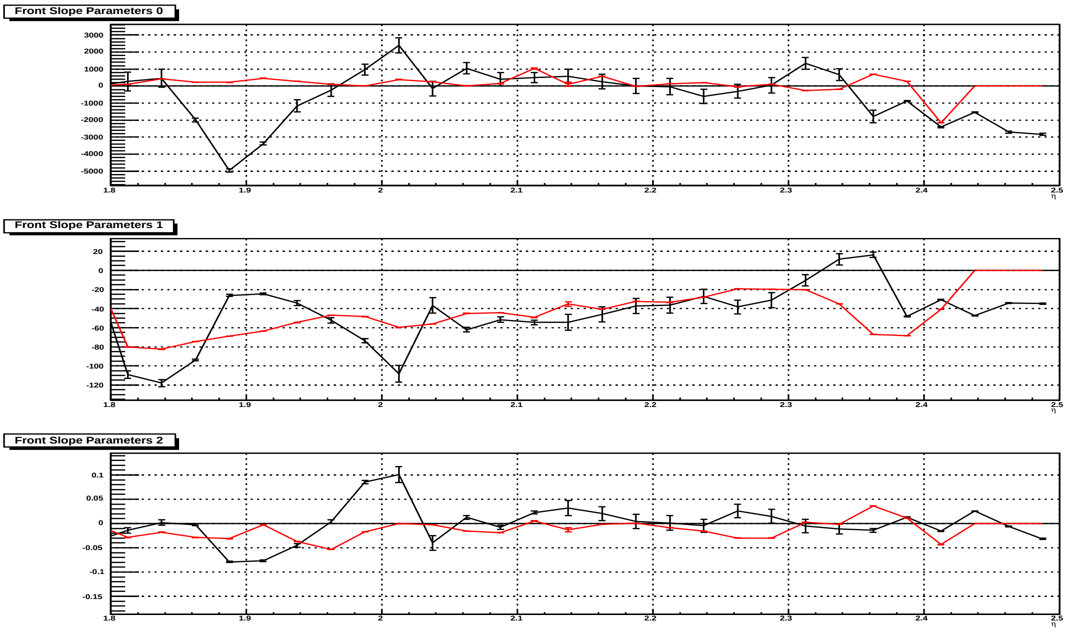

Figure 5.38: Parameters for the first degree coefficient energy parametrization, $1.8<|\eta|<2.5$, for electrons (black) and photons (red)

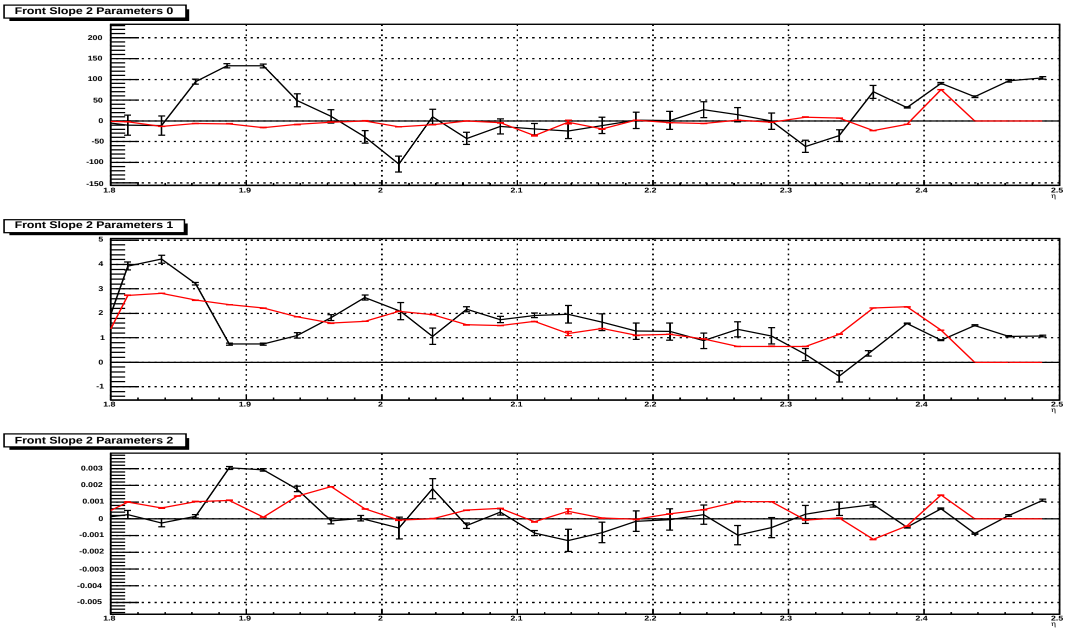

Figure 5.39: Parameters for the second degree coefficient energy parametrization, $1.8<|\eta|<2.5$, for electrons (black) and photons (red)

5.4 Athena package

The proposed method has been included into Athena: it has been implemented as a *CaloClusterCorrection* and all the calibration coefficients, computed as explained in the previous sections, are in the python file named *CaloSwCalibHitsCalibration_v1.py*, containing six different sets of coefficients:

1. CaloSwCalHitsAccordion_v1_XX : corrections for the energy deposited into the accordion in the cluster
2. CaloSWCalHitsOutOfCone_v1_eleXX : corrections for the energy deposited into the accordion out of the reconstructed cluster
3. CaloSWCalHitsLongLeakage_v1_ele : corrections for the energy deposited behind the accordion
4. CaloSWCalHitsEfront_offset_v1_ele : corrections for the energy deposited in front of the calorimeter, offset coefficients
5. CaloSWCalHitsEfront_slope_v1_ele : corrections for the energy deposited in front of the calorimeter, slope coefficients
6. CaloSWCalHitsEfront_P2_v1_ele : corrections for the energy deposited in front of the calorimeter, second degree polynomial parameters for the shower depth parametrization, only for $\eta > 1.8$.

The “XX” in the name of correction stays for the cluster size, while the suffix “ele” stays for electron and will be replaced with “pho” in the photon calibration file. Accordingly with table (5.2), all the corrections with the only exception of number 1 are particle type dependent, and the first two correction are the only cluster size dependent.

5.4.1 Results with the full Athena Reconstruction

We reconstruct all the available samples of electrons and photons running the official Athena reconstruction code, and using both calibration methods, to compare the performances.

The Calibration Hits parameters for the barrel region are computed from the Milan group, while the coefficients for the endcap are provided by the Madrid group: all the parameters (computed as explained in the previous sections), and consequently the method performances, must be taken as preliminary.

In the present Athena implementation of the code for Calibration Hit analysis we can only make use of the calorimeter cuts to clean the sample, because the identification cuts based on the tracker informations are not yet available. For this reason a more severe set of calorimeter cuts were applied to the samples giving rise to some statistical problems that force us to give the results, both resolution and linearity, only for groups of 4 cells, and not cell by cell as in the previous analysis.

In the next plots the result achieved using the calibration method based on longitudinal weights are shown in black, while the ones with the Calibration Hit based method are shown in red.

The reconstructed energy distributions achieved for 100 GeV electrons running the full Athena reconstruction code are shown, as an example, in figures (5.40) and (5.41), for η bins of $\Delta\eta$ =0.1. The energy profiles shapes are very similar using both calibration methods, and the fitted mean values show maximum differences in the order of 3÷4 per mille over all the η range. Similar results are achieved for the others available energies.

The sampling term b and the constant term c of the energy resolution, fitted with the usual $\frac{\sigma(E)}{E}(\%) = \frac{b(\%)}{\sqrt{E(GeV)}} + c(\%)$, are shown in figure (5.42). The two calibration methods provide similar results, both for the sampling and constant term. The sampling term b rise from the 10% in the barrel region to the 30% in the endcap region, as already discussed in the previous sections.

The linearity achieved with the two calibration methods is shown in figure (5.43), for all the various energies: is possible to see that the two methods give comparable results for energies lower than 100 GeV, while at higher energies the Calibration Hits based method gives a better reconstruction of the energy up to 1%.

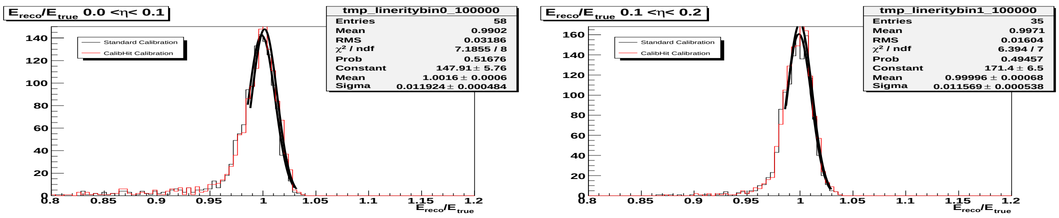

(a) 0≤ η <0.1

(b) 0.1≤ η <0.2

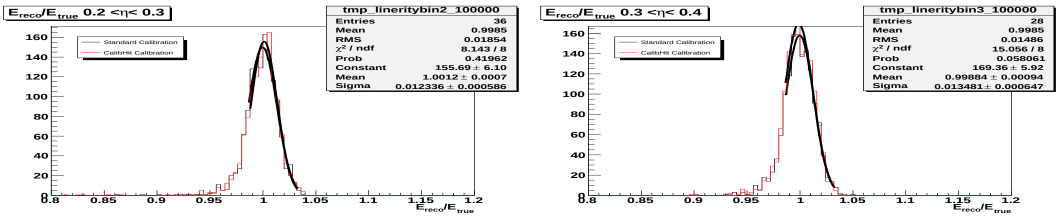

(c) 0.2≤ η <0.3

(d) 0.3≤ η <0.4

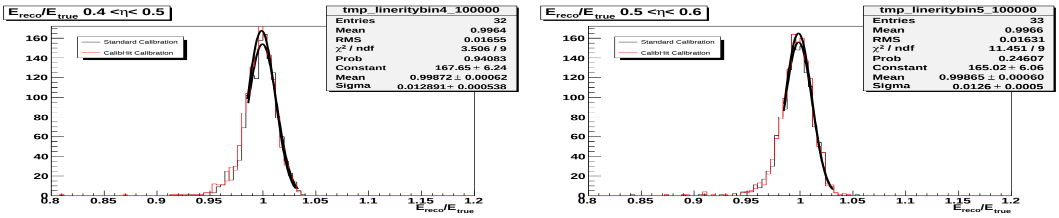

(e) 0.4≤ η <0.5

(f) 0.5≤ η <0.6

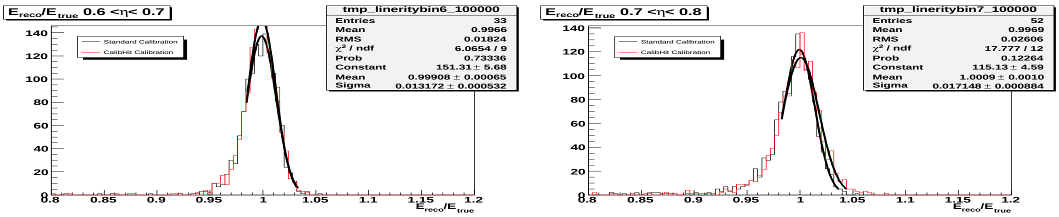

(g) 0.6≤ η <0.7

(h) 0.7≤ η <0.8

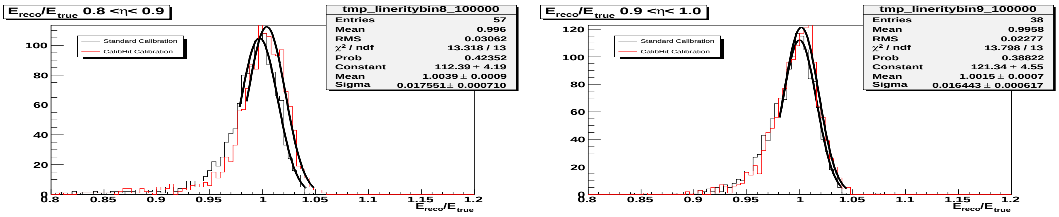

(i) 0.8≤ η <0.9

(j) 0.9≤ η <1.0

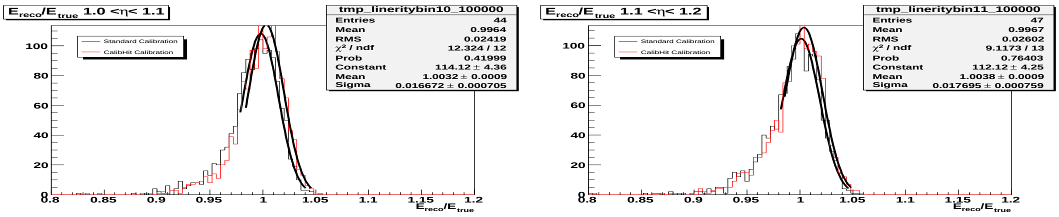

(k) 1.0≤ η <1.1

(l) 1.1≤ η <1.2

Figure 5.40: Reconstructed energy distributions for 100 GeV electrons, for η bins of Δη =0.1. In black are shown the results with longitudinal weight calibration, while in red the Calibration Hits results are shown.

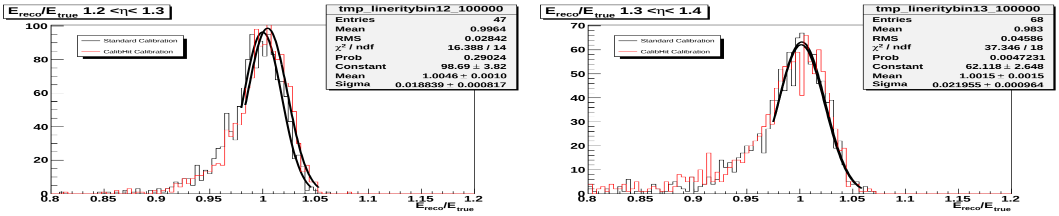

(a) 1.2≤ η <1.3 (b) 1.3≤ η <1.4

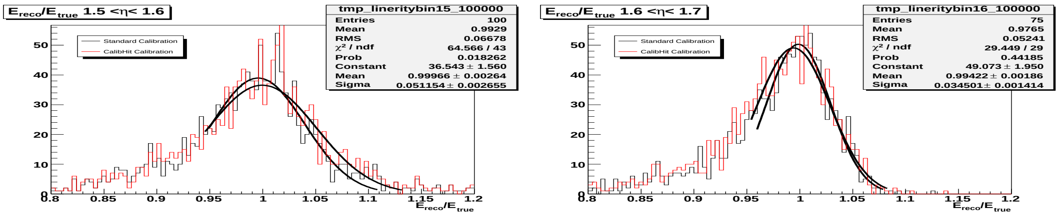

(c) 1.5≤ η <1.6 (d) 1.6≤ η <1.7

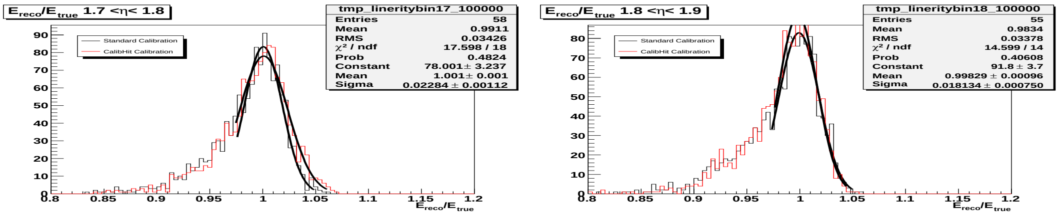

(e) 1.7≤ η <1.8 (f) 1.8≤ η <1.9

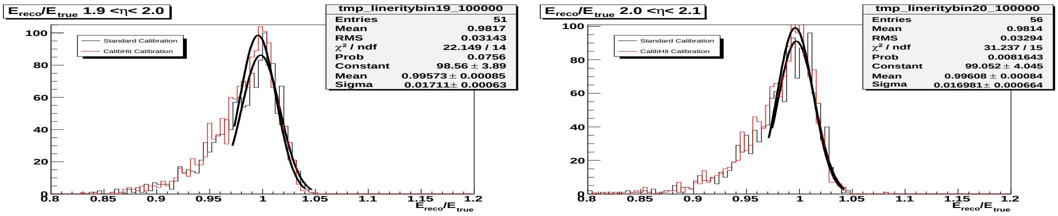

(g) 1.9≤ η <2.0 (h) 2.0≤ η <2.1

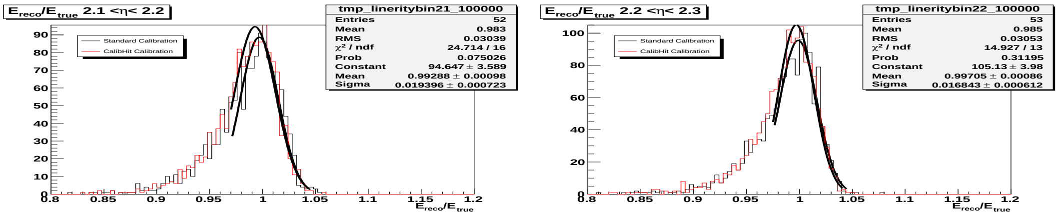

(i) 2.1≤ η <2.2 (j) 2.2≤ η <2.3

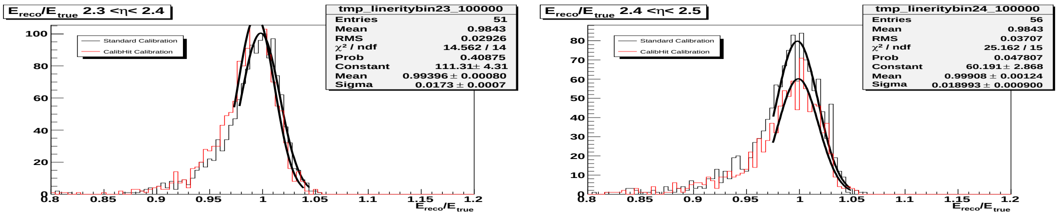

(k) 2.3≤ η <2.4 (l) 2.4≤ η <2.5

Figure 5.41: Reconstructed energy distributions for 100 GeV electrons, for η bins of Δη =0.1. In black are shown the results with longitudinal weight calibration, while in red the Calibration Hits results are shown

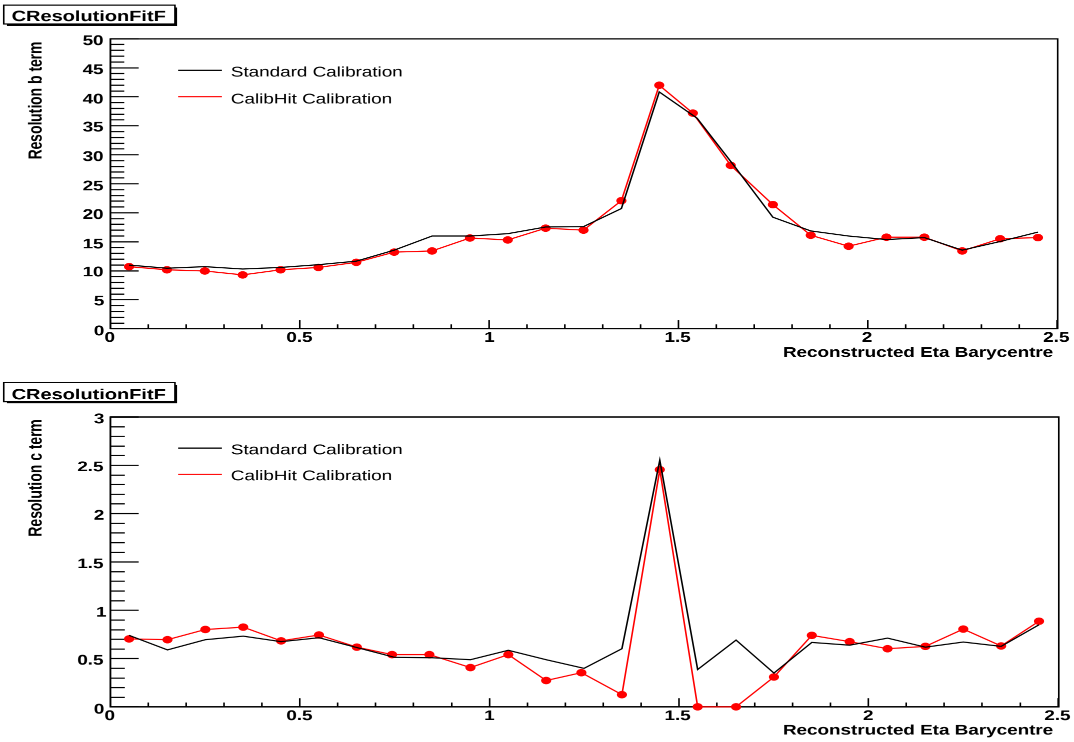

Figure 5.42: Resolution sampling term *b* and constant term *c*. In black are shown the results with longitudinal weight calibration, while in red the Calibration Hits results are shown

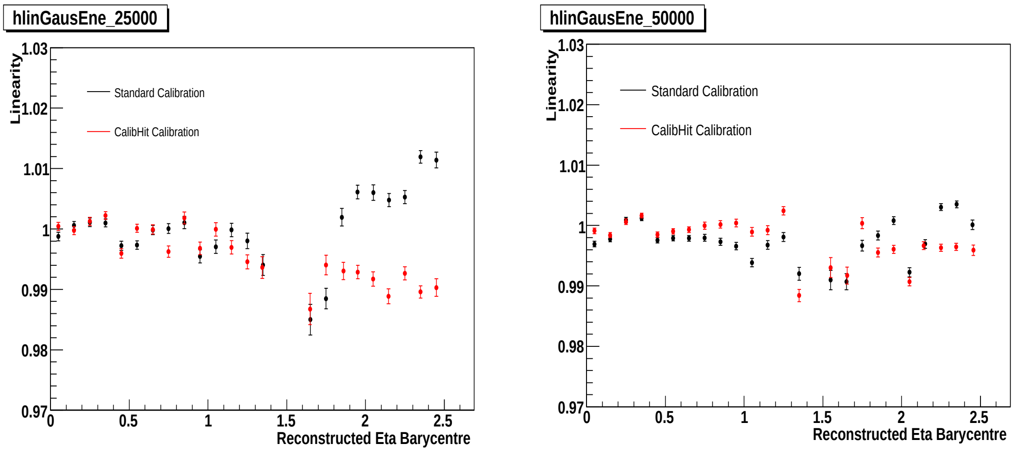

(a) E=25GeV (b) E=50GeV

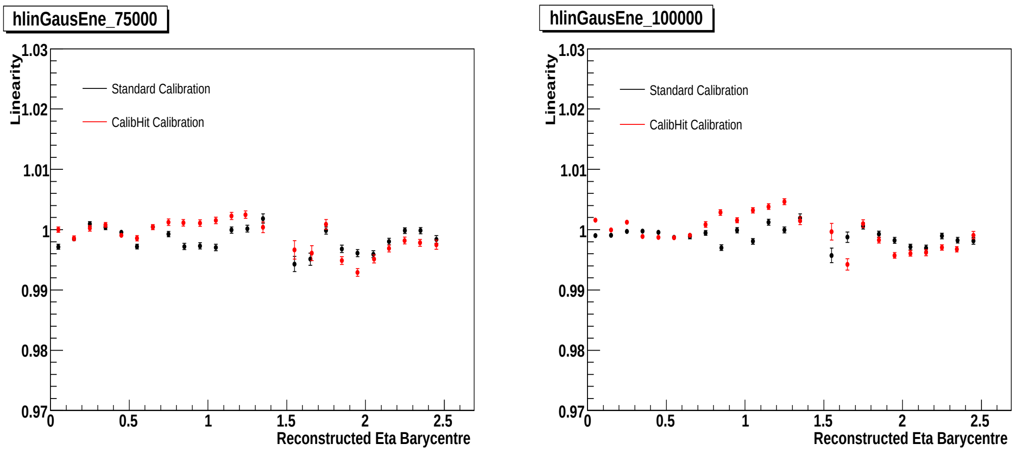

(c) E=75GeV (d) E=100GeV

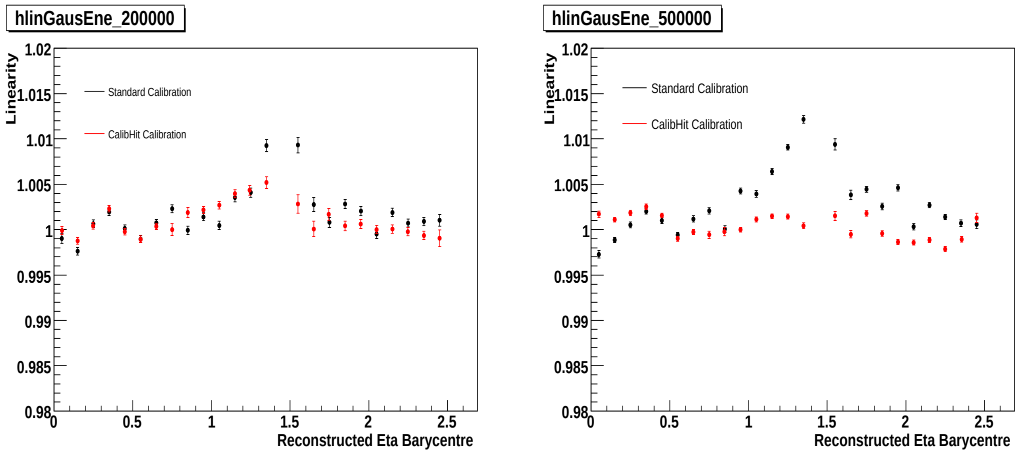

(e) E=200GeV (f) E=500GeV

Figure 5.43: Linearity for various energies. In black are shown the results with longitudinal weight calibration, while in red the Calibration Hits results are shown

5.5 Sensitivity to the amount of material in front of the calorimeter

To test the sensitivity of the proposed calibration method to possible underestimation of the amount of material in front of the calorimeter some studies have been done.

The amount of material in front of the calorimeter is a crucial parameter to well determine the e/γ energy. To mimic the effect of a possible underestimation of the front material we are using sets of coefficients for the front energy reconstruction extracted for cells with different amount of upstream material.

We select the region with $0.9 < |\eta| < 1.2$, in which a smooth variation of the material in front on calorimeter is present. We start reconstruction the energy at η=1.2 with all the coefficients calculated for this cell, achieving the better energy resolution and linearity possible, shown in the first line of table (5.4). At η=1.2 about 4.5 X_0 of material is present in front of the calorimeter. Then we reconstruct the energy at η=1.2 using all the parameters for this cell, except for the ones for the reconstruction of the energy deposited in front of calorimeter, that are taken from cells with less material upstream calorimeter, like the ones with cell center at η=1.175, 1.075, 1.0 and 0.9. In this way we can test the effect of an underestimation of the material in front of the calorimeter on the performances of the calibration method.

In table (5.4) the results are shown for two electron energies, 25 GeV and 100 GeV. The largest variation of the amount of material in front of the calorimeter, about $0.5X_0$ that correspond to a percentual variation of 12.5% in the region with $0.9 < |\eta| < 1.2$, implies a worsening of the energy resolution ($\frac{\sigma}{E}$) of ~5.3% at 25GeV and of ~2% at 100 GeV. The linearity vary almost of 1% at both energies.

The proposed method gives good results in term of energy resolution and linearity also with an underestimation of the material in front of the calorimeter up to ~10%, large amount probably not realistic in the Atlas experiment.

Front Par η	$X(X_0)$	$\Delta X(\%)$	$\frac{\sigma}{E}$	$\Delta(\frac{\sigma}{E})(\%)$ E=25GeV	L(%)	$\frac{\sigma}{E}$	$\Delta(\frac{\sigma}{E})(\%)$ E=100GeV	L(%)
1.200	4.50	-	3.39	-	0.1	1.90	-	0.1
1.175	4.40	2.5	3.43	1.18	0.2	1.91	0.50	0.2
1.075	4.35	3.75	3.45	1.47	0.3	1.92	1.05	0.2
1.000	4.15	8.75	3.54	4.40	0.4	1.93	1.57	0.4
0.900	4.00	12.5	3.57	5.30	0.9	1.94	2.10	0.5

Table 5.4: Sensitivity to the material in front of calorimeter. Energy resolution and linearity for 25 and 100 GeV electrons at η=1.2. The first line shows the results with all the calibration coefficients extracted for the cell at η=1.2, while the other lines show the results for energy reconstruction at η=1.2 achieved using all the parameters for this cell except the front parameters, that come from cells at the η points shown in the first column.

Conclusions and Perspective

The Atlas LAr electromagnetic calorimeter is designed to provide a precise measurement of electrons and photons energies, in order to meet the requirements coming from the LHC physics program. This request of precision makes important to understand the behavior of the detector in all its aspect. Of fundamental importance to achieve the best possible performances is the calibration of the EM calorimeter, and this is the topic of this thesis.

With detailed Monte Carlo simulations of single electrons and photons in the Atlas detector, we find a method to calibrate the electromagnetic calorimeter, based only on the informations that come from it. All the informations needed to develop a calibration method come from the simulations made with the technique of the *Calibration Hits*, that allows to know the energy deposited in all the materials inside the detector volume, and not only in the active layer of each subdetector as possible in the standard simulations, as explained in chapter (3). This technique required a big effort for the development of all the algorithms, because at the time of the firsts rounds of simulations the standard reconstruction code could not work on the calibration hits informations.

The simulations can be grouped into four rounds, with different conditions to disentangle different effects and allow to study in detail the showering process inside the calorimeter.

First step was to study a possible calibration scheme, and we start in the simplest possible condition: electrons hitting the center of a middle compartment cell, without the magnetic field in the inner detector region. Detailed study on this simulations allows us to find a possible calibration procedure, as discussed in great detail in the section (4.1). In this simple condition the performances of the electromagnetic calorimeter barrel have been tested, giving good results in term of energy resolution and linearity, with a sampling term varying in η from the 10% to the 15% and the linearity within 0.5%.

Second step was to introduce the effect of the impact point of the particles inside the cell on the reconstructed energy. This was done simulating electrons with the impact point on the calorimeter spread uniformly over the full middle compartment cell, without the magnetic field in the inner detector. Studies on the reconstruction of the barycenter of the shower and its comparison with the simulated η and ϕ positions have been done, as discussed in section (4.2). Two modulations on the reconstructed energy, due to the η and ϕ positions of the impact point inside the cell, are studied and two correction were included in the method. The performances of the method in term of energy resolution and linearity are slightly affected by the impact point modulations: the resolution goes from 10% to 17% in the barrel region, with a linearity better than 0.5%.

The third step in our analysis was to introduce the magnetic field in the inner detector region. This is the normal condition in the Atlas experiment and need to be studied in great detail. The effect of the magnetic field on the shower development is to deflect the particles of the shower in the ϕ direction, and this effect can be very large for low energy electrons, that can be deflected up to 4 middle cell width. The largest effect of the magnetic field is on the electrons that emit hard bremsstrahlung photons: in this case the presence of two different clusters in the calorimeter is evident and introduce large errors in the evaluation of the energy deposited outside the cluster. This problem is solved with a new method for the reconstruction of the energy deposited outside the cluster and it is discussed, together with other details for the events selection, in section (4.3). The method performances are a little worse: resolution from 10% to 17% and linearity within 0.5%, excluding the 5 GeV electrons.

The first three steps of analysis are done on private data sets that have been simulated with big effort on the Milan computing facility. With the aim of including the proposed calibration procedure in the Athena framework, we focused on the analysis of the data available from the central production, the CSC (Computing System Commissioning) data set, that become available in 2007 and contains all the informations from the calibration hits that are required for the proposed calibration method. This CSC data sets are simulated with the newest detector geometry and are digitized to simulate in the best way the real data that will be given by the detector in the actual operative condition of Atlas. Different energies have been simulated, both for electrons and photons, covering uniformly the full η range of the calorimeter, including also the two endcap regions not simulated before for the limited computing resources available.

The method proposed shows good results both for electrons and photons, and over all the η range of the calorimeter, as discussed in chapter (5), where the difference between the two particle type and the difference in the reply of the various region of calorimeter are discussed.

Finally the proposed calibration method is implemented in the Athena framework, and can be used as an alternative to the standard calibration method based on the longitudinal weights. The performances of the preliminary implementation of the proposed calibration method are shown in chapter (5), in comparison with the performances of the other calibration method.

The method proved also to be not very sensitive to an underestimation of the material in front of the calorimeter: a 10% of variation of the upstream material, change the resolution for 100 GeV electrons of 2% and the linearity of 0.5%.

Some questions are still open and need more investigations, possible only with larger statistic:

- study of a calibration strategy for photons converting at different radius
- define a calibration method in the crack region
- study new parametrization to improve the performances of the method in the region of the endcap without the PreSampler
- study low energy (10 GeV) particles

The proposed method gives, in its first implementation into Athena, results comparable with the ones provided from the other calibration method based on longitudinal weights. The parameter extraction, and consequently the method performances, can be improved, provided that larger statistic will be available. The Cern comunity of liquid argon detector have largely approved this new calibration method, that is recognized as a valid alternative to the standard calibration method.

Acknowledgments

I am really grateful to my supervisor Prof. Luciano Mandelli for giving me the opportunity to become part of the Atlas LAr group of Milan, for his valuable advice and for his support during these three years. I am deeply thankful to him for his guidance and for giving me the opportunity to freely choose the field of research of my thesis.

I am deeply indebted to Leonardo Carminati for his daily professional support: without his help for all the simulation work and his suggestion my job would have been a lot more harder.

I am very grateful to the Milan computing team for the support in jobs processing. I am also very grateful to Tancredi Carli who first suggested the present calibration method and to Guillaume Unal for his suggestions and support.

Bibliography

[1] *The Large Hadron Collider*. Technical Report CERN/AC/95-05, CERN, 1995.

[2] The ATLAS collaboration. *Technical Proposal for a General–Purpose pp Experiment at the Large Hadron Collider at CERN.* Technical Report CERN/LHCC/94-43, CERN, 1994.

[3] The ATLAS collaboration. *Detector and Physics performances Technical Design Report* . Technical Report CERN/LHCC/99-14 and 99-15, CERN, 1999.

[4] The ATLAS collaboration. *Inner Detector Technical Design Report*. Technical Report CERN/LHCC/97-16 and 97-17, CERN, 1997.

[5] The ATLAS collaboration. *Pixel Detector Technical Design Report*. Technical Report CERN/LHCC/98-13, CERN, 1998.

[6] The ATLAS collaboration. *Liquid Argon Calorimeter Technical Design Report*. Technical Report CERN/LHCC/96-41, CERN, 1996.

[7] The ATLAS collaboration. *Tile Calorimeter Technical Design Report*. Technical Report CERN/LHCC/96-42, CERN, 1996.

[8] The ATLAS collaboration. *Muon Spectrometer Technical Design Report*. Technical Report CERN/LHCC/97-22, CERN, 1997.

[9] The ATLAS collaboration. *High–Level Triggers, DAQ and DCS Technical Design Report*. Technical Report CERN/LHCC/2000-17, CERN, 2000.

[10] The ATLAS collaboration. *First Level Trigger Technical Design Report*. Technical Report CERN/LHCC/98-14, CERN, 1997.

[11] The ATLAS collaboration. *ATLAS Computing Technical Design Report*. Technical Report CERN/LHCC/2005-22, CERN, 2005.

[12] R. Brun, R. Hagelberg, M. Hansroul, J.C. Lassalle. *Simulation program for particle physics experiments, GEANT : user guide and reference manual*. CERN-DD-78-2 (CERN, Geneva, 1978).

[13] *GEANT. Detector description and simulation tool.* CERN Program Library Long Write-up W5013 (CERN, Geneva, 1994).

[14] The ATLAS collaboration. *Calorimeter Performance Technical Design Report*. Technical Report CERN/LHCC/96-40, CERN, 1996.

[15] B. Aubert et al. . *Construction, assembly and tests of the ATLAS electromagnetic barrel calorimeter*. *NIM A*, 558:601–623, 2006.

[16] M. Aharrouche. et al. . *Energy linearity and resolution of the ATLAS electromagnetic barrel calorimeter in an electron test-beam*. *NIM A*, 568:601–623, 2006.

[17] J. Colas et al. *Position resolution and particle identification with the ATLAS EM calorimeter* . *NIM A*, 550:96–115, 2005.

[18] Wigmans R. et al. *Intercalibration of the longitudinal segments of a calorimeter system*. *NIM A*, 487:381–395, 2002.

[19] Wigmans R. *Sampling calorimetry*. *NIM A*, 494:277287, 2002.

[20] Wigmans R. et al. *On the calibration of longitudinally segmented calorimeter systems*. *NIM A*, 409:621–628, 1998.

[21] W.E. Cleland and E.G. Stern. *Signal processing considerations for liquid ionization calorimeter in a high rate environment*. *NIM A*, 338, 1984.

[22] M. Citterio, M. Delmastro and M. Fanti. *A study of the electrical properties and of the signal shapes in the ATLAS Liquid Argon Accordion Calorimeter using a hardware model*. *ATLAS Internal Note*, ATL-LARG-2001-018, 2001.

[23] The USA ATLAS collaboration. *The Mother Board system for the Liquid Argon barrel calorimeter*. `http://www.usatlas.bnl.gov/detector/lar/mb/`.

[24] G. Battistoni et al. *Specification Requirements for Warm Preamplifiers*. `http://www.mi.infn.it/~battist/preampl2.html`.

[25] J. Ban, S. Negroni, J. Parsons, S. Simion, B. Sippach. *Design and Implementation of the ATLAS LAr Front End Board*. `http://www.nevis.columbia.edu/~atlas/electronics/ATLASFEB/`.

[26] R. L. Chase, C. de la Taille, J. P. Richer, N. Seguin-Moreau. *A fast monolithic shaper for the ATLAS e.m. calorimeter*. In *Proc. 5th International Conference on Calorimetry in High-energy Physics*, 1994.

[27] L. Neukermans, P.Perrodo and R. Zitoun. *Understanding the electromagnetic barrel pulse shapes and the absolute electronic calibration*. *ATLAS Internal Note*, ATL-LARG-2001-008, 2001.

[28] D.Banfi, M.Delmastro, M.Fanti. *Cell response equalization of the ATLAS electromagnetic calorimeter without the direct knowledge of the ionization signals*. *JINST*, pages 1–P08001, 2006.

[29] Y. Jaquier, C. de La Taille, I. Nikolic, L. Serin. *Strenghs and weakness of digital filtering*. *ATLAS Internal Note*, ATL-LARG-97-080, 1997.

[30] S. Paganis et al. *Combined Intercalibration and Longitudinal Weight Extraction for the ATLAS Liquid-Argon EM Calorimeter*. *ATLAS Internal Note*, ATL-LARG-2004-012, 2004.

[31] M. Delmastro and M. Fanti. *Energy resolution optimization through layers measurements weighting: analytical solutions and numerical strategies*. *ATLAS Internal Note*, ATL-LARG-2002-002, 2002.

[32] Wigmans R. et al. *On the differences between calorimetric detection of electrons and photons*. *NIM A*, 485:38539, 2002.

All ATLAS internal notes approved by the Collaboration are accessible through the web at http://cdsweb.cern.ch/ *by typing the document identifier (e.g.* ATL-LARG-****)* *in the search field.*